

# UC San Diego

## UC San Diego Electronic Theses and Dissertations

### Title

New Insights into the Heterogeneous Chemistry and Photochemistry of Indoor and Outdoor Environments

### Permalink

<https://escholarship.org/uc/item/6006g2q0>

### Author

Alves, Michael Rui Clemente

### Publication Date

2021

Peer reviewed|Thesis/dissertation

UNIVERSITY OF CALIFORNIA SAN DIEGO

New Insights into the Heterogeneous Chemistry and Photochemistry of Indoor and Outdoor  
Environments

A dissertation submitted in partial satisfaction of the requirements for the degree of Doctor of  
Philosophy

in

Chemistry

by

Michael R. Alves

Committee in charge:

Professor Vicki Grassian, Chair  
Professor Lihini Aluwihare  
Professor Francesco Paesani  
Professor Jonathan Slade  
Professor Wei Xiong

2021

Copyright

Michael R. Alves, 2021

All rights reserved

The thesis of Michael R. Alves is approved, and it is acceptable in quality and form for the publication on microfilm and electronically.

University of California San Diego

2021

## DEDICATION

*To my Mae, Palmira Alves, a minha avó*

*and my Titi, Eve Silver*

*and*

*in memory of my grandmother, Bernice “Benny” Possiel.*

*I will always be grateful for the support and love I received from you all.*

*Estarei sempre grato pelo apoio e amor que recebi de todos vós.*

## **EPIGRAPH**

Believe in the power of low effort and low risk opportunities with high rewards  
– surely, they're out there somewhere.

## TABLE OF CONTENTS

DISSERTATION APPROVAL PAGE .....	iii
DEDICATION.....	iv
EPIGRAPH.....	v
TABLE OF CONTENTS .....	vi
LIST OF FIGURES .....	ix
LIST OF TABLES.....	xiii
ACKNOWLEDGMENTS .....	xiv
VITA.....	xxi
ABSTRACT OF THE DISSERTATION.....	xxiv
Chapter 1: An Introduction to Heterogeneous and Multiphase Chemistry and Photochemistry .....	1
1.1 Heterogeneous and Multiphase Chemistry and Photochemistry in Outdoor Environments .....	2
1.1.1 Dissolved Organic Matter in the Marine Environment and Its Impacts .....	2
1.1.2 Analysis of m-DOM .....	4
1.1.3 Photochemistry in the marine environment .....	6
1.2 Heterogeneous and Multiphase Chemistry and Photochemistry in Indoor Environments .....	9
1.1.4 The Indoor Environment.....	9
1.1.5 Surface Chemistry and Photochemistry in the Indoor Environment .....	9
1.1.6 Fate of Semi-volatile Organic Compounds Indoors .....	11
1.1.6 Indoor Use of Caustic Cleaning Substances .....	12
1.3 Description of Thesis Chapters .....	13
1.4 References.....	14
Chapter 2: Experimental Methods and Method Development .....	19
2.1 Extraction of Marine-Dissolved Organic Matter .....	19
2.3 Heated Electrospray Ionization High Resolution Mass Spectrometry (HESI-HRMS) .....	23
2.3 Attenuated Total Reflectance Fourier Transform Infrared (ATR-FTIR) Spectroscopy .....	24
2.4 Teflon Chamber Design, Construction and Operation.....	27
2.5 References.....	28
2.6 Liquid Sampling Atmospheric Glow Discharge Characterization and Application.....	30
2.6.1 Experimental Methods.....	32
2.6.2 Examples.....	35
2.6.3 Acknowledgements.....	48
2.6.4 References.....	48
Chapter 3: Shedding Light on Photosensitizers in the Marine Environment and Their Interactions with Nonanoic Acid .....	52
3.1 Abstract.....	52

3.2 Introduction.....	52
3.3 Experimental Methods.....	55
3.3.1 Chemicals and Production of m-DOM.....	55
3.3.2 TOC Analysis.....	56
3.3.3 Analysis of Photosensitized Reactions with Nonanoic Acid.....	56
3.3.4 Analyses of Photosensitizers.....	58
3.4 Results and Discussion.....	60
3.4.1 Analysis of Photosensitized Reactions for Three Different Photosensitizers.....	60
3.4.2 Comparison of m-DOM and Humic Acid: Molecular Composition and Chromophores.....	71
3.5 Conclusions.....	77
3.6 Acknowledgements.....	79
3.7 Supporting Information.....	79
3.8 References.....	85
Chapter 4: Changes in Light Absorption and Composition of Chromophoric Marine-Dissolved Organic Matter Across a Microbial Bloom.....	88
4.1 Abstract.....	88
4.2 Introduction.....	89
4.3 Experimental Methods.....	90
4.4 Results and Discussion.....	94
4.5 Acknowledgements.....	103
4.6 Supporting Information.....	104
4.7 References.....	109
Chapter 5: Large-Scale Collaborative Effort in Understanding the Properties, Composition, and Reactivity of Marine Dissolved Organic Matter Collected during SeaSCAPE 2019.....	109
5.1 Overview.....	116
5.2 Introduction.....	117
5.3 Collaborative Efforts in the Use of a Central Standard of Marine-DOM.....	118
5.4 Benzothiazoles in the Coastal Marine Environment.....	120
5.4.1 Experimental Methods.....	122
5.4.2 Results and Discussion.....	125
5.4.3 Acknowledgments.....	140
5.4.4 Supporting Information.....	140
5.4.5 References.....	141
Chapter 6: Chemistry and Photochemistry of Pyruvic Acid on Metal Oxide Surfaces.....	148
6.1 Abstract.....	148
6.2 Introduction.....	149
6.3 Experimental Methods.....	152



6.4 Results and Discussion.....	154
6.5 Conclusions.....	169
6.6 Acknowledgements.....	170
6.7 Supporting Information.....	171
6.8 References.....	172
Chapter 7: SiO <sub>2</sub> Interactions with Hypochlorous Acid: Insights into the Interaction of Cleaning Products with Glass Surfaces.....	181
7.1 Abstract.....	181
7.2 Introduction.....	181
7.3 Experimental Methods.....	183
7.4 Results and Discussion.....	184
7.5 Conclusions.....	193
7.6 Acknowledgements.....	194
7.7 References.....	194
Chapter 8: Future Directions .....	196

## LIST OF FIGURES

Figure 1.1 Diagram showing the production of primary and secondary organic aerosol from the ocean surface and the sources of m-DOM. ....	3
Figure 1.2 Negative mode mass spectrum of solid phase extracted m-DOM with zoom-in spectra showing base-line separated peaks at a resolution of ~240,000. ....	5
Figure 1.3. Simplified diagram of an excited state photosensitizer and the intersystem crossing process, where $S_0$ is the singlet ground state, $S_1$ is the singlet excited state, and $T_1$ is the triplet excited state. $k_D$ refers to the rate of relaxation of the forbidden transition between $T_1$ and $S_0$ . ....	7
Figure 1.4. Illustration of the electron-hole pair generation from a $TiO_2$ , or photocatalytic, surface. ....	10
Figure 1.5. Schematic of some of the complex heterogenous and multiphase chemistry that occurs indoors. ....	11
Figure 2.1. General workflow of extracting m-DOM from seawater: (a) sample of seawater; (b) vacuum filtration; (c) filtered seawater; (d) acidification with 1M HCl to pH 2; series of e) solid phase extractions with rinses of (f) water and (g) methanol. ....	20
Figure 2.2. Photo of one of the SPE column “udders” in action. ....	22
Figure 2.3. Chemical structures of $C_7H_{12}O$ as a) cyclohexanal and b) 1-hydroxylmethylcyclohexene. Although the same m/z, there are clear differences between the two molecules that can be determined by infrared spectroscopy. ....	25
Figure 2.4. Diagram of the ATR crystal, housing, and reflected IR radiation. <i>Figure by Isaac Sit</i> . ....	26
Figure 2.5. A schematic of the 0.18 m <sup>3</sup> Teflon chamber used in the HOCl experiments. Zero air is cleaned of organics and carbon dioxide in lab and dried below 5% RH. MFC refers to mass flow controller. ....	28
Figure 2.6 Graphical representation of the LS-APGD. ....	33
Figure 2.7. Averaged mass spectra obtained from HRMS analysis of triglyceride mixture in 100 mM NaCl by ESI (a) and LS-APGD (b). ....	36
Figure 2.8. Triglyceride mixture analysis for neat ESI (a), APGD (b), and ESI at 1mM NaCl (c) ....	38
Figure 2.9. LS-APGD Triglyceride:diglyceride fragmentation ratios from 0.01-100mM for triglyceride mixture samples at constant electrode distance (0.5 mm) and discharge current (30 mA). ....	40
Figure 2.10. HRMS analysis of SRFA, with (black) and without salt (colored), at various electrode currents and positions with corresponding ESI values analyzed using SRFA (no salt) at the same concentration. Relationships shown between: (a) Number of identified molecules averaged mass spectra; (b) hydrogen:carbon ratios and; (c) oxygen:carbon ratios. ....	43
Figure 2.11. Van Krevelen diagrams of m-DOM spectra showing oxygen:carbon (OC) and hydrogen:carbon (HC) ratios, measured by (a) traditional ESI and (b) LS-APGD. A comparison is shown for spectra obtained with (50 mM added NaCl) salt (red circles) and without salt (light blue circles), where the overlap of elemental compositions is also shown (purple circles). ....	44

Figure 2.12. High resolution mass spectra of pure bloom coastal seawater obtained by LS-APGD Orbitrap mass spectrometry. ....	46
Figure 3.1. Select regions of ATR-FTIR difference spectra (final-initial) of 60-minute non-irradiated (gray lines) and irradiated (colored lines) NA in the presence of A) BBA; B) HA and C) m-DOM. Spectra were collected every 10 minutes. Lines become increasingly light with increased time. ....	63
Figure 3.2. Proposed mechanism for the photosensitized reaction of NA. All products shown were present when BBA was used as the photosensitizer. Products highlighted in green and blue were present when HA and m-DOM was the photosensitizer, respectively. Pathway modified from Tinel et al., 2016. <sup>10</sup> .....	70
Figure 3.3. Excitation-emission matrices of A) humic acid and B) m-DOM. Data collected and processed by Mitch Santander in the Prather Research Group. ....	71
Figure 3.4. ATR-FTIR spectra of A) humic acid and B) m-DOM extracted from a lab-grown phytoplankton culture. Peak assignments are listed in Table 2. ....	72
Figure 3.5. Relative abundance of each molecular class in humic acid and m-DOM as determined by HESI-LIT-Orbitrap MS analysis calculated according to the methods section. ....	76
Figure 3.6. ATR-FTIR spectra of thin films of each of the photosensitizers. ....	80
Figure 3.7. ATR-FTIR spectra of nonanoic acid alone and with each of the photosensitizers used in this study. Peak assignments for nonanoic acid are shown in Table S1. ....	81
Figure 3.8. ATR-FTIR difference spectra of 60-minute irradiated A) nonanoic acid (NA) by itself and B) a thin film of m-DOM by itself. Spectra were collected every 10 minutes. Lines become increasingly light with increased time. Changes in the NA spectra and m-DOM spectra alone may be associated with evaporation, thermal effects, or. ....	82
Figure 3.9. Signal detected (counts) for select products analyzed by HESI-LIT-Orbitrap MS in positive (left) and negative (right) mode of irradiated (light colored), non-irradiated (dark colors), and water blanks (grey) of NA alone (control) and NA in the presence of BBA. ....	83
Figure 3.10. Signal detected (counts) for select products analyzed by HESI-LIT-Orbitrap MS in positive (left) and negative (right) mode of irradiated (light colored), non-irradiated (dark colors), and water blanks (grey) of A) NA in the presence of BBA, B) NA in the presence of HA, and C) NA in the presence of m-DOM. ....	84
Figure 4.1. Mass attenuation coefficient spectrum of m-DOM samples, calculated from the UV-VIS spectra, collected from the SeaSCAPE Bloom 3 experiment. All spectra were taken dissolved in methanol. Samples were dissolved to a standard mass concentration of the extracted m-DOM. Inset: The inset spectra show the 1 <sup>st</sup> derivative of the m-DOM. ....	95
Figure 4.2. Analysis of m-DOM composition using high resolution mass spectrometry data correlated to UV-VIS absorbance data across the bloom experiment. van Krevelen plots with all m-DOM formulae as a reference are in light grey, (A) compounds produced post-bacterial bloom, and (B) compounds correlated with spectral slopes $S_{275-295}$ and $S_{350-400}$ . ....	98
Figure 4.3. (a) Dissolved organic carbon measurement by TOC Analysis via combustion catalytic oxidation, (b) chlorophyll a concentration, and (c) heterotrophic bacterial cell counts per liter of seawater. ....	105

Figure 4.4. Van Krevelen diagrams of m-DOM samples collected throughout the bloom, colored by their normalized relative peak intensity. *Figures made by Dr. Elizabeth Coward.* ..... 106

Figure 4.5. (A) Percent change in mean heteroatomic ratios of nitrogen (N), sulfur (S), and phosphorous (P) atoms per carbon (C) atom. (B) Molecular weight (Da) distributions, and (C) aromaticity index  $AI_{mod}$  distributions of all assigned formulae over experimental sampling time.. ..... 107

Figure 4.6. Changes in dissolved organic matter formulae parameters over experimental time. *Figures made by Dr. Elizabeth Coward.* ..... 108

Figure 5.1. Summary of the collaborative research groups using the collect m-DOM/m-CDOM sample. .... 119

Figure 5.2. High resolution mass spectra of the VOCs from bloom water using APCI..... 126

Figure 5.3. Time series of biological activity indicators and water temperature (A) and atmospheric benzothiazoles (B) at SeaSCAPE 2019 bloom 3 experiment. Atmospheric benzothiazole concentrations are differentiated into gas phase BT from the dome (black circles) and submicron nascent sea spray aerosol phase benzothiazoles from the wave chamber (colored bars).. ..... 128

Figure 5.4. Molecular distributions and molecular overlap (by mass) of benzothiazoles observed in DOM (left) and nascent sea spray aerosol (right) at SeaSCAPE 2019. *Data and figures by Emily Barnes-Franklin.* ..... 134

Figure 5.5. Solubility distributions of benzothiazoles weighted by contribution to cumulative observed benzothiazole carbon pools in the dissolved (DOM) and aerosol (SSA) phases. Number of individual species within each solubility bracket in each phase indicated by *n*. ..... 135

Figure 5.6. Nucleation of new particles from benzothiazole oxidation in PAM-OFR. Liquid benzothiazole dissolved in a methanol carrier (1% BT) is introduced at 5 minutes..... 139

Figure 6.1. FTIR spectra of (a)  $Al_2O_3$  following exposure to gas-phase pyruvic acid for 20 minutes under dry conditions as a function of pyruvic acid pressure (5, 10, 20, 50, 100, 634, 856 and 1124 mTorr) in the spectral range from ca. 2500 to 4000  $cm^{-1}$  and 900 to 1900  $cm^{-1}$ ; (b) Exposure of to 20 mTorr of gas-phase pyruvic acid as a function of time in the spectral range extending from 900 to 1950  $cm^{-1}$ . ..... 155

Figure 6.2. (a) FTIR spectra (800 to 4000  $cm^{-1}$ ) of  $TiO_2$  following exposure to gas-phase pyruvic acid for 20 minutes under dry conditions as a function of pressure (10, 30, 75, 190, 310 and 625 mTorr) in the spectral range from ca. 2500 to 4000  $cm^{-1}$  and 900 to 1900  $cm^{-1}$ ; (b) FTIR spectra (900 to 1900  $cm^{-1}$ ) ..... 156

Figure 6.3. FTIR spectra in the region extending from 1250 to 1850  $cm^{-1}$  of  $Al_2O_3$ ,  $TiO_2$ , and  $SiO_2$  following exposure to ca. 50 mTorr of pyruvic acid. Each spectrum was taken 20 minutes after introduction of gas-phase pyruvic acid under dry conditions (RH < 1%). *Data and figure collected and analyzed by Dr. Yuan Fang.*..... 158

Figure 6.4. FTIR difference spectra in the spectral region extending from 950 to 1900  $cm^{-1}$  is shown. Following introduction of 100 mTorr of pyruvic acid followed by evacuation, adsorbed pyruvate remains on the surface of  $Al_2O_3$  and  $TiO_2$ . Each spectrum was collected every 15 minutes for a total 150 minutes.. ..... 162

Figure 6.5. Comparison of the pyruvate loss from Al<sub>2</sub>O<sub>3</sub> and TiO<sub>2</sub> surfaces during irradiation. The peak intensity of the C=O stretch for adsorbed pyruvate (near 1730 cm<sup>-1</sup>) before irradiation is used as I<sub>0</sub>. The first order rate constant determined from the slope  $0.6 \times 10^{-4} \text{ min}^{-1}$  for Al<sub>2</sub>O<sub>3</sub> and  $2.1 \times 10^{-3} \text{ min}^{-1}$  for TiO<sub>2</sub> respectively. *Data and figure collected and analyzed by Dr. Yuan Fang.* .....162

Figure 6.6. Possible photochemical formation pathway for zymonic acid from pyruvic acid (PA). This reaction has also been shown to proceed spontaneously through the dimerization of pyruvic acid. ....164

Figure 6.7. A proposed mechanism, adapted from Rapf and coworkers<sup>48</sup>, involves two excited state adsorbed pyruvate molecules, where one pyruvate undergoes hydrogen-abstraction via another pyruvate, leading to the formation of CO<sub>2</sub>, CH<sub>3</sub>-CO•, and PA•. It is important to note that this mechanism does not proceed to form DMTA, a major product in the aqueous phase photochemistry of pyruvic acid.<sup>98</sup> .....168

Figure 6.8. Relative abundance of chosen assigned molecular formulas normalized to the intensity peak of pyruvate following extraction from Al<sub>2</sub>O<sub>3</sub>.....171

Figure 6.9. Relative abundance of chosen assigned molecular formulas normalized to the intensity peak of pyruvate following extraction from TiO<sub>2</sub>. ....172

Figure 7.1. FTIR difference spectra of SiO<sub>2</sub> following exposure to gas-phase HOCl and Cl<sub>2</sub> for 60 mins under relatively dry conditions (RH < 15%) as a function of time. A spectrum was collected following 60 minutes of dry clean air flowing over the chlorine-exposed silica thin film (shown by the black dashed line). Spectrum used for background subtraction was a clean silica thin film in dry air. ....186

Figure 7.2. Comparison of infrared spectra of HOCl absorbing and reacting with (a) SiO<sub>2</sub> collected using ATR-FTIR spectroscopy, via online analysis, using an AMTIR crystal (solid orange) and, (b) via offline analysis, AFM-PTIR spectroscopy (solid light blue). Controls of unreacted bare silica are shown in the dashed lines for both methods.. ....187

Figure 7.3. Images of the -ClO<sub>2</sub> molecule bonded to an SiO<sub>2</sub> surface in two different hypothetical conformations: a) bridging bidentate and b) monodentate, surrounded by surface hydroxyl groups. The chlorine atoms are colored green, the silicon atoms blue, the oxygen atoms red, and the hydrogen atoms are white. ....188

Figure 7.4. TEM images of a silica nanoparticle that is a) clean and b) exposed to HOCl/Cl<sub>2</sub>. *Images taken by Isaac Sit.*.....191

Figure 7.5. FTIR difference spectra of SiO<sub>2</sub> following exposure to the headspace gases collected from an acidified bleach (Clorox) solution under relatively dry conditions (RH < 15%) as a function of time. A spectrum was collected following 60 minutes of dry clean air flowing over the bleach-exposed silica thin film (shown by the black dashed line). ....192

## LIST OF TABLES

Table 1.1. Photochemical reactions for an excited molecule, M*, adapted from Calvert and Pitts. ....	8
Table 3.1. Signal strength and enrichment ratios for select products as detected by MS analysis for samples of various photosensitizers in the presence of NA. ....	66
Table 3.2. Peak assignments of ATR-FTIR spectra of humic acid and m-DOM. ....	74
Table 3.3. Vibrational peak assignments for nonanoic acid. ....	81
Table 4.1. Averaged mass spectral characteristics of marine dissolved organic samples across bloom experiment comparison to correlated subset data per spectral parameter, weighted by relative intensity. .	99
Table 4.2. Selected classes of compounds that have been shown to be 1) produced naturally in marine environment by microbes and/or 2) have shown to be environmentally relevant photosensitizers characteristics (see references). ....	101
Table 4.3. Summary of analyzed HRMS data .....	104
Table 5.1. Identities, solubilities, and concentrations of benzothiazoles observed at SeaSCAPE. Aerosol phase concentrations are reported as an average and standard deviation of concentrations over the full experimental campaign, while dissolved phase concentrations are reported from the initial pre-experiment sample for comparison to other ambient sampling measurements of benzothiazoles. ....	130
Table 6.1. Vibrational mode assignment ( $\text{cm}^{-1}$ ) for adsorbed pyruvate formed on the surface of $\text{Al}_2\text{O}_3$ and $\text{TiO}_2$ following adsorption of gas-phase pyruvic acid.* .....	160
Table 6.2. Selected Compiled Photochemistry HRMS Data of Adsorbed Pyruvic Acid on $\text{Al}_2\text{O}_3$ .....	165
Table 6.3. Selected Compiled Photochemistry HRMS Data of Adsorbed Pyruvic Acid on $\text{TiO}_2$ .....	166
Table 7.1 Theoretical and Experimental Vibrational Mode Assignments (in $\text{cm}^{-1}$ ) for Adsorbed HOCl (as surface $-\text{ClO}_2$ ) on the Surface of Silica. ....	190

## ACKNOWLEDGMENTS

I did not begin my journey in the sciences with the intent to find something that I love to do or to reach some sort of enlightenment in my life's purpose. Although that latter part still has not happened (fingers crossed), I am constantly shocked at how I ended up in a place in my life where I can genuinely say that I am happy with both my work and personal lives. It is an irrevocable fact that I ended up where I am today because of the people around me and their constant support. Though I like to think myself as opportunistic, it would be a misrepresentation to say that those opportunities were only created by myself. This list of acknowledgements is quite long, but I wouldn't have it any other way.

Working my way through my junior and senior high schools and eventually community college, I faced, what seemed to me at the time, a large number of barriers. Though this will not be shocking to the people close to me, I struggled with my memory, both short- and long-term, extensively throughout my life and to this day. My interest in chemistry grew during my first year in community college as I realized that I was unexpectedly sharp in recalling concepts, numbers, and mechanistic information in way that was impossible for me to do with any other subject or other area of life. This prompted me enough to change my major and the state I was currently living in so that I could pursue this field wholeheartedly. My first mentor, my Titi - Eve Silver, was the beginning in a long list of people who supported this endeavor. During this time, I also met a life-long friend, Anissa Santilli, one of the few outside the STEM field. Even though she says she never understands what I do for a living, the continued support for me and rapid-fire self-deprecating jokes has kept me centered for years to come.

At the Minneapolis Technical and Community College (MCTC), I began my track to receive an associate's degree in chemistry. I was excited to receive this degree and begin the

entry-level position for a nearby chemical company. It was my professors at MCTC, such as Dr. Rekha Ganaganur, that explained to me that not only could I get a bachelor's degree, but that it would also likely be a full-ride situation based on my situation and competence. This, as well as meeting Rebekah Dupont and "Tina" Maria Tavera at Augsburg College (now University), was likely the turning point in the start of my interest in the research sciences. It is both amazing, and somewhat sad, that for a first-generation student – the stars must align for one to be effectively mentored to help find their interests in academia. The AugSTEM and TRiO McNair programs helped exactly with this.

Receiving a paid position to do research with Dr. Dave Hanson at Augsburg College, the pay being a necessary component as I was working full-time at this point, was a thrilling point in my life. Learning how to set up hypotheses and experiments myself, even to the point of building instrumentation to do so, was invaluable to my current success. Also, being a waiter at a dive bar was horrible, so I was happy to throw in my serving apron. The tips were simply not worth it. Other names worth noting include Professors Vivian Feng, Michael Wentzel, Joan Kunz, Jennifer Bankers-Fulbright "Dr. B", and Christopher Huber. All of whom taught me, and made me excited about, key concepts that I still carry today, in my own experiments, and throughout this dissertation. I would be thoughtless to not include one of my best friends, Hilena Frew Gezahagne, in my list of acknowledgements. Our weirdly competitive, likely a bit toxic, friendship was something that I loved and absolutely needed to propel myself into the academic field. To this day, and hopefully even in the future, we continue to push each other to be better and perhaps, one day, more humble versions of ourselves. Additionally, my friends from the house I lived in, the ill-named Chilla Villa, were also consistently supportive of me throughout this journey- Mike, Lauren – and her Russian boy Ilya, Sarah, DJ, and Bri. My friendship with



Lauren Snell is noteworthy and close, as much as she probably wants to punch me, she would equally beat up anyone I didn't like.

Meeting Daniel Ocasio at an undergraduate advantage program at UC Berkeley, was yet another turning point in my life, both academically and personally. Now close to six years in our current relationship, I cannot acknowledge enough how much of a positive impact it has been on my life. Whatever the future may hold, I will be forever grateful for the stalwart support I received during all of the difficult times I've faced this past half decade. Perhaps one of the most important lessons I've learned in this relationship for my professional life, was the value of a work-life balance. I think without his support, I would have been burned myself out at least 6 times over by now. Daniel, I love you, and I'm eagerly waiting for you to finish your PhD program as well.

Quite often, do I get the question, "Why did you attend UC San Diego?" such as in grad student panels, from my mentees, teaching classes, etc. My answer to this question is along some form that I came here because Professor Vicki Grassian was here, not because the school, department, or location had some sort of fantastic incentive. I met Professor Grassian at the ACS San Diego Conference while I was still an undergraduate in 2016. At this point in my life, I knew I wanted to go to graduate school, but as a first-generation student, I was afraid of entering a program I didn't like and thus wasting five plus years of my life. Emailing and meeting many professors during my senior year of undergrad to avoid this, Professor Grassian stood out from the rest. Her style of mentoring and the support she gave me was something that fit my personality and needs exceptionally well. Rather than burning out or becoming uninterested in my studies like many unfortunately do, I was fortunate enough to receive the support I required to continue my interests and reach my goals at my own pace. I greatly acknowledge the help and

mentorship I received from Professor Grassian and I know that the many concepts I learned from her will travel with me to the next stages of my life. I advise anyone looking to attend graduate school, or know someone who might want to, to make sure that the style and type of mentorship they require is something their adviser is able to provide.

Though I might be biased, I think that my coworkers in the Grassian Research Group are much cooler than any of the other groups I've seen on campus. First and foremost, I'd like to thank Dr. Jonathan Trueblood (yes that's his real last name) and Dr. Armando Estillore for being fantastic mentors and dealing with me in my first 1-2 years of my graduate program. Even though Jon constantly stole my candy and food, his support for me both professionally and personally was valuable. Though the time was short, I'd also like to acknowledge Dr. Liz Coward who single handedly whipped me back into shape towards the second half of the COVID-19 pandemic and I will be eternally jealous of her new amazing job and driving skills. A shout out to Dr. Ellen Coddens for mimosa Sundays and her weird obsession with corgis that I regretfully enabled. I am also thankful to the boys, Dr. Victor Or and Izaac Sit, who unwillingly had to deal with me for so long. Especially grateful to Victor, who allowed me to ride his coattails on so many of these publications. Dinner parties at Izaac's was always a blast and Megan Liang, who would always go out on a limb for us. A shout out to Liora Mael, who no doubt placed curses on me during a séance or two, and great talks about cats and her neurodivergent dog. The Latinx club crew, Stephanie Mora Garcia, Mariana Rivas, and my mentee David Gonzales were all especially fun to be around. Duyen Dang and Masiel Belsuzarri, although my mentees, you taught me a lot about myself, and it was a great experience getting to know you both – I hope your futures and goals work out for the best. Deborah Kim is also notable, who fully enabled my obsession with throwing pottery on the wheel at a local studio for

the past few months – taking my mind off writing this entire thesis. I’d also like to thank the really comfortable green couch in the office as it has supplied me with many naps. Lastly, because this group is ridiculously large, I’d like to thank everyone else in the Grassian Research Group. Without everyone, I would not have had this much fun during my PhD program and I’m very grateful for having such a great cohort.

Working with the NSF Center for Aerosol Impacts on the Chemistry of the Environment (NSF-CAICE) was a fantastic opportunity for both research and meeting some great people. Special thanks to Dr. Neal Arakawa, Dr. Kim Prather, Alexia Moore, Emily Barnes-Franklin, Brock Mitts, Clare Morris, Dan Crocker, Ke’La Kimble, and more. Extra thanks to Dr. Kathryn Mayer and Dr. Jon Sauer, who ended up as my close friends and great colleagues in this field. Triple thanks to Monica Castrejon, a stalwart pillar of CAICE and an irreplaceable entity of positivity in this world.

My family had a positive factor in my journey through this program and I would like to acknowledge all their support and interest in it. My mother, Lisamarie, and my brothers, Andrew – and his wife Zee, Joe, and Nathan. My Titis, Eve and Yvette, Uncle Mark and Eliezer, Shannon and the three daughter states. I would like to thank all of you and those who I couldn’t fit here, for your support. To my Mae, Palmira Alves, who was forever supportive in my educational career even though she herself had to leave school in grade 4, I hope that I’ve learned enough for both of us. Portugal is very far away, and I can’t always say it, but I hope you know I think of you and the support you’ve given me constantly. My father, Rui “Roy”, in Portugal as well, his efforts to learn about the sciences and find ways to converse with me on a scientific level was not unnoticed as well as Ana Bela, the Ribeiro family, Nuno, Dylan, and Carlos. I might be preemptive, but I see the Ocasio’s as family too, and I would be remiss to not

acknowledge their obvious support for me. Elizabeth, Tony, Titi Vivian, and Nicholas Ocasio – and his fiancée Gabriella, have always expressed interest in my work and their encouragement is something I always look forward to when visiting.

A portion of Chapter 2 is reproduced with permission from the American Chemical Society: Alves, M. R.; Sauer, J. S.; Prather, K. A.; Grassian, V. H.; Wilkins, C. L. Liquid Sampling-Atmospheric Pressure Glow Discharge Ionization as a Technique for the Characterization of Salt-Containing Organic Samples. *Anal. Chem.* 2020, 92 (13), 8845–8851. The dissertation author was a primary investigator and co-first author of this paper.

Chapter 3 was reproduced with permission from: Trueblood, J. V.; Alves, M. R.; Power, D.; Santander, M. V.; Cochran, R. E.; Prather, K. A.; Grassian, V. H. Shedding Light on Photosensitized Reactions within Marine-Relevant Organic Thin Films. *ACS Earth Sp. Chem.* 2019, 3 (8), 1614–1623. The dissertation author was a primary investigator and co-first author of this paper.

Chapter 4 is in preparation: Alves, M.R.; Coward, E.K.; Gonzales, D.; Sauer, J.S.; Mayer, K.; Prather, K.A.; Grassian, V.H. Changes in Light Absorption and Composition of Chromophoric Marine-Dissolved Organic Matter Across a Microbial Bloom. *Environ. Sci. Technol.* 2021. The dissertation author is the primary investigator and author of this paper.

A portion of Chapter 5 is reproduced with permission from the American Chemical Society, currently under revisions: Barnes, E.B.; Alves, M.R.; Moore, A.N.; Kilgour, D.B.;

Novak, G.A.; Mayer, K.; Sauer, J.; Weber, R.J.; Dang, D.; Winter, M.; Lee, C.; Cappa, C.D.; Bertram, T.H.; Prather, K.A.; Grassian, V.H.; Goldstein, A.H. Atmospheric Benzothiazoles in a Coastal Marine Environment. *Environ. Sci. Technol.* 2021. The dissertation author was a primary investigator and co-first author of this paper.

Chapter 6 was reproduced with permission from: Alves, M. R.; Fang, Y.; Wall, K. J.; Vaida, V.; Grassian, V. H. Chemistry and Photochemistry of Pyruvic Acid Adsorbed on Oxide Surfaces. *J. Phys. Chem. A* 2019, 123 (35), 7661–7671. The dissertation author is the primary investigator and author of this paper.

Chapter 7 is in preparation: Alves, M.R.; Deeleepojananan, C.; Or, V.W.; Sit, I.; Grassian, V.H. SiO<sub>2</sub> Interactions with Hypochlorous Acid: Insights into the Interaction of Cleaning Products with Glass Surfaces. 2021. The dissertation author is the primary investigator and author of this paper.

## VITA

2012-2013 Brookdale Community College  
2013-2015 Minneapolis Community and Technical College  
2015 Associate of Science, Minneapolis Community and Technical College  
2015-2017 Undergraduate Research Assistant, Augsburg College  
2017 Augsburg College  
2017-2021 Graduate Research Assistant, University of California San Diego  
2021 Doctor of Philosophy, University of California San Diego

## PUBLICATIONS

**Alves, M.R.**; Coward, E.K.; Gonzales, D.; Sauer, J.S.; Mayer, K.; Prather, K.A.; Grassian, V.H. Changes in Light Absorption and Composition of Chromophoric Marine-Dissolved Organic Matter Across a Microbial Bloom. *Environ. Sci.* 2021. Under Review.

Or. V.W.; **Alves, M.R.**; Wade, M.; Schwab, S.; Corsi, R.L.; Grassian, V.H. Nanoscopic study of water uptake on glass surfaces with organic thin films and particles from exposure to indoor cooking activities: Comparison to model systems. *Environ. Sci. Technol.* 2021. Accepted.

Barnes, E.B. and **Alves, M.R.**; Moore, A.N.; Kilgour, D.B.; Novak, G.A.; Mayer, K.; Sauer, J.; Weber, R.J.; Dang, D.; Winter, M.; Lee, C.; Cappa, C.D.; Bertram, T.H.; Prather, K.A.; Grassian, V.H.; Goldstein, A.H. Atmospheric Benzothiazoles in a Coastal Marine Environment. *Environ. Sci. Technol.* 2021. Accepted.

Sauer, J. S.; Mayer, K. J.; Lee, C.; **Alves, M. R.**; Amiri, S.; Bahaveolos, C.; Barnes, E. B.; Crocker, D. R.; Dinasquet, J.; Garofalo, L. A.; et al. The Sea Spray Chemistry and Particle Evolution Study (SeaSCAPE): Overview and Experimental Methods. *Environ. Sci. Process. Impacts.* **2021.**

Karimova, N. V.; **Alves, M. R.**; Luo, M.; Grassian, V.; Gerber, R. B. Toward a Microscopic Model of Light Absorbing Dissolved Organic Compounds in Aqueous Environments: Theoretical and Experimental Study. *Phys. Chem. Chem. Phys.* 2021.

Or, V. W.; Wade, M.; Patel, S.; **Alves, M. R.**; Kim, D.; Schwab, S.; Przelomski, H.; O'Brien, R.; Rim, D.; Corsi, R. L.; Vance, M. E.; Farmer, D. K.; Grassian, V. H. Glass Surface Evolution Following Gas Adsorption and Particle Deposition from Indoor Cooking Events as Probed by Microspectroscopic Analysis. *Environ. Sci. Process. Impacts* 2020, 22 (8), 1698–1709.

**Alves, M. R.** and Sauer, J. S.; Prather, K. A.; Grassian, V. H.; Wilkins, C. L. Liquid Sampling-Atmospheric Pressure Glow Discharge Ionization as a Technique for the Characterization of Salt-Containing Organic Samples. *Anal. Chem.* 2020, 92 (13), 8845–8851.

- Luo, M.; Shemesh, D.; Sullivan, M. N.; **Alves, M. R.**; Song, M.; Gerber, R. B.; Grassian, V. H. Impact of PH and NaCl and CaCl<sub>2</sub> Salts on the Speciation and Photochemistry of Pyruvic Acid in the Aqueous Phase. *J. Phys. Chem. A* 2020, 124 (25), 5071–5080.
- Liu, Y.; Bé, A. G.; Or, V. W.; **Alves, M. R.**; Grassian, V. H.; Geiger, F. M. Challenges and Opportunities in Molecular-Level Indoor Surface Chemistry and Physics. *Cell Reports Phys. Sci.* 2020, 1 (11), 100256.
- Alves, M. R.**; Fang, Y.; Wall, K. J.; Vaida, V.; Grassian, V. H. Chemistry and Photochemistry of Pyruvic Acid Adsorbed on Oxide Surfaces. *J. Phys. Chem. A* 2019, 123 (35), 7661–7671.
- Trueblood, J. V.; Wang, X.; Or, V. W.; **Alves, M. R.**; Santander, M. V.; Prather, K. A.; Grassian, V. H. The Old and the New: Aging of Sea Spray Aerosol and Formation of Secondary Marine Aerosol through OH Oxidation Reactions. *ACS Earth Sp. Chem.* 2019, 3 (10), 2307–2314.
- Farmer, D. K.; Vance, M. E.; Abbatt, J. P. D.; Abeleira, A.; **Alves, M. R.**; Arata, C.; Boedicker, E.; Bourne, S.; Cardoso-Saldaña, F.; Corsi, R.; Decarlo, P. F.; Goldstein, A. H.; Grassian, V. H.; Hildebrandt Ruiz, L.; Jimenez, J. L.; Kahan, T. F.; Katz, E. F.; Mattila, J. M.; Nazaroff, W. W.; Novoselac, A.; O'Brien, R. E.; Or, V. W.; Patel, S.; Sankhyan, S.; Stevens, P. S.; Tian, Y.; Wade, M.; Wang, C.; Zhou, S.; Zhou, Y. Overview of HOMEChem: House Observations of Microbial and Environmental Chemistry. *Environ. Sci. Process. Impacts* 2019, 21 (8), 1280–1300.
- Trueblood, J. V. and **Alves, M. R.**; Power, D.; Santander, M. V.; Cochran, R. E.; Prather, K. A.; Grassian, V. H. Shedding Light on Photosensitized Reactions within Marine-Relevant Organic Thin Films. *ACS Earth Sp. Chem.* 2019, 3 (8), 1614–1623.
- Hanson, D.; Abdullahi, H.; Menheer, S.; Vences, J.; **Alves, M. R.**; Kunz, J. H<sub>2</sub>SO<sub>4</sub> and Particle Production in a Photolytic Flow Reactor: Chemical Modeling, Cluster Thermodynamics and Contamination Issues. *Atmos. Chem. Phys.* 2019, 19 (14), 8999–9015.
- Or, V. W.; **Alves, M. R.**; Wade, M.; Schwab, S.; Corsi, R. L.; Grassian, V. H. Crystal Clear? Microspectroscopic Imaging and Physicochemical Characterization of Indoor Depositions on Window Glass. *Environ. Sci. Technol. Lett.* 2018, 5 (8), 514–519.
- Estillore, A. D.; Morris, H. S.; Or, V. W.; Lee, H. D.; **Alves, M. R.**; Marciano, M. A.; Laskina, O.; Qin, Z.; Tivanski, A. V.; Grassian, V. H. Linking Hygroscopicity and the Surface Microstructure of Model Inorganic Salts, Simple and Complex Carbohydrates, and Authentic Sea Spray Aerosol Particles. *Phys. Chem. Chem. Phys.* 2017, 19 (31), 21101–21111.

## FIELDS OF STUDY

Major Field of Study: Chemistry

Studies in Atmospheric and Physical Chemistry

Professor Vicki H. Grassian



**ABSTRACT OF THE DISSERTATION**

New Insights into the Heterogeneous Chemistry and Photochemistry of Indoor and Outdoor  
Environments

by

Michael R. Alves

Doctor of Philosophy in Chemistry

University of California San Diego, 2021

Professor Vicki H. Grassian, Chair

Marine aerosols play a large role in the Earth's climate by cooling via interaction with energy from the sun and altering the chemical and physical properties of clouds. The dissolved organic matter at the ocean surface, where sea spray aerosols and marine gases can be generated, is formed by the microbial loop by circulating nutrients and the ingestion of organisms like phytoplankton or bacteria – with additional inputs from terrestrial sources. The colored fraction of this organic matter, known as marine chromophoric dissolved organic matter, is a subject of considerable interest due to its ability to photosensitize nearby molecules. This indirect photochemical mechanism in the marine environment is not well understood. This dissertation first investigates the composition and properties of this fraction by conducting both simple model experiments in the laboratory and larger experiments such as the use of an indoor ocean-atmosphere facility. The ability to bridge the gap between these two types of study provides this thesis an excellent opportunity to answer various questions regarding the importance of understanding the role of heterogeneous chemistry and photochemistry in our surrounding environment. Lastly, this dissertation applies a similar perspective on photochemistry to explore the multiphase chemistry relevant to indoor environments. Humans spend 20 hours a day on average inside buildings, and while atmospheric pollution has been thoroughly studied, the pollution indoors is widely unknown and unregulated. Inspired by experiments conducted in a real home, various experimental model systems were investigated regarding indoor surfaces. The ultimate goal of the thesis being, to provide insight into the many vital heterogeneous and multiphase processes currently undiscovered in environmental chemistry community.

# Chapter 1: An Introduction to Heterogeneous and Multiphase Chemistry and Photochemistry

Surfaces in our environment have long been a subject of study in many fields of research. In the particulate phase, the oxide and carbonate surfaces of mineral dust have been shown to react with a myriad of important (e.g. NO<sub>2</sub>, SO<sub>2</sub>, etc.) trace gases in the Earth's atmosphere – acting as both a sink and a source of these trace gases.<sup>1,2</sup> In recent years, the top-most surface of the ocean, called the sea surface microlayer (SSML) was revealed to be of great importance to the chemical and physical properties of sea spray aerosols (SSA).<sup>3</sup> In particular, the SSML is enriched with organics largely via biological and other photochemical processes.<sup>4,5</sup> A significant fraction of the organic material at the surface of the ocean is defined as marine-dissolved organic matter (m-DOM). Though it is known that the organic content from the ocean is observed to have large effects on aerosol properties, only a small percentage of m-DOM is characterized on the molecular scale.<sup>6</sup>

The past decade has observed a rapid development in the study of atmospheric and health-related gas or condensed phase chemistry in the environmental community. High-impact discoveries in this field maintain a strong focus on atmospheric aerosols, heterogeneous and multiphase chemistry, greenhouse gas emissions, and overall air quality. Although atmospheric chemistry and outdoor air quality remain important, the average person spends the large majority of their lives (~87%) indoors.<sup>7</sup> Oxidative gases and airborne particulate matter exist indoors at concentrations comparable to, if not usually higher than, those outdoors. In addition, because of differences in lighting conditions, air circulation, and unique chemical sources and sinks, the

impact of indoor air quality on human health is poorly understood.<sup>8</sup> The deficiency of research in this field is also largely due to a lack of awareness regarding indoor air quality.

This thesis focuses on the impacts of heterogeneous and multiphase chemistry in the environment. Several topics are discussed including heterogeneous and multiphase chemistry and photochemistry of marine/outdoor-relevant environmental chemistry and heterogeneous and multiphase chemistry in indoor environments as well as the analytical techniques needed for these studies.

## **1.1 Heterogeneous and Multiphase Chemistry and Photochemistry in Outdoor Environments**

### **1.1.1 Dissolved Organic Matter in the Marine Environment and Its Impacts**

The study of dissolved organic matter (DOM) has been a topic of interest for decades due to its highly mobile nature, including both terrestrial and marine DOM, as well as its massive carbon pool and unknown chemical properties. Current literature is clear that m-DOM, and the chemical and biological processes that control its fate, can be highly dynamic. Depending on the molecular class (e.g. amino acids, carbohydrates, lignin, aromatics, etc.), m-DOM molecules can have lifetimes ranges from millennia<sup>9</sup> to just mere minutes.<sup>10</sup> It has been known for quite a long time, that organic matter from the ocean surface (e.g., m-DOM, particulate matter, volatiles) can be incorporated into marine aerosols.<sup>11</sup> As organic material can contribute between 20-50% of the submicron aerosol mass at mid-troposphere latitudes, and in some cases close to 100%, it must be considered in climate models.<sup>12</sup> Physical parameters in models include the determination of organic aerosol size distributions and processes such as diffusion or mixing. Chemically, these aerosols can age via homogeneous or heterogeneous reactions, and exhibit altered properties such as water uptake.<sup>13</sup> As the characterization of m-DOM at the molecular scale is largely

unknown, including the mechanisms that drive its production of unique molecular classes, it is clear that current climate models could benefit from advancements in understanding m-DOM characterization and reactivity.

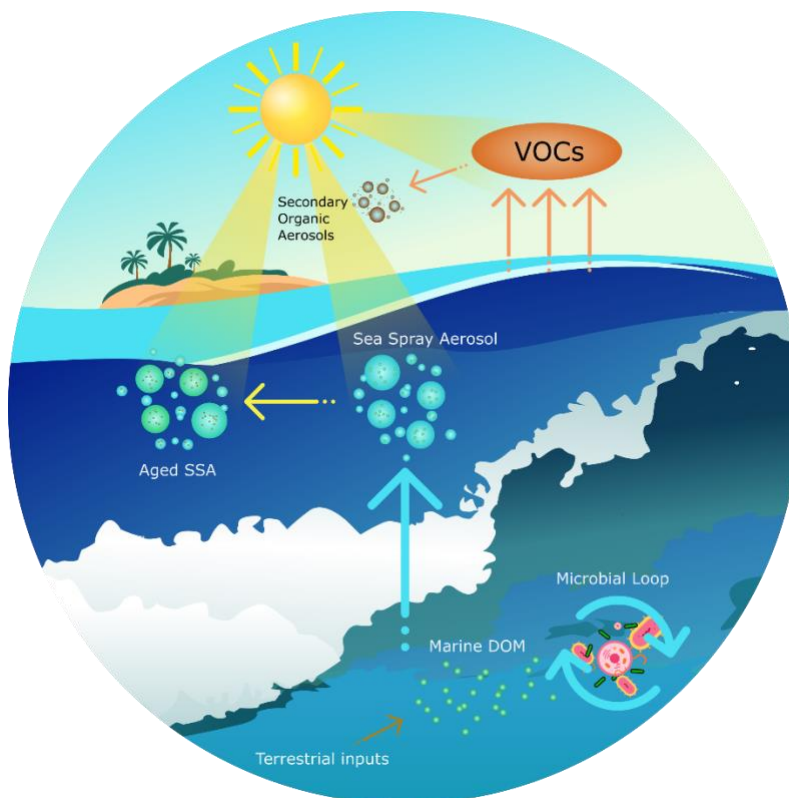


Figure 1.1 Diagram showing the production of primary and secondary organic aerosol from the ocean surface and the sources of m-DOM.

Furthermore, m-DOM is enriched at the air-water interface by a factor of up to nearly ten-fold<sup>14-16</sup>. m-DOM is operationally defined as anything organic in nature the marine environment that is able to pass through 0.2  $\mu\text{m}$  filters.<sup>6,17</sup> The production of m-DOM largely occurs in the euphotic zone, where diverse biogeochemical processes, such as microbial primary production,<sup>18</sup> metabolic turnover,<sup>19</sup> and terrestrial runoff<sup>20</sup> result in broad chemodiversity. Photochemistry of m-DOM will directly produce carbon dioxide and carbon monoxide in an abiotic process.<sup>21</sup> In addition to this, photodegradation of m-DOM will also produce biologically available material for microbial uptake.<sup>22</sup> More recently, studies have suggested that m-DOM

might be a key player in the photochemical production of daytime nitrous acid (HONO) at the ocean surface.<sup>23</sup>

Recently, interest in the photoactive subset of DOM, known as chromophoric dissolve organic matter (CDOM), has been a point of focus due to its ability to perform both direct and indirect photochemical processes in the environment.<sup>24,25</sup> These photochemical drivers responsible for indirect photochemical pathways, also known as photosensitizers, are grossly uncharacterized due to the inherent complexity of DOM as well as the limitations of analytical methods currently available. It is well known that the ocean, particularly its surface, greatly impacts the Earth's atmosphere via production of sea spray aerosol and marine gases.<sup>26,27</sup> The reactivity and characterization of m-DOM and marine chromophoric DOM (m-CDOM) will have a key role in determining the critical processes driving the connection and interface between the ocean and the atmosphere.

### **1.1.2 Analysis of m-DOM**

The amount of m-DOM in the oceans are enough to rival the amount of carbon in the form of CO<sub>2</sub> in the Earth's entire atmosphere.<sup>22</sup> Much of this is due to microbial activity in the form of bacterial or phytoplankton blooms, known to produce and consume large amounts of organic material. Additionally, inputs from terrestrial sources from runoff or rivers are also significant. Commonly known as the marine microbial loop<sup>28</sup>, phytoplankton reduce CO<sub>2</sub> from their surroundings and become a primary source of this m-DOM. This organic matter, as well as other microbes, is further processed by other marine microorganisms such as heterotrophic bacteria, grazers, and viruses.<sup>28,29</sup> Such events where these mechanisms are in abundance are known as microbial blooms. Blooms are a large source, and modulator, of m-DOM chemodiversity.<sup>28</sup> Understanding the connection between m-DOM composition or properties and

the microbial forces driving these changes will provide insight into how the surface of the ocean impacts the Earth's climate.

This assemblage of amino and fatty acids, proteins, and large macromolecular species, whose structures are largely unknown<sup>30</sup>, renders DOM across environments difficult to characterize.<sup>31</sup> As such, a synchrony of different techniques is required to characterize discrete DOM populations. For example, NMR spectroscopy has been successful at characterizing high-molecular weight compounds in DOM18–20 whereas ultrahigh-resolution mass spectrometry (MS) approaches such as Orbitrap and Fourier transform ion cyclotron resonance (FT-ICR) provide insights into molecular formulae present<sup>21,22</sup> but are often biased towards detection of oxygenated, smaller molecules. The low concentration of m-DOM in its natural environment and well as the high amount of salt (~35 g/L) also limits the user's ability to study m-DOM, especially without the use of extraction techniques. Small steps of progress are being made to work around this particular issue with salt, both MS and NMR, including the development of new MS ionization sources and advanced NMR techniques that handle these high salt concentrations.<sup>32–34</sup> Recent advancements in MS/MS characterization allow for structural details

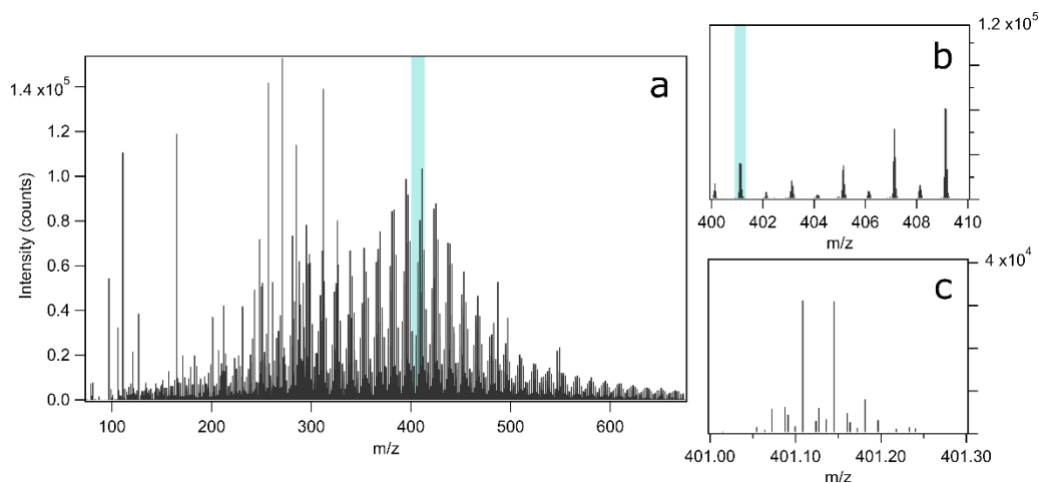


Figure 1.2 Negative mode mass spectrum of solid phase extracted m-DOM with zoom-in spectra showing base-line separated peaks at a resolution of ~240,000.

of targeted/non-targeted molecules by fragmenting portions of individual molecules within DOM to better understand its structure.<sup>35</sup>

While characterizing m-DOM is a challenge in and of itself, there have been some attempts to characterize this complex sample via “bottom-up” approaches - developing fresh m-DOM through the degradation of phytoplankton and phytoplankton-derived aggregates using bacteria.<sup>36,37</sup> Though these experiments are isolated from the many issues faced in the field, such as contamination, anthropogenic inputs, and reproducibility, they are inherently removed from the complexity of the microbial loop and its many inputs that comprises m-DOM. Being able to track the formation of m-DOM throughout the lifetime of a bloom however, can be particularly helpful in the characterization of the many dynamic changes that could be missed in field based experiments.

### **1.1.3 Photochemistry in the marine environment**

Solar radiation catalyzes an extensive array of photochemical reactions and metabolomic pathways at the ocean’s surface - yet many of the photochemical reactions at the SSML are only now being closely examined.<sup>38</sup> Photosensitizers are molecules that produce chemical changes through the absorption of light and transfer of the energy absorbed to a neighboring species. This results in a sort of indirect photochemical mechanism, where molecules in the environment that are not normally absorbing in the actinic region can still undergo photochemistry in the presence of an excited state photosensitizer – such as those that exist in m-DOM. As a photon is absorbed by the photosensitizer molecule, the molecule is excited to its short-lived first singlet state, where it can subsequently decay back to ground state via radiative or non-radiative emission processes. Alternatively, it can enter the much longer-lived triplet excited state via intersystem crossing as shown in Figure 1-x, a state where the forbidden transition back down to ground state can be measured as  $k_D$ . The ability, and probability, of an excited state molecule is its singlet state to



undergo intersystem crossing to its triplet excited state is dependent on the amount of overlap between the two energy level's vibrational states. This overlap is contingent on the molecule's structure, for instance, interaction between  $\pi$  orbitals. This can occur within the molecule itself or as a part of an electronic interaction between two or more chromophores also known as the charge-transfer model.<sup>24</sup> However, this model consisting of electron donor and acceptors is currently under much debate and others have suggested other photophysical mechanisms are likely at play.<sup>39</sup>

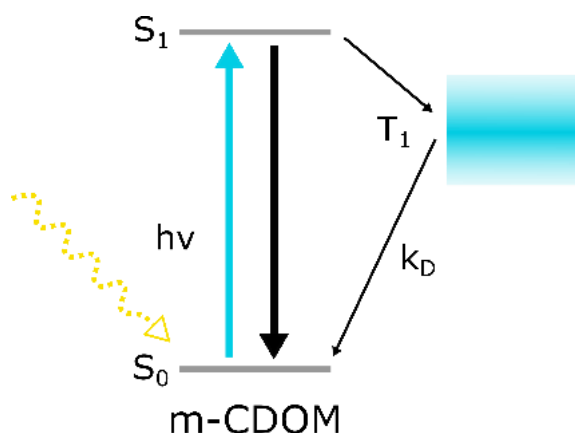


Figure 1.3. Simplified diagram of an excited state photosensitizer and the intersystem crossing process, where  $S_0$  is the singlet ground state,  $S_1$  is the singlet excited state, and  $T_1$  is the triplet excited state.  $k_D$  refers to the rate of relaxation of the forbidden transition between  $T_1$  and  $S_0$ .

Though photosensitization may proceed through the singlet state energy, it is much too short to interact with other molecules except in the case of highly concentrated systems or other specific situations (e.g., triplet yield is very low, thus  $[{}^3\text{CDOM}]_{ss}$  is lower or equal to the singlet). Half-lives of this state range between 150 ps and 3 ns depending on the pool of  ${}^1\text{CDOM}$  (recall that DOM is highly diverse in composition). So even though quantum formation yields  ${}^3\text{CDOM}$  are only between 1-6%, the steady state concentration of  ${}^3\text{CDOM}$  is 2 to 3 magnitudes larger than that of  ${}^1\text{CDOM}$  since its half-life is around 20  $\mu\text{s}$ .<sup>40</sup>

Table 1.1. Photochemical reactions for an excited molecule,  $M^*$ , adapted from Calvert and Pitts.

<b>Reaction pathway</b>	
$R-M^* \rightarrow R\cdot + M\cdot$	free radical formation via photolysis
$M^* \rightarrow N$	photoisomerization/decomposition into stable molecule
$M^* + R-H \rightarrow M-H + R\cdot$	hydrogen abstraction resulting in formation of free radical
$M^* + R \rightarrow M + R^*$	energy transfer, e.g., photosensitization
$M^* + R \rightarrow M^+ + R^-$	electron transfer, e.g., photosensitization

The study of m-DOM, and DOM in general, as a photosensitizer in the lab has many significant hurdles. For one, at the time of writing, there does not exist a standard supply of m-DOM for experimental use. Studies using m-DOM to photosensitize different systems, collect and extract their own sample in widely different locations and times of the year. Some terrestrial systems have a standard supply, such as Pony Lake fulvic acids, Suwannee River DOM, etc. However, these are in limited supply and will change to new collection standards over time. Even if a standard supply of m-DOM does exist, its complexity, mostly unknown composition, and highly labile nature make it difficult to study specific mechanisms. In this case, having a representative molecule (or group of compounds) for DOM would be extremely valuable in the study of environmental photochemistry. Though some terrestrial models are used, such a 4-benzoylbenzoic acid and 1,4-imidazolecarboxyaldehyde, these systems have been shown to not accurately represent marine photosensitization.<sup>41</sup> In later chapters, the search and characterization for a molecular model of m-CDOM is investigated using a myriad of different techniques including high resolution mass spectrometry and spectroscopy as discussed here and across multiple research groups.

## **1.2 Heterogeneous and Multiphase Chemistry and Photochemistry in Indoor Environments**

### **1.1.4 The Indoor Environment**

Organic films are found on most surfaces in indoor environments, and those films include chemicals that exchange dynamically with the gas phase.<sup>42,43</sup> The origins, transformations, and fate of indoor surface films remain poorly characterized, particularly in terms of their relationship to human activities, chemical interactions with common atmospheric oxidants, and heterogeneous interactions between surfaces and the gas phase. The organic chemistry of indoor environments is highly dynamic at least partially because humans spend 90% of their time indoors, performing activities such as cooking, cleaning, and shedding skin oils that directly affect the surface and gas phase organic chemical composition. Indoor chemistry is also influenced by environmental factors such as light, temperature, and humidity. As primary organic molecules are oxidized, secondary species are created with different chemical and physical properties. Semi-volatile organic compounds (SVOCs) are an important subset of organic compounds that are ubiquitous indoors. Diverse sources of SVOCs include cooking, plasticizers, flame retardants, pesticides, personal care products, and even the bio effluents of human occupants themselves.

### **1.1.5 Surface Chemistry and Photochemistry in the Indoor Environment**

Surfaces provide sites for chemical transformations indoors. For instance, paint is a common surface coating that contains titanium dioxide ( $\text{TiO}_2$ ), a semiconductive material with a band gap in the visible spectrum. When irradiated, photogenerated electron-hole pairs can precipitate redox chemistry at the interface, potentially producing secondary (or tertiary) organic species from sorbed primary species shown in Figure 1.4.<sup>44</sup> The indoor environment is distinctive compared to the outdoor atmosphere because of its comparably large surface-to-

volume ratio, higher concentrations of organic chemicals, and generally lower levels of gas phase oxidants.<sup>8</sup> These factors, among others, make the indoor environment a fascinating and important domain of study within the field of environmental chemistry.

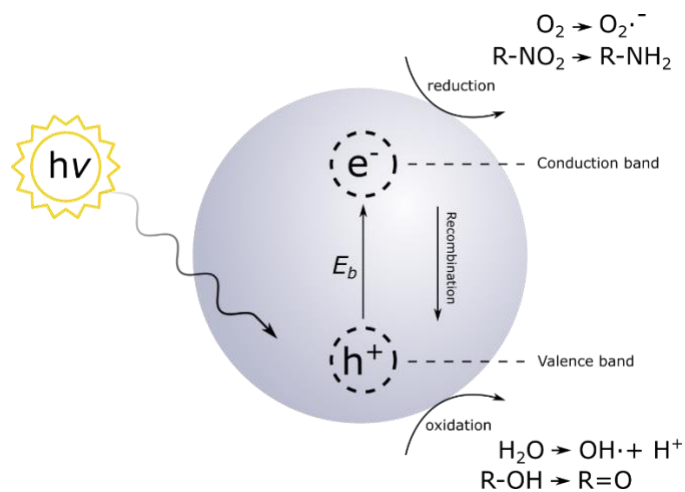


Figure 1.4. Illustration of the electron-hole pair generation from a TiO<sub>2</sub>, or photocatalytic, surface.

The presence of light is, and thus its role in photochemical mechanisms, inherently different indoors compared to outdoors. While sunlight could enter the indoor environment via an open window, most of the light indoors include sunlight filtered through glass and emitted light from fluorescent tubes, light emitting diodes (LEDs), incandescent bulbs, etc. Interestingly, many man-made light sources produce light under ~340 nm – a region where sunlight would normally be filtered at due to the absorption properties of window glass. Indoor surfaces have recently been shown to catalyze many important atmospheric oxidants. Nitrous acid (HONO) is reported to have a significant, and previously unknown, daytime source indoors via heterogeneous chemistry of NO<sub>2</sub> on surfaces with grime (e.g., sorbed species from cooking/human emissions).<sup>45</sup> Produced oxidants indoors are of significant interest due to their possible impacts on human health.

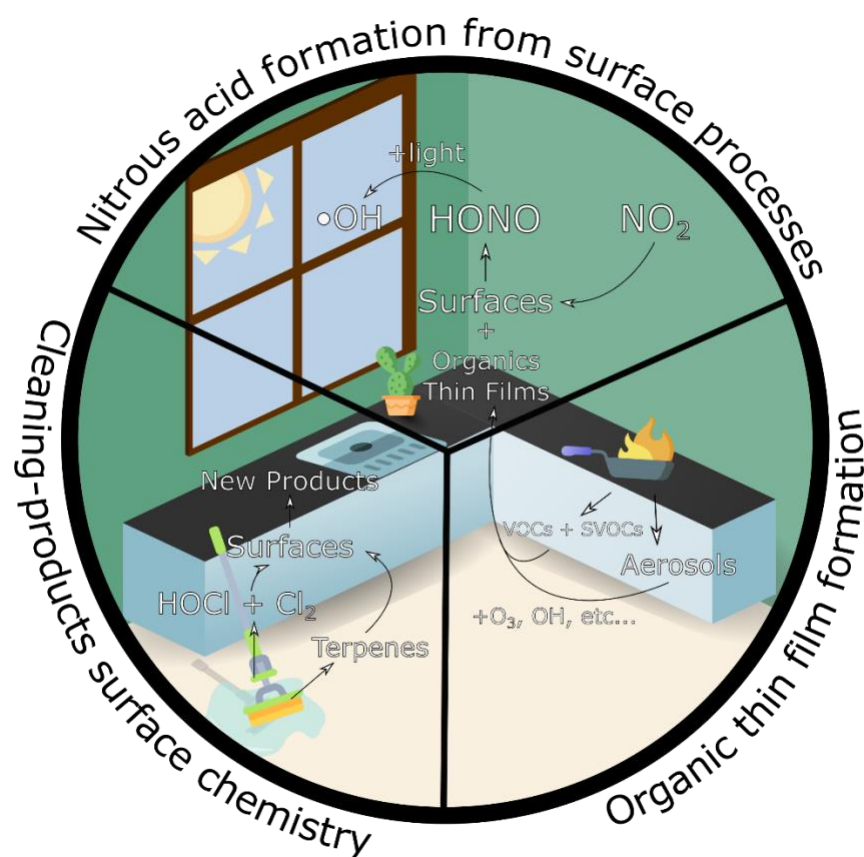


Figure 1.5. Schematic of some of the complex heterogenous and multiphase chemistry that occurs indoors.

### 1.1.6 Fate of Semi-volatile Organic Compounds Indoors

Inadequate understanding of the chemical interactions between SVOCs, volatile organic compounds (VOCs), and surfaces makes it difficult to determine the sources and fates of important indoor chemical species. Therefore, studies aiming to understand the dynamic transformations controlling the ubiquity of organic components are critically needed to understand the environmental chemistry occurring indoors where most human exposure to airborne organic chemicals occurs.<sup>7</sup> Due to their low volatility and few pathways of removal, SVOCs are pervasive throughout the indoor environment. Within the past decade more studies have begun to explore the underlying processes of gas-surface partitioning and chemical

transformations of these compounds beyond empirical observation. For example, exactly which surfaces (such as carpet, paint, etc.) act as major reservoirs and reactive sites for primary and secondary SVOCs is not well understood.<sup>46</sup> Locations in different indoor spaces, differences in light exposure, as well as changes in human activity have been shown to vary the air and surface phase composition, but the mechanisms by which these differences manifest is subject of debate.<sup>47</sup>

The production of many SVOCs and formation of organic films on surfaces, however, is not well understood within the indoor environment. Primary SVOCs are known to degas from carpets, plastics, and even humans.<sup>48</sup> The oxidation of organics could also lead to semivolatile products.<sup>49</sup> Understanding how thin films form will allow models to accurately predict how surfaces impact the chemistry indoors. Currently, a simplified model showing a film growing over time, as a function of the octanol-air coefficient  $k_{OA}$ , is commonly used. However, it is clear that even very flat surfaces, over long periods of time (e.g., 3-6 months), do not produce flat organic films with full coverage.<sup>50,51</sup> In fact, it seems that in even heavily soiled conditions, the surface itself may remain exposed as the organic film represents more as puddles or islands of aggregates. Nevertheless, more work is required to accurately understand the role of organics on surfaces and how such changes in properties, both physical and chemical, may impact the indoor environment.

#### **1.1.6 Indoor Use of Caustic Cleaning Substances**

While the majority of environment and health related research has focused on the air, water, or soil of our surroundings, the understanding of the indoor space is widely unregulated and unmonitored. For instance, standards for PM1 and PM2.5 limits exist for the outdoors; however, these limits are very commonly exceeded indoors.<sup>52</sup> Strong household cleaning products are regularly used in both commercial and private homes using peroxides, chlorine

oxides, ammonia, alcohols, and many more.<sup>53</sup> How these volatile organic and strong oxidizers/reducers impact the indoor chemistry, and by extension public health, is currently unknown. Recent strides, in the past decade, have been made in the indoor chemistry community. A recent field study known as House Observations of Microbial and Environmental Chemistry (HOMEChem), explored the use of indoor cleaners such as bleach and others that use terpenes (e.g., limonene, alpha-pinene). These observations have led to the publications of many interesting findings including the importance of multiphase interactions<sup>54</sup> and other various reaction pathways unique to the indoor environment.<sup>55</sup> In this thesis, the fundamental interactions in multiphase and heterogeneous chemistry will be probed using a variety of methods.

### **1.3 Description of Thesis Chapters**

Chapter two will focus on the experimental methods used in this dissertation research including new analytical tools developed or characterized. Chapter three investigates the impact of photosensitizers, including an m-DOM sample and photo-interactions with nonanoic acid in thin films. Chapter four discusses the further characterization of m-DOM including classification and structural analysis of m-CDOM across a large scale mesocosm microbial bloom (SeaSCAPE 2019). Chapter five combines additional findings from the SeaSCAPE 2019 campaign, such as the atmospheric relevance of anthropogenic benzothiazoles and a large-scale research collaboration concerning the bulk extraction of m-DOM from this mesocosm study. Chapter six begins the investigation of surfaces commonly found in indoor environments, observing the reactions between a simple keto acid (pyruvic acid) and two metal oxides. Chapter seven discusses the interactions between a commonly used cleaning agent, hypochlorous acid, and indoor surfaces.

## 1.4 References

- (1) Goodman, A. L.; Bernard, E. T.; Grassian, V. H. Spectroscopic Study of Nitric Acid and Water Adsorption on Oxide Particles: Enhanced Nitric Acid Uptake Kinetics in the Presence of Adsorbed Water. *J. Phys. Chem. A* **2001**, *105* (26), 6443–6457.
- (2) Usher, C. R.; Al-Hosney, H.; Carlos-Cuellar, S.; Grassian, V. H. A Laboratory Study of the Heterogeneous Uptake and Oxidation of Sulfur Dioxide on Mineral Dust Particles. *J. Geophys. Res. Atmos.* **2002**, *107* (D23).
- (3) Wang, X.; Deane, G. B.; Moore, K. A.; Ryder, O. S.; Stokes, M. D.; Beall, C. M.; Collins, D. B.; Santander, M. V.; Burrows, S. M.; Sultana, C. M.; et al. The Role of Jet and Film Drops in Controlling the Mixing State of Submicron Sea Spray Aerosol Particles. *Proc. Natl. Acad. Sci. U. S. A.* **2017**, *114* (27), 6978–6983.
- (4) Engel, A.; Bange, H. W.; Cunliffe, M.; Burrows, S. M.; Friedrichs, G.; Galgani, L.; Herrmann, H.; Hertkorn, N.; Johnson, M.; Liss, P. S.; et al. The Ocean's Vital Skin: Toward an Integrated Understanding of the Sea Surface Microlayer. *Front. Mar. Sci.* **2017**, *4*, 1–14.
- (5) Clark, C. D.; Zika, R. G. Marine Organic Photochemistry: From the Sea Surface to Marine Aerosols. *Mar. Chem.* **2005**, *5*, 1–33.
- (6) Nebbioso, A.; Piccolo, A. Molecular Characterization of Dissolved Organic Matter (DOM): A Critical Review. *Anal. Bioanal. Chem.* **2013**, *405* (1), 109–124.
- (7) Weschler, C. J. Chemistry in Indoor Environments: 20years of Research. *Indoor Air* **2011**, *21* (3), 205–218.
- (8) Weschler, C. J.; Carslaw, N. Indoor Chemistry. *Environ. Sci. Technol.* **2018**, *52* (5), 2419–2428.
- (9) Stubbins, A.; Niggemann, J.; Dittmar, T. Photo-Lability of Deep Ocean Dissolved Black Carbon. *Biogeosciences* **2012**, *9* (5), 1661–1670.
- (10) Carlson, C. A.; Hansell, D. A. DOM Sources, Sinks, Reactivity, and Budgets. In *Biogeochemistry of Marine Dissolved Organic Matter*; Elsevier, 2015; pp 65–126.
- (11) Blanchard, D. C. The Ejection of Drops from the Sea and Their Enrichment with Bacteria and Other Materials: A Review. *Estuaries* **1989**, *12* (3), 127–137.
- (12) Bertram, T. H.; Cochran, R. E.; Grassian, V. H.; Stone, E. A. Sea Spray Aerosol Chemical Composition: Elemental and Molecular Mimics for Laboratory Studies of Heterogeneous and Multiphase Reactions. *Chem. Soc. Rev.* **2018**, *47* (7), 2374–2400.
- (13) Kanakidou, M.; Seinfeld, J. H.; Pandis, S. N.; Barnes, I.; Dentener, F. J.; Facchini, M. C.; Van Dingenen, R.; Ervens, B.; Nenes, A.; Nielsen, C. J.; et al. Organic Aerosol and



- Global Climate Modelling: A Review. *Atmos. Chem. Phys.* **2005**, 5 (4), 1053–1123.
- (14) Quinn, P. K.; Collins, D. B.; Grassian, V. H.; Prather, K. A.; Bates, T. S. Chemistry and Related Properties of Freshly Emitted Sea Spray Aerosol. *Chem. Rev.* **2015**, 115 (10), 4383–4399.
- (15) van Pinxteren, M.; Barthel, S.; Fomba, K. W.; Müller, K.; von Tümpling, W.; Herrmann, H. The Influence of Environmental Drivers on the Enrichment of Organic Carbon in the Sea Surface Microlayer and in Submicron Aerosol Particles – Measurements from the Atlantic Ocean. *Elem. Sci. Anthr.* **2017**, 5.
- (16) Carlson, D. J. Dissolved Organic Materials in Surface Microlayers: Temporal and Spatial Variability and Relation to Sea State. *Limnol. Oceanogr.* **1983**, 28 (3), 415–431.
- (17) Denis, M.; Jeanneau, L.; Pierson-Wickman, A.C.; Humbert, G.; Petitjean, P.; Jaffrézic, A.; Gruau, G. A Comparative Study on the Pore-Size and Filter Type Effect on the Molecular Composition of Soil and Stream Dissolved Organic Matter. *Org. Geochem.* **2017**, 110, 36–44.
- (18) Castillo, C. R.; Sarmiento, H.; Álvarez-Salgado, X. A.; Gasol, J. M.; Marraséa, C. Production of Chromophoric Dissolved Organic Matter by Marine Phytoplankton. *Limnol. Oceanogr.* **2010**, 55 (1), 446–454.
- (19) Kujawinski, E. B. The Impact of Microbial Metabolism on Marine Dissolved Organic Matter. *Ann. Rev. Mar. Sci.* **2011**, 3 (1), 567–599.
- (20) Murphy, K. R.; Stedmon, C. A.; Waite, T. D.; Ruiz, G. M. Distinguishing between Terrestrial and Autochthonous Organic Matter Sources in Marine Environments Using Fluorescence Spectroscopy. *Mar. Chem.* **2008**, 108 (1–2), 40–58.
- (21) Stubbins, A.; Uher, G.; Law, C. S.; Mopper, K.; Robinson, C.; Upstill-Goddard, R. C. Open-Ocean Carbon Monoxide Photoproduction. *Deep. Res. Part II Top. Stud. Oceanogr.* **2006**, 53 (14–16), 1695–1705.
- (22) Medeiros, P. M.; Seidel, M.; Powers, L. C.; Dittmar, T.; Hansell, D. A.; Miller, W. L. Dissolved Organic Matter Composition and Photochemical Transformations in the Northern North Pacific Ocean. *Geophys. Res. Lett.* **2015**, 42 (3), 863–870.
- (23) Stemmler, K.; Ndour, M.; Elshorbany, Y.; Kleffmann, J.; D’Anna, B.; George, C.; Bonn, B.; Ammann, M. Light Induced Conversion of Nitrogen Dioxide into Nitrous Acid on Submicron Humic Acid Aerosol. *Atmos. Chem. Phys.* **2007**, 7 (16), 4237–4248.
- (24) Sharpless, C. M.; Blough, N. V. The Importance of Charge-Transfer Interactions in Determining Chromophoric Dissolved Organic Matter (CDOM) Optical and Photochemical Properties. *Environ. Sci. Process. Impacts* **2014**, 16 (4), 654–671.

- (25) Nelson, N. B.; Siegel, D. A. The Global Distribution and Dynamics of Chromophoric Dissolved Organic Matter. *Ann. Rev. Mar. Sci.* **2013**, *5* (1), 447–476.
- (26) Fitzgerald, J. W. Marine Aerosols: A Review. *Atmos. Environ. Part A, Gen. Top.* **1991**, *25* (3–4), 533–545.
- (27) Brooks, S. D.; Thornton, D. C. O. Marine Aerosols and Clouds. *Ann. Rev. Mar. Sci.* **2018**, *10*, 289–313.
- (28) Pomeroy, L.; leB. Williams, P.; Azam, F.; Hobbie, J. The Microbial Loop. *Oceanography* **2007**, *20* (2), 28–33.
- (29) Azam, F.; Malfatti, F. Microbial Structuring of Marine Ecosystems. *Nat. Rev. Microbiol.* **2007**, *5* (10), 782–791.
- (30) Repeta, D. J. Chemical Characterization and Cycling of Dissolved Organic Matter. In *Biogeochemistry of Marine Dissolved Organic Matter*; Elsevier, 2015; pp 21–63.
- (31) Wilson, R. M.; Tfaily, M. M. Advanced Molecular Techniques Provide New Rigorous Tools for Characterizing Organic Matter Quality in Complex Systems. *J. Geophys. Res. Biogeosciences* **2018**, *123* (6), 1790–1795.
- (32) Lam, B.; Simpson, A. J. Direct <sup>1</sup>H NMR Spectroscopy of Dissolved Organic Matter in Natural Waters. *Analyst* **2008**, *133* (2), 263–269.
- (33) Alves, M. R.; Sauer, J. S.; Prather, K. A.; Grassian, V. H.; Wilkins, C. L. Liquid Sampling-Atmospheric Pressure Glow Discharge Ionization as a Technique for the Characterization of Salt-Containing Organic Samples. *Anal. Chem.* **2020**, *92* (13), 8845–8851.
- (34) Hall, K. A.; Paing, H. W.; Marcus, R. K. Quantitative Trace Metal Determinations in Cell Culture Media Using LS-APGD-MS and ICP-OES with Free/Bound Species Differentiation Following Polymer Fiber Separations. *Anal. Methods* **2021**, *13* (16), 1945–1954.
- (35) Petras, D.; Koester, I.; Da Silva, R.; Stephens, B. M.; Haas, A. F.; Nelson, C. E.; Kelly, L. W.; Aluwihare, L. I.; Dorrestein, P. C. High-Resolution Liquid Chromatography Tandem Mass Spectrometry Enables Large Scale Molecular Characterization of Dissolved Organic Matter. *Front. Mar. Sci.* **2017**, *4*.
- (36) Kinsey, J. D.; Corradino, G.; Ziervogel, K.; Schnetzer, A.; Osburn, C. L. Formation of Chromophoric Dissolved Organic Matter by Bacterial Degradation of Phytoplankton-Derived Aggregates. *Front. Mar. Sci.* **2018**, *4*.
- (37) Shields, M. R.; Bianchi, T. S.; Osburn, C. L.; Kinsey, J. D.; Ziervogel, K.; Schnetzer, A.; Corradino, G. Linking Chromophoric Organic Matter Transformation with Biomarker

- Indices in a Marine Phytoplankton Growth and Degradation Experiment. *Mar. Chem.* **2019**, *214*, 103665.
- (38) Tinel, L.; Rossignol, S.; Bianco, A.; Passananti, M.; Perrier, S.; Wang, X.; Brigante, M.; Donaldson, D. J.; George, C. Mechanistic Insights on the Photosensitized Chemistry of a Fatty Acid at the Air/Water Interface. *Environ. Sci. Technol.* **2016**, *50* (20), 11041–11048.
- (39) McKay, G.; Korak, J. A.; Erickson, P. R.; Latch, D. E.; McNeill, K.; Rosario-Ortiz, F. L. The Case Against Charge Transfer Interactions in Dissolved Organic Matter Photophysics. *Environ. Sci. Technol.* **2018**, *52* (2), 406–414.
- (40) McNeill, K.; Canonica, S. Triplet State Dissolved Organic Matter in Aquatic Photochemistry: Reaction Mechanisms, Substrate Scope, and Photophysical Properties. *Environ. Sci. Process. Impacts* **2016**, *18* (11), 1381–1399.
- (41) Trueblood, J. V.; Alves, M. R.; Power, D.; Santander, M. V.; Cochran, R. E.; Prather, K. A.; Grassian, V. H. Shedding Light on Photosensitized Reactions within Marine-Relevant Organic Thin Films. *ACS Earth Sp. Chem.* **2019**, *3* (8), 1614–1623.
- (42) Wang, C.; Collins, D. B.; Arata, C.; Goldstein, A. H.; Mattila, J. M.; Farmer, D. K.; Ampollini, L.; DeCarlo, P. F.; Novoselac, A.; Vance, M. E.; et al. Surface Reservoirs Dominate Dynamic Gas-Surface Partitioning of Many Indoor Air Constituents. *Sci. Adv.* **2020**, *6* (8), 1–12.
- (43) Lunderberg, D. M.; Kristensen, K.; Liu, Y.; Misztal, P. K.; Tian, Y.; Arata, C.; Wernis, R.; Kreisberg, N.; Nazaroff, W. W.; Goldstein, A. H. Characterizing Airborne Phthalate Concentrations and Dynamics in a Normally Occupied Residence. *Environ. Sci. Technol.* **2019**, *53* (13), 7337–7346.
- (44) Linsebigler, A. L.; Lu, G.; Yates, J. T. Photocatalysis on TiO<sub>2</sub> Surfaces: Principles, Mechanisms, and Selected Results. *Chem. Rev.* **1995**, *95* (3), 735–758.
- (45) Liu, J.; Deng, H.; Lakey, P. S. J.; Jiang, H.; Mekic, M.; Wang, X.; Shiraiwa, M.; Gligorovski, S. Unexpectedly High Indoor HONO Concentrations Associated with Photochemical NO<sub>2</sub> Transformation on Glass Windows. *Environ. Sci. Technol.* **2020**, *54* (24), 15680–15688.
- (46) Weschler, C. J.; Nazaroff, W. W. Semivolatile Organic Compounds in Indoor Environments. *Atmos. Environ.* **2008**, *42* (40), 9018–9040.
- (47) Farmer, D. K.; Vance, M. E.; Abbatt, J. P. D.; Abeleira, A.; Alves, M. R.; Arata, C.; Boedicker, E.; Bourne, S.; Cardoso-Saldaña, F.; Corsi, R.; Decarlo, P. F.; Goldstein, A. H.; Grassian, V. H.; Hildebrandt Ruiz, L.; Jimenez, J. L.; Kahan, T. F.; Katz, E. F.; Mattila, J. M.; Nazaroff, W. W.; Novoselac, A.; O'Brien, R. E.; Or, V. W.; Patel, S.; Sankhyan, S.; Stevens, P. S.; Tian, Y.; Wade, M.; Wang, C.; Zhou, S.; Zhou, Y. Overview of HOMEChem: House Observations of Microbial and Environmental

Chemistry. *Environ. Sci. Process. Impacts* **2019**, 21 (8), 1280–1300.

- (48) Wu, Y.; Eichler, C. M. A.; Cao, J.; Benning, J.; Olson, A.; Chen, S.; Liu, C.; Vejerano, E. P.; Marr, L. C.; Little, J. C. Particle/Gas Partitioning of Phthalates to Organic and Inorganic Airborne Particles in the Indoor Environment. *Environ. Sci. Technol.* **2018**, 52 (6), 3583–3590.
- (49) Alves, M. R.; Fang, Y.; Wall, K. J.; Vaida, V.; Grassian, V. H. Chemistry and Photochemistry of Pyruvic Acid Adsorbed on Oxide Surfaces. *J. Phys. Chem. A* **2019**, 123 (35), 7661–7671.
- (50) Or, V.; Alves, M.; Wade, M.; Schwab, S.; Corsi, R. L.; Grassian, V. H. Crystal Clear? Microspectroscopic Imaging and Physicochemical Characterization of Indoor Depositions on Window Glass. *Environ. Sci. Technol. Lett.* **2018**, 5, 514–519.
- (51) Or, V. W.; Wade, M.; Patel, S.; Alves, M. R.; Kim, D.; Schwab, S.; Przelomski, H.; O'Brien, R.; Rim, D.; Corsi, R. L.; et al. Glass Surface Evolution Following Gas Adsorption and Particle Deposition from Indoor Cooking Events as Probed by Microspectroscopic Analysis. *Environ. Sci. Process. Impacts* **2020**, 22 (8), 1698–1709.
- (52) Abdullahi, K. L.; Delgado-Saborit, J. M.; Harrison, R. M. Emissions and Indoor Concentrations of Particulate Matter and Its Specific Chemical Components from Cooking: A Review. *Atmos. Environ.* **2013**, 71, 260–294.
- (53) Quirce, S.; Barranco, P. Cleaning Agents and Asthma. *J. Investig. Allergol. Clin. Immunol.* **2010**, 20 (7), 542–550.
- (54) Mattila, J. M.; Lakey, P. S. J.; Shiraiwa, M.; Wang, C.; Abbatt, J. P. D.; Arata, C.; Goldstein, A. H.; Ampollini, L.; Katz, E. F.; DeCarlo, P. F. Multiphase Chemistry Controls Inorganic Chlorinated and Nitrogenated Compounds in Indoor Air during Bleach Cleaning. *Environ. Sci. Technol.* **2020**.
- (55) Collins, D. B.; Farmer, D. K. Unintended Consequences of Air Cleaning Chemistry. *Environ. Sci. Technol.* **2021**.

## **Chapter 2: Experimental Methods and Method Development**

In this chapter, general experimental methods used throughout this dissertation will be described. Methods that have been developed and characterized, such as the new ion source for mass spectrometry or the construction of the Teflon bag, will also be featured in this chapter. In addition, each chapter will provide much greater detail of the more specific techniques and methods relevant for that particular study. This chapter provides an overview of: (i) details of methods to extract m-DOM; (ii) the use of high-resolution mass spectrometry; (iii) the use of specific FTIR spectroscopy methods; (iv) a description of the design, construction and operation of a small teflon bag for indoor chemistry studies and; (v) the development of a liquid sampling atmospheric glow discharge characterization and its application.

### **2.1 Extraction of Marine-Dissolved Organic Matter**

A major undertaking during the SeaSCAPE campaign involved extraction of m-DOM for a variety of different experiments to be performed by CAICE researchers. In addition, m-DOM from other experiments involving smaller mesocosms was also extracted for analysis. The extraction of m-DOM for the various experiments carried out in this thesis, follows closely to the method described by Dittmar and coworkers.<sup>1</sup> Seawater, either from the ocean or from a mesocosm experiment, is immediately filtered down to 0.22 microns. If the volume is small, < 100 mL, the sample can likely be directly filtered with a 0.2-micron filter (also called a 0.22-micron filter) made of polyethersulfone (PES) or Teflon. However, particulate matter makes this difficult with large sample volumes. A series of filtration steps, namely 50-, 7-, 0.7-, and 0.2-micron filters, can be used to 1) minimize the pressure needed to push the sample through the

filter and 2) reduce the number of 0.2 micron filters needed due to clogging. The clogging of filters is a significant issue to pay attention to as increasing the pressure is necessary to push the same volume of sample per unit time with a dirty filter compared to a clean one. Too much back pressure could result in lysing of microbes, physical alteration of larger macromolecules, or cause breakthrough of particulate matter larger than 0.2 microns.<sup>2</sup> In general, for all stages of filtration, the vacuum applied does not exceed 5 psi.

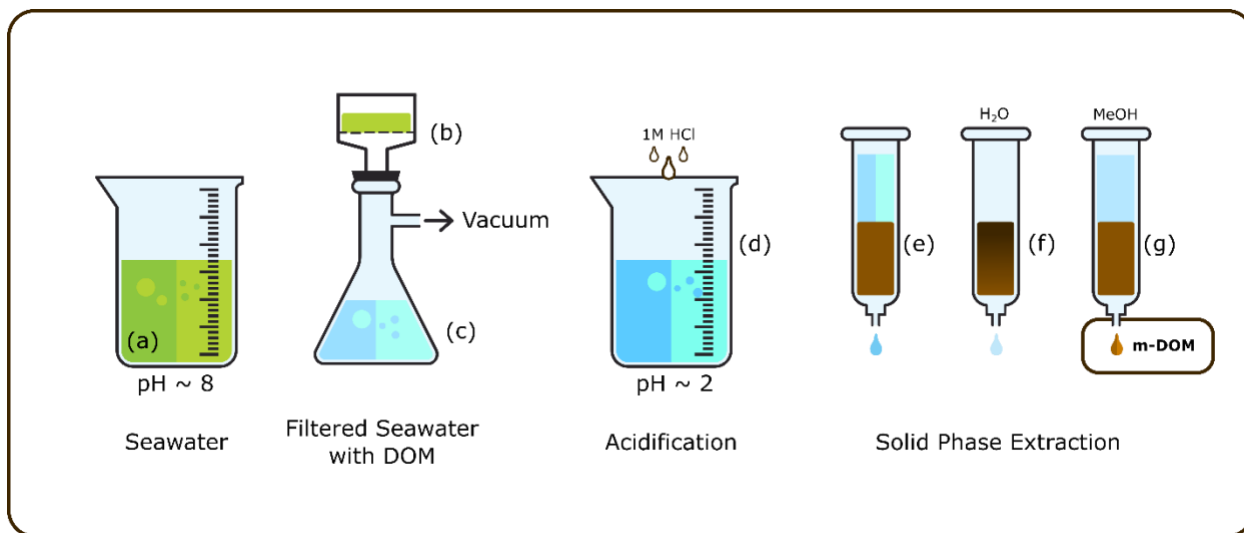


Figure 2.1. General workflow of extracting m-DOM from seawater: (a) sample of seawater; (b) vacuum filtration; (c) filtered seawater; (d) acidification with 1M HCl to pH 2; series of (e) solid phase extractions with rinses of (f) water and (g) methanol.

At the end of the SeaSCAPE 2019 campaign, we attempted to extract m-DOM from a large amount of the bloom water (in its death phase). The purpose of this was twofold: 1) to produce a large stock sample of the same m-DOM for multiple experiment uses, 2) be able to provide collaborators with the same “standard” m-DOM for experiments, rather than the status quo of simply extracting m-DOM from potentially very different natural waters and assuming similar characteristics and properties. There were several complications and difficulties in this endeavor. First, the entirety of the ~12,000 L wave flume could not be extracted in a reasonable amount of time. Second, due to the max loading on the high cost SPE cartridges, many of them

had to be used. Third, because the extraction procedure requires a slow flow rate,  $< 2$  mL/min, to maximize absorption of the dissolved organics, a very extensive parallel setup was needed to successfully extract from a large amount of seawater. In short, around 2,000 L of the bloom water was able to be extracted over the course of 48-72 hours leading to sample of m-DOM weighing around 1.7 g. The 2,000 L of water was pumped into clean polypropylene tanks through a 10-micron mesh filter. These tanks were cleaned three times with methanol and three times with deionized water before use. All materials, including tubing, SPE cartridges, etc., were cleaned with methanol and Milli-Q water before use. All of the holding tanks were covered with cleaned plastic sheets to prevent dust and other material from falling in. A peristaltic pump and 0.5" OD Tygon tubing (McMaster Carr) was used to push the mesocosm seawater through a series membrane filter (AcroPak 1500 Capsule with Supor Membrane – 0.8/0.2  $\mu$ m) into a secondary polypropylene tank. This type of filtering allows for high throughput due to the high surface area of filtration. Likely there were multiple ways of completing this step, but because the bloom water is constantly evolving over time due to biological and chemical activity, it was important to complete in as short amount of time as possible. Multiple of these ‘paks’ were needed throughout this final physical filtration step, which was determined by the state of the peristaltic pump and tubing. Once the flow rate decreased significantly, the filter was exchanged to prevent any additional backpressure from causing lysing, which occurred every 750 L or so. Every 200 liters however, this filter was reversed and “cleaned” using a hose to remove buildup of biological material and approximately 1-2 liters of the seawater were used to rinse the cartridge before putting it back into the secondary holding tank. This significantly increased the lifetime of the expensive filter packs.

Once the seawater was successfully filtered down to 0.2 microns, the water was then prepped for solid phase extraction. This acidification step is necessary to protonate the many acidic species found in ocean water (e.g., fatty acids), as the protonated form of the organics are more readily absorbed to the SPE resin. The metal dissolution and possible chemical alteration of the DOM in this step is a subject of debate and very commonly leads to the term “SPE-DOM”, referring to the subset of DOM that is successfully extracted using this method. A large amount of HPLC-grade 1M HCl (Fisher Scientific) was used to bring the pH of the filtered seawater down to about ~2. The large holding tanks were stirred with a large metal stick found on the floor and covered with clean plastic wrap as the HCl was added. Masks and eye protection were used to minimize exposure to any produced gaseous species. Once the pH was measured close to 2, the tanks of acidified and filtered seawater was ready for the extraction setup.



Figure 2.2. Photo of one of the SPE column “udders” in action.

Unlike the previous steps, the SPE step requires a specific flow rate through the column to maximize absorption efficiency. At a flow rate of 40 mL/min, using a single column at a time would result in an extraction length of ~34 days. However, this long time period was avoided by



incorporating sixteen, 5 gram (the largest available), SPE-PPL cartridges in parallel as shown in Figure 2.1. These so-called “SPE udders” were used to cut this time down to under 48 hours. Tygon tubing connecting the udders together while the columns were varied in length until the flow rate of each column were the same. The amount of sample water per g of adsorber was kept below 20 L, however the actual number may be higher due to uncertainty in the flow rates. This likely caused a drop in the DOM recovery % of the extraction procedure. All samples from these extractions were stored in baked glassware in freezers set to -18 °C or below. Any samples that were shipped to other research groups or other laboratories for analyses were sent on dry ice to maintain this frozen state.

### **2.3 Heated Electrospray Ionization High Resolution Mass Spectrometry (HESI-HRMS)**

Heated Electrospray Ionization High Resolution Mass Spectrometry (HESI-HRMS) is used as an important analytical tool throughout this thesis. The instrument used was housed in UCSD’s Environmental Complex and Analysis Laboratory (ECAL) on the second floor in Urey Hall. Using the ThermoFisher Orbitrap mass spectrometer, extremely high resolution can be achieved due to the orbitrap detector. Internal calibrations were done using a set standard solution before runs at the beginning of the day. Specifics on which calibration solutions are used change from experiment to experiment, so additional information can be found in each of the chapters. Similarly, the flow rates (e.g., auxiliary, sheath, etc.) and voltage/currents used in the ionization source also depend on the day’s calibration and are listed in specific chapters where HRMS is used. At a mass resolution of 120,000-240,000, the third or fourth decimal place in an experimentally observed ion is accurate. Data collected from the HRMS is automatically loaded into Xcalibur, one of ThermoFisher’s programs. Once collected, the raw data is quickly transferred to MATLAB for compositional analysis. Various open-access codes exist for HRMS

as each mass spectrometer and experiment is different – the code should be tailored for that specific study. For instance, a study looking at the change in dissolved organic sulfur specific and oxidation with sulfur dioxide or dimethyl sulfide, should have carefully constructed filters in the code to allow for accurate matching of sulfur containing species. Whereas a simple model experiment containing carbon, hydrogen, oxygen, and light, does not need such filtering or considerations for sulfur atoms beyond the presence of contaminants. As such, a code similar to that which was used throughout this thesis, albeit edited to fit certain studies, can be found a 2020 paper by Hawkes and co-workers.<sup>3</sup> The idea of using interlab comparisons to measure up one high resolution mass spectrometer to another is a fantastic idea. However, the lack of marine relevant systems in this DOM paper reflects the status quo of the terrestrially focused environmental chemistry community.

### **2.3 Attenuated Total Reflectance Fourier Transform Infrared (ATR-FTIR) Spectroscopy**

The use of spectroscopy is highly complementary to mass spectrometry data provides an in situ method of molecular analysis. Without the use of advanced analytical methods or tandem mass spectrometry, it is very difficult to ascertain certain chemical groups from one another. For instance, the difference between an aldehyde and an alcohol. The structure of cyclohexanal and 1-hydroxymethylcyclohexene are clearly very different as shown in Figure 2.2. The theoretical masses of both of these compounds ( $C_7H_{12}O$ ) is  $m/z$  112.08882 and thus, indistinguishable from one another in the mass spectrum. Using liquid chromatography would be able to separate these components, but the chemical analysis would still be lacking without standards or time intensive MS/MS techniques. However, Fourier Transform Infrared (FTIR) spectroscopy easily differentiates these two species as the  $\nu(O-H)$ ,  $\nu(C=C)$ , and  $\nu(C=O)$  stretching frequencies are very distinct and arise a specific frequency in the spectrum.

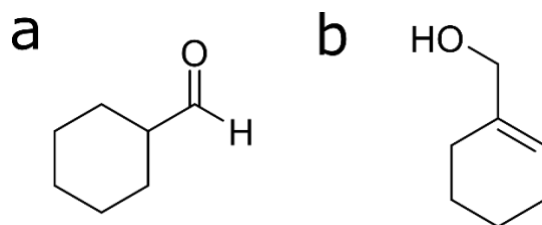


Figure 2.3. Chemical structures of  $C_7H_{12}O$  as a) cyclohexanal and b) 1-hydroxymethylcyclohexene. Although the same  $m/z$ , there are clear differences between the two molecules that can be determined by infrared spectroscopy.

In this dissertation, both transmission FTIR and ATR-FTIR (ThermoFisher Scientific) spectroscopies are used, with the latter being the used for the majority of the research done here. The ATR-FTIR system utilizes an ATR element where a thin film of a solid or liquid sample can be place on top of as shown in Figure 2.3. The infrared light that passes through the crystal will internally reflect off of the surface at an angle greater than the critical angle and back towards the bottom of the crystal – where it will repeat this process  $n$  times depending on the angle of incidence of the light, the nature of material that makes up the element, and the length of the element. The type of ATR element use mainly throughout this thesis is amorphous material transmitting infrared radiation (AMTIR), with the compound formula of  $Ge_{33}As_{12}Se_{55}$ . At the interface, an evanescent wave is formed. While the details of the process have been described elsewhere,<sup>4</sup> the most crucial point is that an evanescent wave forms and falls off at the interface between air and the high refractive index element. This occurs because the electromagnetic wave, the IR light, cannot be absent or “discontinuous” at this interfacial point and thus extends a little beyond, on the order of 1 micrometer, as it is internally reflected. Though this is of course a gross simplification of this phenomena. A review by Milan Milosevic<sup>5</sup> relates the “propagation” qualities of the evanescent wave to that of a screw being turned, where the threads appear to be moving along with the screw itself (the incident and reflected IR light), but are actually just

remaining in place. Thus, it is not actually a propagating wave and allows us to measure loss of energy due to absorption of the thin film without it being scattered.

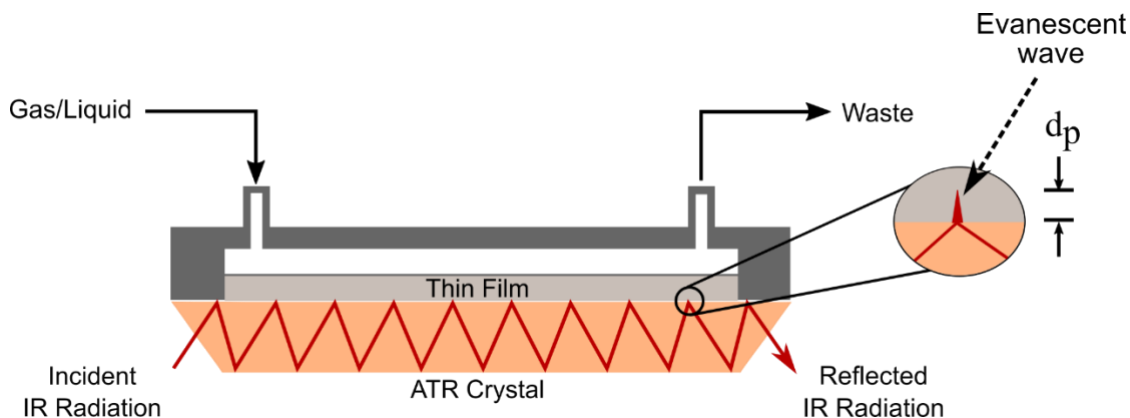


Figure 2.4. Diagram of the ATR crystal, housing, and reflected IR radiation. *Figure by Izaac Sit.*

For the case of an AMTIR crystal, the depth penetration ( $d_p$ ) past the crystal medium is approximately 1.70 microns at  $1000\text{ cm}^{-1}$ . A thin film of a solid can be made by depositing half a mL of a 5 mg/mL solution of water and a suspended solid. Different solvents such as methanol, acetonitrile, etc. may be used but the quick drying sometimes causes the film to crack and lift from the surface. For that case of  $\text{SiO}_2$  and  $\text{TiO}_2$ , this mixture creates a film between 3 and 10 microns thick, which can be verified by a cross section in a method such as scanning electron microscopy. Observations of photochemical interactions can be done in ATR-FTIR by using a sample holding cell with a quartz window top. The instrument top is covered with a plastic bag and taped down to ensure positive pressure from the clean dry air, as the light source is positioned over the sample. For this dissertation, an LCS-100 Solar Simulator (Oriel, Model 94011A) is used in photochemical experiments. The light source utilizes a xenon arc lamp with an AM1.5G filter to simulate the solar output down to 300 nm. An additional water filter is used to block infrared radiation and helps with preventing thermal reactions from being mixed up with the photochemical ones. It is advised that a fan be used, or the dry air aimed towards the

enclosed sample, so that any heat that does arise is quickly dissipated. For many experiments, the resulting surface thin film is collected for additional analysis – specifically for surface adsorbed organic species. This is done by filling the sample trough with approximately 300 microliters of solvent (usually HPLC-grade methanol or acetonitrile) and the surface lifted with a clean plastic or wooden spatula very carefully as to not scratch the crystal surface. The solution is then pipetted into a 1 mL GC vial that has been baked to 500 °C prior to use. A baked Pasteur pipette works well here, as its diameter is large enough to allow the flakes of thin film material to be sucked into the pipette. Another 200 microliters of solvent are used to pick up the remaining surface material. A method blank is advised here, rather than just a solvent blank, where a clean and empty sample holder is filled with the solvent and the spatula used, so that an accurate picture of contaminants can be made.

## **2.4 Teflon Chamber Design, Construction and Operation**

To simulate indoor activities, a 0.18 m<sup>3</sup> environmental polyfluorotetraethylene (Teflon) chamber (0.56 m x 0.56 m x 0.56 m) was constructed (Figure 3.4). One side of the chamber walls was connected to zero air and gas flow via Teflon tubing. Relative humidity can be controlled by attaching a third line from a bubbled flask containing Milli-Q and measured using a sensor (Sensidyne). Any flow made from bubbling a solution is interrupted by a HEPA filter before entering the chamber in the case that unwanted aerosols are formed. For bleach cleaning, gas-phase HOCl was generated by bubbling clean air at a known flow rate to a solution of sodium hypochlorite (NaOCl) buffered with sodium phosphate monobasic monohydrate (NaH<sub>2</sub>PO<sub>4</sub>•H<sub>2</sub>O) to achieve a pH of 6.5 in which the production of HOCl<sub>(g)</sub> is maximized.<sup>6</sup> For other organic gases, such as oleic acid or limonene, a slow flow of dry clean air is blown over a reservoir of the organic and diluted into the main clean air line. Surfaces in the chamber can be

used to interact with the incoming gas phase or particle phase species. Window glass, for instance, is vertically held in place using a Teflon holder. Powdered metal oxides or nanoparticles such as powdered SiO<sub>2</sub> sample can be placed on a petri dish or made into a thin film, exposing it to a sample for a desired time period. During exposure, all sides of the chamber were covered with a black cloth to minimize light interference. This was especially important for HOCl, since it can photolyze to form OH and Cl radicals. Future experiments concerning the presence of light on HOCl exposure with different types of surfaces (e.g. TiO<sub>2</sub>) will also be carried out.

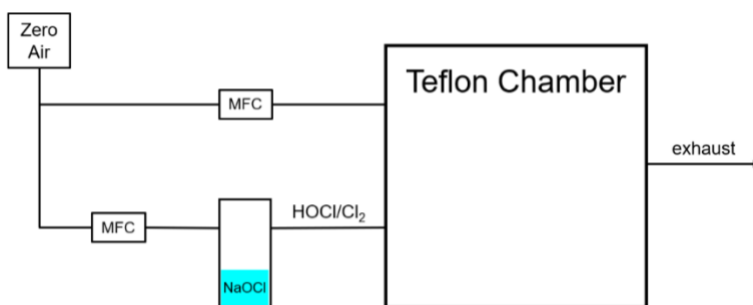


Figure 2.5. A schematic of the 0.18 m<sup>3</sup> Teflon chamber used in the HOCl experiments. Zero air is cleaned of organics and carbon dioxide in lab and dried below 5% RH. MFC refers to mass flow controller.

## 2.5 References

- (1) Dittmar, T.; Koch, B.; Hertkorn, N.; Kattner, G. A Simple and Efficient Method for the Solid-Phase Extraction of Dissolved Organic Matter (SPE-DOM) from Seawater. *Limnol. Oceanogr. Methods* **2008**, *6* (6), 230–235.
- (2) Kido Soule, M. C.; Longnecker, K.; Giovannoni, S. J.; Kujawinski, E. B. Impact of Instrument and Experiment Parameters on Reproducibility of Ultrahigh Resolution ESI FT-ICR Mass Spectra of Natural Organic Matter. *Org. Geochem.* **2010**, *41* (8), 725–733.
- (3) Hawkes, J. A.; D’Andrilli, J.; Agar, J. N.; Barrow, M. P.; Berg, S. M.; Catalán, N.; Chen, H.; Chu, R. K.; Cole, R. B.; Dittmar, T.; Gavard, R.; Gleixner, G.; Hatcher, P.G.; He, C.; Hess, N.J.; Hutchins, R.H.S.; Ijaz, A.; Jones, H.E.; Kew, W.; Khaksari, M.; Palacio Lozano, D.C.; Lv, J.; Mazzoleni, L.R.; Noriega-Ortega, B.E.; Osterholz, H.; Radoman, N.; Remucal, C.K.; Schmitt, N.D.; Schum, S.K.; Shi, Q.; Simon, C.; Singer, G.; Sleighter, R.L.; Stubbins, A.; Thomas, M.J.; Tolic, N.; Zhang, S.; Zito, P. An International Laboratory Comparison of Dissolved Organic Matter Composition by High Resolution Mass Spectrometry: Are We Getting the Same Answer? *Limnol. Oceanogr. Methods* **2020**, *18* (6), 235–258. <https://doi.org/10.1002/lom3.10364>.

- (4) Mudunkotuwa, I. A.; Minshid, A.; Grassian, V. H. ATR-FTIR Spectroscopy as a Tool to Probe Surface Adsorption on Nanoparticles at the Liquid-Solid Interface in Environmentally and Biologically Relevant Media. *Analyst* **2014**, *139* (5), 870–881.
- (5) Milosevic, M. Internal Reflection and ATR Spectroscopy. *Appl. Spectrosc. Rev.* **2004**, *39* (3), 365–384.
- (6) Deborde, M.; von Gunten, U. Reactions of Chlorine with Inorganic and Organic Compounds during Water Treatment-Kinetics and Mechanisms: A Critical Review. *Water Res.* **2008**, *42* (1–2), 13–51. <https://doi.org/10.1016/j.watres.2007.07.025>.

## 2.6 Liquid Sampling Atmospheric Glow Discharge Characterization and Application

Analysis of complex environmental samples using mass spectrometry represents a challenging problem due to low concentrations of target analyte(s), chemical lability, and the presence of matrix materials such as salts.<sup>1</sup> Despite these challenges, numerous improvements which utilize unique methods for sample preparation, introduction, and data analysis have been made over the past several decades.<sup>2</sup> Samples containing dissolved organic matter (DOM), an abundant component in terrestrial and marine environments and operationally defined as molecular species that passes through a 0.45  $\mu\text{m}$  filter<sup>3</sup>, can contain over 10,000 different molecular signatures<sup>1</sup>, most of which are not fully characterized. Even selectively filtered samples from field studies aiming to look at specific classes of molecules, fatty acids or lipids at the ocean-air interface for example, can contain hundreds of unique structures as well as salts.<sup>4</sup> Besides the complex organic nature of environmental samples, the interfering presence of salt is a limitation for in-depth mass spectrometry analysis of samples such as marine-DOM.

Electrospray ionization (ESI) is the predominant ionization method used in high resolution mass spectrometry for environmental samples because it can ionize a wide range of molecules with respect to polarity and molecular weight.<sup>5</sup> However, sea salts nominally at  $\sim 0.6\text{M}$  NaCl, can greatly affect signal intensity even with concentrations below 0.1 mM.<sup>6</sup> There are a few modified ESI methods that can deal with elevated salt concentrations - however, these modified methods are specific to protein relevant systems and often result in either low ion signal or high sample consumption rates.<sup>7-9</sup> Other methods exist to circumvent this salt issue entirely, such as using solid phase extraction (SPE) to collect marine-dissolved organic matter (m-DOM or sometimes known as SPE-DOM), described in detail by Dittmar and coworkers in 2008.<sup>10</sup> However, concentrating and removing salt from natural organic matter samples (via



ultrafiltration, SPE, reverse osmosis, etc.) can result in recovery issues depending on the type of sample<sup>11,12</sup> and possibly alter the chemical nature of the sample.<sup>13</sup> Thus, there is a need to analyze complex salt-containing environmental samples in both the field and lab without extensive pre-processing. Herein we have applied a new ionization method for the analysis of complex marine samples containing high concentrations of salts, liquid sampling-atmospheric pressure glow discharge (LS-APGD). This method shows high sensitivity, is field-ready, and leads to reasonably low levels of molecular fragmentation.

The LS-APGD ion source used in this study was purchased from Clemson University and has been described previously by Marcus and coworkers,<sup>14</sup> and briefly, the source operates similarly to a traditional atmospheric pressure chemical ionization (APCI) source using a corona discharge. However, in this case, a  $\sim 1 \text{ mm}^3$  helium-based plasma is formed at the end of the capillary where the liquid sample would normally be vaporized before contact with the APCI corona. This plasma assists in the vaporization of the liquid samples into ionized gas phase molecules. The relatively low power (maximum of 60 mA and 500 V) of the plasma-forming electrode, compared to common 3-6 kV corona or glow discharge sources, enables practical requirements for field deployment.

Initially, LS-APGD was developed for elemental and isotopic analysis, where it produces ng/L detection limits of select metals such as Cs and U, and  $\mu\text{g/L}$  detection for Fe, Ni, Cu, In, Cd, and Pb.<sup>14-16</sup> The simple and field-ready LS-APGD has detection limits that are semi-competitive with ICP-MS. Because the source is optimized for aqueous salts and metals, samples with ocean salinity levels would not be a large issue as it is with other ionization sources. With such a low power plasma, it has already been shown that LS-APGD can analyze intact organic species, therefore the analysis of organics in seawater is possible<sup>17</sup>. Thus, we show here the

capabilities of LS-APGD for the analysis of samples that are expected in a marine environment, with and without salt, are demonstrated through investigations of three distinct sample types, a simple well-characterized triglyceride mixture (C8-C16), and highly complex samples of Suwannee river fulvic acid (SRFA) and m-DOM. LS-APGD and ESI are contrasted to identify the spectral features acquired for each sample type.

### **2.6.1 Experimental Methods**

An initial model sample was prepared for this study. A certified triglyceride reference mixture was purchased from Sigma Aldrich (Supelco). This reference mixture is composed of five saturated triglycerides of chain length C8-16 at approximately equal mass fractions. The mixture was dissolved in acetonitrile and all analyzed samples were run at a concentration of 9 mg/L. Samples of triglyceride mixture and environmental mimics were prepared in saltless or 0.20 M NaCl in 1:2 H<sub>2</sub>O/MeOH and teed at 15  $\mu$ L/min into an isocratic stream of 1:2 H<sub>2</sub>O/MeOH + 0.1% Formic Acid with 1:200 Ultramark calibration mix also flowing at 15  $\mu$ L/min using the pump, gas controller, and high voltage assembly (Fusion 100T, Chemyx, Stafford TX). The LS-APGD spectra were collected at a range of probe conditions from 20-30 mA and an electrode spacing 0.25-1.5 mm past the plasma ignition point (Figure 2.6). Sample flow rates were chosen to maximize stability of the plasma and reduce deposition of involatile material on the inlet. Mass spectral data were extracted using Thermo XCalibur data analysis software and imported into R-Studio or Igor (Wavemetrics) for further analysis.

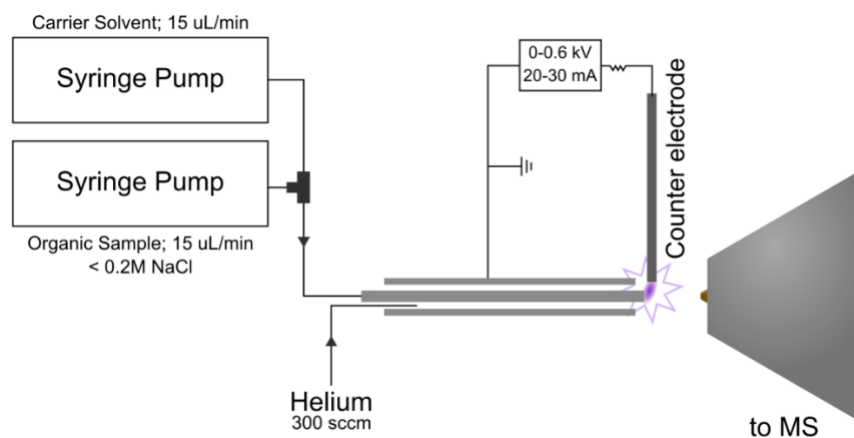


Figure 2.6 Graphical representation of the LS-APGD

### *Ultra-High Resolution Mass Spectrometry*

To compare the LS-APGD source to a universal ionization method, a heated electrospray ionization-linear ion trap Orbitrap high-resolution mass spectrometer (HESI-LIT-Orbitrap, Thermo Fisher Scientific) was used for this study. Samples were directly injected into the electrospray source at 5-15  $\mu\text{L}/\text{min}$ . Peaks were detected and analyzed in positive mode at a capillary voltage set to 2.8 kV, where the capillary was maintained at a temperature of 325  $^{\circ}\text{C}$ . HESI gases (arbitrary units) were set to: sheath at 30, auxiliary at 10, and sweep at 0. The HESI-LIT-Orbitrap was always calibrated before both HESI and LS-APGD configurations using a calibration mix (Pierce ESI Ion Calibration Solutions, Thermo Fisher Scientific) to maintain mass accuracy below 2 ppm. During data acquisition, the Orbitrap mass range is set to  $m/z$  50-2000 with the mass resolution set at 120,000. All solutions in this study contained 0.1% formic acid. Mass error drift was prevented by mass locking the data acquisition to persistent signals from the calibration solutions, giving a range from  $m/z$  195 to 1250.

Using the Orbitrap, in both HESI and LS-APGD modes, masses of thousands to tens of thousands of unique molecular signatures were observed for the complex mixtures. Molecular formula assignments were acquired using the Xcalibur Thermo Fisher Scientific software. The

following element ranges were used:  $^{12}\text{C}$ , 0–100;  $^1\text{H}$ , 0–200;  $^{16}\text{O}$ , 0– 50;  $^{14}\text{N}$ , 0–5;  $^{32}\text{S}$ , 0–2; and  $^{23}\text{Na}$ , 0–1. These element ranges were chosen based on past studies attempts on mass spectral characterization of highly complex organic samples<sup>18,19</sup>. Formulae with an O/C ratio below 0 or greater than 2.5, as well as a relative double bond equivalence values above 25 or below zero, were excluded. In addition, formulas were required to be below a mass error of 2 ppm and have a relative intensity greater than 0.1% of the base peak. Based on these strict heuristic filtering rules and depending on the sample, only between ~30-60% of the ions detected during data acquisition were assigned a molecular formula.

Two environmentally complex samples were used in this study to test the LS-APGD ability to ionize complex systems: Suwannee River fulvic acid (Standard III, International Humic Substances Society) and m-DOM (collected from Scripps Pier, La Jolla). The collection and purification of m-DOM in this study is described by Dittmar and coworkers.<sup>10</sup> Briefly, coastal ocean water was passed through a 50 micron mesh is collected from the pier. Nutrients, f/2 algae growth medium (Proline, Aquatic Eco-Systems) as well as solutions of sodium metasilicate, were added to the water. The m-DOM was collected after the subsequent bloom and senescent-phase of phytoplankton over 1-3 weeks. The water was then passed through a series of filters: 10, 0.7, and 0.2 micron pore sizes. The samples to be extracted were acidified to a pH value at or close to 2.0 using 1 M HCl (Sigma Aldrich). The acidified solution was gravity filtered through a solid phase extraction column (Bond Elut PPL, Agilent) at no more than 5 mL/min or about 2 drops per second. The column was then washed and eluted using methanol and the resulting yellow/orange solution was quickly (under an hour) dried using a rotary evaporator. All glassware used was combusted at 500°C for 8 hours to remove trace organics before use. The solid sample was stored at -21°C under nitrogen.

## 2.6.2 Examples

*Examples of Simple Molecular Systems.* For the majority of measurements shown in this work, salt concentrations were kept at 0.2 M or lower. For marine samples, this was done by simply diluting with methanol. A few measurements on samples containing up to 0.6 M salt (seawater salinity) were performed, however significant deposition of material on the MS inlet capillary prevented extended operation before cleaning was required. Further improvements of the LS-APGD source to reduce salt buildup, such as positioning the LS-APGD capillary orthogonal to the MS inlet or the introduction of an auxiliary sweep gas are warranted. Furthermore, it is recommended that upstream instrument orifices and ion optics such as transfer capillaries and S-lenses be cleaned more frequently after sustained periods of analysis of salt-containing samples.

*Analysis of a Triglyceride Reference Material Mixture*

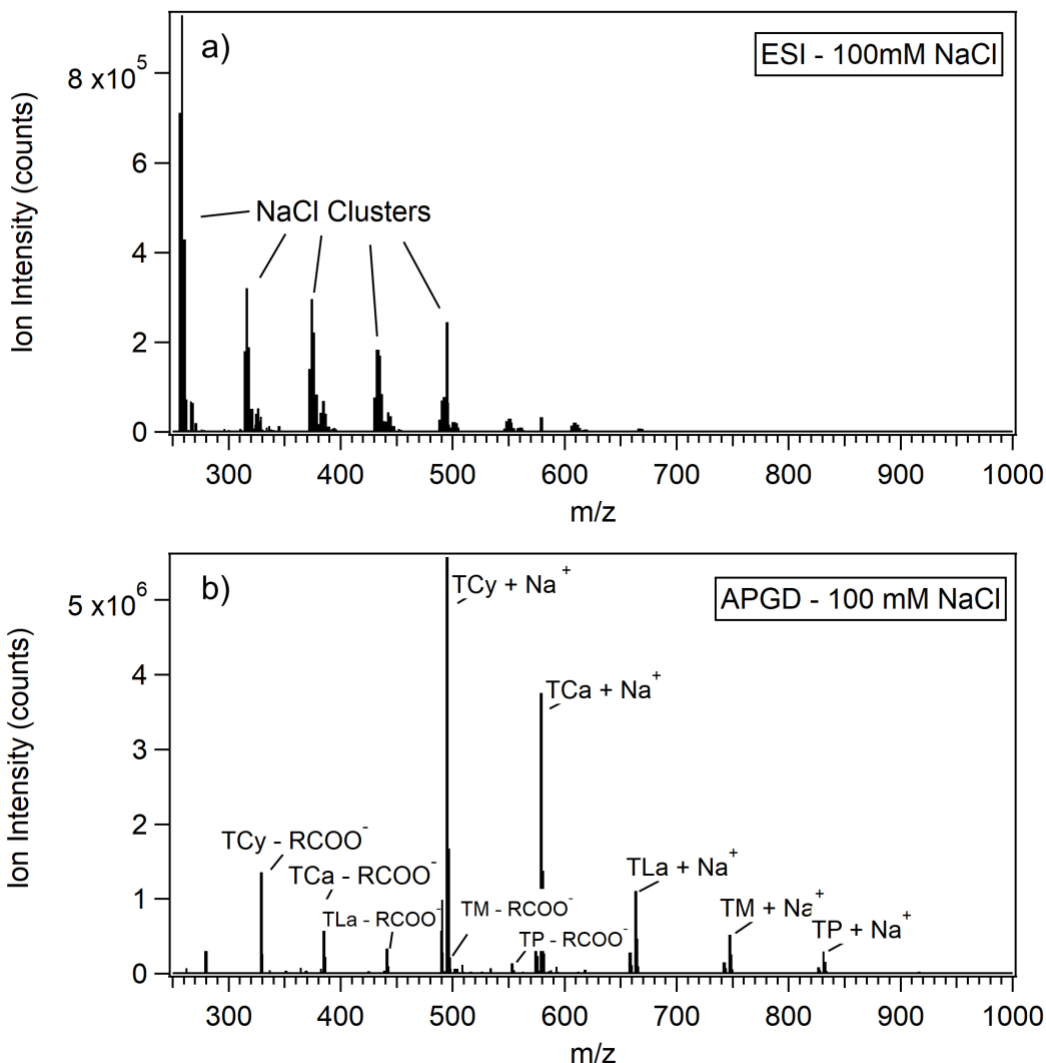


Figure 2.7. Averaged mass spectra obtained from HRMS analysis of triglyceride mixture in 100 mM NaCl by ESI (a) and LS-APGD (b).

Normalized averaged mass spectra of the triglyceride mixture by electrospray and LS-APGD are shown in Figure 2.7 at 100 mM NaCl. Further analysis conditions of non-saline triglyceride mixtures by LS-APGD and ESI are shown in Scheme 2.2. Both the neat ESI and LS-APGD analysis preferentially formed cationized triglyceride ions adducted with  $\text{NH}_4^+$  (Figure 2.8a,b). However, at 0.1 M NaCl for the LS-APGD (Figure 2.8c), the prevalence of sodium adducted species was significantly higher in proportion to the ammoniated ion. This effect is

driven by the preferential binding of sodium over ammonium to triglycerides previously observed in ESI mass spectrometric studies in lipidomics.<sup>20,21</sup> For ESI at 0.1 M NaCl, the production of NaCl ion clusters completely eclipses the production of the sodiated triglyceride cations (Figure 2.7a), and is not effective at ionizing triglycerides above 1 mM (Figure 2.8c).<sup>22</sup> Triglyceride precursor ion counts for LS-APGD were equal to or 10-20% greater than those produced by ESI, suggesting that the ionization technique is comparably sensitive for the sample type. (Figure 2.7a, b; Figure 2.8a, b, c) Furthermore, LS-APGD was more capable of ionizing higher-mass triglycerides in greater proportion to the total ion count than ESI (Figure 2.7b). Notably, significant differences in the ratio of quasi-molecular ions to their primary decomposition products ( $M\text{-RCOO}^-$ ) between neat and saline conditions stimulated an investigation to understand the influence of salinity and LS-APGD conditions (current and electrode distance) on the production and fragmentation of triglyceride species.

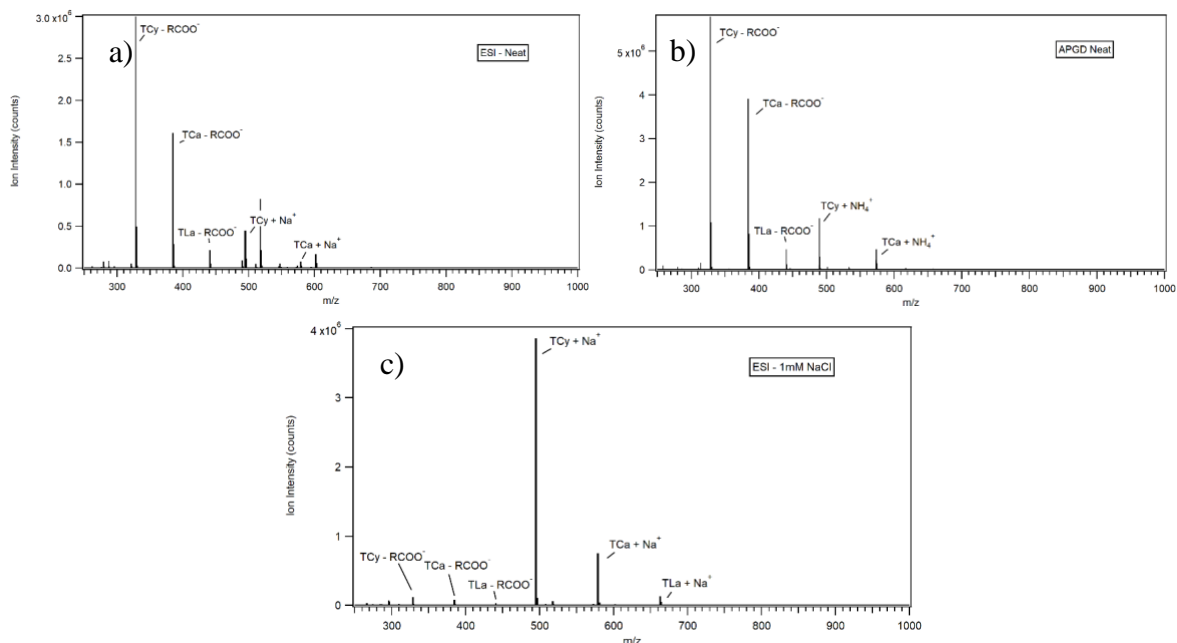


Figure 2.8. Triglyceride mixture analysis for neat ESI (a), APGD (b), and ESI at 1mM NaCl (c)

Here we define the fragmentation ratio from the measured ion intensity of triglyceride precursor and product species in Equation 2.1:

$$(2.1) \quad F_{Triglyceride} = \frac{[TAG+Na]_I + [TAG+NH_4]_I}{[TAG-RCOO^-]_I}$$

Where  $I$  is the average raw ion intensity of each species and the selection of the diglyceride fragment of the ammoniated and sodiated species is based on the observation that very little other fragmentation products are observed in the mass spectrum. Observations of diglyceride fragments from both collisionally activated  $-Na^+$ ,  $-NH_4^+$ , and protonated triglycerides in the literature have also been commonly identified.<sup>23–25</sup> A list of the selected ions can be found in Table 1 of the supplementary information.

Figures S2a-e (see paper) explore the influence of discharge current and electrode distance under saline conditions. Various tradeoffs were observed in the production of precursor cations, with higher ratios of precursor to product ion at further electrode distances (Figure S3 – see paper). However, for the current parameters studied, higher electrode currents favored the



production of precursor cations and decreased fragmentation (S3). Differences in fragmentation ratio with triglyceride carbon tail chain length (S3a) are likely due to general reduced stability with increased length, a common feature in organic species. These results contrast recent investigations of LS-APGD parameters for analysis of caffeine, where electrode distance showed little effect on fragmentation conditions.<sup>17</sup> In addition, for the present investigations with triglycerides there is a general increase in fragmentation ratio with discharge current observed. In conclusion, it is further suggested that ionization behavior, especially fragmentation, in LS-APGD requires a compound-class dependent investigation to optimize analysis conditions.

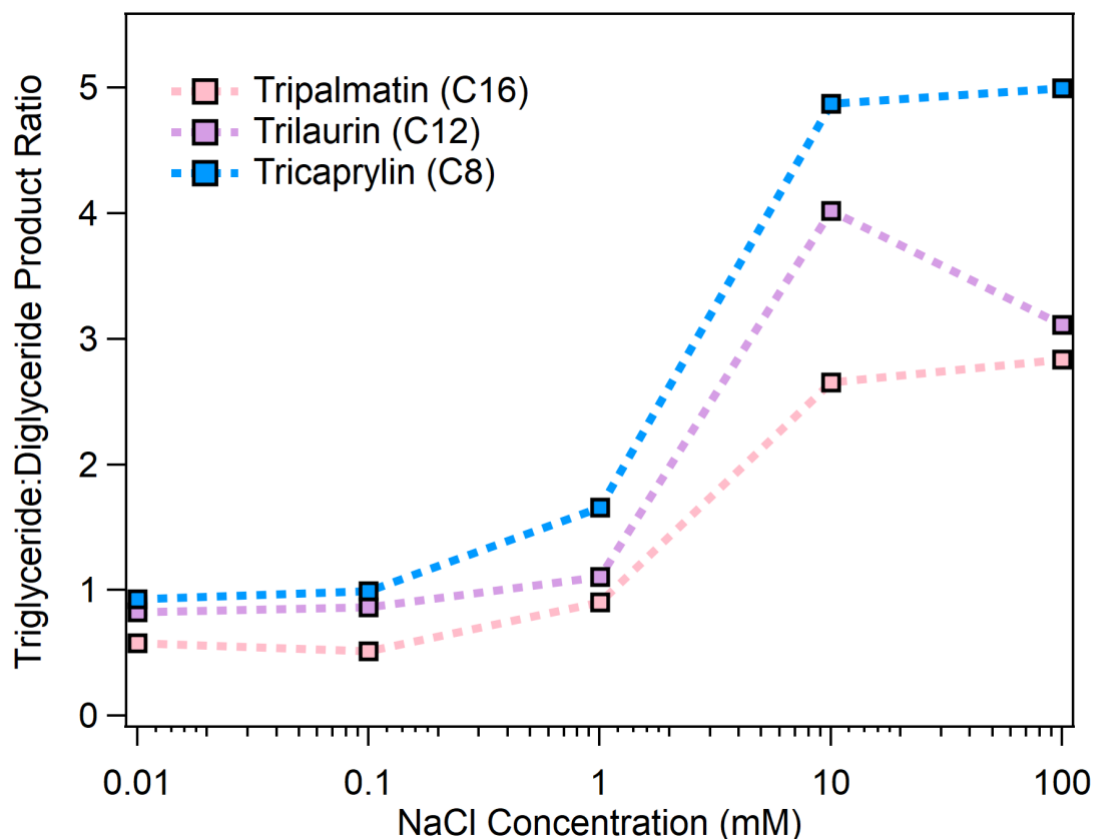


Figure 2.9. LS-APGD Triglyceride:diglyceride fragmentation ratios from 0.01-100mM for triglyceride mixture samples at constant electrode distance (0.5 mm) and discharge current (30 mA).

Interestingly, LS-APGD fragmentation ratios between the neat and saline samples were significantly different at the same LS-APGD conditions, with reduced fragmentation in the saline samples. To explore this behavior further, triglyceride mixture samples were analyzed over 5 orders of magnitude of [NaCl]. The resultant fragmentation ratios are shown in Figure 2.9. Fragmentation ratios at 0.01 mM NaCl are below 1, indicating the majority of all triglycerides under these conditions are fragmented to diglyceride or other fragments, barring differences in ion transfer efficiency. In contrast, at 1 mM, the fragmentation ratio favors the production of the sodiated cations over fragmentation. This observation is attributed to the altered adduct

distribution in the saline analysis, which is supported by studies of collisionally induced dissociation of triglyceride species.<sup>26</sup>

It has been observed that the generation of products via collisionally induced dissociation requires significantly larger collisional energies for sodiated triglycerides over ammoniated triglycerides, likely due to strong coordination between the Na<sup>+</sup> cation and the electron donating groups on the triglycerides.<sup>21</sup> Thus, it is proposed that in-source adduct assisted stabilization of the ionized triglyceride significantly enhanced the persistence of the pseudomolecular ion from thermal decomposition in the LS-APGD source. In support of this hypothesis, Figure S4 (see paper) shows the ratio of sodiated to ammoniated cations over varying NaCl concentrations, indicating a significant shift in adduct distribution towards sodium with increasing [NaCl]. This trend is driven primarily by increases in the production of sodiated molecular ions as opposed to a decrease in ammoniated precursor species, as evidenced in Figure S5a,b (see paper) where sodiated species increase with added [NaCl] and ammoniated species remain relatively constant. Curiously, the trends in both the fragmentation and adduct ratios reflect different dependencies on salt concentration. It is further hypothesized that this effect is caused by the reduction of excited, but unionized triglyceride species at increasing salt concentrations as they are preferentially sodiated. Unfortunately, production of protonated triglyceride species was not particularly effective and cannot be used to verify this hypothesis further. This result adds interesting detail to the aspects of salt-containing analysis as the alteration of the overall adduct state may enhance, or possibly hinder the observation of intended species through changes in fragmentation. Although changes in adduct state with varying salinity add interesting features and detail to LS-APGD that must be considered, the source successfully analyzes triglycerides in

the presence of high salt concentration in comparison to ESI where salts render the spectra unusable.

### *Examples of Complex Environmental Samples*

DOM in the Earth's oceans is the single largest pool of reduced carbon.<sup>27</sup> Complex DOM samples are notoriously difficult to characterize and therefore a suite of instrumental techniques has been developed.<sup>1</sup> This study aims to provide a possible alternative to the current approaches used historically for DOM collection, extraction, and analysis. Since m-DOM is particularly understudied due to its relatively low concentration in the ocean (~ 1 mg/L) and high concentration of salts, it was selected as a model system to be tested by this new approach in this study.

Since the composition of DOM and humic like substances can change significantly based on location and/or time<sup>28</sup>, SRFA was used as a standard in this study. SRFA and Suwannee River DOM have been extensively studied over the past two decades.<sup>18</sup> Though much of the identity of species in terrestrial DOM remains elusive, this system provided a reasonable benchmark for LS-APGD for comparison to other ionization techniques.

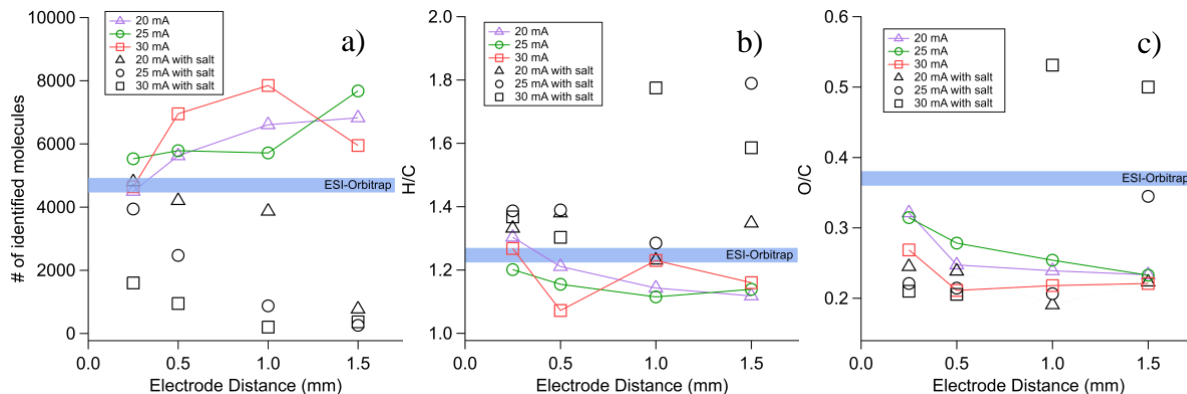


Figure 2.10. HRMS analysis of SRFA, with (black) and without salt (colored), at various electrode currents and positions with corresponding ESI values analyzed using SRFA (no salt) at the same concentration. Relationships shown between: (a) Number of identified molecules averaged mass spectra; (b) hydrogen:carbon ratios and; (c) oxygen:carbon ratios.

The electrode distance and plasma current in the LS-APGD have a significant impact on the ability to ionize species in the SRFA sample. Figure 2.10 shows that the lowest current and shortest electrode distances result in the most similar spectral characteristics between neat and saline samples. This is largely attributed to the fact that the smaller and weaker plasma results in softer ionization. Comparisons between salt-containing and salt-free samples in LS-APGD indicate that the incidence of  $\text{Na}^+$  adducts increases by 15% or more depending on the LS-APGD source parameters such as electrode distance and current, indicating that these effects must be accounted for in data analyses of salt-containing samples. Notably, fragmentation of organic species (most commonly  $\text{C}_9\text{H}_7^+$  and  $\text{C}_{10}\text{H}_8^+$ ) was prevalent in both salt-containing and salt-free samples, a drawback to the technique when the composition of the sample is mostly unknown.

In Figures 2.10a and 2.10b, the LS-APGD ionization of the SRFA, both with and without salt, shows good agreement when compared to ESI. However, in Figure 2.10c, a notable difference in the O/C ratio is observed, where LS-APGD analysis of the SRFA sample consistently measures a lower O/C value (between 0.20 and 0.33). In this study, ESI of SRFA

produced an O/C ratio of about 0.38, which is within the range of literature values of 0.3 to 0.6.<sup>18,29</sup> The observations of a lower O/C ratio in the LS-APGD experiment is attributed to the source more efficiently ionizing non-polar or low-polarity organics compared to ESI, comparable to a corona-based ionization source such as APCI. This finding makes LS-APGD an attractive option for studying complex organic samples due to its apparently wide range of potential species, polar and nonpolar, to be ionized. A more detailed comparison of SRFA molecular composition by LS-APGD and ESI is planned for a future study.

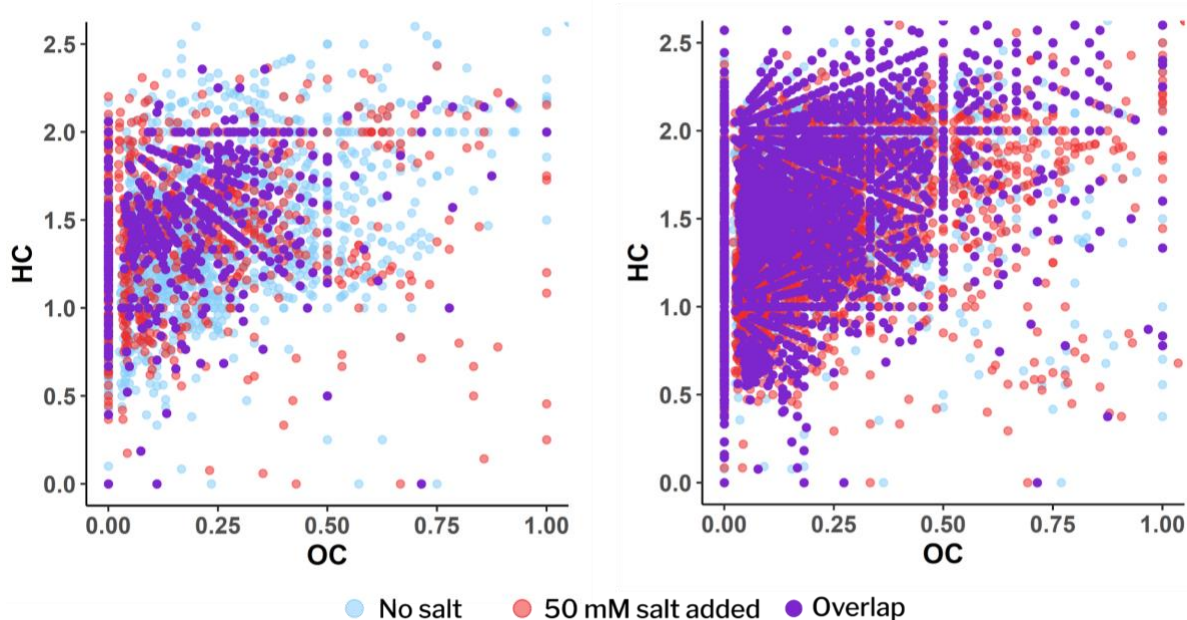


Figure 2.11. Van Krevelen diagrams of m-DOM spectra showing oxygen:carbon (OC) and hydrogen:carbon (HC) ratios, measured by (a) traditional ESI and (b) LS-APGD. A comparison is shown for spectra obtained with (50 mM added NaCl) salt (red circles) and without salt (light blue circles), where the overlap of elemental compositions is also shown (purple circles).

A sample of m-DOM was extracted from seawater collected off Scripps Pier in La Jolla, California. The m-DOM was analyzed with both heated-ESI and the LS-APGD ion sources with direct infusion at 5  $\mu\text{L}/\text{min}$  and 15  $\mu\text{L}/\text{min}$  respectively. Sample collection was relatively fast, in part due to the high throughput of the Orbitrap, resulting in sample consumption less than 60  $\mu\text{L}$

for the LS-APGD. The ESI and LS-APGD mass spectra of non-salt containing m-DOM were similar in overall spectral range from 150-600 m/z (S6 – see paper), with the LS-APGD spectra differing due to the appearance of aforementioned ion fragmentation signatures as well as a factor of ten increase in total ion intensity. Adding 50 mM of NaCl to the m-DOM sample, the ESI shows a vastly different spectrum compared to the no-salt spectra, with multiple groups of peaks separated by 23 m/z units due to the formation of a large number of sodium adducts. Figure 2.11a shows the small overlap in the no-salt and salt-containing m-DOM (less than 20%) analyzed by ESI in a Van Krevelen diagram.<sup>30</sup> Conversely, Figure 2.11b shows significant overlap between the no-salt and salt containing m-DOM when ionizing with the LS-APGD (above 80%). There is also a significant increase in identified features (such as condensed aromatics, shown below 0.25 O/C ratio and below 1.25 H/C ratio) in the LS-APGD mass spectra compared to the ESI, possibly in part due to fragmentation, but more likely a result of: 1) LS-APGD being able to ionize non-polar compounds more efficiently than ESI and 2) an increase in total ion signal, thus increasing sensitivity for a wider range of low concentration compounds. Comparisons of unique molecular signatures detected using traditional ESI and LS-APGD show that around 33% of exact masses (including adducts) found in ESI were also detected using the LS-APGD (S7 – see paper).

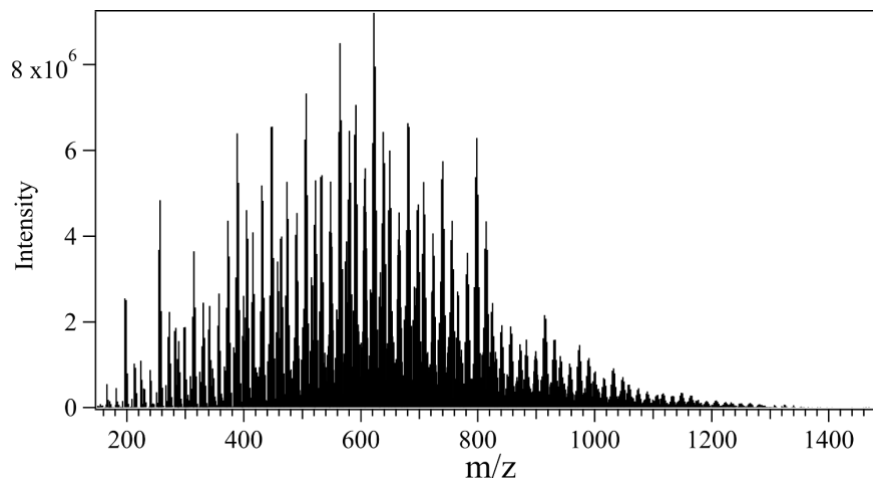


Figure 2.12. High resolution mass spectra of pure bloom coastal seawater obtained by LS-APGD Orbitrap mass spectrometry.

The ability of LS-APGD to analyze organics in complex matrices was further demonstrated by directly measuring seawater acquired during a phytoplankton bloom with no pre-concentration or extraction step (Figure 2.12). This experiment cannot be compared to traditional ESI mass spectrometry due to the high amount of salt clogging the ESI probe tip and rendering it unusable. The spectrum is composed of many spectral envelopes, similar to those observed in ESI Fourier Transform ion cyclotron resonance mass spectra using the PPL SPE method and contains over 7,000 unique masses.<sup>10,28</sup> To our knowledge, this is the first full-mass spectrum of DOM in pure seawater without any sample preparation required.

Overall, the application of using liquid sampling-atmospheric pressure glow discharge ionization has been shown to ionize complex organic samples successfully in the presence of environmentally relevant salt concentrations. Optimization of the ionization source, using a triglyceride mixture, SRFA, and mDOM led to the conclusion that the operational conditions for the analysis of marine relevant organics depend on sample type and need to be optimized on a case-by-case basis. Mass spectra of environmentally complex compounds (humics, triglycerides,



etc), in the presence of salt, produced more informative ion signals via LS-APGD in comparison to ESI. Such characterization was based on the comparison of the diglyceride:triglyceride fragmentation ratios as well as the ensemble metrics concerning the spectra of SRFA. Notably, the presence of salts can significantly alter the fraction of adducts which may hinder, or possibly assist fragmentation depending on the stability of the coordinated ion complex. For LS-APGD, which has been shown to fragment some organic species, high salinity analysis may enhance sensitivity to the molecular ion. Additionally, changes in the fragmentation patterns due to adducts forming in LS-APGD indicate the need for salinity-dependent calibrations when quantitatively analyzing and comparing samples that have varying salt concentrations.

Preliminary analysis of coastal seawater and m-DOM using LS-APGD points to interesting possibilities for compositional analysis, providing an avenue for field analysis of these complex systems. More work on identifying these species is planned for a future study. Besides being able to analyze discrete complex environmental samples, the LS-APGD has the potential to be used for real-time measurements of aqueous systems in the presence of salts to capture temporal changes in chemistry. Future work using LS-APGD and salt-containing samples will aim to investigate its potential for ionizing sea spray aerosol - where organic fractions can reach up to 80% by mass and salt concentrations can exceed 10 M depending on the size of the aerosol particle.<sup>31</sup> The ability of LS-APGD Orbitrap mass spectrometry to successfully ionize m-DOM in seawater without any sample preparation has far-reaching implications for analyzing m-DOM in the future – where using direct analysis techniques, without inadvertent sample modification, will lead to a more complete characterization of a complex and important component in the marine environment.

### 2.6.3 Acknowledgements

The authors gratefully acknowledge the Marcus Research Group from Clemson University for their support and assistance with the installation of the ionization source and pump assembly. We acknowledge the support of the National Science Foundation through the Centers of Chemical Innovation Program via the Center for Aerosol Impacts on Chemistry of the Environment (CHE-1801971) and the National Science Foundation Graduate Research Fellowship Program (DGE1650112). We also appreciate the support from Dr. Neal Arakawa at the Environmental Complex Analysis Laboratory (ECAL) during this study.

A portion of Chapter 2 is reproduced with permission from the American Chemical Society: Alves, M. R.; Sauer, J. S.; Prather, K. A.; Grassian, V. H.; Wilkins, C. L. Liquid Sampling-Atmospheric Pressure Glow Discharge Ionization as a Technique for the Characterization of Salt-Containing Organic Samples. *Anal. Chem.* 2020, 92 (13), 8845–8851. The dissertation author was a primary investigator and co-first author of this paper.

### 2.6.4 References

- (1) Nebbioso, A.; Piccolo, A. Molecular Characterization of Dissolved Organic Matter (DOM): A Critical Review. *Anal. Bioanal. Chem.* **2013**, 405 (1), 109–124.
- (2) Artifon, V.; Zanardi-Lamardo, E.; Fillmann, G. Aquatic Organic Matter: Classification and Interaction with Organic Microcontaminants. *Sci. Total Environ.* **2019**, 649, 1620–1635.
- (3) Thurman, E. M. *Organic Geochemistry of Natural Waters*; 1985.
- (4) Kennicutt, M. C.; Jeffrey, L. M. Chemical and GC-MS Characterization of Marine Dissolved Lipids. *Mar. Chem.* **1981**, 10 (5), 367–387.
- (5) Banerjee, S.; Mazumdar, S. Electrospray Ionization Mass Spectrometry: A Technique to Access the Information beyond the Molecular Weight of the Analyte. *Int. J. Anal. Chem.*

- 2012**, *2012*, 1–40.
- (6) Constantopoulos, T. L.; Jackson, G. S.; Enke, C. G. Effects of Salt Concentration on Analyte Response Using Electrospray Ionization Mass Spectrometry. *J. Am. Soc. Mass Spectrom.* **1999**, *10* (7), 625–634.
  - (7) Chang, D. Y.; Lee, C. C.; Shiea, J. Detecting Large Biomolecules from High-Salt Solutions by Fused-Droplet Electrospray Ionization Mass Spectrometry. *Anal. Chem.* **2002**, *74* (11), 2465–2469.
  - (8) Mandal, M. K.; Chen, L. C.; Hashimoto, Y.; Yu, Z.; Hiraoka, K. Detection of Biomolecules from Solutions with High Concentration of Salts Using Probe Electrospray and Nano-Electrospray Ionization Mass Spectrometry. *Anal. Methods* **2010**, *2* (12), 1905–1912.
  - (9) Karki, S.; Shi, F.; Archer, J. J.; Sistani, H.; Levis, R. J. Direct Analysis of Proteins from Solutions with High Salt Concentration Using Laser Electrospray Mass Spectrometry. *J. Am. Soc. Mass Spectrom.* **2018**, *29* (5), 1002–1011.
  - (10) Dittmar, T.; Koch, B.; Hertkorn, N.; Kattner, G. A Simple and Efficient Method for the Solid-Phase Extraction of Dissolved Organic Matter (SPE-DOM) from Seawater. *Limnol. Oceanogr. Methods* **2008**, *6* (6), 230–235.
  - (11) Simjouw, J. P.; Minor, E. C.; Mopper, K. Isolation and Characterization of Estuarine Dissolved Organic Matter: Comparison of Ultrafiltration and C18 Solid-Phase Extraction Techniques. *Mar. Chem.* **2005**, *96* (3–4), 219–235.
  - (12) Guo, L.; Santschi, P. H. A Critical Evaluation of the Cross-Flow Ultrafiltration Technique for Sampling Colloidal Organic Carbon in Seawater. *Mar. Chem.* **1996**, *55* (1–2), 113–127.
  - (13) Kruger, B. R.; Dalzell, B. J.; Minor, E. C. Effect of Organic Matter Source and Salinity on Dissolved Organic Matter Isolation via Ultrafiltration and Solid Phase Extraction. *Aquat. Sci.* **2011**, *73* (3), 405–417.
  - (14) Marcus, R. K.; Quarles, C. D.; Barinaga, C. J.; Carado, A. J.; Koppelaar, D. W. Liquid Sampling-Atmospheric Pressure Glow Discharge Ionization Source for Elemental Mass Spectrometry. *Anal. Chem.* **2011**, *83* (7), 2425–2429.
  - (15) Quarles, C. D.; Carado, A. J.; Barinaga, C. J.; Koppelaar, D. W.; Marcus, R. K. Liquid Sampling-Atmospheric Pressure Glow Discharge (LS-APGD) Ionization Source for Elemental Mass Spectrometry: Preliminary Parametric Evaluation and Figures of Merit. *Anal. Bioanal. Chem.* **2012**, *402* (1), 261–268.
  - (16) Hoegg, E. D.; Barinaga, C. J.; Hager, G. J.; Hart, G. L.; Koppelaar, D. W.; Marcus, R. K. Preliminary Figures of Merit for Isotope Ratio Measurements: The Liquid Sampling-

- Atmospheric Pressure Glow Discharge Microplasma Ionization Source Coupled to an Orbitrap Mass Analyzer. *J. Am. Soc. Mass Spectrom.* **2016**, *27* (8), 1393–1403.
- (17) Zhang, L. X.; Kenneth Marcus, R. Mass Spectra of Diverse Organic Species Utilizing the Liquid Sampling-Atmospheric Pressure Glow Discharge (LS-APGD) Microplasma Ionization Source. *J. Anal. At. Spectrom.* **2016**, *31* (1), 145–151.
- (18) Stenson, A. C.; Marshall, A. G.; Cooper, W. T. Exact Masses and Chemical Formulas of Individual Suwannee River Fulvic Acids from Ultrahigh Resolution Electrospray Ionization Fourier Transform Ion Cyclotron Resonance Mass Spectra. *Anal. Chem.* **2003**, *75* (6), 1275–1284.
- (19) Koch, B. P.; Witt, M.; Engbrodt, R.; Dittmar, T.; Kattner, G. Molecular Formulae of Marine and Terrestrial Dissolved Organic Matter Detected by Electrospray Ionization Fourier Transform Ion Cyclotron Resonance Mass Spectrometry. *Geochim. Cosmochim. Acta* **2005**, *69* (13), 3299–3308.
- (20) Hsu, F. F.; Turk, J. Electrospray Ionization Multiple-Stage Linear Ion-Trap Mass Spectrometry for Structural Elucidation of Triacylglycerols: Assignment of Fatty Acyl Groups on the Glycerol Backbone and Location of Double Bonds. *J. Am. Soc. Mass Spectrom.* **2010**, *21* (4), 657–669.
- (21) Adams, J.; Gross, M. L. Energy Requirements for Remote Charge Site Ion Decompositions and Structural Information from Collisional Activation of Alkali Metal Cationized Fatty Alcohols. *J. Am. Chem. Soc.* **1986**, *108* (22), 6915–6921.
- (22) Hao, C.; March, R. E.; Croley, T. R.; Smith, J. C.; Rafferty, S. P. Electrospray Ionization Tandem Mass Spectrometric Study of Salt Cluster Ions. Part 1 - Investigations of Alkali Metal Chloride and Sodium Salt Cluster Ions. *J. Mass Spectrom.* **2001**, *36* (1), 79–96.
- (23) Kalo, P. J.; Ollilainen, V.; Rocha, J. M.; Malcata, F. X. Identification of Molecular Species of Simple Lipids by Normal Phase Liquid Chromatography–Positive Electrospray Tandem Mass Spectrometry, and Application of Developed Methods in Comprehensive Analysis of Low Erucic Acid Rapeseed Oil Lipids. *Int. J. Mass Spectrom.* **2006**, *254* (1–2), 106–121.
- (24) Asbury, G. R.; Al-saad, K.; Siems, W. F.; Hannan, R. M.; Hill, H. H. Analysis of Triacylglycerols and Whole Oils by Matrix-Assisted Laser Desorption/Ionization Time of Flight Mass Spectrometry. **2000**, *0305* (99).
- (25) Rezanka, T.; Sigler, K. The Use of Atmospheric Pressure Chemical Ionization Mass Spectrometry with High Performance Liquid Chromatography and Other Separation Techniques for Identification of Triacylglycerols. *Curr. Anal. Chem.* **2007**, *3* (4), 252–271.
- (26) Duffin, K. L.; Henion, J. D.; Shieh, J. J. Electrospray and Tandem Mass Spectrometry

- Characterization of Acylglycerol Mixtures That Are Dissolved in Nonpolar Solvents. *Anal. Chem.* **1991**, *63* (17), 1781–1788.
- (27) Hansell, D. A. Recalcitrant Dissolved Organic Carbon Fractions. *Ann. Rev. Mar. Sci.* **2013**, *5* (1), 421–445.
- (28) D’Andrilli, J.; Cooper, W. T.; Foreman, C. M.; Marshall, A. G. An Ultrahigh-Resolution Mass Spectrometry Index to Estimate Natural Organic Matter Lability. *Rapid Commun. Mass Spectrom.* **2015**, *29* (24), 2385–2401.
- (29) Kovács, K.; Gáspár, A.; Sajgó, C.; Schmitt-Kopplin, P.; Tombácz, E. Comparison of Humic Substances Isolated from Thermal Water and Surface Water by Electrospray Ionization Fourier Transform Ion Cyclotron Resonance Mass Spectrometry. *Eur. J. Mass Spectrom.* **2010**, *16* (5), 625–630.
- (30) Kim, S.; Kramer, R. W.; Hatcher, P. G. Graphical Method for Analysis of Ultrahigh-Resolution Broadband Mass Spectra of Natural Organic Matter, the Van Krevelen Diagram. *Anal. Chem.* **2003**, *75* (20), 5336–5344.
- (31) Bertram, T. H.; Cochran, R. E.; Grassian, V. H.; Stone, E. A. Sea Spray Aerosol Chemical Composition: Elemental and Molecular Mimics for Laboratory Studies of Heterogeneous and Multiphase Reactions. *Chem. Soc. Rev.* **2018**, *47* (7), 2374–2400.

# **Chapter 3: Shedding Light on Photosensitizers in the Marine Environment and Their Interactions with Nonanoic Acid**

## **3.1 Abstract**

Photochemical processes drive much of the daytime gas-phase chemistry in the atmosphere. Within condensed phases such as aerosol particles and thin films enriched in organics, much less is understood about these processes. An investigation aimed at better understanding photosensitized reactions that can occur within marine-relevant systems is described herein. In particular, photosensitized reactions have been investigated between a fatty acid model system and different photosensitizers in thin organic films representative of molecular species found in the sea surface microlayer and sea spray aerosols. Photosensitized reactions of thin films containing nonanoic acid and three different photosensitizers, including 4-benzoyl benzoic acid (BBA), humic acid (HA), and marine-derived dissolved organic matter (m-DOM), were probed using a suite of analytical techniques, including vibrational spectroscopy, excitation emission matrix spectroscopy, and ultra-high-resolution mass spectrometry. Considerable differences were found in the photosensitizing capability for each of these systems. We also present an analysis of the molecular differences between the different photosensitizers to explain their unique characteristics and light absorbing properties. Overall, this study sheds light on the relevance of such reactions in the marine environment.

## **3.2 Introduction**

Air-water interfaces are ubiquitous throughout the Earth, existing in lakes, ocean, rivers, and at the surface of aerosols. An important property of the air-water interface is its ability to concentrate certain surface-active chemical species relative to the underlying bulk water, thereby exposing them to conditions ripe for chemical and physical processing. One such species found

in elevated concentrations at air-water interfaces is dissolved organic matter (DOM), which is operationally defined as the organic matter content of natural waters that passes through 0.45 or 0.22  $\mu\text{m}$  filters.<sup>1</sup>

The portion of DOM that interacts with light ranging from  $\sim 300$  to 800 nm, known as chromophoric dissolved organic matter (CDOM),<sup>2</sup> is particularly important as it can proceed through a variety of photochemical pathways upon excitation by irradiation. Specifically, intersystem crossing to an excited triplet state is an important photochemical pathway for CDOM.<sup>3</sup> As a result of its relatively long lifetime, photoexcited triplet state CDOM is known to efficiently degrade and react with organic compounds and contaminants in the aqueous phase. Such reactions occur either directly through H-abstraction and charge transfer reactions, or indirectly through the formation of other photochemically produced reactive intermediate species (e.g., hydroxyl radicals,  $\text{H}_2\text{O}_2$ , peroxy radicals, singlet oxygen) which then react with the organic substrates.<sup>4,5</sup> In this manuscript, we define such indirect photochemical reactions between an excited state molecule and a substrate molecule as photosensitized reactions. For reactions in the bulk phase, these have been extensively studied and are known to form various low molecular weight saturated alcohols, aldehydes, and ketones.<sup>6</sup>

Recent studies using simple CDOM mimics and model systems (e.g., 4-benzoyl benzoic acid (BBA), commercial humic acid, and single component organic substrates like nonanoic acid and octanol) placed at the air-water interface have highlighted the role of a previously unknown class of photosensitized reactions in the formation of unsaturated and functionalized volatile organic compounds (VOCs) and condensed phase products, including hexene, hexenal, heptadiene, and octenal, among others.<sup>7,8,9,10</sup> Photosensitized reactions are thought to serve as a

source of secondary organic aerosol (SOA) precursors, and are unique to the air-water interface due to its concentrating ability, allowing for efficient interaction between formed radical species.

As two thirds of the Earth is covered in oceans, photosensitized reactions may be of great importance either at the sea surface microlayer (SSML), which is known to be enriched with DOM, or within sea spray aerosol (SSA) produced at the SSML air interface. Indeed, the total pool of DOM in marine environments (termed m-DOM) accounts for one of the largest carbon reservoirs on Earth (662 Pg).<sup>11</sup> Since a portion of this large m-DOM pool consists of light absorbing chromophoric components, termed m-CDOM, there is an abundance of molecules available to potentially serve as photosensitizers in such regions. However, experiments investigating potential photosensitized reactions within marine environments have, to date, used simple photosensitizer model systems (e.g., 4-BBA), leaving uncertainty in how effective m-DOM, and its associated fraction of m-CDOM, behaves as a photosensitizer.

Currently, the main chromophores in m-CDOM remain poorly defined in comparison to their terrestrial counterparts.<sup>2</sup> In addition to lignin phenols from terrestrial runoff, m-CDOM is thought to acquire its photoactive properties from aromatic amino acids and a large class of poorly defined marine humic substances produced by the microbial and photochemical processing of phytoplankton exudates.<sup>12,13</sup> Because of its unique formation mechanism and molecular structure (*vide infra*), m-CDOM is therefore expected to have different photochemical properties than the terrestrially-derived humic acid and simple model systems used in previous studies investigating photosensitized reactions.<sup>6</sup> For this reason, more complex and authentic photosensitizing systems need to be analyzed to determine the relevance of these photosensitizers at the air-water interfaces of the SSML and SSA.



This chapter presents the results from studies comparing the ability of three different photosensitizing systems to initiate photosensitized reactions with nonanoic acid at the air-water interface: 1) the simple model system molecule benzoyl benzoic acid (BBA); 2) commercially purchased terrestrial humic acid (HA) and; 3) authentic m-DOM, which includes m-CDOM, grown from a phytoplankton lab culture. The goal of this study was to better understand the role of m-CDOM in this new class of photosensitizing reactions in hopes of better determining the relevancy of these reactions in the marine environment.

### **3.3 Experimental Methods**

#### **3.3.1 Chemicals and Production of m-DOM**

Nonanoic acid (NA), a fatty acid commonly found in SSML and SSA, was used as the organic substrate. Three different systems of increasing complexity were used as photosensitizers: A well-known photosensitizer molecule 4-benzoylbenzoic acid (BBA) (Sigma Aldrich), humic acid (Sigma Aldrich), and authentic m-CDOM as discussed below.

To produce authentic m-DOM, which contains m-CDOM, three liters of seawater were taken from Scripps Institution of Oceanography pier and placed into a large glass flask. The seawater was spiked with Guillard's *f/2* medium to induce a phytoplankton bloom. A fluorescent tube (Full Spectrum Solutions, model 205457; T8 format, color temperature 5700 K, 2950 lumens) above the flask was used to promote the growth of phytoplankton. The progress of the phytoplankton bloom was occasionally monitored by measuring *in vivo* chlorophyll fluorescence using a handheld fluorimeter (Turner Designs, Aquafluor).

After approximately 3-4 weeks, the m-DOM material was extracted based on a styrene divinyl benzene polymer (PPL, BondElut Agilent) solid phase extraction (SPE) procedure described previously.<sup>14</sup> Briefly, the acidified cultured seawater (pH 2) was filtered first with 0.7 mm Whatman glass filter (GF/F) followed by a 0.2 mm GTTP filter to remove organisms and

particulate matter. The SPE cartridges were pre-rinsed once with methanol, three times with dilute acid, three times with Milli-Q water, and three times with methanol. Filtered seawater was then passed through the SPE cartridges, followed by further rinsing with dilute acid three times (0.01 M HCl), Milli-Q water three times, and then dried under N<sub>2</sub>. The m-DOM was then extracted from the SPE cartridge by eluting three times with methanol. The m-DOM methanol solution was then dried using a rotary evaporator and the dried sample was stored in a freezer.

### **3.3.2 TOC Analysis**

To aid in comparison of humic acid and m-DOM, aliquots of each sample in Milli-Q water were sent to Nelson Labs (Salt Lake City, UT) for total organic carbon (TOC) analysis. A solution of 3.5 mg/mL of HA in methanol was prepared and sonicated for 10 minutes. 500 µl of the HA/methanol solution was then extracted, evaporated, and then reconstituted in 40 mL of Milli-Q water. For TOC analysis of m-DOM, 5 mL of methanol was mixed with the dry m-DOM sample, sonicated for 10 minutes, and then 500 µl was extracted and evaporated and reconstituted with 40 mL of Milli-Q water. Both solutions were further sonicated for 10 minutes after addition of H<sub>2</sub>O and sent to Nelson Labs for TOC analysis.

### **3.3.3 Analysis of Photosensitized Reactions with Nonanoic Acid**

#### *Attenuated Total Reflection Fourier Transform Infrared Spectroscopy (ATR-FTIR)*

Attenuated total reflection Fourier transform infrared (ATR-FTIR) spectroscopy was used to monitor the condensed phase of irradiated and non-irradiated NA in the presence of various photosensitizer systems. An LCS-100 Solar Simulator (Oriel, Model 94011A) equipped with an AM1.5G filter to simulate solar output and a water filter to block infrared radiation was used to irradiate the systems. To mimic the organic-rich interface of the SSML and SSA particles, 400 µL of NA was placed on top of a thin film of photosensitizer that was formed on the surface of an AMTIR crystal. The thin photosensitizer films were made by first creating a

solution of the photosensitizer species in ethanol: 15.9 M for BBA, 3500 mg/L for humic acid or 136.8 mg C/L based on TOC analysis and reconstituting the m-DOM in 5 mL ethanol for a concentration of 640 mg C/L. The 450  $\mu$ L of the photosensitizer/ethanol solution was then placed onto the AMTIR crystal, and dry air was passed over it for ~60 minutes to ensure solvent evaporation. Evaporation was assumed complete when subsequent ATR-FTIR scans revealed no further spectral changes or contributions from ethanol.

After evaporation of ethanol and formation of the photosensitizer thin film, 400  $\mu$ L of nonanoic acid was placed on top of the thin photosensitizer film. To reduce evaporative losses, the AMTIR crystal was then covered using a trough plate fitted with a UV port window to allow light onto the sample. After 10 minutes of equilibration time, the solar simulator was either turned on for irradiation experiments or remained off for non-irradiation experiments. Spectra were then collected every 10 minutes for the next 60 minutes. At a spectral resolution of 8  $\text{cm}^{-1}$ , 128 scans were averaged across the spectral range of 800 to 4000  $\text{cm}^{-1}$ . After each experiment, the crystal was visually inspected to ensure the thin film of photosensitizer had not been removed from the crystal interface by dissolution in the NA medium. While it is still possible that small amounts of photosensitizer were dissolved into solution, we do not expect large differences in the resulting spectra as the penetration depth of the evanescent beam (~2 mm) was still large enough that it would interact with the photosensitizer in solution phase.

#### *Ultra High Resolution Mass Spectrometry of Reaction Products*

To tentatively identify the organic products formed during the light and dark reactions, the solution from the AMTIR crystal was extracted and stored at -20  $^{\circ}\text{C}$  and then analyzed via ultra-performance liquid chromatography tandem heated electrospray-linear ion trap Orbitrap high resolution mass spectrometer (UPLC-HESI-LIT-Orbitrap, Thermo Fisher Scientific) as

adopted from Tinel et al., 2016.<sup>10</sup> In brief, samples were separated using a reverse phase Hypersil GOLD™ aQ column (3 mm, 50 x 2.1 mm, Thermo Fisher Scientific) using a gradient elution method with mixtures of acetonitrile (Optima-grade, Thermo Fisher Scientific) and water (ultrapure), each containing 0.1% formic acid (Optima grade, Thermo Fisher Scientific). Peaks were detected in both positive and negative mode at a capillary voltage set to 2.8 kV and 3.2 kV for negative and positive mode, respectively, with the electrospray needle and capillary maintained at 325°C. The HESI gases were set as follows (arbitrary units): sheath at 30, auxiliary at 10, and sweep at 0. The HESI-LIT-Orbitrap was mass calibrated the day of sample analysis for each experiment, using pre-made mixtures specific to positive and negative ionization modes (Pierce ESI Ion Calibration Solutions, Thermo Fisher Scientific), and maintaining mass accuracies  $\leq 3$  ppm mass error. With these solutions, mass calibration was performed in the ranges of  $m/z$  195–1921 and  $m/z$  265–1986 for positive and negative ionization modes, respectively. All data acquisitions were performed with the mass range set to  $m/z$  80–2000 and the mass resolution set to 120,000. Samples run in positive mode were derivatized with PFBHA prior to analysis to effectively identify organic products containing aldehyde and ketone in a similar manner as Tinel and coworkers.<sup>10</sup> Samples run in negative mode were not derivatized. All extracts were prepared by diluting 25  $\mu$ L of the sample to 1 mL with a 1:1 acetonitrile:water mixture. Aliquots were then analyzed after a 24-hour period.

### **3.3.4 Analyses of Photosensitizers**

#### *Ultra High Resolution Mass Spectrometry of Photosensitizers*

To determine the chemical structure and hence better understand the photochemical properties of complex photosensitizers (HA and m-DOM), ultra-high resolution mass spectrometry was again utilized. Extracts of each photosensitizer were introduced into a heated electrospray ionization linear ion trap Orbitrap (HESI-LIT-Orbitrap) mass spectrometer via

direct injection at a flow rate of 5  $\mu\text{L min}^{-1}$ , with the electrospray needle maintained at 50 °C and the capillary at 325 °C. The HESI gases were set as follows (arbitrary units): sheath at 5, auxiliary at 0, and sweep at 0. While it was understood that ionization suppression could potentially limit the observation and identification of many species with the DOM sample, chromatographic separation was not used in this case due to the difficulty in separating components in DOM, which is known to contain tens of thousands of unique molecular species.

Utilizing the ability of HESI-LIT-Orbitrap MS to separate complex mixtures, thousands of molecular signatures were still detected. Molecular formula assignments were performed using the Xcalibur (ThermoFisher) software with the following element ranges:  $^{12}\text{C}$ , 0-30;  $^1\text{H}$ , 0-50;  $^{16}\text{O}$ , 0-30;  $^{14}\text{N}$ , 0-5;  $^{32}\text{S}$ , 0-2;  $^{23}\text{Na}$ , 0-1 (sodium adduct for positive mode species only). Compositions including phosphorus (P) were excluded in this analysis due to the uncertainty of their presence in our samples.<sup>15,16</sup> Formulas with a relative double bond greater than 15 and/or with an O/C ratio less than zero or greater than 2.5 were rejected. Additionally, peaks were chosen with a mass error of less than 3 ppm and with a relative intensity greater than 0.05% of the largest detected peak. The majority of ions in both photosensitizers (HA and m-DOM) were found in positive mode and the previously stated parameters set for composition analysis resulted in ~40-66% of ions being successfully characterized for both modes.

Assigned formulas were then categorized by compound class based upon elemental stoichiometries as done previously.<sup>17</sup> Modified aromaticity index ( $\text{AI}_{\text{mod}}$ ) was calculated according to Equation 1:

$$\text{AI}_{\text{mod}} = (1 + \text{C} - 0.5\text{O} - \text{S} - 0.5\text{H}) / (\text{C} - 0.5\text{O} - \text{S} - \text{N} - \text{P}) \quad (\text{Eq. 1})$$

Where  $\text{P} = 0$  for our identified compounds. Compound classes were then identified as follows:  $\text{AI}_{\text{mod}} 0.5$  to  $0.67 =$  aromatic,  $\text{AI}_{\text{mod}} > 0.67 =$  condensed aromatic, highly unsaturated =

$AI_{\text{mod}} < 0.5$ ,  $H/C < 1.5$ ; aliphatic =  $HC$  1.5 to 2.0,  $O/C < 0.9$ ,  $N = O$ ; peptide =  $H/C$  1.5 to 2.0,  $O/C < 0.9$ ,  $N > 0$ . As noted in previous work, compounds identified as peptides have molecular formulas of peptides, but the actual structure may differ.<sup>17</sup>

#### *Fluorescence excitation-emission matrices (EEMs)*

Fluorescence excitation-emission matrices (EEMS) of HA and m-DOM were obtained using a spectrofluorometer (Horiba Scientific, Aqualog with extended range). Dry samples were resuspended in 5 mL of ultrapure water. A small aliquot (1.5 mL) was then used to obtain EEMs. Excitation wavelengths ranged from 235-450 nm. Emission ranged from 250-800 nm. A background spectrum acquired with ultrapure water was then subtracted from all EEMs. EEMs were corrected for inner-filter effects based on absorbance spectra measured simultaneously. Finally, Rayleigh scattering (1st and 2nd order) was removed.

### **3.4 Results and Discussion**

#### **3.4.1 Analysis of Photosensitized Reactions for Three Different Photosensitizers**

Analysis of products formed during irradiated and non-irradiated NA with three different photosensitizers was conducted using ATR-FTIR spectroscopy and UPLC-HESI-LIT-Orbitrap MS. As mentioned, a thin film of the photosensitizer was first formed on an AMTIR ATR-FTIR crystal. Individual spectra for each of the three photosensitizers are shown in Supporting Information (Figure 3.5). After creation of the photosensitizer thin film, NA was placed on top. The full signal spectrum of each photosensitizer with NA system is largely dominated by NA (also shown in SI, see Figure 3.6).

After preparation of the NA and photosensitizer thin film, the system was then either kept in the dark for one hour, or irradiated with a solar simulator, with spectra collected every ten minutes. Figure 1A-C shows select regions of ATR-FTIR difference spectra (final-initial) for the

irradiated and non-irradiated NA in the presence of all three photosensitizers as a function of time over one hour. Increasingly bright colored lines correspond to increasing irradiation time, while gray lines show the difference spectra for samples kept in the dark (i.e., no irradiation). Control experiments in which only either nonanoic acid or m-DOM were irradiated are shown in the Supporting Information (Figure 3.6). After irradiation and analysis by ATR-FTIR, samples were extracted, derivatized, and analyzed using UPLC-HESI-LIT-Orbitrap MS for identification of specific molecular species. Table 3.1 shows signal strength and ratio (irradiated/non-irradiated) of counts of select products found upon analysis in positive and negative mode, respectively. It should be noted that the analysis of mixtures via HRMS ESI mass spectrometry is not entirely quantitative due to differences in ionization efficiencies of the samples.

To comparatively assess the photochemical production of identified species between experiments, four thresholds relative to the signal of the HRMS's total ion count (TIC) spectra were calculated and used to create four categories to describe the relative intensities of each product. The categories were assigned in a manner similar to previous studies,<sup>18</sup> and are calculated as follows. First, "below threshold" was determined as ten times greater than the average noise for that system. The following three categories (termed "weak," "medium" and "strong") were then each identified as being an order of magnitude higher than the previous threshold. For example, for the system of NA in the presence of BBA, the noise average was  $10^2$  counts, giving a "below threshold" value of  $10^3$  counts. "Weak" signals then had intensities greater than  $10^4$  counts, "medium" signals had intensities greater than  $10^5$  counts, and strong signals had intensities greater than  $10^6$  counts. Light: Dark ratios counts were also calculated, indicating the extent to which irradiation produced observed products. Graphs showing ion

counts for each system as well as water blanks in irradiated and non-irradiated conditions are shown in SI Figure 3.7. An in-depth discussion of the findings for each system is now given.



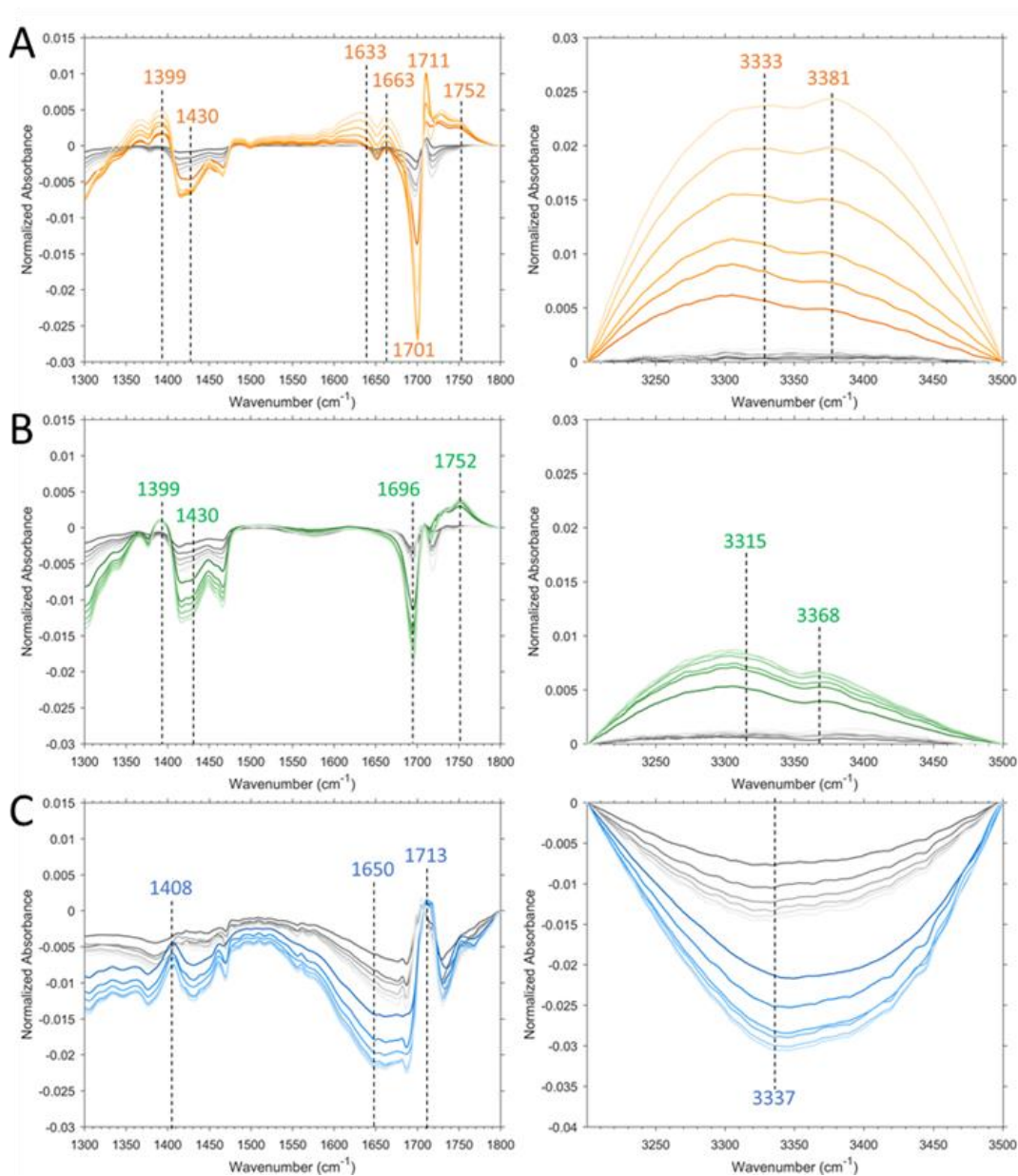


Figure 3.1. Select regions of ATR-FTIR difference spectra (final-initial) of 60-minute non-irradiated (gray lines) and irradiated (colored lines) NA in the presence of A) BBA; B) HA and C) m-DOM. Spectra were collected every 10 minutes. Lines become increasingly light with increased time.

### *BBA and Nonanoic Acid*

Fig. 3.1A shows the difference spectra in the fingerprint region from 1300-1500  $\text{cm}^{-1}$  and the region from 3200-3500  $\text{cm}^{-1}$  for the system consisting of BBA and NA. Considering the expected products based upon previous results in the literature, we attribute the broad negative going peak centered at  $\sim 1310 \text{ cm}^{-1}$  to C-O stretching of nonanoic acid.<sup>19,20,21</sup> The broad positive region with a maximum at  $1399 \text{ cm}^{-1}$  is due to a combination of C-H bending and O-H in-plane bending from the formation of aldehydes and oxygenated species, respectively.<sup>21</sup> The negative peak centered at  $1430 \text{ cm}^{-1}$  is due to the loss of O-H in-plane bending modes of nonanoic acid.<sup>20,21</sup> It should be noted this peak also overlaps with a peak in the BBA spectrum (SI). While BBA is not expected to undergo direct photolysis, it is possible that the formation of combination products of BBA with various radicals may be responsible for some of the changes in the spectra at this wavenumber.

The two positive absorptions at  $1633$  and  $1663 \text{ cm}^{-1}$  are assigned as stretching of C=C alkenes and C=O stretching of unsaturated aldehydes, respectively.<sup>22</sup> The large negative peak at  $1701 \text{ cm}^{-1}$  is due to the loss of C=O groups as nonanoic acid is consumed. The band of positive-going peaks from  $1711$ - $1800 \text{ cm}^{-1}$  are likely C=O stretches due to the formation of multiple aliphatic ketone/aldehyde species.<sup>21</sup> It is possible these peaks are also caused by changes in the hydrogen-bonding state of the nonanoic acid. Loss of carboxylic acid dimers due to hydrogen bond disruption has been shown to cause the C=O peak to increase in wavenumber.<sup>20</sup> It is possible that even with an IR filter in place, irradiation of the sample by the solar simulator may cause changes in hydrogen bonding state. Nonetheless, in light of the other changes to the spectra, we are confident that the changes are not exclusively a result of changes in the hydrogen

bonding state. Finally, further evidence for the formation of oxygenated species is seen in the broad positive band caused by O-H stretching, with peaks at 3333 and 3381  $\text{cm}^{-1}$ .

Table 3.1. Signal strength and enrichment ratios for select products as detected by MS analysis for samples of various photosensitizers in the presence of NA.

Molecular Formula	Assigned Structure <sup>a</sup>	Irradiated BBA	BBA Light:Dark	Irradiated HA	HA Light:Dark	Irradiated m-DOM	m-DOM Light:Dark
<b>Combination Products</b>							
C <sub>23</sub> H <sub>28</sub> O <sub>5</sub>	NA+BBA <sup>c</sup>	strong	>200000	below threshold	NA	below threshold	NA
C <sub>18</sub> H <sub>34</sub> O <sub>4</sub>	2NA-2H <sup>c</sup>	medium	>100	below threshold	NA	medium	0.92
<b>Carboxylic Acids</b>							
C <sub>8</sub> H <sub>16</sub> O <sub>2</sub>	Octanoic acid	medium	>200000	medium	1.07	strong	1.02
C <sub>8</sub> H <sub>14</sub> O <sub>2</sub>	Octenoic acid	weak	>10000	below threshold	NA	below threshold	NA
C <sub>9</sub> H <sub>16</sub> O <sub>2</sub>	Nonenoic acid	weak	>10000	below threshold	NA	below threshold	NA
C <sub>7</sub> H <sub>14</sub> O <sub>2</sub>	Heptanoic acid	weak	1.5	medium	1.09	medium	1.02
<b>Oxygenated Acids</b>							
C <sub>9</sub> H <sub>16</sub> O <sub>3</sub>	Oxo-NA	strong	42.81	strong	1.11	strong	0.93
C <sub>9</sub> H <sub>16</sub> O <sub>4</sub>	Hydroxy-oxo-NA	medium	22.27	strong	1.01	strong	0.99
C <sub>9</sub> H <sub>18</sub> O <sub>3</sub>	Hydroxy-NA	medium	5.77	strong	1.07	strong	1.12
C <sub>6</sub> H <sub>10</sub> O <sub>4</sub>	Hydroxy-oxo-octanoic acid	medium	1.73	strong	1.02	medium	1.02
<b>Aldehydes/Ketones</b>							
C <sub>7</sub> H <sub>12</sub> O <sub>2</sub>	Heptanedial	weak	11.53	below threshold	NA	below threshold	NA
C <sub>6</sub> H <sub>10</sub> O <sub>2</sub>	Hexanedial	weak	7.75	below threshold	NA	below threshold	NA
C <sub>8</sub> H <sub>14</sub> O	Octenal	strong	3.26	medium	0.99	strong	1
C <sub>9</sub> H <sub>16</sub> O	Nonenal	weak	2.14	below threshold	NA	weak	0.96
C <sub>8</sub> H <sub>16</sub> O	Octanal	strong	1.79	medium	9828.14	strong	1.04
C <sub>9</sub> H <sub>16</sub> O <sub>2</sub>	Nonanedial	medium	1.21	medium	1.26	strong	0.99
C <sub>9</sub> H <sub>18</sub> O	Nonanal	weak	1.2	weak	0.48	strong	0.71
C <sub>6</sub> H <sub>10</sub> O	Hexenal	medium	1.19	weak	1.24	medium	0.97
C <sub>7</sub> H <sub>14</sub> O	Heptanal	weak	1.17	below threshold	NA	medium	1.04
C <sub>6</sub> H <sub>12</sub> O	Hexanal	medium	1.1	below threshold	NA	below threshold	NA
C <sub>5</sub> H <sub>8</sub> O	Pentenal	below threshold	NA	medium	1.26	below threshold	NA

The results from MS analysis of this system (Table 3.1) generally agree with the results from the ATR-FTIR spectra. Looking at the signal strength for irradiated systems in conjunction with the light:dark ratio gives an indication as to which products were most abundant and whether they were formed through thermal dark reactions or light induced reactions. The combination product NA+BBA had a strong signal and was largely produced as a result of irradiation. Tentatively identified saturated and unsaturated fatty acids (e.g., octenoic, nonenoic, heptanoic) acids only had weak to medium signal. Despite this, their signal was still enhanced relative to the non-irradiated experiments. Finally, oxygenated C8/C9 acids as well as saturated and unsaturated C8 ketones/aldehydes exhibited strong signals in both irradiated and non-irradiated, but their production was clearly increased upon irradiation, with production ratios ranging from 3.26 for octenal and 1.79 for octanal to 42.81 for oxo-nonanoic acid. Overall, these results, showing the strong production of saturated and unsaturated oxygenated species with minimal production of carboxylic acids from mixture of NA and BBA, are in agreement with previous studies.<sup>10</sup>

#### *Humic Acid and Nonanoic Acid*

The products formed upon irradiation of the more complex model system of humic acid with nonanoic acid was also examined with ATR-FTIR and mass spectrometry. Figure 3.1B shows the irradiated and non-irradiated ATR-FTIR difference spectra for the system consisting of NA and the photosensitizer humic acid over 1 hour. Similar to the system of NA in the presence of BBA, Fig. 3.1B shows that irradiated NA with HA has positive-going peaks found at  $1401\text{ cm}^{-1}$  which we again assign to aldehydic C-H deformation and in plane O-H bending of alcohol functional groups.<sup>21</sup> The negative-going peak at  $1429\text{ cm}^{-1}$  and  $1470\text{ cm}^{-1}$  are again attributed to the O-H in plane bending associated with nonanoic acid.<sup>21,22</sup> Fig. 3.1B shows a

negative peak at  $1696\text{ cm}^{-1}$  presumably due to loss of C=O stretching groups associated with nonanoic acid, and a positive band centered at  $1752\text{ cm}^{-1}$  due to C=O stretching of various formed aldehydes and ketones. In contrast to the NA with BBA system, the NA with HA system has much smaller changes in the C=C and C=O region from  $1630\text{-}1660\text{ cm}^{-1}$ , indicating it less efficiently produces unsaturated species. Finally, Figure 3.1B shows a broad positive band from  $3100\text{-}3500\text{ cm}^{-1}$  due to the formation of OH groups.

Table 3.1 shows the strength of signal and ratio of counts (irradiated:non-irradiated) for select products from MS analysis of the system consisting of NA in the presence of HA. Unsurprisingly, the BBA+NA combination product ion is absent. Signals from carboxylic acids are only slightly elevated in the irradiated systems (1.07 irradiated:non-irradiated for octanoic acid, 1.09 for heptanoic acid). Interestingly, the ketone/aldehyde with the greatest signal in irradiated samples relative to non-irradiated samples is octanal (9828.14), with lower values for nonanedial (1.26) and hexenal (1.24) and no enhancement for octenal (0.99). This perhaps indicates a specific pathway is favored for this system. Finally, the production of oxygenated acids is favored only slightly in irradiated systems, with oxononanoic acid at 1.11 and hydroxy-nonanoic acid at 1.07. Overall, HA appears to be a less efficient photosensitizing system than BBA.

#### *m-DOM and Nonanoic Acid*

ATR-FTIR difference spectra of m-DOM and NA in Figure 3.1C show that m-DOM is appears to be poor producer of condensed-phase products upon irradiation, as indicated by the presence of only slightly negative-going peaks. Figure 3.1C has no positive going peaks and instead features only a broad decrease at  $1650\text{ cm}^{-1}$ . Given the complicated chemical nature of m-DOM, this peak could be due to any number of functional groups and their combinations,

including C=C, C=O, N=C, and N-H. The peak that is unaffected at  $1713\text{ cm}^{-1}$  is likely due to the presence of nonanoic acid which does not appear to be reacting. The negative-going peak at  $1731\text{ cm}^{-1}$  indicates the loss of C=O species in the m-DOM. Further, the large losses centered at  $3337\text{ cm}^{-1}$  and  $1430\text{ cm}^{-1}$  in Fig. 3.1C indicate loss of O-H species. The peaks lost in Fig. 3.1C seem to indicate m-DOM could be undergoing direct photolysis and subsequent evaporation of low-volatility products. Difference spectra of an irradiated thin film of m-DOM (without NA coating) verified that m-DOM undergoes direct photolysis (Figure 3.6).

Ion counts in Table 3.1 show little to no enhancement in irradiated m-DOM and NA relative to non-irradiated samples for most products. Indeed, many systems feature an irradiated:non-irradiated ratio of  $\sim 1$  or less than 1, including octenal and octanal, which were highly enhanced in systems containing either BBA or HA. The overall findings therefore are that BBA is an efficient photosensitizer, producing oxygenated species and unsaturated ketones/aldehydes, humic acid to a lesser extent, while m-CDOM appears to exhibit little to no photosensitizing capability with the nonanoic acid substrate. It should be noted that ATR-FTIR is limited to the analysis of condensed phase species, and therefore is unable to determine potential gas phase products formed upon irradiation.

The monitoring of gas-phase species would help to better explain the photochemistry of such systems. Furthermore, differences between the spectra of irradiated m-DOM with NA and m-DOM by itself were observed and are indicative of a potentially more complicated process than photosensitization (e.g., direct photolysis of m-DOM followed by reaction of intermediates with NA) (see discussion in Supporting Information). Future studies are therefore needed to investigate the photochemical reactivity of m-DOM both by itself and in the presence of other species including organic matter and water.

From these results, a general mechanism for the photosensitized reaction of NA with various photosensitizer molecules is modified from previous studies of just BBA (Figure 3.2).<sup>10</sup>

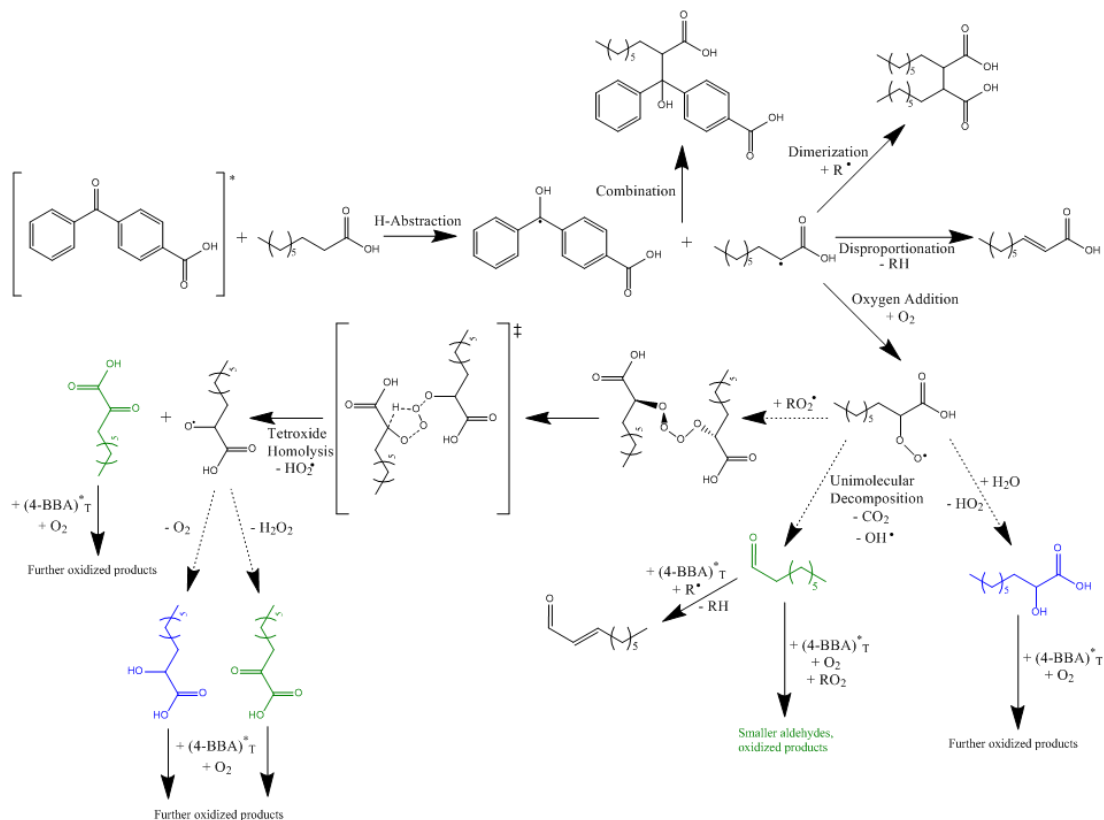


Figure 3.2. Proposed mechanism for the photosensitized reaction of NA. All products shown were present when BBA was used as the photosensitizer. Products highlighted in green and blue were present when HA and m-DOM was the photosensitizer, respectively. Pathway modified from Tinel et al., 2016.<sup>10</sup>

The reaction begins with H-abstraction of the photosensitizer, leading to addition of molecular oxygen or radical-radical interactions. Depending on the photosensitizer used, different pathways were more important. For example, disproportionation reactions leading to unsaturated fatty acid (nonenoic acid) or unsaturated aldehydes (i.e., octenal) were relevant only for BBA, while the pathways leading to saturated aldehydes and oxygenated species were more relevant for HA. The differences in reaction pathways and products are observed are likely due to the molecular properties of each photosensitizer, which is discussed in the following section.



### 3.4.2 Comparison of m-DOM and Humic Acid: Molecular Composition and Chromophores

To better understand the differences between humic acid and m-DOM as they compare to BBA, we conducted a series of experiments to better understand their molecular structure and associated chromophores.

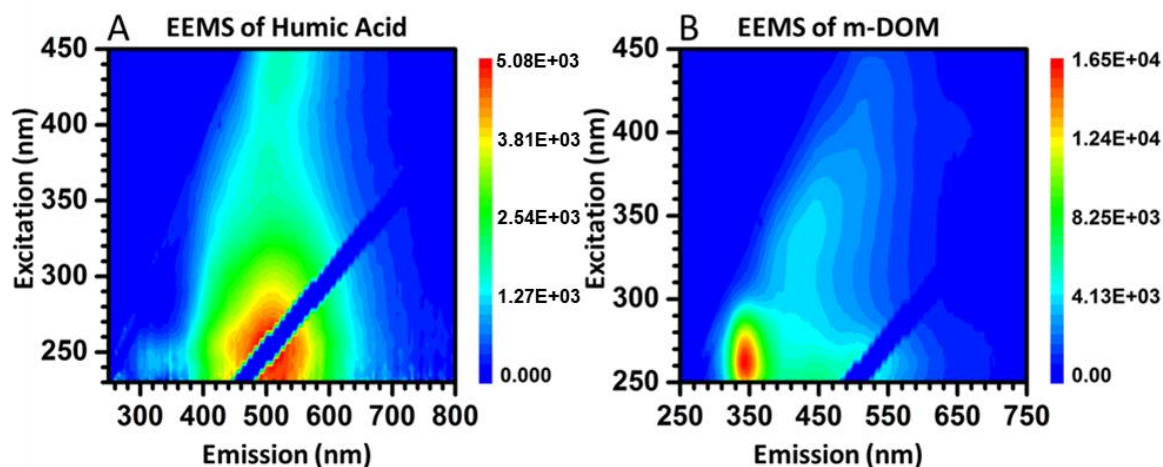


Figure 3.3. Excitation-emission matrices of A) humic acid and B) m-DOM. Data collected and processed by Mitch Santander in the Prather Research Group.

#### *EEMS*

Figure 3.3A,B shows the EEMS spectra of humic acid and m-DOM. Figure 3.3A has an EEMS spectrum that has a main peak at  $\lambda_{ex}/\lambda_{em}= 250/500$  nm that stretches into higher excitation wavelengths up to 450/500 nm. Comparison with literature<sup>13</sup> reveals the fluorescent component of HA has contributions from terrestrial fulvic and humic acids. Furthermore, the excitation at longer wavelengths is indicative of highly aromatic species. The EEMS spectrum for m-DOM shown in Figure 3.2B has a peak at  $\lambda_{ex}/\lambda_{em}= 250-280/350$  nm and a band that stretches to higher excitation wavelengths from 300-400/450 nm. Comparison of this with literature<sup>13</sup> reveals m-DOM contains proteins and marine humic substances with a lesser degree of aromaticity relative to terrestrial humic acids.

## ATR-FTIR Spectroscopy

Figure 3.4A,B shows the ATR-FTIR spectra of HA and m-DOM, respectively. Due to the complex nature of these systems, the resulting spectra are broad, with each peak likely a composite of multiple vibrating functional groups. For this reason, a broad description of each region is given, with possible assignments for peaks in each region shown in Table 3.2.

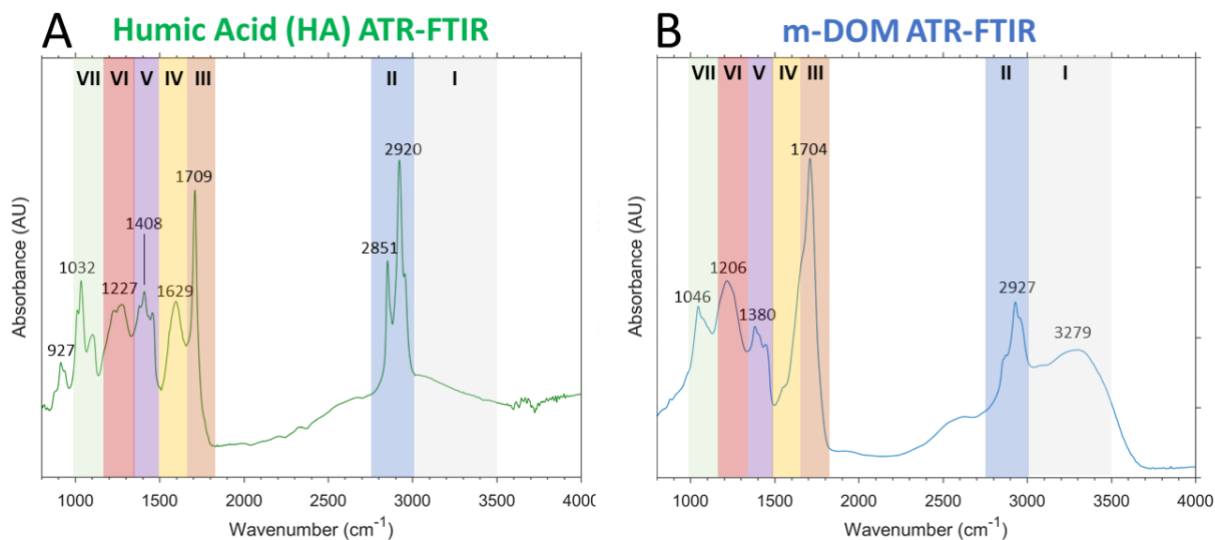


Figure 3.4. ATR-FTIR spectra of A) humic acid and B) m-DOM extracted from a lab-grown phytoplankton culture. Peak assignments are listed in Table 2.

Fig. 3.4A shows the ATR-FTIR spectrum of commercial HA with assignments based upon relevant literature.<sup>21–26</sup> The broad peak in region I ranging from 3400–2500  $\text{cm}^{-1}$  is due to O-H and N-H stretching. The shape of the peak and the fact that it extends to 2500  $\text{cm}^{-1}$  is evidence that this peak is associated mainly with the presence of carboxylic acids. The strong peaks of region II at 2920  $\text{cm}^{-1}$  and 2850  $\text{cm}^{-1}$  are indicative of large contributions from aliphatic  $\text{CH}_2$  and  $\text{CH}_3$  stretching, respectively. The peak in region III at 1709  $\text{cm}^{-1}$  is due to C=O vibrations of carboxylic acids, aldehydes, and ketones. Region IV has a peak at 1593  $\text{cm}^{-1}$  that can be attributed to a number of species and combinations thereof, including aromatic and olefinic C=C and C-C vibrations, C=N aliphatic imines, and C=O stretching of quinones. The

low wavenumber seen for HA (i.e.,  $< 1630\text{ cm}^{-1}$ ), however, suggests the presence of aromatic moieties. The cluster of peaks surrounding  $1408\text{ cm}^{-1}$  in region V also indicate aromaticity, as they can be attributed to ring breathing modes, as well as deformation of aliphatic C-H, O-H stretching of phenols and alcohols. The broad doublet of Region VI around  $1227\text{ cm}^{-1}$  is possibly due to O-H stretching of phenols and alcohols, as well as C-O stretching and O-H deformation of carboxylic acids. Region VII has a cluster of peaks around  $1032\text{ cm}^{-1}$  from C-O stretching of polysaccharide-like structures and in plane C-H bending of benzene ring as well as peaks at  $\sim 915\text{ cm}^{-1}$  due to aromatic out-of-plane C-H bends.

Table 3.2. Peak assignments of ATR-FTIR spectra of humic acid and m-DOM.

Region	Assignment
I	O-H, N-H stretches
II	Aliphatic C-H stretches
III	C=O of carboxylic acids,, aldehydes, and ketones
IV	C=O of quinones and amide I, C=N of imines, C=C and C-C of alkenes or aromatics
V	Ring breathing of aromatics, C-H deformation, O-H deformation of phenols and alcohols
VI	O-H stretching of phenols and alcohols, C-O stretching and O-H deformation of carboxylic acids
VII	C-O stretching of polysaccharide-like substances, C-H in plane bending of rings, C-H out-of-plane bends of aromatics

Generally speaking, the same analysis for humic acid can be applied to m-DOM (Figure 3.4B). However, the relative contributions and presence or absence of key peaks reveal molecular differences compared to humic acid. First, there is a larger contribution at  $3279\text{ cm}^{-1}$  in region I compared to the HA spectrum, indicating a greater contribution of O-H and N-H groups. Furthermore, the aliphatic C-H stretching peaks in region II are smaller relative to peaks in Region III indicating a greater degree of oxygenation. The peak at  $1707\text{ cm}^{-1}$  is broader,

representative of a greater variety of species containing the carbonyl group. Unlike HA, there is no isolated peak at  $1629\text{ cm}^{-1}$ . Instead, the peak at  $1709$  is broadened with a shoulder extending into Region IV. This shift, in addition to the larger peak observed in region I, points towards the presence of nitrogen-containing groups, such as amides and amines. Furthermore, the blue-shifting of the peak ( $>1630\text{ cm}^{-1}$ ) could be due to a greater contribution of olefinic C=C rather than aromatic species. Taken together, these results indicate that the m-DOM sample is more oxidized, non-aromatic, and has an abundance of nitrogen-containing functional groups, while HA contains an abundance of aromatic species with high degrees of carboxylic acid functional groups. These results are in general agreement with the EEMS analysis.

#### *HESI-LIT-Orbitrap MS Analysis*

Figure 3.5 shows the contribution of molecular species in humic acid and m-DOM based on analysis upon direct injection of each sample into HESI-LIT-Orbitrap MS. Immediately apparent is the fact that the m-DOM sample is much more chemically complex than the HA sample. A total of 3,496 species were identified for m-DOM, compared to just 684 for humic acid. The average O/C ratio of m-DOM is 0.301 compared to .2795 for HA. Figure 3.4 also shows that m-DOM has more nitrogen containing species than HA (59.73% vs 38.89% of total identified formulas, respectively), and is less aromatic (12% vs 38%). The fraction of nitrogen containing species observed in our HA sample agrees well with a previous study that analyzed groundwater DOM and found that 15-38% of identified species contained nitrogen.<sup>27</sup> Furthermore, the higher fraction of CHON species in m-DOM compared to terrestrial DOM in our study is in agreement with a previous experiment in which terrestrial and marine DOM were directly compared.<sup>16</sup> Interestingly, both m-DOM and HA have high percentages of highly unsaturated species (36% and 41%). Previous studies have identified the main contributors to the

“highly unsaturated” category as either carboxylic rich alicyclic molecules (CRAM) formed from autochthonous microbial sources or as aromatic lignin from terrestrial sources.<sup>17</sup> Given that the m-DOM was produced in a laboratory without input from terrestrial sources, it is more likely the highly unsaturated species are due to CRAM molecules, while the highly unsaturated species in HA is from lignin. This would again explain the differences in the impact of m-DOM as a photosensitizer, as CRAM is less photo-active than lignin, which is highly aromatic. Overall, the results from MS analysis agree with the ATR-FTIR and EEMS spectra of these two complex systems, which show that m-DOM is more oxygenated, less aromatic, and has more nitrogen-containing species.

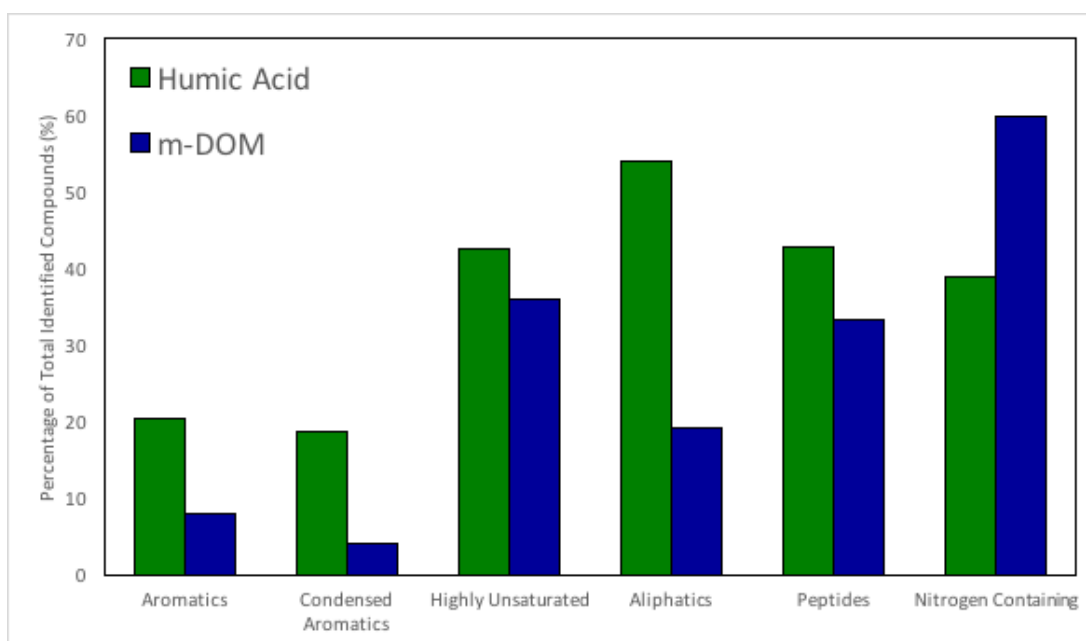


Figure 3.5. Relative abundance of each molecular class in humic acid and m-DOM as determined by HESI-LIT-Orbitrap MS analysis calculated according to the methods section.

### 3.5 Conclusions

In this study, we compared the three different potential photosensitizers with increasing chemical complexity (i.e., BBA, HA, m-DOM) to initiate photosensitized reactions with the fatty acid nonanoic acid in an organic rich environment. ATR-FTIR and high-resolution MS results revealed that BBA is an efficient photosensitizer, leading to the production of several unsaturated and functionalized products, including saturated and unsaturated C8 aldehydes/ketones, combination products (BBA+NA), and hydroxy-nonanoic acid. HA was found to be a less efficient photosensitizer than BBA, yet still produced similar unsaturated and functionalized products. Irradiation of NA in the presence of m-DOM led to no enrichment of condensed phase products, indicating the m-DOM and associated chromophores produced by marine microbes appear to be less efficient photosensitizers within a rich organic layer.

Analysis of HA and m-DOM by EEMS, ATR-FTIR, and HESI-LIT-Orbitrap MS reveal that HA was photoactive due to its presence of aromatic species, while m-DOM was less photoactive due to its high abundance of CRAM, which is less aromatic. Interestingly, despite its poor photosensitizing capability, the m-DOM still appeared to undergo photochemistry itself, an avenue that should be investigated further in future studies.

It should be noted that while this study points towards the low photosensitizing capability of microbially produced DOM, it does not preclude the importance of such reactions in the open ocean or SSA surfaces altogether, as other sources of CDOM in these regions exist. For example, previous work has shown that highly chromophoric dissolved polycyclic aromatics are formed thermogenically in the deep ocean.<sup>26</sup> Furthermore, terrestrial input of photo-active lignin-type molecules can also add to the number of chromophores found at the air-water interface of the ocean in coastal regions.<sup>28</sup> Finally, despite our best efforts to create an accurate mimic of marine-

derived DOM, the production of DOM in the real ocean system is a highly complex process that includes a range of factors that may not be accounted for in our method (e.g., cell lysis and nutrient stress). Future studies should investigate the photosensitizing ability of freshly up-welled deepwater DOM and coastal region DOM, as well as work towards understanding the chemical composition and characteristics of marine-derived DOM under varying microbial conditions.

Additional consideration regarding the scope of our experiment should be given with respect to differences between our experimental setup and real-world systems. First, the solid films of photosensitizer employed in our study may exhibit different photochemical properties from the purely liquid films found in the real environment. Second, our study was conducted to specifically probe the formation of condensed phase products, and therefore lacks information regarding the formation of gas phase species. A similar study investigating the photosensitized reactions between octanol and two different photosensitizers (i.e., BBA-4 and imidazole 2-carboxaldehyde) observed that the condensed phase products formed when employing thin films of octanol and photosensitizer were similar to the gas phase products formed when using an octanol-coated aqueous solution of photosensitizer.<sup>9</sup> While these results lend credence to the idea that the thin films used in our study are accurate mimics of interfacial systems, future studies should be conducted to determine the photochemical products of condensed and gaseous products at aqueous surfaces coated with organic films and photosensitizer.

Overall, the findings in this chapter are important in that they lend further knowledge of the variability of DOM from various sources (here, marine derived DOM) to serve as a photosensitizer. These results point towards the need for studies using complex, authentic model systems in such experiments to further our understanding of different photochemical processes occurring in naturally occurring aquatic environments.



### **3.6 Acknowledgements**

The authors would like to gratefully acknowledge supported by the National Science Foundation through the Center for Aerosol Impacts on Chemistry of the Environment funded under the Centers for Chemical Innovation Program Grant CHE1801971. The authors would also like to thank Professor Michael Tauber and Samantha Doyle for m-DOM sample preparation and extraction.

Chapter 3 was reproduced with permission from: Trueblood, J. V.; Alves, M. R.; Power, D.; Santander, M. V.; Cochran, R. E.; Prather, K. A.; Grassian, V. H. Shedding Light on Photosensitized Reactions within Marine-Relevant Organic Thin Films. *ACS Earth Sp. Chem.* 2019, 3 (8), 1614–1623. The dissertation author was a primary investigator and co-first author of this paper.

### **3.7 Supporting Information**

Supporting information contains three figures and one table. Figure 3.5 contains ATR-FTIR spectra of thin films of each of the photosensitizer systems used in this experiment. Figure 3.6 contains ATR-FTIR spectra of nonanoic acid and each of the systems containing a thin film of photosensitizer with nonanoic acid. Figure 3.6 contains ATR-FTIR difference spectra of irradiated nonanoic acid and m-DOM alone. Figure 3.7 contains signal detected (counts) for select products analyzed by HESI-LIT-Orbitrap MS for control NA and NA+BBA. Table 3.3 contains peak assignments for nonanoic acid. Figure 3.8 contains signal detected (counts) for select products analyzed by HESI-LIT-Orbitrap MS analysis. This material is available free of charge on the ACS Publications website at <http://pubs.acs.org/>.

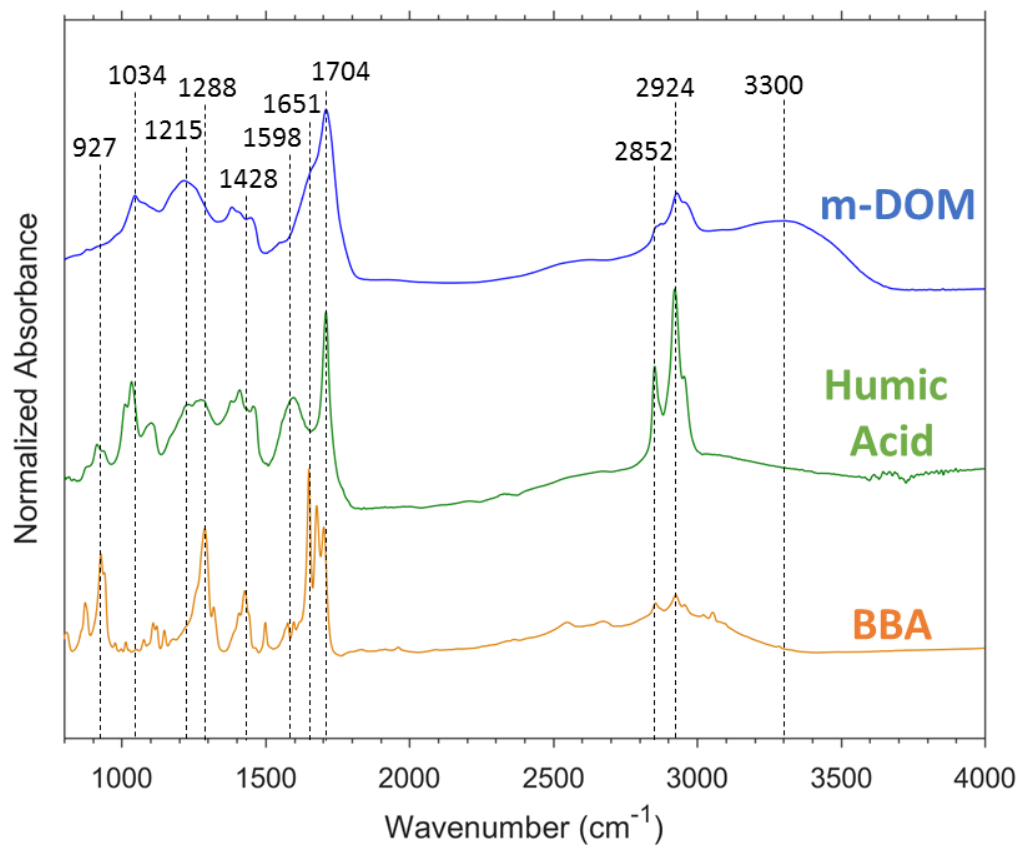


Figure 3.6. ATR-FTIR spectra of thin films of each of the photosensitizers.

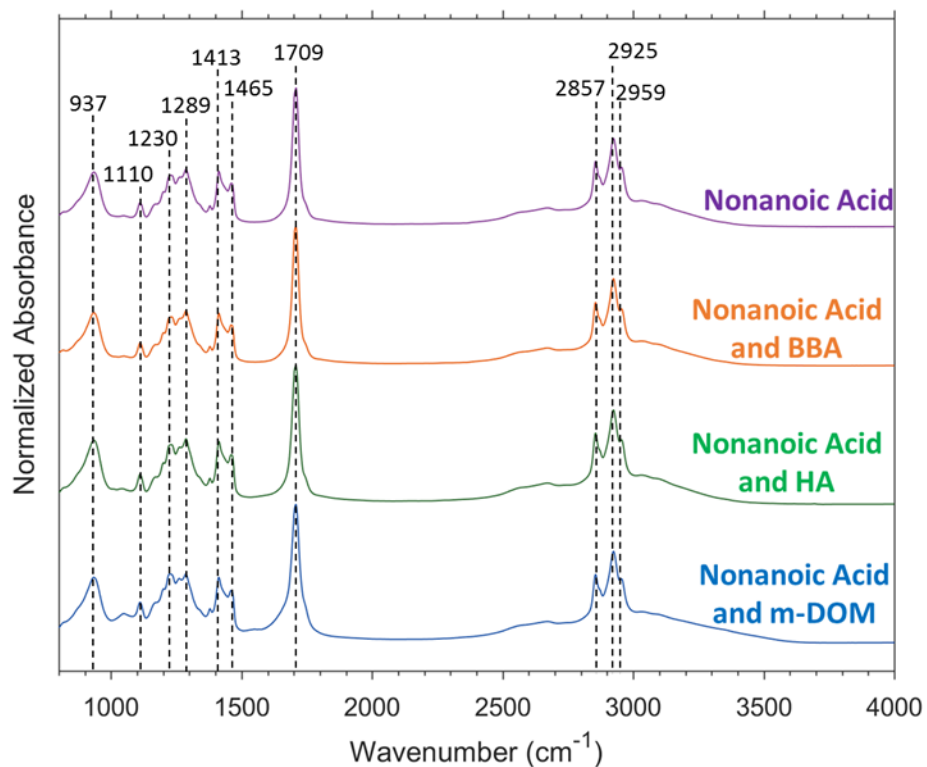


Figure 3.7. ATR-FTIR spectra of nonanoic acid alone and with each of the photosensitizers used in this study. Peak assignments for nonanoic acid are shown in Table S1.

Table 3.3. Vibrational peak assignments for nonanoic acid.

Peak (cm <sup>-1</sup> )	Assignment
937	O-H bending
1285	CO stretching
1413,1462	OH bending, CH <sub>2</sub> scissoring
1708	C=O stretching
2856	Symmetric CH stretching
2926	Asymmetric CH stretching
2500-3400	OH stretching

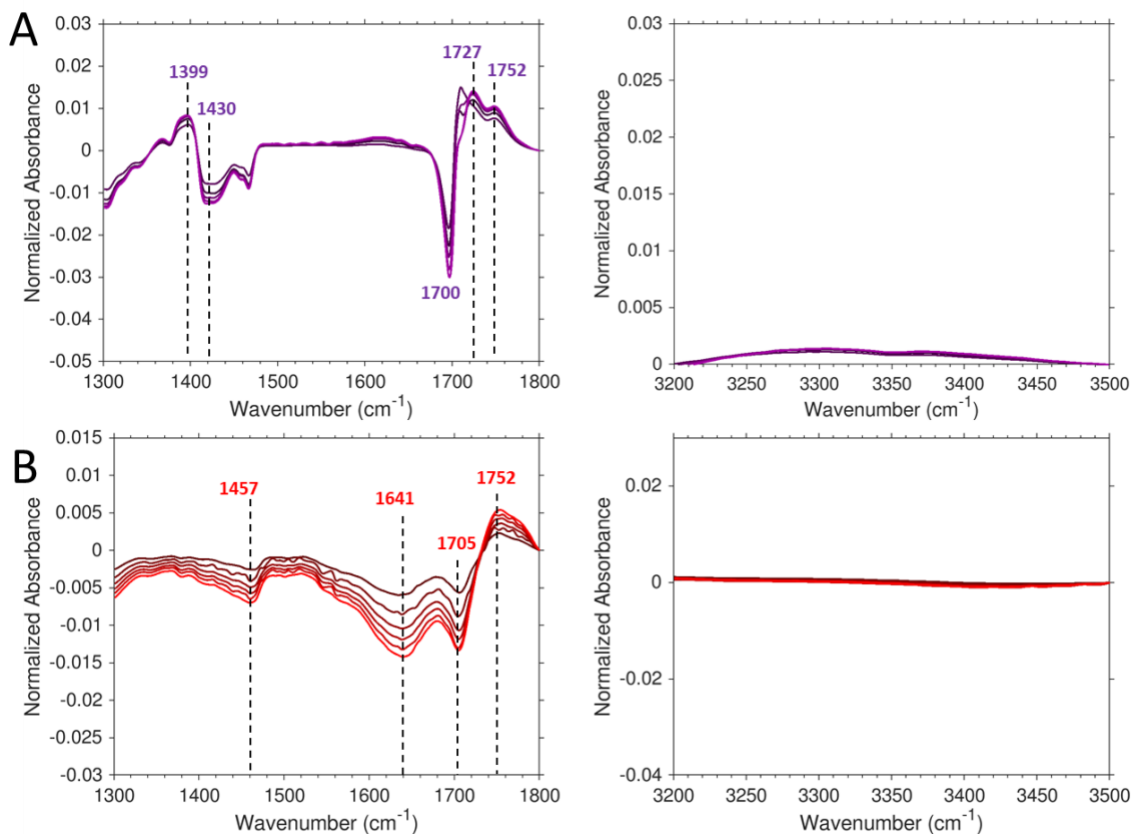


Figure 3.8. ATR-FTIR difference spectra of 60-minute irradiated A) nonanoic acid (NA) by itself and B) a thin film of m-DOM by itself. Spectra were collected every 10 minutes. Lines become increasingly light with increased time. Changes in the NA spectra and m-DOM spectra alone may be associated with evaporation, thermal effects, or small amounts of contamination as mass spectral data show only when there is a photosensitizer and light do photoproducts form to any great extent. Changes in the m-DOM ATR-FTIR spectra and MS data show that m-DOM is undergoing photochemistry in the presence and absence of NA.



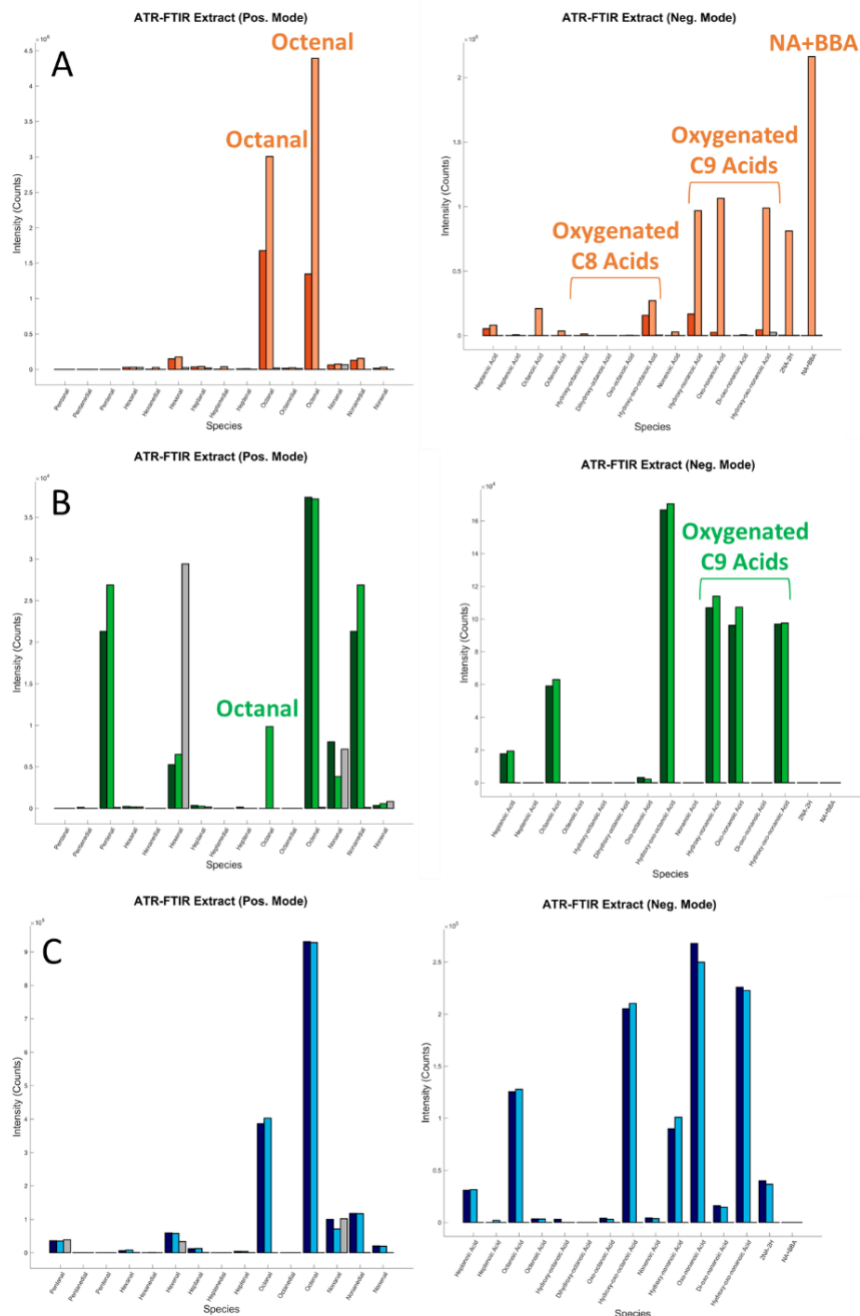


Figure 3.10. Signal detected (counts) for select products analyzed by HESI-LIT-Orbitrap MS in positive (left) and negative (right) mode of irradiated (light colored), non-irradiated (dark colors), and water blanks (grey) of A) NA in the presence of BBA, B) NA in the presence of HA, and C) NA in the presence of m-DOM.

### 3.8 References

- (1) Thurman, E. M. Organic Geochemistry of Natural Waters. *Usgs* **1985**, 497.
- (2) Timko, S. A.; Maydanov, A.; Pittelli, S. L.; Conte, M. H.; Cooper, W. J.; Koch, B. P.; Schmitt-Kopplin, P.; Gonsior, M. Depth-Dependent Photodegradation of Marine Dissolved Organic Matter. *Front. Mar. Sci.* **2015**, *2* (September), 1–13.
- (3) Vione, D.; Calza, P. Chapter 1: Introduction. In *Surface Water Photochemistry*; The Royal Society of Chemistry: Cambridge, 2016; pp 1–15.
- (4) Canonica, S. Oxidation of Aquatic Organic Contaminants Induced by Excited Triplet States. *Chimia (Aarau)*. **2007**, *61* (61), 641–644.
- (5) McNeill, K.; Canonica, S. Triplet State Dissolved Organic Matter in Aquatic Photochemistry: Reaction Mechanisms, Substrate Scope, and Photophysical Properties. *Environ. Sci. Process. Impacts* **2016**, *18* (11), 1381–1399.
- (6) Clark, C.; Zika, R. Marine Organic Photochemistry: From the Sea Surface to Marine Aerosols. *Mar. Chem.* **2000**, *5*, 1–33.
- (7) Ciuraru, R.; Fine, L.; Van Pinxteren, M.; D’Anna, B.; Herrmann, H.; George, C. Photosensitized Production of Functionalized and Unsaturated Organic Compounds at the Air-Sea Interface. *Sci. Rep.* **2015**, *5* (March), 1–10.
- (8) Ciuraru, R.; Fine, L.; Pinxteren, M. Van; D’Anna, B.; Herrmann, H.; George, C. Unravelling New Processes at Interfaces: Photochemical Isoprene Production at the Sea Surface. *Environ. Sci. Technol.* **2015**, *49* (22), 13199–13205.
- (9) Fu, H.; Ciuraru, R.; Dupart, Y.; Passananti, M.; Tinel, L.; Rossignol, S.; Perrier, S.; Donaldson, D. J.; Chen, J.; George, C. Photosensitized Production of Atmospherically Reactive Organic Compounds at the Air/Aqueous Interface. *J. Am. Chem. Soc.* **2015**, *137* (26), 8348–8351.
- (10) Tinel, L.; Rossignol, S.; Bianco, A.; Passananti, M.; Perrier, S.; Wang, X.; Brigante, M.; Donaldson, D. J.; George, C. Mechanistic Insights on the Photosensitized Chemistry of a Fatty Acid at the Air/Water Interface. *Environ. Sci. Technol.* **2016**, *50* (20), 11041–11048.
- (11) Hansell, D.; Carlson, C.; Repeta, D.; Schlitzer, R. Dissolved Organic Matter in the Ocean: A Controversy Stimulates New Insights. *Oceanography* **2009**, *22* (4), 202–211.
- (12) Nelson, N. B.; Siegel, D. A. The Global Distribution and Dynamics of Chromophoric Dissolved Organic Matter. *Ann. Rev. Mar. Sci.* **2013**, *5* (1), 447–476.

- (13) Coble, P. G. Marine Optical Biogeochemistry: The Chemistry of Ocean Color. *Chem. Rev.* **2007**, *107* (2), 402–418.
- (14) Dittmar, T.; Koch, B.; Hertkorn, N.; Kattner, G. A Simple and Efficient Method for the Solid-Phase Extraction of Dissolved Organic Matter (SPE-DOM) from Seawater. *Limnol. Oceanogr. Methods* **2008**, *6* (6), 230–235.
- (15) Koch, B. P.; Witt, M.; Engbrodt, R.; Dittmar, T.; Kattner, G. Molecular Formulae of Marine and Terrigenous Dissolved Organic Matter Detected by Electrospray Ionization Fourier Transform Ion Cyclotron Resonance Mass Spectrometry. *Geochim. Cosmochim. Acta* **2005**, *69* (13), 3299–3308.
- (16) Kujawinski, E. B.; Longnecker, K.; Blough, N. V.; Del, R.; Finlay, L.; Kitner, J. B.; Giovannoni, S. J. Identification of Possible Source Markers in Marine Dissolved Organic Matter Using Ultrahigh Resolution Mass Spectrometry. *Geochim. Cosmochim. Acta* **2009**, *73* (15), 4384–4399.
- (17) Stubbins, A.; Dittmar, T. Illuminating the Deep: Molecular Signatures of Photochemical Alteration of Dissolved Organic Matter from North Atlantic Deep Water. *Mar. Chem.* **2015**, *177*, 318–324.
- (18) Rapf, R. J.; Perkins, R. J.; Carpenter, B. K.; Vaida, V. Mechanistic Description of Photochemical Oligomer Formation from Aqueous Pyruvic Acid. *J. Phys. Chem. A* **2017**, *121* (22), 4272–4282.
- (19) Wang, Z.; Sun, J.; Xie, S.; Ma, G.; Jia, Y. Thermal Properties and Reliability of a Lauric Acid/Nonanoic Acid Binary Mixture as a Phase-Change Material for Thermal Energy Storage. *Energy Technol.* **2017**, *5* (12), 2309–2316.
- (20) Stuart, B. H. *Infrared Spectroscopy: Fundamentals and Applications*; John Wiley and Sons Ltd: Chichester, **2004**.
- (21) Smith, B. *Infrared Spectral Interpretation: A Systematic Approach*; CRC Press: Boca Raton, Florida, **1999**.
- (22) Coates, J. Interpretation of Infrared Spectra, A Practical Approach. In *Encyclopedia of Analytical Chemistry*; John Wiley and Sons Ltd: Chichester, **2006**.
- (23) Pospíšilová, L.; Fasurova, N. Spectroscopic Characteristics of Humic Acids Originated in Soils and Lignite. *Soil Water Res.* **2009**, *4* (4), 168–175.
- (24) Tatzber, M.; Stemmer, M.; Spiegel, H.; Katzlberger, C.; Haberhauer, G.; Mentler, A.; Gerzabek, M. H. FTIR-Spectroscopic Characterization of Humic Acids and Humic Fractions Obtained by Advanced NaOH, Na<sub>4</sub>P<sub>2</sub>O<sub>7</sub>, and Na<sub>2</sub>CO<sub>3</sub> Extraction Procedures. *J. Plant Nutr. Soil Sci.* **2007**, *170* (4), 522–529.



- (25) Ribeiro, J. S.; Ok, S. S.; Garrigues, S.; De la Guardia, M. FTIR Tentative Characterization of Humic Acids Extracted from Organic Materials. *Spectrosc. Lett.* **2001**, *34* (2), 179–190.
- (26) Dittmar, T. The Molecular Level Determination of Black Carbon in Marine Dissolved Organic Matter. *Org. Geochem.* **2008**, *39* (4), 396–407.
- (27) Longnecker, K.; Kujawinski, E. B. Composition of Dissolved Organic Matter in Groundwater. *Geochim Cosmochim AC.* **2011**, *75*, 2752-2761.
- (28) Stubbins, A.; Spencer, R. G. M.; Chen, H.; Hatcher, P. G.; Mopper, K.; Hernes, P. J.; Mwamba, V. L.; Mangangu, A. M.; Wabakanghanzi, J. N.; Six, J. Illuminated Darkness: Molecular Signatures of Congo River Dissolved Organic Matter and Its Photochemical Alteration as Revealed by Ultrahigh Precision Mass Spectrometry. *Limnol. Oceanogr.* **2010**, *55* (4), 1467–1477.

## **Chapter 4: Changes in Light Absorption and Composition of Chromophoric Marine-Dissolved Organic Matter Across a Microbial Bloom**

### **4.1 Abstract**

Marine chromophoric dissolved organic matter (m-CDOM) mediates many vital photochemical processes in the surface ocean. Isolating m-CDOM within the chemical complexity of marine dissolved organic matter has remained an analytical challenge. The SeaSCAPE campaign, a large-scale mesocosm experiment, provided a unique opportunity to probe the *in-situ* production of m-CDOM across phytoplankton and microbial blooms. Results from mass spectrometry coupled with UV-VIS spectroscopy reveal production of a chemodiverse set of compounds well-correlated with increases in absorbance after a bacterial bloom, indicative of autochthonous m-CDOM production. Notably, many compounds were found to be enriched in nitrogen, which may be essential to chromophore function. From these results, quinoids, porphyrins, flavones, and amide-like compounds were identified via structural analysis and may serve as important photosensitizers in the marine boundary layer. Overall, this study demonstrates a step forward in identifying and characterizing m-CDOM using temporal mesocosm data and integrated UV-VIS spectroscopy and mass spectrometry analyses.

## 4.2 Introduction

The photoactive, or chromophoric, subset of marine dissolved organic matter (referred to here as m-CDOM), is a ubiquitous constituent of one of the largest global carbon (C) reservoirs and the greatest pool of reduced carbon (~660 Pg C) in marine environments.<sup>1</sup> Capable of performing direct and indirect photochemical processes in the environment,<sup>2,3</sup> and driving the amount of UV-radiation and visible light absorption at the surface ocean,<sup>4</sup> m-CDOM is thought to be a complex mixture of compounds derived from both allochthonous and autochthonous sources, such as phytoplankton and bacterial blooms.<sup>5-9</sup> The composition and structures of m-CDOM drive an extensive array of photochemical reactions and metabolomic pathways catalyzed by solar radiation in the photic zone,<sup>10</sup> including potential light-driven production of nitrous acid - an important atmospheric oxidant.<sup>11,12</sup> Despite the importance of speciation in modulating behavior, the molecular composition of m-CDOM has yet to be elucidated.

Much of this uncertainty is rooted in the diverse production pathways of m-CDOM, identification limitations within the broader chemical complexity of marine organic matter, and the inherent photo-reactivity of such compounds.<sup>13,14</sup> Characterizing natural organic matter is universally a complex analytical endeavor, given the number and chemodiversity of compounds that make up these samples across different environments.<sup>15,16</sup> As such, a synchrony of different techniques, such as nuclear magnetic resonance (NMR) spectroscopy and high-resolution mass spectrometry (MS), is required to isolate and characterize discrete DOM populations.<sup>17-21</sup> Identification of m-CDOM compounds, more specifically, within bulk marine DOM has largely been accomplished using low-resolution approaches such as excitation-emission matrices (EEMs), which do not provide the molecular-level resolution critical to understanding and predicting m-CDOM behavior in marine systems.<sup>22</sup> Some studies have attempted to separate

CDOM based on assumed structure composition (e.g. aromatic) and incorporate mass spectrometry in conjunction with spectroscopic measurements.<sup>23</sup> However, results are limited to simple characterizations such as molecular weight and formulae.

This work aims to isolate and characterize m-CDOM formation at the molecular level using integrated absorbance measurements and mass spectrometry during sequential microbial blooms within a large-scale mesocosm flume. The sequential exponential growth of phytoplankton, which reduce CO<sub>2</sub> from their surroundings, and subsequent marine bacterial growth from decayed substrates,<sup>24,25</sup> is a documented autochthonous pathway of m-CDOM production.<sup>26,27</sup> Thus, organic matter composition was characterized throughout a large-scale (12,000 L wave channel) mesocosm experiment, the 2019 Sea Spray Chemistry and Particle Evolution (SeaSCAPE) study at Scripps Institution of Oceanography (Sauer et al., 2021) throughout sequential phytoplankton and bacterial blooms under controlled conditions.<sup>28</sup> Using integrated UV-VIS spectroscopy and high-resolution mass spectrometry to characterize temporal organic matter composition, this work aims to provide insight into the composition of m-CDOM, an elusive yet critical photochemical driver in the surface ocean.

### **4.3 Experimental Methods**

#### *SeaSCAPE wave channel and experimental design of microbial bloom*

The collaborative SeaSCAPE 2019 campaign project, which aimed to characterize realistic ocean-atmosphere chemistry during microbial blooms in a wave channel, has been previously detailed by Sauer et al., 2021.<sup>29</sup> Briefly, approximately 11,800 L of seawater was collected from Ellen Browning Scripps Memorial Pier in La Jolla, California (32.8663° N, 117.2546° W) and immediately filtered to 50 microns to remove the majority of non-microbial

biota and large grazers. The filtered seawater was then transferred into a cleaned glass wave channel and allowed to equilibrate at ambient temperature for 24 hours. An electromagnetically driven paddle was used to generate waves down the 33-meter wave channel onto an artificial beach made of fiberglass. Nutrients were then added to the wave channel and fluorescent lights were installed along the walls of the flume to support a diurnal light cycle. Three separate microbial blooms were studied during this campaign project, though only the third one, a 22-day long observation, will be the focus of this study. The wave flume was cleaned and rinsed with acetic acid and Milli-Q, and refilled with seawater from Scripps Pier, between each bloom. This experiment observed two distinct microbial blooms, a first proliferation of phytoplankton species followed by a second largely bacterial bloom, although viral contributions were observed. A more comprehensive description of the biodiversity and population dynamics during the SeaSCAPE campaign can be found in Sauer et al., 2021.<sup>29</sup>

#### *m-DOM isolation and purification*

At eight intervals over the course of 23 days in July and August of 2019, 20 L of water was collected from the flume channel. Sampling occurred on T0, T2, T6, T9, T13, T16, T19, and T22 in which samples are denoted by the numbers of days passed from experimental start corresponding to July 24<sup>th</sup>, 26<sup>th</sup>, 30<sup>th</sup>, and August 2<sup>nd</sup>, 6<sup>th</sup>, 9<sup>th</sup>, 12<sup>th</sup>, and 15<sup>th</sup> respectively. All materials used to collect each sample, such as the carboy, tubing, and filters, were pre-rinsed with HPLC-grade methanol (MeOH) and Milli-Q water three times before each collection. The carboy was additionally rinsed inside with water from the wave channel 3x before being filled to a pre-measured 20 L mark. From each of these eight 20 L samples, dissolved organic matter (DOM) was isolated via sequential filtration through 10  $\mu\text{m}$  nylon mesh, 0.7  $\mu\text{m}$ , and 0.2  $\mu\text{m}$

filters (Polyethersulfone, 47 mm, MilliporeSigma), maintaining a pressure below 5 psi to avoid lysing any cells present. After filtration, the seawater was acidified to pH 2 using 1M HCl to remove any inorganic carbon contributions and increase sample interaction with the resin by protonation. The resultant DOM was purified via solid-phase extraction (SPE) as described by Dittmar et al.,<sup>30</sup> using 5g Priority PolLutant (Bond Elut PPL, Agilent) cartridges. With the cartridges having a max loading of 50 L of seawater, the loading of m-DOM onto the SPE cartridges was kept under 10 L per gram of absorbing material, and concentration of m-DOM throughout the mesocosm experiment did not exceed 2 mg/L. The DOM eluent post-SPE processing was dried in a rotary evaporator and then stored in a freezer at -21 °C prior to further analyses.

#### *Elemental characterization*

Analysis of total organic carbon (TOC) concentrations have been previously reported by Sauer et al., 2021.<sup>29</sup> Briefly, duplicate 40 mL aliquots of flume seawater were collected at each sampling interval and filtered into combusted glass vials through a 0.7 µm Whatman GF/F filter. Filtrate samples were immediately acidified to pH 2 with concentrated HCl prior to analysis on a Shimadzu TOC-VCSH catalytic combustion oxidation instrument.

#### *Absorbance characterization and spectral slope derivation*

Absorbance spectra were also collected from all temporal samples using a Shimadzu UV-3600 UV-VIS-NIR spectrophotometer. For each sample, 4 mL of m-DOM was isolated and analyzed across these wavelengths and then corrected for mass once the solution was dried down, to obtain the mass attenuation coefficient (MAC). Absorbance spectral slopes for each

sample were also calculated for the wavelength ranges of 275-295 nm ( $S_{275-295}$ ) and 350-400 nm ( $S_{350-400}$ ) via a single exponential decay function (Eq. 1) by nonlinear regression, as reported in Stubbins et al., using SigmaPlot software (SPSS Inc.).<sup>31</sup>

$$a_l = Ae^{-S \cdot l} \quad \text{Eq. 1}$$

Slope values over these discrete spectral ranges have been previously shown to directly correlate with m-CDOM degradation and molecular weight.<sup>32,33</sup>

### *High-resolution mass spectrometry and post-processing*

The molecular compositions of all SPE eluent samples were characterized via Orbitrap mass spectrometry (Thermo Fisher Scientific). The Orbitrap was externally calibrated for mass accuracy on the day of analysis using the manufacturer's guidelines and a standard calibration solution (Pierce ESI Ion Calibration Solutions, Thermo Fisher Scientific). Samples were resuspended in MS-grade MeOH to a concentration of 0.5 mg/ml, and loaded to the heated electrospray ionization (HESI) through direct injection at a flow rate of 5  $\mu$ l/min. After ionization, ions were then transferred into a linear ion trap and subsequently the Orbitrap cell. Broad-band mass spectra were then recorded between 150 and 1500  $m/z$ . A total of 120 scans were accumulated, and subsequent  $m/z$ , intensity, and resolution data for all peaks were exported to individual mass lists.

After analysis, only  $m/z$  values with a signal-to-noise ratio (S/N)  $\geq 10$  were exported for formula assignment. As previously published,<sup>34,35</sup> empirical formula matches were assigned to all resolved peaks within the bounds of  $C_{1-50}H_{1-100}O_{1-30}N_{0-5}S_{0-2}P_{0-2}$ , and molecular formula were assigned based on the following: (1) Kendrick mass defect analysis, (2) least number of nonoxygen heteroatoms, and (3) lowest parts per million  $m/z$  deviation, with calculated

theoretical  $m/z$  values of the assigned formulas within an error value of  $\leq 0.5$  ppm of measured  $m/z$  values. Over 10,000 unique molecular formulae were assigned amongst all samples, which were further binned into assigned compound classes according to elemental ratios and a modified aromaticity index ( $AI_{mod}$ ), shown in equation 2.<sup>36</sup>

$$AI_{mod} = (I + C - 0.5O - S - 0.5H)/(C - 0.5O - S - N - P) \quad Eq. 2$$

Compound classes were assigned as follows: condensed polycyclic aromatics ( $AI_{mod} > 0.66$ ), polyphenols ( $0.66 \geq AI_{mod} > 0.50$ ), highly unsaturated ( $AI_{mod} \leq 0.50$  and  $H/C < 1.5$ ), aliphatic compounds ( $2.0 \geq H/C \geq 1.5$ ) with (+N) or without (-N) nitrogen, and saturated compounds ( $H/C > 2$ ). Lastly, compounds present in only one sample were removed from further analyses, including compound class statistics, heteroatomic content calculations, and Spearman's rank correlations. Spearman ranking is a statistical measure of the dependence between two non-parametric variables to correlate absorption parameters to sum-normalized compound intensities derived from Orbitrap mass spectrometry in compounds present in at least 6 out of 8 timepoints.<sup>37,38</sup> Correlations were deemed significant if they had a  $p$ -value  $\leq 0.05$ .

## 4.4 Results and Discussion

### *Evolution of m-DOM absorbance during sequential biotic blooms*

Changes in m-DOM concentration (i.e. all of the marine dissolved organic matter, m-DOM, and not just the light absorbing component), absorbance and potential m-CDOM production were characterized using UV-VIS spectroscopy throughout a microbial bloom progression (Fig. 4.1, Fig. 4.3 – see Supporting Information). As noted in Sauer et al., 2021,<sup>29</sup> total organic carbon (TOC) steadily increased in concentration throughout the experimental time course, due to both primary and bacterial production, consistent with previous bloom incubation experiments.<sup>39</sup> Introduced phytoplankton populations experienced a growth phase during the first



week of wave channel operation (T6), followed by abrupt decay (T9), represented by Chl a concentrations (Fig. 4.3b). Subsequent rapid growth in bacterial biomass was observed, reaching peak cell counts at T13 before declining at the conclusion of experimental operations (T22) (Fig. 4.3c). Absorbance increased over the experimental time course, with a marked increase observed after peak bacterial growth at T13 (Fig. 4.3c), suggesting the production and persistence of photo-absorbing compounds via microbial mineralization of phytoplankton biomass, as previously observed by Kinsey et al., 2018.<sup>26</sup>

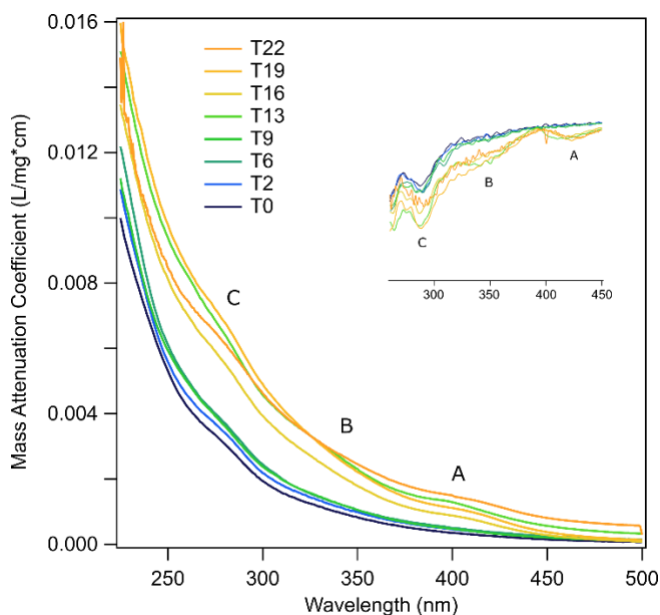


Figure 4.1. Mass attenuation coefficient spectrum of m-DOM samples, calculated from the UV-VIS spectra, collected from the SeaSCAPE Bloom 3 experiment. All spectra were taken dissolved in methanol. Samples were dissolved to a standard mass concentration of the extracted m-DOM. Inset: The inset spectra show the 1<sup>st</sup> derivative of the m-DOM to better identify the A, B, and C peaks that are contributing to the broad spectrum.

Specifically, three distinct spectral regions – 280, 350, and 410 nm – displayed enhanced absorbance denoted by peaks C, B, and A respectively. Shoulders at 280 and 350 nm were seen throughout the entire experiment, becoming more distinct over time. This behavior is consistent with spectroscopic measurements of microbial growth in laboratory and field experiments. A

distinct peak at 410 nm only appears during and after the microbial bloom peak, persisting throughout the bloom time course. Absorbance at 410 nm, the A band, has only infrequently been observed in prior examinations of m-CDOM, and previously only appears after peak microbial growth, suggesting the associated compounds are likely produced biotically.<sup>40,41</sup> In theoretical work by Karimova et al. 2021, this A band has been proposed to arise from electronic transitions of carbon chains with diol- and oxy- groups, though additional experimental work is needed to validate such proposed structures.<sup>42</sup> The C band, at 280 nm and higher energy wavelengths, is associated with aromatic rings and aromaticity in general, particularly the  $\pi \rightarrow \pi^*$  transitions. The B band, at 350 nm, is commonly associated with the  $n \rightarrow \pi^*$  but can also be in combination with  $\pi \rightarrow \pi^*$  modes.<sup>42</sup> This very broad peak can be composed of peptides, amino acids, flavins, tannins, etc.<sup>43,44</sup> However, as noted above, this subset is vastly uncharacterized.

#### *Integrated UV-VIS spectroscopy and HRMS: Signatures of CDOM production*

We integrated absorbance analyses to high-resolution Orbitrap mass spectrometry to isolate the production of m-CDOM within broader shifts in m-DOM chemodiversity. Within the 10,000+ unique formulae identified, relative abundance within the compound classes assigned did not vary significantly over the course of the experiment (Table S1; Figure S2). Broader shifts in heteroatom content (Fig. S3A), molecular weight (MW; Fig. S3B), and aromaticity (Fig. S3C), were observed as microbial populations, and thus metabolic pathways, evolved. Notably, after the peak bacterial cell counts, m-DOM was highly enriched in N, depleted in sulfur (S), and of greater aromaticity than before the bacterial bloom.

Amidst observed m-DOM chemodiversity dynamics, m-CDOM production was isolated through (i) identification of novel compounds produced post-bacterial bloom peak, and (ii)

Spearman's ranking correlations between compound relative abundances and absorbance parameters (Fig. 4.2). Indices of absorbance used were the intensity of absorption at 410 nm,  $\epsilon_{410}$ , and simple exponential fits of spectra between 275-295 nm ( $S_{275-295}$ ) and 350-400 nm ( $S_{350-400}$ ) (Eq. 1), reflective of photochemically induced shifts in MW and degradation (See Methods for further details).<sup>32</sup> Of the formulae assigned, 397 were produced after the bacterial bloom peak and observed in all subsequent timepoints (Fig. 4.2A), enriched in polycyclic and polyphenolic compounds (Fig. 4.2C). Spearman's ranking, considering compounds present in at least 75% of samples, indicated strong compositional similarity between bacterially produced (Fig. 4.2A) and photoactive (Fig. 4.2B) populations, evident in van Krevelen space. Such photoactive compounds ( $n = 282$ ), those well-correlated with  $S_{275-295}$  and  $S_{350-400}$ , represented an increasingly aromatic subset, in agreement with previously published findings of m-CDOM aromaticity and chromophore signatures (Fig. 4.2C).<sup>45</sup> Markedly, those compounds with higher correlation values ('enriched') to  $S_{350-400}$  were nearly 70% aromatic, while those to  $S_{275-295}$  were of greater unsaturation (Fig. 4.2C). The  $\epsilon_{410}$  displays more unique subset of compounds compared to  $S_{275-295}$  and  $S_{350-400}$  (Fig. S4), all increasingly produced compounds toward the latter half of the bloom where the 410 nm peak first appeared. However, all subsets contained compounds across all structural classes, suggesting that m-CDOM is even more chemodiverse than previously considered.<sup>22</sup>

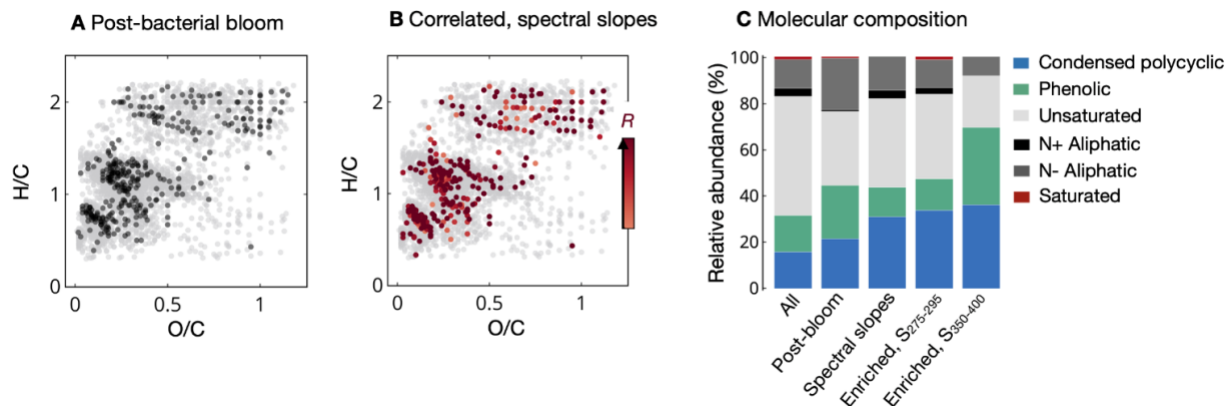


Figure 4.2. Analysis of m-DOM composition using high resolution mass spectrometry data correlated to UV-VIS absorbance data across the bloom experiment. van Krevelen plots with all m-DOM formulae as a reference are in light grey, (A) compounds produced post-bacterial bloom, and (B) compounds correlated with spectral slopes  $S_{275-295}$  and  $S_{350-400}$ . The relative abundance of these subsets, and those compounds enriched in one spectral slope subset or the other, are displayed in (C). *Figures made, and analyses assisted, by Dr. Elizabeth Coward.*

Notably, the population of compounds well-correlated in abundance to absorbance values, thus thought to encompass m-CDOM, were also found to be enriched in nitrogen (N) (Table 4.1). The carbon-nitrogen ratio C/N of all DOM was calculated, weighted by intensity, to be 13.0, similar to past literature, where Nissenbaum and Kaplan have reported between 9.4 and 13.9 in the southern California coastal region.<sup>46</sup> Formulae subsets  $S_{350-400}$ ,  $S_{275-295}$ , and  $\epsilon_{410}$ , in contrast, displayed significantly lower weighted C/N ratios of 8.6, 7.2, and 8.0, respectively. The enrichment of N-containing compounds, evidenced by decreases in C/N, in photo-active subsets suggests preferential incorporation during the formation of chromophores. This preferential enrichment of N appears element-specific, as subset H/C and O/C ratios were not significantly (< 10%) different from those of bulk m-DOM as shown in Table 4.1, and both exhibited only minor shifts (< 12%) throughout the mesocosm experiment. Similar to past studies using electrospray ionization-based mass spectrometry, the average intensity-weighted H/C and O/C ratios of bulk m-DOM were 1.21 and 0.38 respectively.<sup>47</sup>

Table 4.1. Averaged mass spectral characteristics of marine dissolved organic samples across bloom experiment comparison to correlated subset data per spectral parameter, weighted by relative intensity.

Spectral Parameter	H/C	O/C	C/N	MW	n
Entire Bloom	1.21	0.38	13.0	601.4	10,945
S <sub>275-295</sub>	1.30	0.40	7.2	454.6	266
S <sub>350-400</sub>	1.26	0.38	8.6	509.0	282
ε <sub>410</sub>	1.34	0.38	8.0	501.6	226

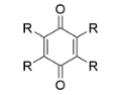
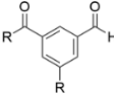
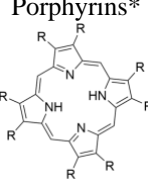
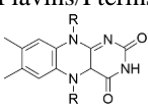
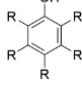
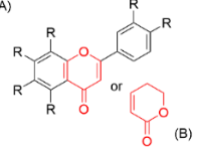
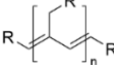
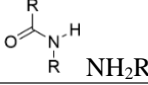
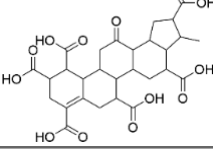
### *Towards an m-CDOM chemotype*

Our efforts to identify and characterize m-CDOM production at the molecular level reveal evidence for autochthonous production of primarily polycyclic, aromatic, and even unsaturated compounds, enriched in N, capable of enhanced light absorbance. Leveraging the controlled mesocosm blooms of the SeaSCAPE 2019 campaign to control for m-CDOM production without ongoing natural or anthropogenic inputs or contamination normally observed in coastal environments, we propose a first step towards an m-CDOM chemotype, and suggest that nitrogen-containing structures might also play a role in nascently produced m-CDOM – something that has only been recently, and tentatively, posited.<sup>26,29,48</sup> Coupling high resolution mass spectrometry and UV-VIS spectrometry have allowed for molecular-level speciation, advancing from the excitation emission matrix spectroscopy and parallel factor analysis often employed to detect chromophores.<sup>22</sup>

As Orbitrap mass spectrometry is not capable of resolving structural information, it is recommended that future studies should employ secondary tandem mass spectrometry, preferably in conjunction with spectroscopic techniques, such as UV-VIS, to single out chromophoric subsets. As such, we analyzed an open-access Orbitrap MS/MS dataset collected from tandem samples taken throughout the SeaSCAPE campaign on the same instrument using the Global Natural Products Social (GNPS) Molecular Networking database.<sup>49</sup> As m-DOM was

isolated for MS and MS/MS analyses in identical fashion, comparisons between datasets are assumed to be viable, with the consideration that MS/MS assignments are capable of identifying structures for only a fraction of detected peaks. In this MS/MS dataset, the GNPS molecular network assigned 586 m-DOM confirmed structural assignments out of the thousands of masses observed throughout the experimental time course examined here. To identify potential m-CDOM candidates within these 586 assignments, Spearman's ranking correlations between peak abundance and the three major spectral parameters of the m-CDOM samples ( $S_{350-400}$ ,  $S_{275-295}$ , and  $\epsilon_{410}$ ) were employed, resulting in five, well-correlated, identified structures (Table 4.2). Two of these were metal-free, porphyrin-based compounds: coproporphyrin I and III byproducts of heme synthesis and degradation. Of note, other porphyrins were observed in this structurally defined dataset but were not well correlated with the m-CDOM parameters. One of these, Pheophorbide A, was observed to weakly correlate ( $R = 0.45$ ) with  $S_{350-400}$ . The other three structures observed were 5,7-dihydroxyisoflavone, 1,9-hydroxyisorhodoptilometrin, and N-phenethylcinnamamide which can be described as a flavone, an anthraquinone/quinoid, and a cinnamamide/aromatic amide, respectively. These structures have been detected in marine systems and many of these have been used as photosensitizers (see references in Table 4.2).

Table 4.2. Selected classes of compounds that have been shown to be 1) produced naturally in marine environment by microbes and/or 2) have shown to be environmentally relevant photosensitizers characteristics (see references).

<i>Mass Spectral Classification</i>	<b>Major Compound Types</b>	<b>Representative, Naturally-Produced Analogs</b>	<b>References</b> <sup>27,40,57–63,48,50–56</sup>
<i>Condensed Polycyclic Aromatic</i>	Aromatic Carbonyls	<p>Quinoids*</p>  <p>Aromatic Ketones/Aldehydes</p> 	<sup>b</sup> Ehrhardt 1984, <sup>a</sup> Choudhry 1984, <sup>b</sup> Goldstone 2000, <sup>a</sup> Wang 2020
	Heterocyclic Aromatics	<p>Porphyrins*</p>  <p>Flavins/Pterins</p> 	<sup>a</sup> Rottgers 2012, <sup>b</sup> D'Ambrosio 2020  <sup>a</sup> Dunlap 1985, <sup>b</sup> Dunlap 1986, <sup>b</sup> McNeill 2016
	Polyphenolic	<p>Phenols and lignin phenols</p>  <p>(A) Flavones/(B) Coumarines/related*</p> 	<sup>a</sup> Hernes and Benner 2003, <sup>b</sup> Opsahl 1998  <sup>a</sup> Hartmann 2018, <sup>a</sup> Martins 2019, <sup>b</sup> McNeill 2016
<i>Highly unsaturated</i>	Olefins	<p>Linear Terpenoids</p> 	<sup>a</sup> Blunt 2010, <sup>a</sup> Medeiros 2015, <sup>a</sup> Arakawa 2017
<i>Aliphatic N+</i>	Amines/Amide-like	<p>Amides and peptides*</p> 	<sup>a</sup> Shields 2019, <sup>b</sup> William 2014
<i>Aliphatic N-</i>	Carboxyl-rich alicyclic molecules (CRAM)		Structure, isomer I, adapted from <sup>a</sup> Hetkorn et. al. 2006.

<sup>a</sup>.

\*Detected structures in *m*-DOM samples collected from SeaSCAPE 2019 using molecular neural networking.

<sup>b, a</sup> Detected in marine samples

<sup>c, b</sup> Photosensitizer

Thus, even with a limited number of structures detected due to limitations in known structures of marine organic matter in assignment databases, a molecular picture of m-CDOM begins to emerge from these measurements. We identify an array of diverse marine chromophores, ranging in aromaticity and saturation, many containing nitrogen, N (Table 4.2). Some compounds in this analysis are seemingly non-chromophoric, such as aliphatic-like molecules, or non-photosensitizing species like olefins. However, it is important to mention that these classes can have important role in other indirect photochemical mechanisms such as the production of superoxide and radicals or the sink of singlet or triplet state energies.<sup>64,65</sup> Though this table and the classes of compounds identified are largely supported by the results of this study, it is by no means comprehensive. Even smaller molecular mimics are often desirable for fundamental experimental and theoretical studies to better understand light absorption within chromophores and the environmental factors that impact these transition energies. These may include compounds such as 4-benzylbenzoic acid,<sup>66</sup> pyruvic acid,<sup>67</sup> and benzoic acid,<sup>68</sup> as well as possibly more marine relevant<sup>42</sup> and nitrogen-containing structures such as imidazole-2-carboxaldehyde.<sup>69</sup> It is important to note that the focus of this study is on discrete molecular entities that can be involved in intra- and inter-molecular light absorption involving different chromophores and charge transfer processes, respectively.<sup>2,70</sup> Nevertheless, towards building a realistic model of m-CDOM, in terms of chemical properties and photochemical interactions, this current analysis and tabulated classes of compounds serve as a sufficient point of reference to facilitate future studies. These compounds are in stark contrast to the presumed humic-dominated chromophoric fraction of terrestrial DOM, which has dominated investigation for decades,<sup>51,71</sup> and highlight the need for further inquiry into this unique fraction of marine dissolved organic matter. Overall, the findings in this study are important in that they demonstrate the ability to



capture both composition and structure of at least a portion of the chromophores found in marine waters. Future work incorporating structural-sensitive techniques such as tandem mass spectrometry or NMR with optical spectroscopy, specifically across time-resolved scales, will be needed to take the next steps in understanding the composition and reactivity of m-CDOM.

## **4.5 Acknowledgements**

The authors gratefully acknowledge the support of the National Science Foundation through the Centers of Chemical Innovation Program via the Center for Aerosol Impacts on the Chemistry of the Environment (CHE-1801971) and the National Science Foundation Graduate Research Fellowship Program (DGE1650112). We appreciate the support and help with m-DOM extraction process and UV-VIS data collection from Vanessa Tian, Duyen Dang, and Michael Tauber. We would also like to thank Daniel Petras, Tyler Price, Hannah Karp, and the GNPS collaboration for their efforts to establish the open-source Molecular Networking database for SeaSCAPE samples. The SeaSCAPE 2019 campaign would not have been possible without the support from the 50+ person team involved, especially Tim Bertram, Chris Cappa, and Chris Lee for their leadership and organization of the campaign, and the authors would like to thank everyone for their guidance and collaboration.

Chapter 4 is in preparation: Alves, M.R.; Coward, E.K.; Gonzales, D.; Sauer, J.S.; Mayer, K.; Prather, K.A.; Grassian, V.H. Changes in Light Absorption and Composition of Chromophoric Marine-Dissolved Organic Matter Across a Microbial Bloom. *Environ. Sci. Technol.* 2021. The dissertation author is the primary investigator and author of this paper.

## 4.6 Supporting Information

Table 4.3. Summary of analyzed HRMS data

	<b>T0</b>	<b>T2</b>	<b>T6</b>	<b>T9</b>	<b>T13</b>	<b>T16</b>	<b>T19</b>	<b>T22</b>
Formula count (n)	1598	2343	2463	2441	1780	2168	2289	2090
<i>Compound class abundance, %</i>								
Polycyclic Aromatics	22.71%	16.76%	22.76%	23.44%	16.60%	20.81%	20.40%	21.87%
Highly Aromatic	15.14%	11.84%	16.47%	14.27%	11.78%	14.47%	16.32%	15.62%
Highly Unsaturated	40.70%	42.43%	38.35%	40.46%	42.30%	40.15%	37.97%	39.71%
Unsaturated Aliphatic-no N	9.51%	9.38%	11.27%	8.45%	11.34%	9.69%	11.73%	11.45%
Unsaturated Aliphatic-N	8.84%	14.84%	9.18%	10.07%	11.78%	12.51%	11.73%	9.96%
Saturated	3.09%	4.75%	1.97%	3.30%	6.19%	2.37%	1.85%	1.39%
<i>Mean population parameters</i>								
H:C	1.11	1.23	1.11	1.11	1.25	1.18	1.18	1.18
O:C	0.39	0.32	0.39	0.35	0.35	0.35	0.36	0.36
DBE	15.6	14.9	15.8	17.2	14.4	15.5	15.0	14.9
MW (Da)	552	601	593	621	583	580	566	567
AI <sub>mod</sub>	0.42	0.36	0.45	0.45	0.38	0.43	0.42	0.44

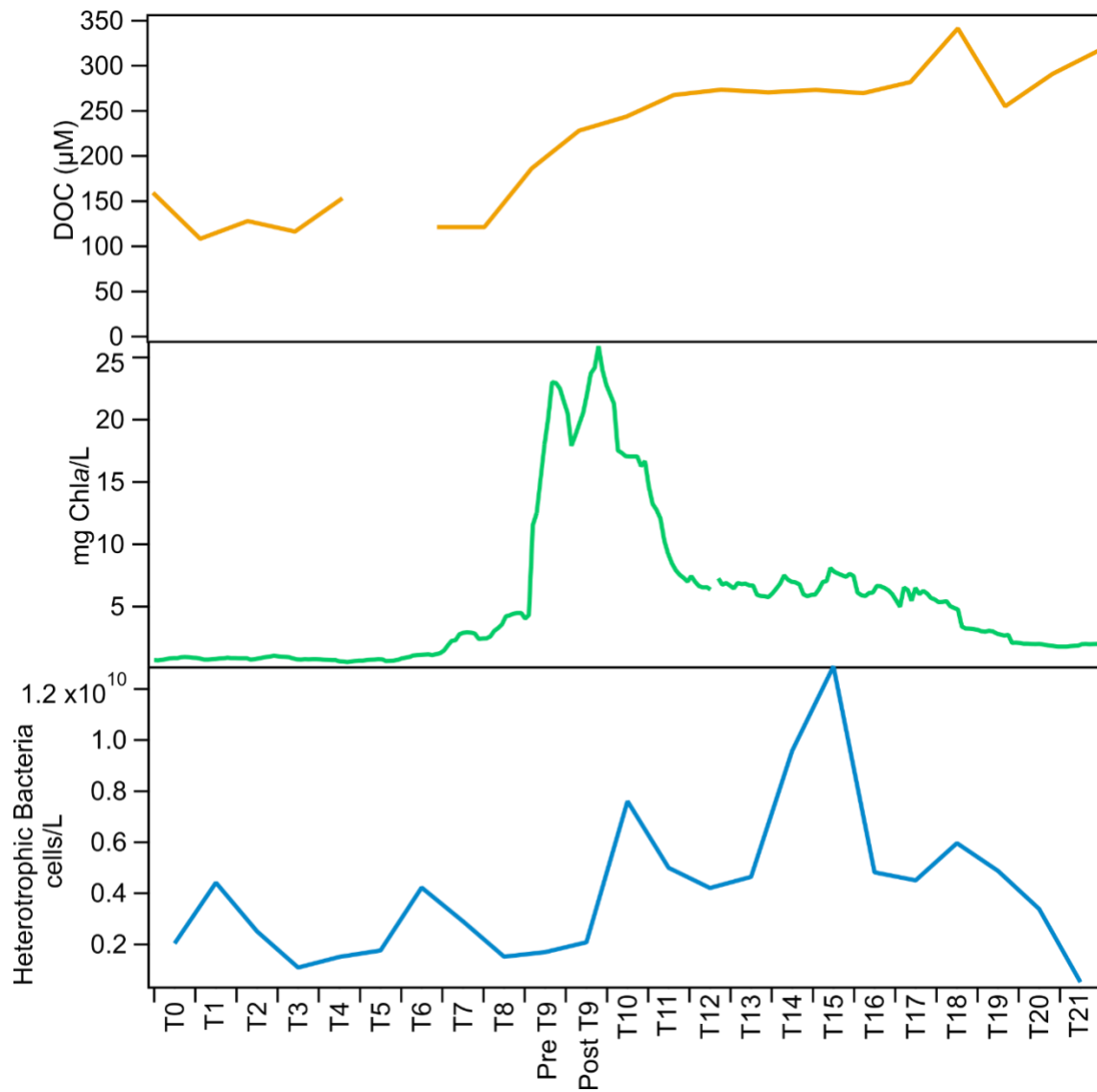


Figure 4.3. (a) Dissolved organic carbon measurement by TOC Analysis via combustion catalytic oxidation, (b) chlorophyll a concentration, and (c) heterotrophic bacterial cell counts per liter of seawater.

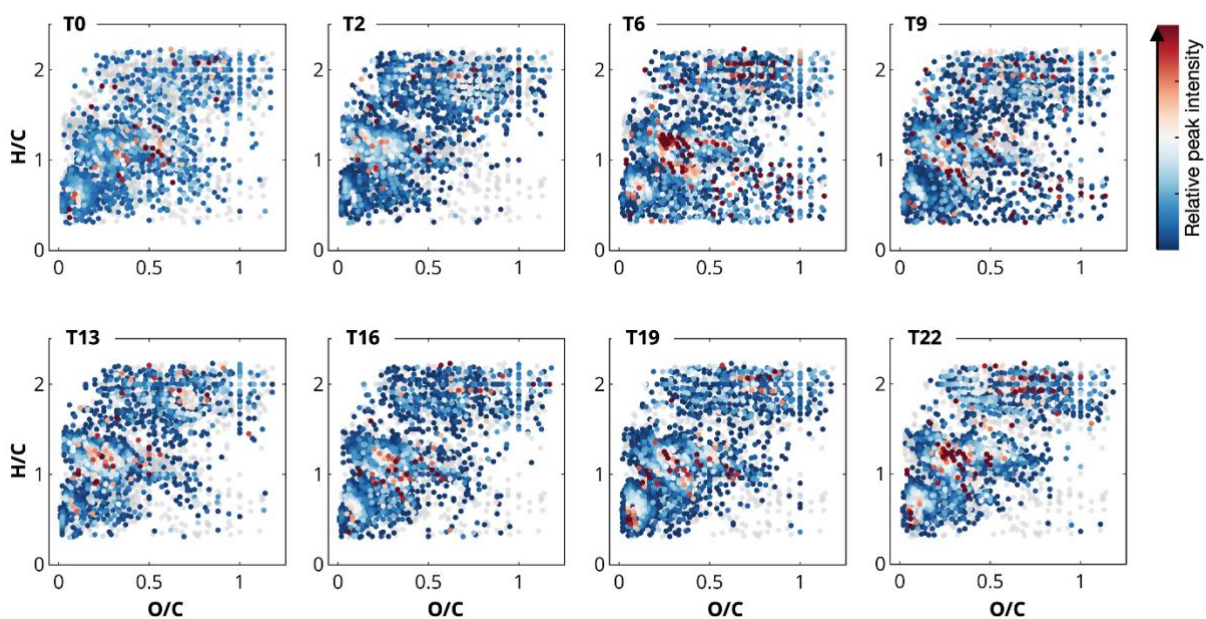


Figure 4.4. Van Krevelen diagrams of m-DOM samples collected throughout the bloom, colored by their normalized relative peak intensity. *Figures made by Dr. Elizabeth Coward.*

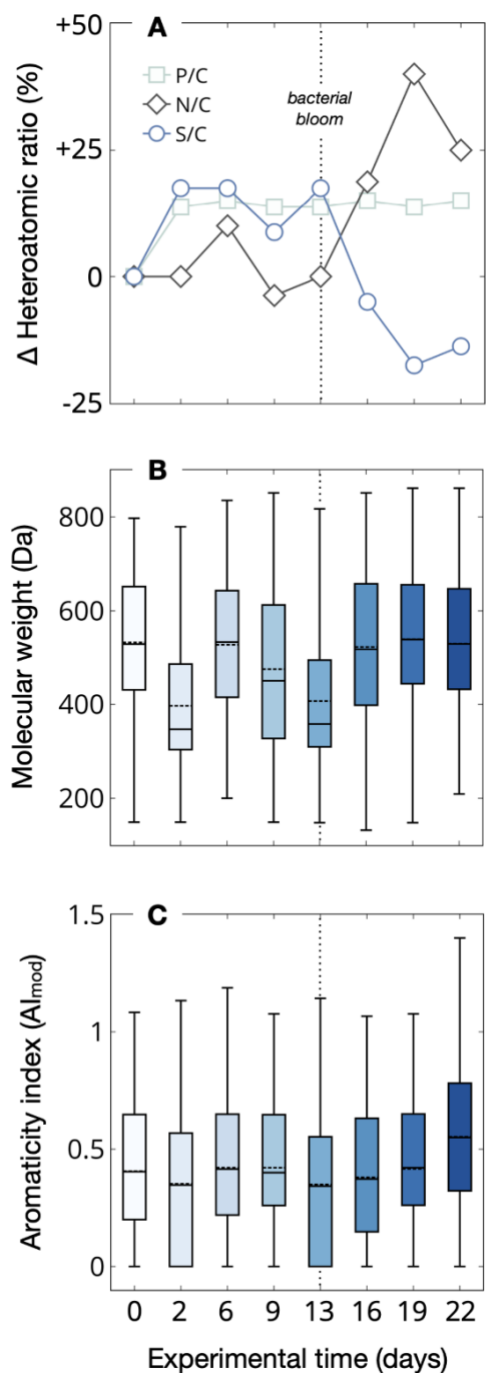


Figure 4.5. (A) Percent change in mean heteroatomic ratios of nitrogen (N), sulfur (S), and phosphorous (P) atoms per carbon (C) atom. (B) Molecular weight (Da) distributions, and (C) aromaticity index  $AI_{mod}$  distributions of all assigned formulae over experimental sampling time. Medians and means in box plots (B) and (C) are denoted by solid and dashed lines, respectively. *Figures made by Dr. Elizabeth Coward.*

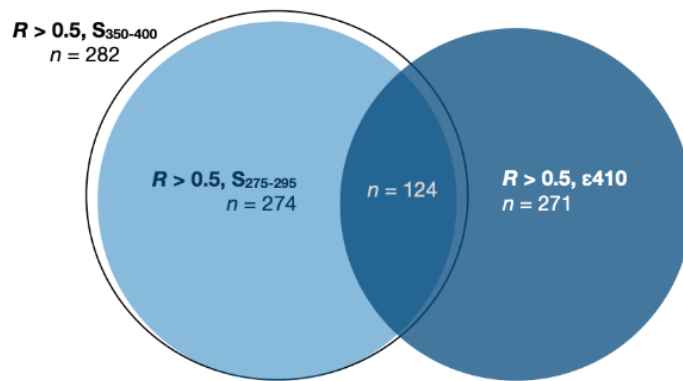


Figure 4.6. Changes in dissolved organic matter formulae parameters over experimental time. *Figures made by Dr. Elizabeth Coward.*

## 4.7 References

- (1) Hansell, D.; Carlson, C.; Repeta, D.; Schlitzer, R. Dissolved Organic Matter in the Ocean: A Controversy Stimulates New Insights. *Oceanography* **2009**, *22* (4), 202–211.
- (2) Sharpless, C. M.; Blough, N. V. The Importance of Charge-Transfer Interactions in Determining Chromophoric Dissolved Organic Matter (CDOM) Optical and Photochemical Properties. *Environ. Sci. Process. Impacts* **2014**, *16* (4), 654–671.
- (3) Nelson, N. B.; Siegel, D. A. The Global Distribution and Dynamics of Chromophoric Dissolved Organic Matter. *Ann. Rev. Mar. Sci.* **2013**, *5* (1), 447–476.
- (4) Bricaud, A.; Morel, A.; Prieur, L. Absorption by Dissolved Organic Matter of the Sea (Yellow Substance) in the UV and Visible Domains. *Limnol. Oceanogr.* **1981**, *26* (1), 43–53.
- (5) Hedges, J. I. Global Biogeochemical Cycles: Progress and Problems. *Mar. Chem.* **1992**, *39* (1–3), 67–93.
- (6) Maie, N.; Scully, N. M.; Pisani, O.; Jaffé, R. Composition of a Protein-like Fluorophore of Dissolved Organic Matter in Coastal Wetland and Estuarine Ecosystems. *Water Res.* **2007**, *41* (3), 563–570.
- (7) Qualls, R. G.; Haines, B. L. Geochemistry of Dissolved Organic Nutrients in Water Percolating through a Forest Ecosystem. *Soil Sci. Soc. Am. J.* **1991**, *55* (4), 1112–1123.
- (8) Rochelle-Newall, E. J.; Fisher, T. R. Chromophoric Dissolved Organic Matter and Dissolved Organic Carbon in Chesapeake Bay. *Mar. Chem.* **2002**, *77* (1), 23–41.
- (9) Tzortziou, M.; Neale, P. J.; Osburn, C. L.; Megonigal, J. P.; Maie, N.; Jaffé, R. Tidal Marshes as a Source of Optically and Chemically Distinctive Colored Dissolved Organic Matter in the Chesapeake Bay. *Limnol. Oceanogr.* **2008**, *53* (1), 148–159.
- (10) Mopper, K.; Kieber, D. J.; Stubbins, A. Marine Photochemistry of Organic Matter. In *Biogeochemistry of Marine Dissolved Organic Matter*; Elsevier, 2015; pp 389–450.
- (11) George, C.; Ammann, M.; D’Anna, B.; Donaldson, D. J.; Nizkorodov, S. A. Heterogeneous Photochemistry in the Atmosphere. *Chem. Rev.* **2015**, *115* (10), 4218–4258.
- (12) Stemmler, K.; Ammann, M.; Donders, C.; Kleffmann, J.; George, C. Photosensitized Reduction of Nitrogen Dioxide on Humic Acid as a Source of Nitrous Acid. *Nature* **2006**, *440* (7081), 195–198.
- (13) Mopper, K.; Stubbins, A.; Ritchie, J. D.; Bialk, H. M.; Hatcher, P. G. Advanced Instrumental Approaches for Characterization of Marine Dissolved Organic Matter:

- Extraction Techniques, Mass Spectrometry, and Nuclear Magnetic Resonance Spectroscopy. *Chem. Rev.* **2007**, *107* (2), 419–442.
- (14) Alves, M. R.; Sauer, J. S.; Prather, K. A.; Grassian, V. H.; Wilkins, C. L. Liquid Sampling-Atmospheric Pressure Glow Discharge Ionization as a Technique for the Characterization of Salt-Containing Organic Samples. *Anal. Chem.* **2020**, *92* (13), 8845–8851.
- (15) Repeta, D. J. Chemical Characterization and Cycling of Dissolved Organic Matter. In *Biogeochemistry of Marine Dissolved Organic Matter*; Elsevier, 2015; pp 21–63.
- (16) Wilson, R. M.; Tfaily, M. M. Advanced Molecular Techniques Provide New Rigorous Tools for Characterizing Organic Matter Quality in Complex Systems. *J. Geophys. Res. Biogeosciences* **2018**, *123* (6), 1790–1795.
- (17) Lam, B.; Simpson, A. J. Direct <sup>1</sup>H NMR Spectroscopy of Dissolved Organic Matter in Natural Waters. *Analyst* **2008**, *133* (2), 263–269.
- (18) Hertkorn, N.; Harir, M.; Cawley, K. M.; Schmitt-Kopplin, P.; Jaffé, R. Molecular Characterization of Dissolved Organic Matter from Subtropical Wetlands: A Comparative Study through the Analysis of Optical Properties, NMR and FTICR/MS. *Biogeosciences* **2016**, *13* (8), 2257–2277.
- (19) Hedges, J. I.; Hatcher, P. G.; Ertel, J. R.; Meyers-Schulte, K. J. A Comparison of Dissolved Humic Substances from Seawater with Amazon River Counterparts by <sup>13</sup>C-NMR Spectrometry. *Geochim. Cosmochim. Acta* **1992**, *56* (4), 1753–1757.
- (20) Kido Soule, M. C.; Longnecker, K.; Giovannoni, S. J.; Kujawinski, E. B. Impact of Instrument and Experiment Parameters on Reproducibility of Ultrahigh Resolution ESI FT-ICR Mass Spectra of Natural Organic Matter. *Org. Geochem.* **2010**, *41* (8), 725–733.
- (21) Pan, Q.; Zhuo, X.; He, C.; Zhang, Y.; Shi, Q. Validation and Evaluation of High-Resolution Orbitrap Mass Spectrometry on Molecular Characterization of Dissolved Organic Matter. *ACS Omega* **2020**, *5* (10), 5372–5379.
- (22) Nebbioso, A.; Piccolo, A. Molecular Characterization of Dissolved Organic Matter (DOM): A Critical Review. *Anal. Bioanal. Chem.* **2013**, *405* (1), 109–124.
- (23) Stabenau, E. R.; Zika, R. G. Correlation of the Absorption Coefficient with a Reduction in Mean Mass for Dissolved Organic Matter in Southwest Florida River Plumes. *Mar. Chem.* **2004**, *89* (1–4), 55–67.
- (24) Azam, F.; Malfatti, F. Microbial Structuring of Marine Ecosystems. *Nat. Rev. Microbiol.* **2007**, *5* (10), 782–791.
- (25) Pomeroy, L.; leB. Williams, P.; Azam, F.; Hobbie, J. The Microbial Loop. *Oceanography*



- 2007, 20 (2), 28–33.
- (26) Kinsey, J. D.; Corradino, G.; Ziervogel, K.; Schnetzer, A.; Osburn, C. L. Formation of Chromophoric Dissolved Organic Matter by Bacterial Degradation of Phytoplankton-Derived Aggregates. *Front. Mar. Sci.* **2018**, 4.
- (27) Shields, M. R.; Bianchi, T. S.; Osburn, C. L.; Kinsey, J. D.; Ziervogel, K.; Schnetzer, A.; Corradino, G. Linking Chromophoric Organic Matter Transformation with Biomarker Indices in a Marine Phytoplankton Growth and Degradation Experiment. *Mar. Chem.* **2019**, 214, 103665.
- (28) Wilhelm, S. W.; Suttle, C. A. Viruses and Nutrient Cycles in the Sea. *Bioscience* **1999**, 49 (10), 781–788.
- (29) Sauer, J. S.; Mayer, K. J.; Lee, C.; Alves, M. R.; Amiri, S.; Bahaveolos, C.; Barnes, E. B.; Crocker, D. R.; Dinasquet, J.; Garofalo, L. A.; et al. The Sea Spray Chemistry and Particle Evolution Study (SeaSCAPE): Overview and Experimental Methods. *Environ. Sci. Process. Impacts* **2021**.
- (30) Dittmar, T.; Koch, B.; Hertkorn, N.; Kattner, G. A Simple and Efficient Method for the Solid-Phase Extraction of Dissolved Organic Matter (SPE-DOM) from Seawater. *Limnol. Oceanogr. Methods* **2008**, 6 (6), 230–235.
- (31) Helms, J. R.; Stubbins, A.; Ritchie, J. D.; Minor, E. C.; Kieber, D. J.; Mopper, K. Absorption Spectral Slopes and Slope Ratios as Indicators of Molecular Weight, Source, and Photobleaching of Chromophoric Dissolved Organic Matter. *Limnol. Oceanogr.* **2008**, 53 (3), 955–969.
- (32) John, R. H.; Stubbins, A.; Ritchie, J. D.; Minor, E. C.; Kieber, D. J.; Mopper, K. Erratum: Absorption Spectral Slopes and Slope Ratios as Indicators of Molecular Weight, Source, and Photobleaching of Chromophoric Dissolved Organic Matter (Limnology and Oceanography 53 955-969). *Limnol. Oceanogr.* **2009**, 54 (3), 1023.
- (33) Twardowski, M. S.; Boss, E.; Sullivan, J. M.; Donaghay, P. L. Modeling the Spectral Shape of Absorption by Chromophoric Dissolved Organic Matter. *Mar. Chem.* **2004**, 89 (1–4), 69–88.
- (34) Coward, E. K.; Ohno, T.; Sparks, D. L. Direct Evidence for Temporal Molecular Fractionation of Dissolved Organic Matter at the Iron Oxyhydroxide Interface. *Environ. Sci. Technol.* **2019**, 53 (2), 642–650.
- (35) Ohno, T.; Ohno, P. E. Influence of Heteroatom Pre-Selection on the Molecular Formula Assignment of Soil Organic Matter Components Determined by Ultrahigh Resolution Mass Spectrometry. *Anal. Bioanal. Chem.* **2013**, 405 (10), 3299–3306.
- (36) Koch, B. P.; Dittmar, T. From Mass to Structure: An Aromaticity Index for High-Resolution Mass Data of Natural Organic Matter. *Rapid Commun. Mass Spectrom.* **2006**,

20 (5), 926–932.

- (37) Herzsprung, P.; Von Tümpling, W.; Hertkorn, N.; Harir, M.; Büttner, O.; Bravidor, J.; Friese, K.; Schmitt-Kopplin, P. Variations of DOM Quality in Inflows of a Drinking Water Reservoir: Linking of van Krevelen Diagrams with EEMF Spectra by Rank Correlation. *Environ. Sci. Technol.* **2012**, *46* (10), 5511–5518.
- (38) Helms, J. R.; Stubbins, A.; Perdue, E. M.; Green, N. W.; Chen, H.; Mopper, K. Photochemical Bleaching of Oceanic Dissolved Organic Matter and Its Effect on Absorption Spectral Slope and Fluorescence. *Mar. Chem.* **2013**, *155*, 81–91.
- (39) Wang, X.; Sultana, C. M.; Trueblood, J.; Hill, T. C. J.; Malfatti, F.; Lee, C.; Laskina, O.; Moore, K. A.; Beall, C. M.; McCluskey, C. S. Microbial Control of Sea Spray Aerosol Composition: A Tale of Two Blooms. *ACS Cent. Sci.* **2015**, *1* (3), 124–131.
- (40) Powers, L. C.; Del Vecchio, R.; Blough, N. V.; McDonald, N.; Schmitt-Kopplin, P.; Gonsior, M. Optical Properties and Photochemical Transformation of the Dissolved Organic Matter Released by Sargassum. *Front. Mar. Sci.* **2020**, *7* (November).
- (41) Röttgers, R.; Koch, B. P. Spectroscopic Detection of a Ubiquitous Dissolved Pigment Degradation Product in Subsurface Waters of the Global Ocean. *Biogeosciences* **2012**, *9* (7), 2585–2596.
- (42) Andrew, A. A.; Del Vecchio, R.; Subramaniam, A.; Blough, N. V. Chromophoric Dissolved Organic Matter (CDOM) in the Equatorial Atlantic Ocean: Optical Properties and Their Relation to CDOM Structure and Source. *Mar. Chem.* **2013**, *148*, 33–43.
- (43) Karimova, N. V.; Alves, M. R.; Luo, M.; Grassian, V.; Gerber, R. B. Toward a Microscopic Model of Light Absorbing Dissolved Organic Compounds in Aqueous Environments: Theoretical and Experimental Study. *Phys. Chem. Chem. Phys.* **2021**.
- (44) Seritti, A.; Morelli, E.; Nannicini, L.; Del Vecchio, R. Production of Hydrophobic Fluorescent Organic Matter by the Marine Diatom *Phaeodactylum Tricornutum*. *Chemosphere* **1994**, *28* (1), 117–129.
- (45) Stedmon, C. A.; Nelson, N. B. *The Optical Properties of DOM in the Ocean*, Second Edi.; Elsevier Inc., 2015.
- (46) Singh, S.; D'Sa, E. J.; Swenson, E. M. Chromophoric Dissolved Organic Matter (CDOM) Variability in Barataria Basin Using Excitation-Emission Matrix (EEM) Fluorescence and Parallel Factor Analysis (PARAFAC). *Sci. Total Environ.* **2010**, *408* (16), 3211–3222.
- (47) Nissenbaum, A.; Kaplan, I. R. Chemical and Isotopic Evidence for the in Situ Origin of Marine Humic Substances. *Limnol. Oceanogr.* **1972**, *17* (4), 570–582.
- (48) Kujawinski, E. B.; Longnecker, K.; Barott, K. L.; Weber, R. J. M.; Soule, M. C. K.

- Microbial Community Structure Affects Marine Dissolved Organic Matter Composition. *Front. Mar. Sci.* **2016**, *3* (APR), 1–15.
- (49) McNeill, K.; Canonica, S. Triplet State Dissolved Organic Matter in Aquatic Photochemistry: Reaction Mechanisms, Substrate Scope, and Photophysical Properties. *Environ. Sci. Process. Impacts* **2016**, *18* (11), 1381–1399.
- (50) Wang, M.; Carver, J. J.; Phelan, V. V.; Sanchez, L. M.; Garg, N.; Peng, Y.; Nguyen, D. D.; Watrous, J.; Kapon, C. A.; Luzzatto-Knaan, T. Sharing and Community Curation of Mass Spectrometry Data with Global Natural Products Social Molecular Networking. *Nat. Biotechnol.* **2016**, *34* (8), 828–837.
- (51) Ehrhardt, M.; Petrick, G. On the Sensitized Photo-Oxidation of Alkylbenzenes in Seawater. *Mar. Chem.* **1984**, *15* (1), 47–58.
- (52) Choudhry, G. G. Humic Substances. Structural Aspects, and Photophysical, Photochemical and Free Radical Characteristics. In *Handbook of Environmental Chemistry*; 1984; Vol. 1, pp 1–24.
- (53) Goldstone, J. V.; Voelker, B. M. Chemistry of Superoxide Radical in Seawater: CDOM Associated Sink of Superoxide in Coastal Waters. *Environ. Sci. Technol.* **2000**, *34* (6),
- (54) D'Ambrosio, M.; Santos, A. C.; Alejo-Armijo, A.; Parola, A. J.; Costa, P. M. Light-Mediated Toxicity of Porphyrin-Like Pigments from a Marine Polychaeta. *Mar. Drugs* **2020**, *18* (6), 1–14.
- (55) Dunlap, W. C.; Susic, M. Determination of Pteridines and Flavins in Seawater by Reverse-Phase, High-Performance Liquid Chromatography with Fluorometric Detection. *Mar. Chem.* **1985**, *17* (3), 185–198.
- (56) Dunlap, W. C.; Susic, M. Photochemical Decomposition Rates of Pteridines and Flavins in Seawater Exposed to Surface Solar Radiation. *Mar. Chem.* **1986**, *19* (2), 99–107.
- (57) Hernes, P. J.; Benner, R. Photochemical and Microbial Degradation of Dissolved Lignin Phenols: Implications for the Fate of Terrigenous Dissolved Organic Matter in Marine Environments. *J. Geophys. Res. Ocean.* **2003**, *108* (9).
- (58) Opsahl, S.; Benner, R. Photochemical Reactivity of Dissolved Lignin in River and Ocean Waters. *Limnol. Oceanogr.* **1998**, *43* (6), 1297–1304.
- (59) Hartmann, A.; Ganzera, M.; Karsten, U.; Skhirtladze, A.; Stuppner, H. Phytochemical and Analytical Characterization of Novel Sulfated Coumarins in the Marine Green Macroalga *Dasycladus Vermicularis* (Scopoli) Krasser. *Molecules* **2018**, *23* (11).
- (60) Martins, B. T.; Correia da Silva, M.; Pinto, M.; Cidade, H.; Kijjoo, A. Marine Natural Flavonoids: Chemistry and Biological Activities. *Nat. Prod. Res.* **2019**, *33* (22), 3260–

- 3272.
- (61) Blunt, J. W.; Copp, B. R.; Munro, M. H. G.; Northcote, P. T.; Prinsep, M. R. Marine Natural Products. *Nat. Prod. Rep.* **2010**, *27* (2), 165–237.
- (62) Medeiros, P. M.; Seidel, M.; Powers, L. C.; Dittmar, T.; Hansell, D. A.; Miller, W. L. Dissolved Organic Matter Composition and Photochemical Transformations in the Northern North Pacific Ocean. *Geophys. Res. Lett.* **2015**, *42* (3), 863–870.
- (63) Arakawa, N.; Aluwihare, L. I.; Simpson, A. J.; Soong, R.; Stephens, B. M.; Lane-Coplen, D. Carotenoids Are the Likely Precursor of a Significant Fraction of Marine Dissolved Organic Matter. *Sci. Adv.* **2017**, *3* (9), 1–12.
- (64) Arnold, W. A. One Electron Oxidation Potential as a Predictor of Rate Constants of N-Containing Compounds with Carbonate Radical and Triplet Excited State Organic Matter. *Environ. Sci. Process. Impacts* **2014**, *16* (4), 832–838.
- (65) Wang, X.; Dalton, E. Z.; Payne, Z. C.; Perrier, S.; Riva, M.; Raff, J. D.; George, C. Superoxide and Nitrous Acid Production from Nitrate Photolysis Is Enhanced by Dissolved Aliphatic Organic Matter. *Environ. Sci. Technol. Lett.* **2021**, *8* (1), 53–58.
- (66) Sharpless, C. M.; Blough, N. V. The Importance of Charge-Transfer Interactions in Determining Chromophoric Dissolved Organic Matter (CDOM) Optical and Photochemical Properties. *Environ. Sci. Process. Impacts* **2014**, *16* (4), 654–671.
- (67) Trueblood, J. V.; Alves, M. R.; Power, D.; Santander, M. V.; Cochran, R. E.; Prather, K. A.; Grassian, V. H. Shedding Light on Photosensitized Reactions within Marine-Relevant Organic Thin Films. *ACS Earth Sp. Chem.* **2019**, *3* (8), 1614–1623.
- (68) Shemesh, D.; Luo, M.; Grassian, V. H.; Gerber, R. B. Absorption Spectra of Pyruvic Acid in Water: Insights from Calculations for Small Hydrates and Comparison to Experiment. *Phys. Chem. Chem. Phys.* **2020**, *22* (22), 12658–12670.
- (69) Karimova, N. V.; Luo, M.; Grassian, V. H.; Benny Gerber, R. Absorption Spectra of Benzoic Acid in Water at Different PH and in the Presence of Salts: Insights from the Integration of Experimental Data and Theoretical Cluster Models. *Phys. Chem. Chem. Phys.* **2020**, *22* (9), 5046–5056.
- (70) González Palacios, L.; Corral Arroyo, P.; Aregahegn, K. Z.; Steimer, S. S.; Bartels-Rausch, T.; Nozière, B.; George, C.; Ammann, M.; Volkamer, R. Heterogeneous Photochemistry of Imidazole-2-Carboxaldehyde: HO<sub>2</sub> Radical Formation and Aerosol Growth. *Atmos. Chem. Phys.* **2016**, *16* (18), 11823–11836.
- (71) McKay, G.; Korak, J. A.; Erickson, P. R.; Latch, D. E.; McNeill, K.; Rosario-Ortiz, F. L. The Case Against Charge Transfer Interactions in Dissolved Organic Matter Photophysics. *Environ. Sci. Technol.* **2018**, *52* (2), 406–414.

- (72) McKay, G. Emerging Investigator Series: Critical Review of Photophysical Models for the Optical and Photochemical Properties of Dissolved Organic Matter. *Environ. Sci. Process. Impacts* **2020**, 22 (5), 1139–1165.

## **Chapter 5: Large-Scale Collaborative Effort in Understanding the Properties, Composition, and Reactivity of Marine Dissolved Organic Matter Collected during SeaSCAPE 2019**

### **5.1 Overview**

With the aim to study a wide variety of marine relevant climate processes such as the production and chemistry of seas spray aerosol (SSA) and secondary marine aerosol (SMA), away from constant anthropogenic inputs, a large collaborative mesocosm experiment was carried out in the Summer of 2019. The 2019 Sea Spray Chemistry and Particle Evolution (SeaSCAPE) study utilized a 11,800-liter wave channel that was modified for atmospheric measurements. In this chapter, the studies and collaborations that resulted from the collection of marine dissolved organic matter (m-DOM) will be highlighted. Collected samples from this experiment were sent to twelve research groups across eight institutions, mainly within the NSF Center for Aerosol Impacts on the Chemistry of the Environment (NSF-CAICE). As m-DOM is not yet commercially available, having a central bulk sample utilized across multiple different experiments has developed into a large-scale collaboration focused on understanding four core aspects: characterization, reactivity, properties, and the identification of model systems. More specifically, the roles of photochemistry, oxidation, composition, and properties in aerosols are explored in-depth. Additionally, this chapter will also venture into the presence and persistence of anthropogenic dissolved organic matter compounds such as benzothiazoles. Their transfer into the gas and particle phase as well as their oxidation products and tendency to form secondary aerosols will be investigated.

## 5.2 Introduction

Ocean-atmosphere studies have been a central field of research in understanding the Earth's climate. As sea spray aerosol (SSA) represent the largest source ( $3\text{-}30 \text{ Pg yr}^{-1}$ ) of particles in the atmosphere by mass, the ocean has a clear and major role in the climate.<sup>1</sup> The majority of literature regarding the study of marine aerosols have focused mainly on freshly produced SSA via field studies, bubbler frits, and ocean-atmosphere simulators. However, recent studies have shown that reacted (e.g., aged) SSA and secondary marine aerosol (SMA) formed from oxidized gas-phase organics can have very different chemical and physical properties and thus a different impact on climate processes such as cloud formation. At the Scripps Institute of Oceanography, a newly constructed, 33 meter long, wave channel was used in the 2-month long SeaSCAPE 2019 campaign focusing on the measurement of produced marine aerosols and development of the biology and chemical composition of the seawater. Around 11,800 liters of seawater was collected from Scripps Pier, La Jolla, filtered down to 50 microns, and spiked with nutrients to produce a microbial bloom. A magnetically controlled paddle produced waves that then crashed onto a submerged fiberglass ramp or "beach". The aerosols and gases produced from these breaking waves were collected and sampled for both online and offline techniques.

Photochemistry in the marine environment, especially that of the abiotic nature, has recently become a focus in the ocean-atmosphere community. Two major pathways can be considered when studying environmental photochemistry: direct and indirect. A well-known example of direct photochemistry in the atmosphere is the photodissociation reaction of oxygen ( $\text{O}_2$ ) and ozone ( $\text{O}_3$ ). Direct photochemistry also occurs in the ocean in the aqueous phase, such as where nitrite ( $\text{NO}_2^-$ ) is photolyzed to primarily produce NO and OH free radicals.<sup>2</sup> Indirect photochemistry occurs when a light absorbing component, the photosensitizer, absorbs a photon

and transfers the energy to a neighboring molecule providing the necessary energy to perform reactions. A more in-depth explanation on this process can be found in Chapter 3. Likewise, in the aforementioned chapter, m-CDOM is a known photosensitizer with a largely unknown composition.

### **5.3 Collaborative Efforts in the Use of a Central Standard of Marine-DOM**

Explained in much greater detail in Chapter 2, a ‘large’ amount of m-DOM was extracted from about 2000 liters of seawater on the last day of the SeaSCAPE campaign. This m-DOM, totaling around 1.7 grams, was sent to twelve research groups mostly within NSF-CAICE. Shown in Figure 5.1, a summary of the groups involved, and research aims are outlined. Among the many groups the m-DOM was sent to, the interests in using the samples can be divided into four major groups: characterization, properties, reactivity, and the identification of possible model systems. The goal of this collaborative project, other than the study of m-DOM itself, was to facilitate a combined effort between groups and ultimately, lead to high impact publication. An in-depth characterization of the sample m-DOM and unique m-CDOM molecules, using high resolution mass spectrometry, can be found in Chapter 4.



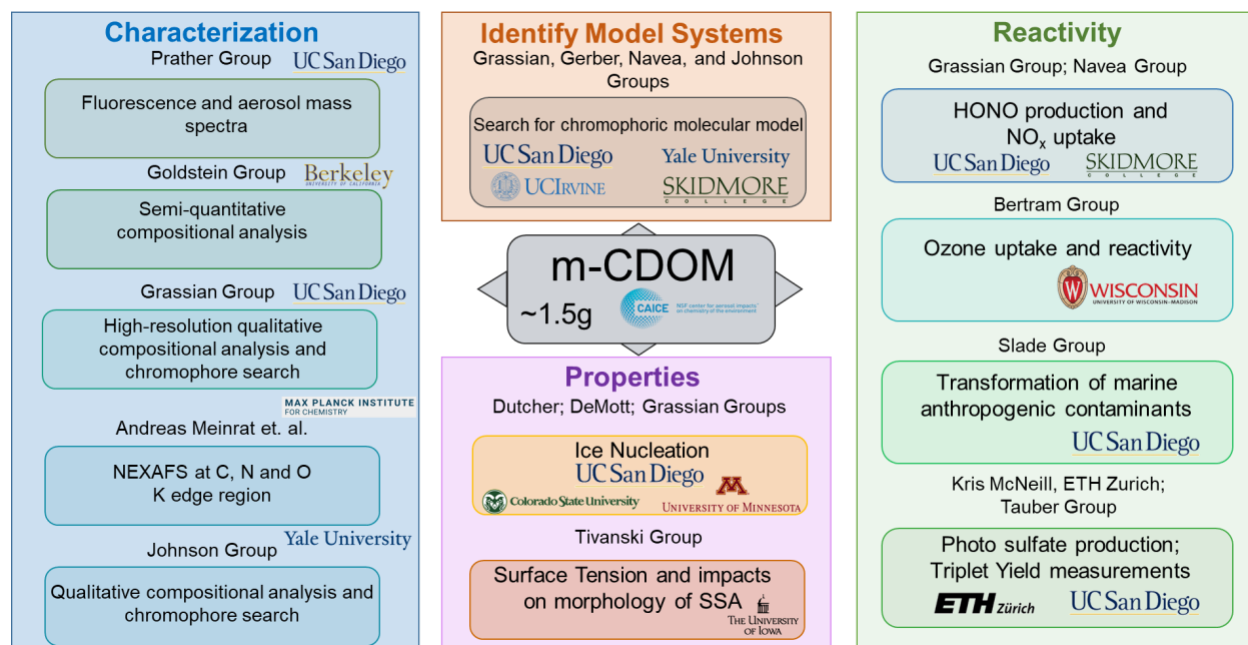


Figure 5.1. Summary of the collaborative research groups using the collect m-DOM/m-CDOM sample.

The identification of model systems for m-CDOM is particularly interesting; as currently, all known molecular models for photoactive DOM have been derived from terrestrially related publications rather than marine. In Chapter 3, it was shown that this is likely not the best method for studying marine relevant DOM and CDOM at the molecular scale. Efforts being made at this scale include the work of Karimova and coworkers with attempts to model the UV-VIS spectrum of m-CDOM using molecular dynamics.<sup>3</sup> Simple models that have been extensively tested within this collaboration thus far include pyruvic acid, benzoic acid, and 4-benzoylbenzoic acid.<sup>4-7</sup> Additionally, many groups have been interested in the organics at the ocean surface and their impacts on atmospherically relevant oxidants like ozone and NO<sub>x</sub>. Interestingly, a newer type of marine DOM has also garnered attention. Anthropogenic dissolved organic carbon (ADOC) in the ocean originates from man-made compounds that infiltrate the water column through dumping, runoff, etc. Such compounds were found in the collected m-DOM samples, unsurprisingly, since it was extracted from coastal seawater. How these ADOC components

impact the overall chemistry and composition of m-DOM is currently a growing but small field of research. In the next section, a particular set of molecules will be focused on in respect to this collaborative effort.

## **5.4 Benzothiazoles in the Coastal Marine Environment**

Coastal oceans are often enriched with organic species from both biogenic and anthropogenic sources. Biogenic sources include phytoplankton, which convert CO<sub>2</sub> to ocean biomass that is then transformed by the microbial loop.<sup>8,9</sup> Direct anthropogenic sources of marine organics in seawater include wastewater discharge and urban runoff (often enriched with personal care products), trash, and shipping pollution.<sup>10,11,12</sup> Phytoplankton blooms occur naturally, but also can be induced by anthropogenic discharges of fertilizer enriched runoff, and can be enhanced by climate change induced perturbations to ocean temperatures and chemistry.<sup>13,14,15,16</sup> Ocean-derived organic species can be transferred from the ocean to the atmosphere through two major mechanisms, both of which can influence atmospheric chemistry over the ocean. The first of these produces sea spray aerosol (SSA) from bubble bursting and wind shear at the surface.<sup>17</sup> The second method involves the emission of volatile organic compounds (VOC)s from the ocean surface, either through volatilization or interfacial reactions producing volatile products.<sup>18,19,20</sup>

The composition and properties of organic material emitted from the ocean are important areas of atmospheric research, as they influence marine atmospheric chemistry and public health. Salt and organics have different cloud and ice nucleation properties, meaning that organic enrichment of SSA is important for climate.<sup>21,22,23,24</sup> Marine VOCs oxidize in the atmosphere, where they can form secondary marine aerosols (SMA).<sup>25</sup> Recent laboratory and field studies have suggested that SMA may play a significant role in cloud formation over the ocean,<sup>26,27</sup> making the emission and oxidation processes of marine volatile organics a critical area of

atmospheric chemistry research. Organic enriched marine aerosols are also a growing area of concern in public health, as they can expose coastal communities to marine toxins and pollutants, including biogenic toxins from harmful algal blooms, pesticides, and phthalates.<sup>28,29,30</sup>

Production of plasticizers, pharmaceuticals, pesticides, and more, over the course of the last century, has led to a portion of dissolved organic matter (DOM) in marine ecosystems being classified as anthropogenic dissolved organic carbon (ADOC).<sup>31</sup> The 100,000+ commercialized synthetic compounds produced by humans have been continually increasing in both number and concentration in many environments.<sup>32,33</sup> These human-produced compounds tend to be hydrophobic, and for the most part, have completely unknown breakdown by-products, toxicities, and fates in the environment.<sup>34,35</sup> Though there is no study to our knowledge that has reported total anthropogenic DOM concentrations in coastal waters near populated areas, it is expected that this number will be greater than the < 1 uM, or 0.05 to 1% of total DOM, reported for water collected from the open ocean due to the more concentrated coastal inputs and sources.<sup>31,36</sup> The hydrophobic fraction of these species will be highly concentrated at the surface of the ocean, joining biogenically formed molecules in a 1 to 100 μm thick region known as the sea surface microlayer (SSML).<sup>37</sup> Many studies have shown that the ocean surface is a source of organic material for both SSA and SMA, significantly contributing to the overall chemistry and properties of these aerosols.<sup>22,38,20,39</sup>

Benzothiazoles are a class of anthropogenic pollutants that have been previously reported and in a variety of freshwater and coastal aquatic environments, including the southern California coast,<sup>40,41,42,43,44,45</sup> but they are also produced biogenically from select marine microbiological species.<sup>46,47</sup> Benzothiazole (hereafter BT) (C<sub>7</sub>H<sub>5</sub>NS) is an aromatic heterocyclic organic compound containing both sulfur and nitrogen. Benzothiazoles are here defined as

compounds containing a benzothiazole moiety. Benzothiazoles are high production volume chemicals used in a wide range of industrial and consumer products, with significant sources including rubber production, leather and paper production, antifreeze, herbicides, textiles, and plastics.<sup>40</sup> They are found in both urban runoff and wastewater, with urban runoff frequently the more concentrated of the two source groups.<sup>48</sup> A review of the ranges of measured concentrations of dissolved BT and 2-(Methylthio)benzothiazole in stormwater runoff and wastewater effluent at sites along the southern California coast (ranging from 0.05 to 0.5  $\mu\text{g/L}$  for BT and 0.04 to 0.3  $\mu\text{g/L}$  for 2-(Methylthio)benzothiazole) can be found in Zeng et al., 2004.<sup>45</sup> Benzothiazoles have been observed in the dissolved-phase in a variety of coastal marine settings and used as tracers of wastewater discharge.<sup>43,45,42,41</sup> This compound class is a growing area of concern in both marine ecosystem and public health; benzothiazole derivatives from rubber leachates are toxins hazardous to marine microbiology, and various benzothiazoles are human dermal sensitizers, endocrine disruptors, carcinogens, and genotoxins.<sup>40,49,50,51</sup>

In this chapter, we investigate the transfer of benzothiazoles from coastal water into the atmosphere through a controlled mesocosm study. While dissolved benzothiazoles have been reported in the water in a variety of coastal regions, we report observations of benzothiazoles in sea spray aerosols and emitted VOCs, showing for the first time that polluted coastal oceans likely emit these chemicals to the atmosphere. Furthermore, we explore the atmospheric oxidation and aerosol formation potential of gas-phase BT, which has implications for air quality in both polluted coastal regions and urban or industrial centers in which benzothiazoles are most concentrated.

#### **5.4.1 Experimental Methods**

*Experimental Campaign, Sample Collection, and Online Analysis*

The results from this study derive primarily from Sea Spray Chemistry And Particle Evolution (SeaSCAPE) 2019, a collaborative mesocosm experiment described in Sauer, Mayer, and Lee et al., 2021.<sup>52</sup> Coastal water (12,000 L) from Ellen Browning Scripps Memorial Pier (hereafter Scripps Pier) in La Jolla, California was transported into an indoor wave chamber facility (hereafter referred to as the wave channel), in which mechanically generated waves break on an artificial beach to create realistic sea spray aerosols. The natural coastal water was amended with nutrients to initiate an algal bloom of the naturally existing phytoplankton species, including three bloom experiments, replicating methodology described in Wang et al., 2015.<sup>53</sup> Water from the wave channel was diverted through an inert glass and Teflon chamber forming an isolated sampling vessel (ISV), allowing analysis of gas-phase marine emissions. This analysis focuses on the third algal bloom experiment, which lasted 20 days from July 24th to August 12th, 2019 and is described in detail in Sauer, Mayer, and Lee et al., 2021.<sup>52</sup>

Periodically over the course of the bloom, water from the SeaSCAPE channel was collected for offline analysis of headspace gasses (described below) and of extracted DOM chemical composition (also described below). One water sample directly from Scripps Pier was collected on July 23<sup>rd</sup> for DOM extraction and analysis of dissolved analytes under ambient conditions. Submicron aerosol samples from the channel were collected on quartz fiber filters (Pallflex Tissuequartz) using a custom designed automated sequential sampler. Additional sample collection and storage details can be found in Supporting Information (SI). ISV VOCs were collected on custom triple bed sorbent tubes (Camsco). 2 L samples were collected every 2-3 days during the early stages of the bloom and 1-2 times per day during peak biological activity. Sorbent tube material and sampling details can be found in SI. VOCs both within the ISV and in the channel were additionally measured by Vocus proton-transfer-reaction time-of-

flight mass spectrometer (Vocus PTR-TOF by Aerodyne/Tofwerk).<sup>52</sup> Following the conclusion of SeaSCAPE, the Vocus was relocated to the end of the Scripps Pier for ambient coastal VOC sampling. A full description of Scripps Pier VOC sampling can be found in SI.

Collection and extraction of marine DOM was performed using solid-phase extraction (SPE) by PPL resin (Bond Elut, Agilent), following methods previously characterized in Dittmar et al., 2008 and described in detail in SI.<sup>54</sup>

### *Offline Analysis*

A high resolution Orbitrap spectrometer equipped with a modified Atmospheric Pressure Chemical Ionization source (APCI-Orbitrap, ThermoFisher) was used to detect VOCs in the headspace of collected water during the SeaSCAPE campaign in a method adapted from Roveretto and coworkers in 2019.<sup>55</sup> Operational details can be found in SI.

Aerosol filters, DOM, and VOC sorbent tubes were all analyzed by thermal desorption two-dimensional gas chromatography coupled with electron ionization time of flight mass spectrometry (TD-GCxGC-ToF-MS) on two separate instruments covering differing volatility ranges, with DOM and aerosol samples analyzed on GCxGC A, while VOC sorbent tubes were analyzed on GCxGC B (details in SI). DOM and aerosol samples were normalized by internal standard and derivatized to enhance recovery of polar organics. TD-GCxGC methodology is described in detail in Worton et al. 2017, and details specific to this analysis can be found in SI.<sup>56</sup>

From SeaSCAPE samples, 754 unique aerosol organics and 991 unique DOM organics were compiled into libraries of mass spectra and retention indices (internal standard normalized position in the volatility dimension) were catalogued. Of these unique organic species, 12 SSA organics and 6 DOM organics were identified as benzothiazoles based on matches and similarities to authentic standards and species catalogues in the NIST-14 mass spectral database

according to 4 classes of identification certainty (see Table 1). Each observed benzothiazole was assigned to a benzothiazole external standard chemical proxy for quantification based on exact match or chemical similarity and proximity in GCxGC space. Proxy assignments and additional details can be found in SI.

### *Benzothiazole Oxidation Study*

To complement the mesocosm study and better understand the atmospheric fate of gas-phase BT, we used a Potential Aerosol Mass Oxidation Flow Reactor (PAM-OFR) in a separate laboratory oxidation study to produce BT oxidation products. PAM-OFR operation and calibration details can be found in SI. BT was introduced into the PAM-OFR through two methods; in the first, liquid BT dissolved in a methanol carrier was introduced in a plug injection experiment at a constant exposure setting. In the second, a BT permeation tube continuously introduced gas-phase BT at different OH concentrations (2.9, 3.5, and 4.9 days equivalent aging). Particle formation and size distributions, SO<sub>2</sub> production, and HSO<sub>4</sub><sup>-</sup> production from the BT oxidation experiments were all monitored, the details of which can be found in SI.

Reported herein we show that BT and benzothiazole-moiety compounds are not just present in sea spray aerosols but also show an ability to form secondary aerosols using an oxidative flow reactor to simulate photochemical aging.

## **5.4.2 Results and Discussion**

### *Gas-Phase Benzothiazole Observations*

In the early stages of the SeaSCAPE experiment, a significant and unexpected peak was observed to correspond to C<sub>7</sub>H<sub>5</sub>NSH<sup>+</sup> (BT) by APCI-Orbitrap headspace VOC analysis – as shown in Figure X. Gas-phase BT and its isomeric identity was confirmed using the Orbitrap's

tandem mass spectrometry capabilities and the clear observation of the benzene and cyclic ring (containing the nitrogen and sulfur) fragments. This peak's identity was later confirmed and quantified by offline TD-GCxGC-ToF-MS analysis of sorbent tube samples collected from the SeaSCAPE ISV (14 ev and 70 ev EI spectra illustrated in SI Figure S1). Time resolved measurements of the ion corresponding to gas-phase benzothiazole were obtained by the Vocus throughout SeaSCAPE. A quantitative comparison of GCxGC and Vocus benzothiazole and summed monoterpene ISV measurements is in SI (Figure S3); while absolute quantities measured by each instrument differ, variability over the SeaSCAPE bloom and relative abundances of significant observed gases agree, with  $R^2$  of 0.91 and 0.98 for benzothiazole and summed monoterpenes respectively.

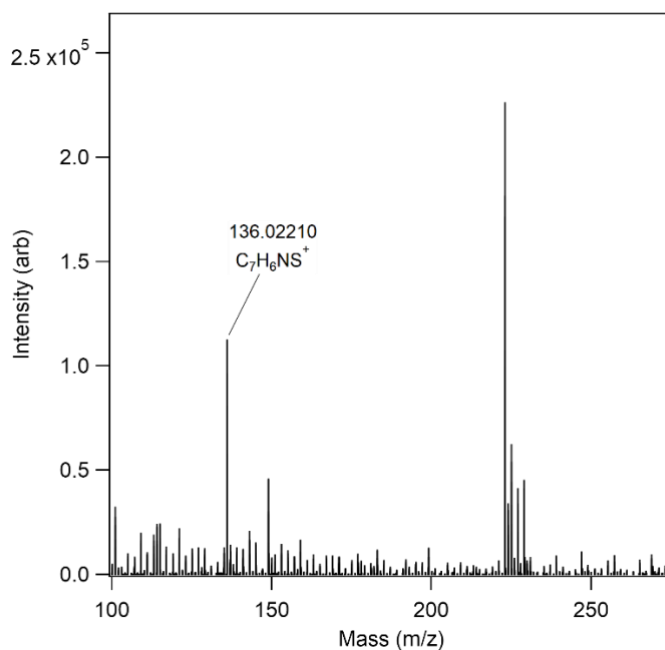


Figure 5.2. High resolution mass spectra of the VOCs from bloom water using APCI.

Gas-phase benzothiazole has been reported in atmospheric measurements in the contexts of freshly shredded rubber,<sup>40</sup> urban traffic, and coal burning in a region with plastic production,<sup>57</sup> but emissions of gas-phase benzothiazole from coastal waters are, to our knowledge, a novel



finding. As benzothiazole is a common anthropogenic contaminant that could potentially be added if the water were mishandled, we confirmed the presence of benzothiazoles in the collected coastal water absent perturbations from transport into the SeaSCAPE wave channel. Benzothiazole was consistently found in all monitored phases (dissolved, aerosol, and gas) (Table 5.1; Figure 5.3), and dissolved-phase concentrations did not increase between the first sample (collected directly at Scripps Pier) and the next DOM sample, collected from the channel two days following transport. Additionally, the ion corresponding to gas-phase BT was observed by the Vocus PTR-MS at the end of Scripps Pier directly following the SeaSCAPE experimental campaign, confirming that gas-phase BT is present in the local coastal marine atmosphere. End-of-pier BT concentrations averaged 2.5 ppt (compared to a detection limit of 0.5 ppt for a 10 s averaging time, averaged over the entire ~1 month measurement period), and SeaSCAPE ISV concentrations (as quantified by GCxGC) averaged 53 ppt. Given the elevated water temperature, enclosed conditions, and low gas-phase flow rate of the SeaSCAPE ISV (described in Sauer, Mayer, and Lee et al., 2021), absolute gas-phase ISV concentrations exceeding ambient concentrations at the end of the pier is indicative of emissions to the gas-phase.<sup>52</sup>

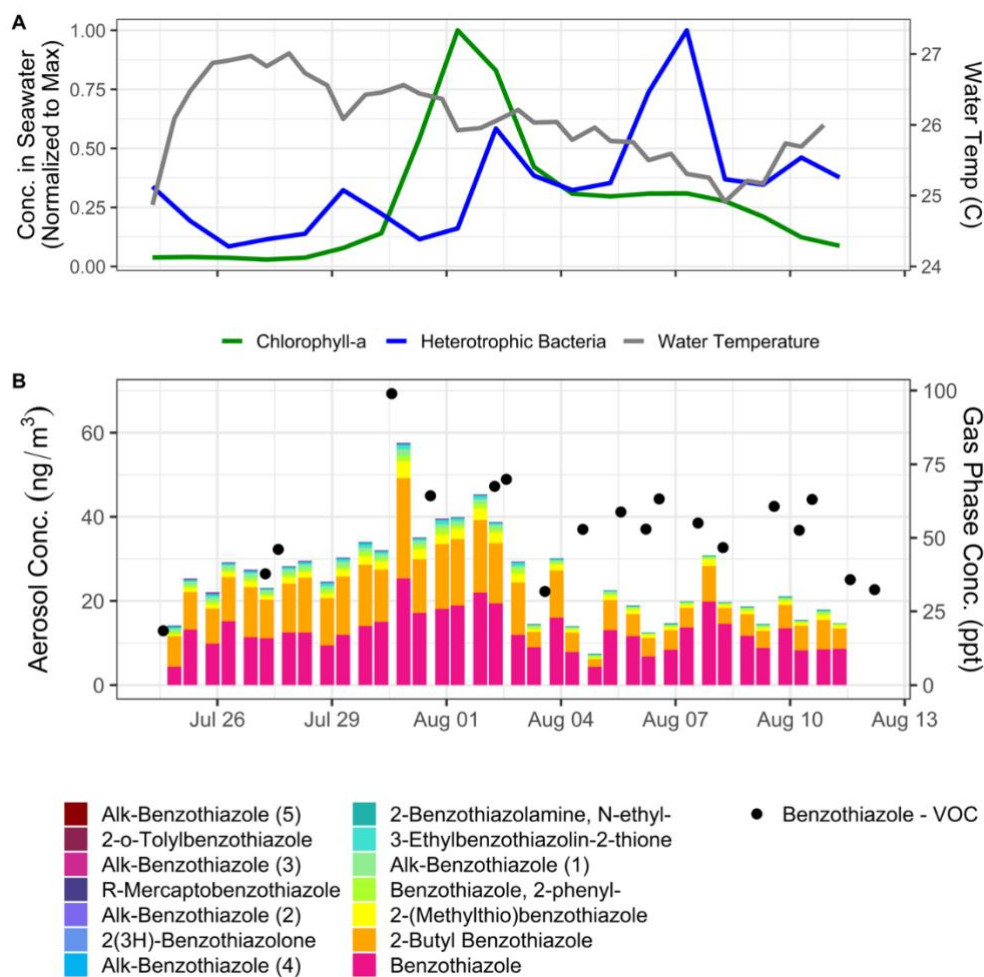


Figure 5.3. Time series of biological activity indicators and water temperature (A) and atmospheric benzothiazoles (B) at SeaSCAPE 2019 bloom 3 experiment. Atmospheric benzothiazole concentrations are differentiated into gas phase BT from the dome (black circles) and submicron nascent sea spray aerosol phase benzothiazoles from the wave chamber (colored bars). Detailed discussion of uncertainties can be found in supplemental information. *Data and figures by Emily Barnes-Franklin.*

Previously reported Henry's law constants for BT ( $K_H$ , estimated from vapor pressure and solubility in Reddy et al 1997, predicted from structure through various methods as reported in Sander 2015, and predicted from structure based on HENRYWIN v. 3.10, EPA EPI Suite) range from  $1.5 \times 10^{-5}$  to  $2.6 \times 10^{-4}$  (dimensionless gas over liquid, converted assuming 25 °C).<sup>58,59</sup> Under the aqueous concentration ( $0.29 \mu\text{g/L}$  at day 1 sampling time, as shown in Table 1) and temperature conditions observed at SeaSCAPE, this would imply a maximum equilibrium gas concentration of BT between 0.7 and 12 ppt, a factor of 75-4.4 below the average concentrations

observed in the ISV (53 ppt). A simplified partitioning experiment using benzothiazole and reference species dissolved in simplified simulated sea water in concentrations mirroring those identified in the SeaSCAPE DOM (described in detail in SI) did not detect benzothiazole above a detection limit of 10 ppt, supporting the conclusion that observed gas-phase concentrations of benzothiazole in the SeaSCAPE ISV cannot be adequately explained by ideal air water partitioning governed by Henry's law. One plausible explanation for this phenomenon may be that benzothiazole concentrates in the SSML (which would not be present in the synthetic sea water), which would enable higher volatilization from the concentrated surface layer compared to the dilute bulk, although it should be noted that the SSML has been demonstrated to more typically depress rather than enhance sea-air gas exchange, particularly for soluble gases.<sup>39,18</sup> It should also be noted that the lowest reported Henry's law constant of BT, that reported by HENRYWIN v. 3.10, EPA EPI Suite, is the most commonly referenced value across popular chemical information repositories (such as PubChem and ChemSpider) and has been used to assume negligible volatilization of benzothiazole from organic rich aquatic systems (wastewater), rendering this finding of elevated benzothiazole emissions from real organic-rich aquatic systems particularly important.<sup>60</sup>

#### *Aerosol and DOM Benzothiazole Observations and Comparisons*

In addition to BT, a suite of larger compounds containing a benzothiazole moiety were observed in both the aerosol and dissolved phases (Table 5.1). BT accounts for 50% of the total mean benzothiazole carbon pool in the aerosol phase and is the second most significant contributor to dissolved benzothiazoles at 43% of the mean DOM benzothiazole carbon pool. DOM BT concentrations measured directly at the pier ( $0.29 \pm 0.15$  ug/L), reported in Table 5.1, fall within reported ranges of observed BT in freshwater aquatic environments along the

southern California coast, which range from 0.05 to 0.5  $\mu\text{g/L}$ .<sup>45</sup> 2-(Methylthio)benzothiazole, a commonly reported tracer species for benzothiazoles originating from waste water or runoff,<sup>45,48</sup> is the most abundant benzothiazole species observed in the dissolved phase at 47% of mean DOM benzothiazole carbon pool. Butyl-benzothiazole, a species not previously reported in environmental measurements and present at near detection limit levels in the dissolved phase, contributes the second highest fraction of the aerosol benzothiazole carbon pool (37%), while 2-(Methylthio)benzothiazole contributes the third highest fraction at 6%.

Table 5.1. Identities, solubilities, and concentrations of benzothiazoles observed at SeaSCAPE. Aerosol phase concentrations are reported as an average and standard deviation of concentrations over the full experimental campaign, while dissolved phase concentrations are reported from the initial pre-experiment sample for comparison to other ambient sampling measurements of benzothiazoles. BQL indicates a species detected but present at below quantification limit levels.

Compound Identity	Solubility (mg/L)	Aerosol-Phase Mean Concentration [s.d.] (ng/m <sup>3</sup> )	DOM-Phase Concentration- 7/23 Ambient Sample ( $\mu\text{g/L}$ )
Benzothiazole <sup>A</sup>	1684	13 [4.7]	.29
Phenyl Benzothiazole <sup>A†</sup>	8.804	.64 [.30]	.0093
2-(Methylthio) benzothiazole <sup>A</sup>	66.61	1.4 [.77]	.96
Butyl Benzothiazole <sup>C</sup>	12.8	9.2 [4.8]	.017
Alk-Benzothiazole (1) <sup>B</sup>	12.8 <sup>1</sup>	.59 [.44]	
Alk-Benzothiazole (2) <sup>B</sup>	12.8 <sup>1</sup>	.032 [.033]	
Alk-Benzothiazole (3) <sup>B</sup>	12.8 <sup>1</sup>	.028 [.031]	
Alk-Benzothiazole (4) <sup>B</sup>	12.8 <sup>1</sup>	.045 [.043]	
Alk-Benzothiazole (5) <sup>B</sup>	12.8 <sup>1</sup>	.0067 [.0071]	
2-o-Tolylbenzothiazole <sup>C</sup>	4.81	.012 [.0088]	
3-Methyl-3H-benzothiazol-2-one <sup>C</sup>	1319		.31
3-Ethylbenzothiazolin-2-thione <sup>D</sup>		.32 [.26]	
N-Ethyl-2-Benzothiazoleamine <sup>D</sup>	142.2 <sup>2</sup>	.17 [.043]	
R-Mercaptobenzothiazole <sup>E</sup>	0.05096 <sup>2</sup>	.030 [.021]	
R- 2(3H)-Benzothiazolone <sup>D</sup>	2354 <sup>2</sup>	.032 [.039]	.016

<sup>a</sup> A: Isomer specific identification confirmed via authentic standard

<sup>b</sup> B: Series of alkyl benzothiazoles, identified via high (>750) match factor with spectrum of butylbenzothiazole and location in GCxGC space. Based on Kovats indices, likely C4-C7 straight and branched chain alkyl benzothiazoles

<sup>c</sup> C: Identified via high (>800) match factor with NIST14 mass spectral database entry along with Kovats index matches from previous published isolation where available

<sup>d</sup> D: Classified as benzothiazole due to relatively high (>700, <800) NIST match factor with named benzothiazole or by high match factor but Kovats index disagreement; novel compound without published mass spectra, tentatively identified as benzothiazole due to mass spectral indicators.

<sup>e</sup> E: Identity unknown, but based on mass spectrum assigned identity of R-mercaptobenzothiazole, with R an unknown group likely containing heteroatom(s).

<sup>f</sup> † Note that there are two distinct speciations of phenyl benzothiazoles observed between the two phases - 2-phenyl benzothiazole is observed in the aerosol phase, while an undetermined alternate phenyl benzothiazole isomer is observed in the dissolved phase.

<sup>1</sup> 1. No predicted or experimental solubility values for C5+ benzothiazoles, therefore assigned solubility of butyl benzothiazole

<sup>2</sup> 2. Note that the exact identities of these species are unknown, but that the solubilities are those of the identified chemically similar benzothiazoles named in column 1

The time series of gas and aerosol-phase benzothiazoles provide valuable insights into likely sources and transfer processes governing marine benzothiazole emissions (Figure 5.3). Prior to August 5<sup>th</sup>, a key biological transition period between peak chlorophyll and peak heterotrophic bacteria during which many key biogenic gases peak (as illustrated in SI Figure S2), gas and aerosol-phase BT are highly correlated ( $R^2 = 0.78$ ). In both phases, BT begins relatively low before increasing (by a factor of 5 in the gas phase and a factor of 3 in the aerosol phase) to a peak on July 30<sup>th</sup>, after which it declines, back to initial concentrations for the aerosol phase and to approximately double initial concentrations in the gas phase. There is no clear temperature, biological, or perturbation-based explanation for the July 30<sup>th</sup> peak, but in the gas phase it is observed for BT across all instruments and sampling strategies (GCxGC, Vocus PTR-ToF, and APCI-Opbitrap) and is common to an array of anthropogenic gases, as illustrated in SI Figure S2. After August 5<sup>th</sup> however, the BT traces of the two phases are loosely anticorrelated with an  $R^2$  of 0.11. As previously noted, the composition and thickness of the sea surface microlayer has been observed, modeled, and demonstrated to play an important role in the transfer of marine gases,<sup>18,39</sup> and given the gas-phase evidence for significant organic transformation around August 5<sup>th</sup>, a significant change in SSML characteristics influencing BT partitioning could at least partially explain the lack of correlation over the second half of the bloom.

Although there are some similarities between the temporal variability of benzothiazoles and biological indicators (specifically chlorophyll-a concentrations in the bulk water), the time series of both gas and aerosol-phase benzothiazoles are much more similar to anthropogenic

species than to any known biogenic products. In the aerosol phase, the total benzothiazole carbon pool time series is strongly correlated across the entire bloom ( $R^2 = 0.85$ , see SI Figure S7) with that of tetradecamethyl-cycloheptasiloxane (more commonly known as D7), an anthropogenic species attributable to personal care products,<sup>61</sup> wastewater,<sup>62</sup> and sewage, and also observed to bioaccumulate in marine ecosystems.<sup>63</sup> In the gas phase, BT also displays similar temporal dynamics to anthropogenic species (SI Figure S2), specifically benzophenone (a common sunscreen and personal care product component)<sup>64</sup> and naphthalene (a polycyclic aromatic hydrocarbon (PAH), previously identified as a coastal marine contaminant off the Southern California coast and likely originating from some combination of petroleum and combustion sources).<sup>11</sup> While the correlations between BT and benzophenone and naphthalene are not strong ( $R^2 = 0.25$  and  $0.35$  respectively), they are far stronger than the correlations with any of the known biogenic gases; the  $R^2$  of the correlations between BT and isoprene, DMS, and beta-cyclocitral are all below 0.005. While there may be some degree of biogenic contribution to observed atmospheric benzothiazoles, there is no compelling evidence for such a source in the temporal variability. A full discussion of potential sources and justification for a conclusion of a dominant anthropogenic origin based on additional chemical indicators can be found in the following section.

One observed aerosol-phase species deserving particular attention is butyl-benzothiazole. Although butyl benzothiazole sulphenamides are broadly characterized rubber vulcanization agents<sup>65</sup> and butyl benzothiazole has been synthesized in laboratory environments, it has never to our knowledge been reported in the environment. During the bloom, butyl-benzothiazole decreases both in terms of absolute mass concentration and as a fraction of the total benzothiazole carbon pool and drives the majority of the decrease in the total aerosol-phase

benzothiazole carbon pool. To our knowledge there are no studies investigating the biodegradation of butyl benzothiazole in marine settings, but this finding in conjunction with the significant observed aerosol levels indicates that butyl-benzothiazole biodegradation may be an important environmental process. No identified benzothiazoles are observed to increase significantly as the aerosol benzothiazole carbon pool shrinks (see SI Figure S6). There are several probable contributions to this phenomenon. The biodegradation of butyl-benzothiazole has not been studied in marine contexts and its products may not have published mass spectra allowing them to be confirmed as benzothiazole biodegradation products. Additionally, benzothiazole degradation products with published mass spectra may fall outside the TD-GCxGC's sensitivity range, as biological degradation often produces highly oxygenated species not amenable to GC analysis, as described in Nowak et al., 2018.<sup>66</sup> Benzothiazoles may also bioaccumulate in the biological species within the channel, partition into suspended organic matter or onto the organic film on the wave channel surfaces, or decrease as a relative fraction of submicron organics emitted from bubble bursting processes due to changes in the structure and composition of the SSML.

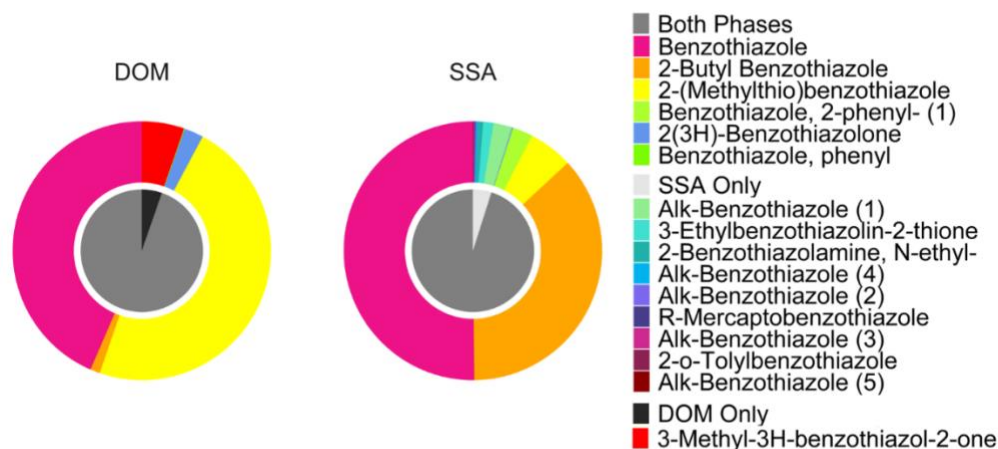


Figure 5.4. Molecular distributions and molecular overlap (by mass) of benzothiazoles observed in DOM (left) and nascent sea spray aerosol (right) at SeaSCAPE 2019. *Data and figures by Emily Barnes-Franklin.*

While the most abundant benzothiazole species are common to both dissolved and aerosol phases, unique isomers are observed in each and the relative distribution of common species differ (Figure 5.4), leading to a significant discrepancy between the solubility distributions of the benzothiazole carbon pools in the bulk and aerosol phases; bulk-phase benzothiazoles are more soluble, and less diverse in low solubility species, compared to aerosol-phase benzothiazoles (Figure 3). Water solubilities are estimated from  $\log K_{ow}$  (WSKOW v. 1.41, EPA EPI Suite) with all alkyl benzothiazoles parameterized as equal in solubility to butyl benzothiazole. The solubility distribution discrepancy is likely due to the concentration of low-solubility organics in the SSML<sup>67</sup> and previously reported film-jet sea spray aerosol formation dynamics, which cause SSML organics to preferentially aerosolize into smaller aerosol particles from film drops.<sup>68</sup> While the different benzothiazoles' implications for climate and public health relevant properties of sea spray aerosol lie beyond the scope of this publication, the differing chemical distributions between phases, in particular the abundance of low solubility benzothiazoles not observed in the bulk water, highlight that measurements of bulk-phase



organics in ocean waters are imperfect indicators of which organic species enrich the submicron aerosol particles with the longest atmospheric lifetimes that dominate the marine aerosol surface area distribution and have the potential to be transported farthest inland. This has implications for marine pollutant human exposure in coastal regions; marine pollutant monitoring focuses nearly exclusively on the bulk water, but as this study demonstrates, bulk water and aerosol-phase organic distributions and concentrations differ significantly, meaning that bulk water toxin measurements may not accurately reflect the sea spray aerosol concentrations of hazardous marine pollutants including carcinogens and respiratory irritants not reported in this work.

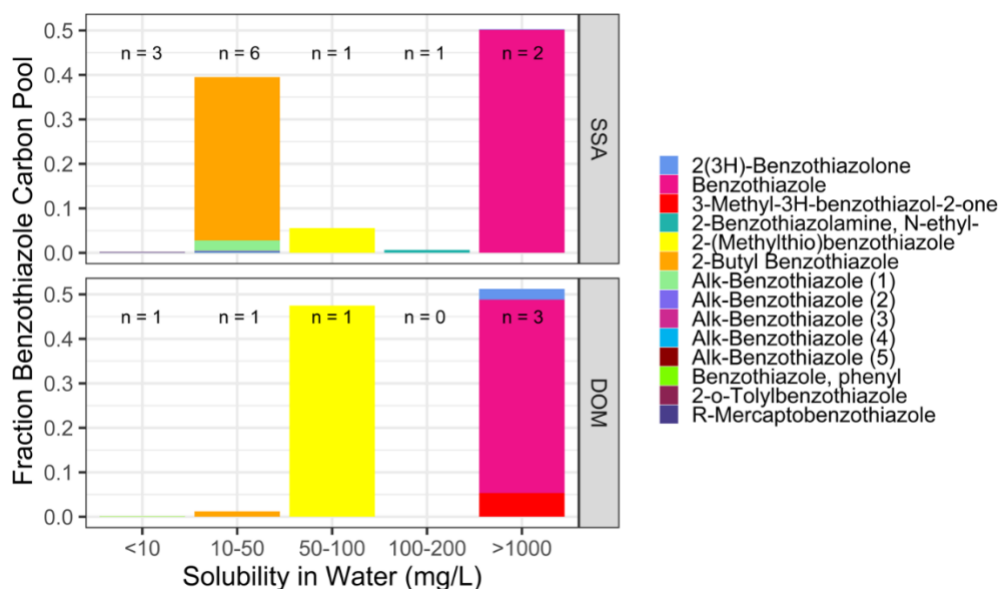


Figure 5.5. Solubility distributions of benzothiazoles weighted by contribution to cumulative observed benzothiazole carbon pools in the dissolved (DOM) and aerosol (SSA) phases. Number of individual species within each solubility bracket in each phase indicated by n. No solubility information for 3-Ethylbenzothiazolin-2-thione is available and it is therefore excluded from visualization. *Data and figures by Emily Barnes-Franklin.*

### *Evidence for Anthropogenic Origin*

While benzothiazoles are high-volume industrial chemicals and are commonly studied as wastewater contaminants in coastal areas, there are also marine biogenic sources of benzothiazoles.<sup>46,47</sup> Coupled with the early bloom increase in gas and aerosol-phase

benzothiazole levels that cannot be explained by (do not correlate with) either the rising temperatures or indicators of biological activity (including chlorophyll-a concentrations, heterotrophic bacteria concentrations, and peaks in typical biogenic gases such as DMS and isoprene) (Figure 1), this necessitates a more nuanced investigation of the most probable origins of the benzothiazoles observed at the SeaSCAPE campaign and in ambient air at Scripps Pier. Prominent among benzothiazoles in both dissolved and aerosol phases and observed in particularly high abundance in the dissolved phase was 2-(Methylthio)benzothiazole, a known and commonly reported tracer of anthropogenic benzothiazoles originating from runoff or wastewater.<sup>45,69,40</sup> Compared to other anthropogenic benzothiazole tracers, 2-(Methylthio)benzothiazole is relatively resistant to both photochemical and biological degradation, and is itself a biodegradation product of another commonly reported anthropogenic benzothiazole, 2-Mercaptobenzothiazole.<sup>42</sup> While multiple naturally occurring benzothiazoles have been characterized and reported, notably including several originating from the marine bacterium species *Micrococcus* sp.<sup>46</sup>, to our knowledge none (with the exception of BT) overlap with those observed in this study. Furthermore, the majority of reported biogenic benzothiazoles contain hydroxy groups, a functional group that is notably absent from all benzothiazole species observed in the dissolved and aerosol phases.<sup>46,70</sup> On the water collection day for SeaSCAPE bloom 3 (July 23 2019), the coastal current near San Diego ran from north to south at ~0.3 m/s (SCCOOS HR radar online mapping, documented in Harlan et al. 2010)<sup>71</sup>, which would have transported the wastewater from the nearest up-current wastewater discharge point, Oceanside Outfall, to Scripps Pier on a timescale of 36 hours (see SI Figure S4 for details). While enrichment of benzothiazoles from the Oceanside Outfall is certainly a potential contributing factor, given distance and dilution more local sources also merit consideration. As illustrated in

SI Figure S5, there are multiple runoff, storm drain, and residential use discharge points along the beach surrounding the Scripps Pier sampling location, all of which could have washed road residues enriched in benzothiazoles into the coastal waters.

Finally, when compared to confidently identified biogenic and anthropogenic gas species, the temporal profile of gas-phase BT is more similar to those of multiple positively identified anthropogenic species than to any positively identified biogenic species or biological indicators, as illustrated in SI Figure S2 and previously noted in greater detail. The temporal evolution of a suite of anthropogenic gases suggests that some process related to the establishment of thermal, physical, and chemical equilibrium within the wave channel and ISV caused a lagged peak in some anthropogenic VOCs compared to bulk water temperatures and is not indicative of a significant source of benzothiazole within the wave channel. The identification of known tracers of anthropogenic benzothiazole pollution, multiple logical local sources of anthropogenic benzothiazole runoff, similarity in benzothiazole and some other known anthropogenic VOC temporal profiles, and absence of known biogenic benzothiazoles all lead to the conclusion that the source of benzothiazoles in the SeaSCAPE and Scripps Pier studies is primarily anthropogenic in nature. Scripps Pier lies within the San Diego Scripps State Marine Conservation Area, a relatively clean and protected area of coastline. Given this, the results from this chapter may be considered a relatively conservative lens into the extent to which these anthropogenic marine contaminants may influence the composition of aerosol and gas-phase emissions in coastal areas.

#### *Benzothiazole Oxidation and Secondary Aerosol Formation*

In order to better understand the eventual fate of atmospheric benzothiazole in both coastal marine and urban settings, this chapter investigates the atmospheric oxidation and aerosol formation potential of gas-phase BT in a controlled laboratory oxidation experiment. When a plug of BT (62 ug in 5 uL of MeOH or 1%) was oxidized in the PAM-OFR to an equivalent 5 days of atmospheric aging, secondary aerosol formed, as illustrated by the new particle formation event in Figure 5.6. From this experiment, we produced a cumulative mass of 7.2  $\mu\text{g}$  of aerosol during the plug injection experiment. Further experiments are necessary to determine the aerosol yield of BT under typical atmospheric conditions, but these results suggest it could be significant. Products formed from this aging, analyzed using previously described HESI Orbitrap mass spectrometry, primarily include reduced nitrogen and CHON species, with aerosol sulfur primarily in the form of sulfuric acid as shown in the identified molecular species listed in SI Table S4. In the second previously described benzothiazole oxidation experiment, in which a constant source of gas-phase benzothiazole from a perm tube diluted to 12.8 ppb was oxidized at three aging equivalents ranging from 2.9 to 4.7 days, both aerosol and  $\text{SO}_2$  production were observed to increase with oxidative aging over this range, as illustrated in SI Figure S9. Aerosol mass concentrations ranged from  $9 \pm 2 \mu\text{g}/\text{m}^3$  at 2.9 days to  $19 \pm 2 \mu\text{g}/\text{m}^3$  at 4.7 days, and produced  $\text{SO}_2$  concentrations ranged from  $.67 \pm .08 \text{ ppb}$  at 2.9 days to  $1.3 \pm .12 \text{ ppb}$  at 4.7 days.

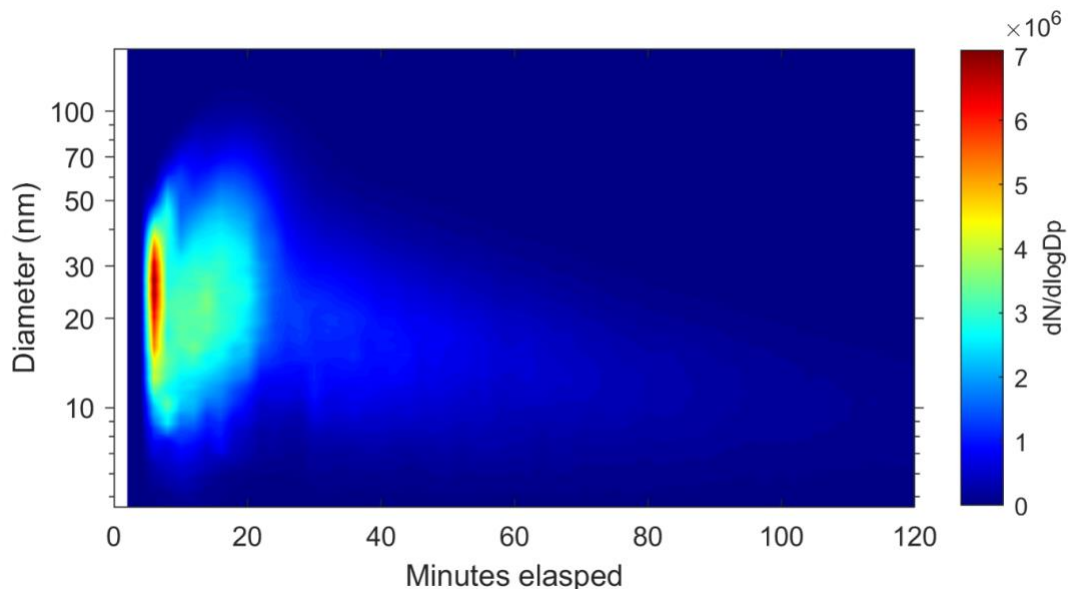


Figure 5.6. Nucleation of new particles from benzothiazole oxidation in PAM-OFR. Liquid benzothiazole dissolved in a methanol carrier (1% BT) is introduced at 5 minutes

The aerosol size distributions peak near 20 nm particle diameter for all exposure experiments, indicating new particle formation from benzothiazole oxidation (Figure S10). While conditions in the PAM-OFR do not directly mimic those of the ambient atmosphere, the results of the benzothiazole oxidation study indicate two things: first, gas-phase BT has the capacity to contribute to SMA (or more generally secondary aerosol) formation and second, BT oxidation has the capacity to form sulfur dioxide and sulfuric acid in the atmosphere, possibly suggesting the presence of sulfate aerosol produced during BT oxidation. This finding has relevance for both more polluted coastal marine environments, in which both benzothiazole and other anthropogenic marine pollutants should be evaluated for their potential influence on the abundance and characteristics of secondary marine aerosol, and for urban environments, in which benzothiazoles are highly abundant and may contribute to secondary organic aerosol formation and urban smog.

### 5.4.3 Acknowledgments

We would like to thank the NSF Center for Aerosol Impacts on Chemistry of the Environment (an NSF Chemical Innovation Center, (CHE-1801971)) and the entire experimental campaign team which participated in the SeaSCAPE for their support of this work. We specifically thank Julie Dinasquet, Francesca Malfatti, Clare Morris, and Daniel Crocker for their contribution of biological indicator data in support of this publication. The authors gratefully acknowledge the support of the National Science Foundation Graduate Research Fellowship Program (DGE-1650112) as well as Neal Arakawa and the use of facilities at the Environment Complex Analysis Laboratory (ECAL) at the University of California San Diego.

A portion of Chapter 5 is reproduced with permission from the American Chemical Society, currently under revisions: Barnes, E.B.; Alves, M.R.; Moore, A.N.; Kilgour, D.B.; Novak, G.A.; Mayer, K.; Sauer, J.; Weber, R.J.; Dang, D.; Winter, M.; Lee, C.; Cappa, C.D.; Bertram, T.H.; Prather, K.A.; Grassian, V.H.; Goldstein, A.H. Atmospheric Benzothiazoles in a Coastal Marine Environment. *Environ. Sci. Technol.* 2021. The dissertation author was a primary investigator and co-first author of this paper.

### 5.4.4 Supporting Information

Supporting Information includes 23 pages, 13 figures, and 4 tables. See publication for information regarding the SI as it is freely available to download from the American Chemical Society's website. Tables:

- Table S1: GCxGC Manufacturers and Methods, *p. S3*
- Table S2: Benzothiazole GCxGC quantification proxies and uncertainties for all observed aerosol phase species, *p. S6*
- Table S3: Literature review of reported dissolved phase benzothiazoles in aquatic environments, *p. S18*
- Table S4: Background subtracted BZT oxidation products from PAM, *p. S20*

Figures:

- Figure S1: Annotated TOC graphic, *p. S8*
- Figure S2: Benzothiazole Spectra, *p. S9*

- Figure S3: Time series of biological indicators, biogenic gasses, and anthropogenic gasses at SeaSCAPE, *p. S10*
- Figure S4: Quantitative Comparison, VOCUS and GCxGC VOC measurements, *p. S11*
- Figure S5: Oceanside Outfall and Currents Near Scripps Pier, *p. S12*
- Figure S6: Wastewater and Municipal Storm Water Discharges near Scripps Pier, *p. S13*
- Figure S7: Individual Time Series of Aerosol Phase Benzothiazoles at SeaSCAPE, *p. S14*
- Figure S8: Sea Spray Aerosol D7 Siloxane and Benzothiazole Carbon Pool Time Series at SeaSCAPE, *p. S15*
- Figure S9: Fractional Changes in the Sea Spray Aerosol Benzothiazole Carbon Pool at SeaSCAPE, *p. S16*
- Figure S10: Enrichment Analysis of Common Benzothiazoles in SSA and DOM Phases, *p. S17*
- Figure S11: Aerosol and SO<sub>2</sub> production from Benzothiazole Oxidation Experiment, *p. S22*
- Figure S12: Size Distributions of Particles Formed from Benzothiazole Oxidation Experiment, *p. S23*
- Figure S13: PAM-OFR Calibration, *p. S23*

#### 5.4.5 References

- (1) Lewis, R.; Schwartz, E. *Sea Salt Aerosol Production: Mechanisms, Methods, Measurements and Models—A Critical Review*; Geophysical Monograph Series; American Geophysical Union: Washington, D. C., 2004; Vol. 152.
- (2) Zafiriou, O. C.; True, M. B. Nitrate Photolysis in Seawater by Sunlight. *Mar. Chem.* **1979**, *8* (1), 33–42.
- (3) Karimova, N. V.; Alves, M. R.; Luo, M.; Grassian, V.; Gerber, R. B. Toward a Microscopic Model of Light Absorbing Dissolved Organic Compounds in Aqueous Environments: Theoretical and Experimental Study. *Phys. Chem. Chem. Phys.* **2021**.
- (4) Karimova, N. V.; Luo, M.; Grassian, V. H.; Benny Gerber, R. Absorption Spectra of Benzoic Acid in Water at Different pH and in the Presence of Salts: Insights from the Integration of Experimental Data and Theoretical Cluster Models. *Phys. Chem. Chem. Phys.* **2020**, *22* (9), 5046–5056.
- (5) Shemesh, D.; Luo, M.; Grassian, V. H.; Gerber, R. B. Absorption Spectra of Pyruvic Acid in Water: Insights from Calculations for Small Hydrates and Comparison to Experiment. *Phys. Chem. Chem. Phys.* **2020**, *22* (22), 12658–12670.
- (6) Luo, M.; Shemesh, D.; Sullivan, M. N.; Alves, M. R.; Song, M.; Gerber, R. B.; Grassian, V. H. Impact of pH and NaCl and CaCl<sub>2</sub> Salts on the Speciation and Photochemistry of Pyruvic Acid in the Aqueous Phase. *J. Phys. Chem. A* **2020**, *124* (25), 5071–5080.
- (7) Trueblood, J. V.; Alves, M. R.; Power, D.; Santander, M. V.; Cochran, R. E.; Prather, K. A.; Grassian, V. H. Shedding Light on Photosensitized Reactions within Marine-Relevant Organic Thin Films. *ACS Earth Sp. Chem.* **2019**, *3* (8), 1614–1623.
- (8) Azam, F.; Fenchel, T.; Field, J.; Gray, J.; Meyer-Reil, L.; Thingstad, F. The Ecological

- Role of Water-Column Microbes in the Sea. *Mar. Ecol. Prog. Ser.* **1983**, 10, 257–263.
- (9) Cochran, R. E.; Laskina, O.; Trueblood, J. V.; Estillore, A. D.; Morris, H. S.; Jayarathne, T.; Sultana, C. M.; Lee, C.; Lin, P.; Laskin, J. Molecular Diversity of Sea Spray Aerosol Particles: Impact of Ocean Biology on Particle Composition and Hygroscopicity. *Chem* **2017**, 2 (5), 655–667.
  - (10) Tovar-Sánchez, A.; Sánchez-Quiles, D.; Basterretxea, G.; Benedé, J. L.; Chisvert, A.; Salvador, A.; Moreno-Garrido, I.; Blasco, J. Sunscreen Products as Emerging Pollutants to Coastal Waters. *PLoS One* **2013**, 8 (6), e65451.
  - (11) Zeng, E. Y.; Vista, C. L. Organic Pollutants in the Coastal Environment off San Diego, California. 1. Source Identification and Assessment by Compositional Indices of Polycyclic Aromatic Hydrocarbons. *Environ. Toxicol. Chem.* **1997**, 16 (2), 179–188.
  - (12) Elliott, J. E.; Elliott, K. H. Tracking Marine Pollution. *Science*. American Association for the Advancement of Science May 2013, pp 556–558.
  - (13) Glibert, P. M.; Maranger, R.; Sobota, D. J.; Bouwman, L. The Haber Bosch-Harmful Algal Bloom (HB-HAB) Link. *Environ. Res. Lett.* **2014**, 9 (10), 105001.
  - (14) Kahru, M.; Mitchell, B. G. Ocean Color Reveals Increased Blooms in Various Parts of the World. *Eos (Washington, DC)*. **2008**, 89 (18), 170.
  - (15) Dale, B.; Edwards, M.; Reid, P. C. Climate Change and Harmful Algal Blooms. *Ecol. Stud.* **2006**, 189, 367–378.
  - (16) Paerl, H.; Huisman, J. Blooms like It Hot. *Science (80-. )*. **2008**.
  - (17) BLANCHARD, D. C. Bubble Scavenging and the Water-to-Air Transfer of Organic Material in the Sea. *Adv. Chem.* **1975**, 145, 360–387.
  - (18) Carpenter, L. J.; Archer, S. D.; Beale, R. Ocean-Atmosphere Trace Gas Exchange. *Chem. Soc. Rev.* **2012**, 41 (19), 6473–6506.
  - (19) O’Dowd, C. D.; De Leeuw, G. Marine Aerosol Production: A Review of the Current Knowledge. *Philosophical Transactions of the Royal Society A: Mathematical, Physical and Engineering Sciences*. Royal Society July 2007, pp 1753–1774.
  - (20) Trueblood, J. V.; Wang, X.; Or, V. W.; Alves, M. R.; Santander, M. V.; Prather, K. A.; Grassian, V. H. The Old and the New: Aging of Sea Spray Aerosol and Formation of Secondary Marine Aerosol through OH Oxidation Reactions. *ACS Earth Sp. Chem.* **2019**, 3 (10), 2307–2314.
  - (21) O’Dowd, C. D.; Facchini, M. C.; Cavalli, F.; Ceburnis, D.; Mircea, M.; Decesari, S.; Fuzzi, S.; Young, J. Y.; Putaud, J. P. Biogenically Driven Organic Contribution to Marine



- Aerosol. *Nature* **2004**, *431* (7009), 676–680.
- (22) Lee, H. D.; Morris, H. S.; Laskina, O.; Sultana, C. M.; Lee, C.; Jayarathne, T.; Cox, J. L.; Wang, X.; Hasenecz, E. S.; Demott, P. J.; Bertram T.H; Cappa, C.D.; Stone, E.A.; Prather, K.A., Grassian, V.H.; Tivanski, A.V. Organic Enrichment, Physical Phase State, and Surface Tension Depression of Nascent Core-Shell Sea Spray Aerosols during Two Phytoplankton Blooms. *ACS Earth Sp. Chem.* **2020**, *4* (4), 650–660.
- (23) Hodas, N.; Zuend, A.; Mui, W.; Flagan, R. C.; Seinfeld, J. H. Influence of Particle-Phase State on the Hygroscopic Behavior of Mixed Organic–Inorganic Aerosols. *Atmos. Chem. Phys.* **2015**, *15* (9), 5027–5045.
- (24) Fuentes, E.; Coe, H.; Green, D.; McFiggans, G. On the Impacts of Phytoplankton-Derived Organic Matter on the Properties of the Primary Marine Aerosol - Part 2: Composition, Hygroscopicity and Cloud Condensation Activity. *Atmos. Chem. Phys.* **2011**, *11* (6), 2585–2602.
- (25) Myriokefalitakis, S.; Vignati, E.; Tsigaridis, K.; Papadimas, C.; Sciare, J.; Mihalopoulos, N.; Facchini, M. C.; Rinaldi, M.; Dentener, F. J.; Ceburnis, D.; et al. Global Modeling of the Oceanic Source of Organic Aerosols. *Adv. Meteorol.* **2010**, *2010*, 1–16.
- (26) Mayer, K. J.; Wang, X.; Santander, M. V.; Mitts, B. A.; Sauer, J. S.; Sultana, C. M.; Cappa, C. D.; Prather, K. A. Secondary Marine Aerosol Plays a Dominant Role over Primary Sea Spray Aerosol in Cloud Formation. *ACS Cent. Sci.* **2020**.
- (27) Zheng, G.; Kuang, C.; Uin, J.; Watson, T.; Wang, J. Large Contribution of Organics to Condensational Growth and Formation of Cloud Condensation Nuclei (CCN) in the Remote Marine Boundary Layer. *Atmos. Chem. Phys.* **2020**, *20* (21), 12515–12525.
- (28) Kirkpatrick, B.; Fleming, L. E.; Squicciarini, D.; Backer, L. C.; Clark, R.; Abraham, W.; Benson, J.; Cheng, Y. S.; Johnson, D.; Pierce, R.; Zaias, J.; Bossart, G.D.; Baden, D.G. Literature Review of Florida Red Tide: Implications for Human Health Effects. *Harmful Algae*. Elsevier April 2004, pp 99–115.
- (29) Grattan, L. M.; Holobaugh, S.; Morris, J. G. Harmful Algal Blooms and Public Health. *Harmful Algae*. Elsevier B.V. July 2016, pp 2–8.
- (30) Walsh, J. J.; Lenes, J. M.; Weisberg, R. H.; Zheng, L.; Hu, C.; Fanning, K. A.; Snyder, R.; Smith, J. More Surprises in the Global Greenhouse: Human Health Impacts from Recent Toxic Marine Aerosol Formations, Due to Centennial Alterations of World-Wide Coastal Food Webs. *Marine Pollution Bulletin*. Elsevier Ltd March 2017, pp 9–40.
- (31) Vila-Costa, M.; Cerro-Gálvez, E.; Martínez-Varela, A.; Casas, G.; Dachs, J. Anthropogenic Dissolved Organic Carbon and Marine Microbiomes. *ISME J.* **2020**, *14* (10), 2646–2648.

- (32) Wang, Z.; Walker, G. W.; Muir, D. C. G.; Nagatani-Yoshida, K. Toward a Global Understanding of Chemical Pollution: A First Comprehensive Analysis of National and Regional Chemical Inventories. *Environ. Sci. Technol.* **2020**, *54* (5), 2575–2584.
- (33) Bernhardt, E. S.; Rosi, E. J.; Gessner, M. O. Synthetic Chemicals as Agents of Global Change. *Front. Ecol. Environ.* **2017**, *15* (2), 84–90.
- (34) Ott, A.; Martin, T. J.; Whale, G. F.; Snape, J. R.; Rowles, B.; Galay-Burgos, M.; Davenport, R. J. Improving the Biodegradability in Seawater Test. *Sci. Total Environ.* **2019**, *666*, 399–404.
- (35) Cincinelli, A.; Stortini, A. M.; Perugini, M.; Checchini, L.; Lepri, L. Organic Pollutants in Sea-Surface Microlayer and Aerosol in the Coastal Environment of Leghorn. *Mar. Chem.* **2001**, *76* (1–2), 77–98.
- (36) Cerro-Gálvez, E.; Dachs, J.; Lundin, D.; Fernández-Pinos, M. C.; Sebastián, M.; Vila-Costa, M. Responses of Coastal Marine Microbiomes Exposed to Anthropogenic Dissolved Organic Carbon. *Environ. Sci. Technol.* **2021**.
- (37) Cunliffe, M.; Engel, A.; Frka, S.; Gašparović, B. Ž.; Guitart, C.; Murrell, J. C.; Salter, M.; Stolle, C.; Upstill-Goddard, R.; Wurl, O. Sea Surface Microlayers: A Unified Physicochemical and Biological Perspective of the Air-Ocean Interface. *Progress in Oceanography*. Pergamon February 2013, pp 104–116.
- (38) Prather, K. A.; Bertram, T. H.; Grassian, V. H.; Deane, G. B.; Stokes, M. D.; DeMott, P. J.; Aluwihare, L. I.; Palenik, B. P.; Azam, F.; Seinfeld, J. H.; Moffet, R.C.; Molina M.J.; Cappa, C.D.; Geiger, F.M.; Roberts G.C.; Russell, L.M.; Ault, A.P.; Baltrusaitis, J.; Collins, D.B.; Corrigan, C.E.; Cuadra-Rodriguez, L.A.; Ebben, C.J.; Forestieri, S.D.; Guasco, T.L.; Hersey, S.P.; Kim, M.J.; Lambert, W.F.; Modini, R.L.; Mui, W.; Pedler, B.E.; Ruppel, M.J.; Ryder, O.S.; Shoepf, N.G.; Sullivan, R.C.; Zhao, D. Bringing the Ocean into the Laboratory to Probe the Chemical Complexity of Sea Spray Aerosol. *Proc. Natl. Acad. Sci. U. S. A.* **2013**, *110* (19), 7550–7555.
- (39) Engel, A.; Bange, H. W.; Cunliffe, M.; Burrows, S. M.; Friedrichs, G.; Galgani, L.; Herrmann, H.; Hertkorn, N.; Johnson, M.; Liss, P. S.; Quinn, P.K.; Schartau, M.; Soloviev, A.; Stolle, C.; Upstill-Goddard, R.C.; van Pinxteren, M.; Zanker, B. The Ocean's Vital Skin: Toward an Integrated Understanding of the Sea Surface Microlayer. *Front. Mar. Sci.* **2017**, *4*, 1–14.
- (40) Liao, C.; Kim, U. J.; Kannan, K. A Review of Environmental Occurrence, Fate, Exposure, and Toxicity of Benzothiazoles. *Environ. Sci. Technol.* **2018**, *52* (9), 5007–5026.
- (41) Halsband, C.; Sørensen, L.; Booth, A. M.; Herzke, D. Car Tire Crumb Rubber: Does Leaching Produce a Toxic Chemical Cocktail in Coastal Marine Systems? *Front. Environ. Sci.* **2020**, *8*, 125.
- (42) De Wever, H.; Verachtert, H. Biodegradation and Toxicity of Benzothiazoles. *Water Res.* **1997**, *31* (11), 2673–2684.

- (43) Fries, E.; Gocht, T.; Klasmeier, J. Occurrence and Distribution of Benzothiazole in the Schwarzbach Watershed. *J. Environ. Monit.* **2011**, *13* (10), 2838–2843.
- (44) Brownlee, B. G.; Carey, J. H.; Fox, M. E. A Review of Benzothiazoles in the Aquatic Environment, Scientific Series No. 126. Inland Waters Directorate 1981.
- (45) Zeng, E. Y.; Tran, K.; Young, D. Evaluation of Potential Molecular Markers for Urban Stormwater Runoff. *Environ. Monit. Assess.* **2004**, *90* (1–3), 23–43.
- (46) Stierle, A. A.; Cardellina, J. H.; Singleton, F. L. Benzothiazoles from a Putative Bacterial Symbiont of the Marine Sponge *Tedania ignis*. *Tetrahedron Lett.* **1991**, *32* (37), 4847–4848.
- (47) Chhalodia, A. K.; Rinkel, J.; Konvalinkova, D.; Petersen, J.; Dickschat, J. S. Identification of Volatiles from Six Marine *Celeribacter* Strains. *Beilstein J. Org. Chem.* **2021**, *17* (1), 420–430.
- (48) Kloepfer, A.; Jekel, M.; Reemtsma, T. Occurrence, Sources, and Fate of Benzothiazoles in Municipal Wastewater Treatment Plants. *Environ. Sci. Technol.* **2005**, *39* (10), 3792–3798.
- (49) Sorahan, T. Bladder Cancer Risks in Workers Manufacturing Chemicals for the Rubber Industry. *Occup. Med. (Chic. Ill.)* **2008**, *58* (7), 496–501.
- (50) Sorahan, T. Cancer Risks in Chemical Production Workers Exposed to 2-Mercaptobenzothiazole. *Occup. Environ. Med.* **2009**, *66* (4), 269–273.
- (51) Liao, X.; Zou, T.; Chen, M.; Song, Y.; Yang, C.; Qiu, B.; Chen, Z. F.; Tsang, S. Y.; Qi, Z.; Cai, Z. Contamination Profiles and Health Impact of Benzothiazole and Its Derivatives in PM<sub>2.5</sub> in Typical Chinese Cities. *Sci. Total Environ.* **2021**, *755*, 142617.
- (52) Sauer, J.; Mayer, K.; Lee, C.; Alves, M.; Amiri, S.; Bahaveolos, C.; Barnes, E.; Crocker, D.; Dinasquet, J.; Garofalo, L.; Kaluarachchi, C.; Dang, D.; Kilgour, D.; Mael, L.; Mitts, B.; Moon, D.; Morris, C.; Moore, A.; Ni, C.; Pendergraft, M.; Petras, D.; Simpson, R.; Smith, S.; Tumminello, P.; Walker, J.; Demott, P.; Farmer, D.; Goldstein, A.; Grassian, V.; Jaffe, J.; Malfatti, F.; Martz, T.; Slade, J.; Tivanski, A.; Bertram, T.; Cappa, C.; Prather, K. The Sea Spray Chemistry and Particle Evolution Study (SeaSCAPE): Overview and Experimental Methods. *Environ. Sci. Process. Impacts* **2021**.
- (53) Wang, X.; Sultana, C. M.; Trueblood, J.; Hill, T. C. J.; Malfatti, F.; Lee, C.; Laskina, O.; Moore, K. A.; Beall, C. M.; McCluskey, C. S.; et al. Microbial Control of Sea Spray Aerosol Composition: A Tale of Two Blooms. *ACS Cent. Sci.* **2015**, *1* (3), 124–131.
- (54) Dittmar, T.; Koch, B.; Hertkorn, N.; Kattner, G. A Simple and Efficient Method for the Solid-Phase Extraction of Dissolved Organic Matter (SPE-DOM) from Seawater. *Limnol.*

- Oceanogr. Methods* **2008**, 6 (6), 230–235.
- (55) Roveretto, M.; Li, M.; Hayeck, N.; Brüggemann, M.; Emmelin, C.; Perrier, S.; George, C. Real-Time Detection of Gas-Phase Organohalogenes from Aqueous Photochemistry Using Orbitrap Mass Spectrometry. *ACS Earth Sp. Chem.* **2019**, 3 (3), 329–334.
- (56) Worton, D. R.; Decker, M.; Isaacman-VanWertz, G.; Chan, A. W. H.; Wilson, K. R.; Goldstein, A. H. Improved Molecular Level Identification of Organic Compounds Using Comprehensive Two-Dimensional Chromatography, Dual Ionization Energies and High Resolution Mass Spectrometry. *Analyst* **2017**, 142 (13), 2395–2403.
- (57) Dörter, M.; Odabasi, M.; Yenisoy-Karakaş, S. Source Apportionment of Biogenic and Anthropogenic VOCs in Bolu Plateau. *Sci. Total Environ.* **2020**, 731, 139201.
- (58) Reddy, C. M.; Quinn, J. G. Environmental Chemistry of Benzothiazoles Derived from Rubber. *Environ. Sci. Technol.* **1997**, 31 (10), 2847–2853.
- (59) Sander, R. Compilation of Henry's Law Constants (Version 4.0) for Water as Solvent. *Atmos. Chem. Phys.* **2015**, 15 (8), 4399–4981.
- (60) Kowalska, K.; Felis, E.; Sochacki, A.; Bajkacz, S. Removal and Transformation Pathways of Benzothiazole and Benzotriazole in Membrane Bioreactors Treating Synthetic Municipal Wastewater. *Chemosphere* **2019**, 227, 162–171.
- (61) Tran, T. M.; Kannan, K. Occurrence of Cyclic and Linear Siloxanes in Indoor Air from Albany, New York, USA, and Its Implications for Inhalation Exposure. *Sci. Total Environ.* **2015**, 511, 138–144.
- (62) Bletsou, A. A.; Asimakopoulos, A. G.; Stasinakis, A. S.; Thomaidis, N. S.; Kannan, K. Mass Loading and Fate of Linear and Cyclic Siloxanes in a Wastewater Treatment Plant in Greece. *Environ. Sci. Technol.* **2013**, 47 (4), 1824–1832.
- (63) Hong, W. J.; Jia, H.; Liu, C.; Zhang, Z.; Sun, Y.; Li, Y. F. Distribution, Source, Fate and Bioaccumulation of Methyl Siloxanes in Marine Environment. *Environ. Pollut.* **2014**, 191, 175–181.
- (64) Mao, F.; He, Y.; Gin, K. Y. H. Occurrence and Fate of Benzophenone-Type UV Filters in Aquatic Environments: A Review. *Environmental Science: Water Research and Technology*. Royal Society of Chemistry February 2019, pp 209–223.
- (65) Aprem, A. S.; Joseph, K.; Mathew, T.; Altstaedt, V.; Thomas, S. Studies on Accelerated Sulphur Vulcanization of Natural Rubber Using 1-Phenyl-2, 4-Dithiobiuret/Tertiary Butyl Benzothiazole Sulphenamide. *Eur. Polym. J.* **2003**, 39 (7), 1451–1460.
- (66) Nowak, J. A.; Shrestha, P. M.; Weber, R. J.; McKenna, A. M.; Chen, H.; Coates, J. D.; Goldstein, A. H. Comprehensive Analysis of Changes in Crude Oil Chemical

- Composition during Biosouring and Treatments. *Environ. Sci. Technol.* **2018**, 52 (3), 1290–1300.
- (67) Hardy, J. T. The Sea Surface Microlayer: Biology, Chemistry and Anthropogenic Enrichment. *Progress in Oceanography*. Pergamon January 1982, pp 307–328.
- (68) Wang, X.; Deane, G. B.; Moore, K. A.; Ryder, O. S.; Stokes, M. D.; Beall, C. M.; Collins, D. B.; Santander, M. V.; Burrows, S. M.; Sultana, C. M.; Prather, K.A. The Role of Jet and Film Drops in Controlling the Mixing State of Submicron Sea Spray Aerosol Particles. *Proc. Natl. Acad. Sci. U. S. A.* **2017**, 114 (27), 6978–6983.
- (69) Fiehn, O.; Reemtsma, T.; Jekel, M. Extraction and Analysis of Various Benzothiazoles from Industrial Wastewater. *Anal. Chim. Acta* **1994**, 295 (3), 297–305.
- (70) Le Bozec, L.; Moody, C. J. Naturally Occurring Nitrogensulfur Compounds. the Benzothiazole Alkaloids. *Aust. J. Chem.* **2009**, 62 (7), 639–647.
- (71) Harlan, J.; Terrill, E.; Hazard, L.; Keen, C.; Barrick, D.; Whelan, C.; Howden, S.; Kohut, J. The Integrated Ocean Observing System High-Frequency Radar Network: Status and Local, Regional, and National Applications NOAA IOOS Program. *Mar. Technol. Soc. J.* **2010**, 44 (6).

## Chapter 6: Chemistry and Photochemistry of Pyruvic Acid on Metal Oxide Surfaces

### 6.1 Abstract

The surface chemistry and photochemistry of gas-phase pyruvic acid ( $\text{CH}_3\text{COCOOH}$ ) on two oxides,  $\text{Al}_2\text{O}_3$  and  $\text{TiO}_2$ , have been investigated using transmission Fourier Transform Infrared (FTIR) Spectroscopy and mass spectrometry. At 298K, the carboxylic acid group within pyruvic acid is found to react with surface hydroxyl groups (M-OH, where M=Al or Ti) to yield pyruvate as the predominant adsorbed organic species. Upon broadband UV irradiation,  $\lambda > 280$  nm, there is a loss of adsorbed pyruvate with the concomitant formation of new products. The photochemical loss of pyruvate is higher on  $\text{TiO}_2$  than  $\text{Al}_2\text{O}_3$  indicating that photochemistry is enhanced on the surface of a semiconductor oxide,  $\text{TiO}_2$ , compared to an insulator oxide,  $\text{Al}_2\text{O}_3$ . Analysis of products extracted from the surface with mass spectrometry shows the formation of several new compounds that includes zymonic acid, which is found to be present under both dark and light conditions, and other higher molar mass oligomeric species such as parapryuvic acid, acetolactic acid, and 2,4-dihydroxy-2-methyl-5-oxohexanoic acid (DMOHA) that form only under irradiation. In this chapter, we show that there are some parallels between aqueous phase photochemistry of pyruvic acid and the photochemistry of adsorbed pyruvic acid in terms of the products that form. However, there are also distinct differences with several new products observed on these oxide surfaces including lactic acid dimers and trimers and a significant amount of even larger oligomeric photoproducts not seen in the aqueous phase. Thus overall, this chapter provides insights into the surface chemistry and photochemistry of pyruvic acid on different oxides ( $\text{Al}_2\text{O}_3$ , and  $\text{TiO}_2$ ). Furthermore, because of the role of pyruvic acid, the simplest of the alpha-keto acids, in the atmosphere and in metabolic pathways, these results have

implications to the chemistry that occurs in both indoor and outdoor environments and during prebiotic Earth conditions.

## 6.2 Introduction

Sunlight, the major source of energy in the atmosphere, drives the complex chemical cycles that determine the composition of the atmosphere through direct photochemistry and the formation of secondary reactive species.<sup>1-7</sup> It is crucial to understand these photochemical processes as they affect the lifetime of atmospherically relevant molecules. For example, pyruvic acid (PA),  $\text{CH}_3\text{COCOOH}$ , an important atmospheric  $\alpha$  – keto acid, is formed in the atmosphere primarily from reaction of hydroxyl radical ( $\text{OH}\cdot$ ) and hydrated methylglyoxal from isoprene photo-oxidation via particle-phase aqueous chemistry. The lifetime of pyruvic acid is determined to a large extent by photo-initiated processes,<sup>6</sup> with wet deposition and its reaction with hydroxyl radical acting as additional secondary sinks.<sup>5,8</sup> Pyruvic acid has been detected in numerous field studies in the gas-phase (10-100 ppt), in aerosols (up to  $140 \text{ ng m}^{-3}$ ), in snow, in rainwater, and in carbonaceous meteorites.<sup>5,9,18,19,10-17</sup> Pyruvate, the deprotonated form of pyruvic acid, serves as an intermediate for both aerobic and anaerobic metabolism and has been proposed to be a promising prebiotic molecule initializing primitive metabolism.<sup>20-24</sup>

Pyruvic acid chemistry and photochemistry in the gas- and condensed-phases<sup>25-34</sup>, under atmospheric conditions<sup>6,30,35,36</sup>, through hydroxyl radical oxidation<sup>35,37,38</sup>, thermal decomposition<sup>39,40</sup> and vibrational overtone induced decarboxylation<sup>41-43</sup> have all been investigated. Computational studies<sup>44-46</sup> of the different conformations of pyruvic acid have provided insights into the electronic structure and reaction barriers for these different pathways. Early studies on the photochemistry of pyruvic acid vapor, using high energy photons, were carried out at approximately 1 Torr of pyruvic acid at room temperature using low buffer gas

pressures.<sup>31,47,48</sup> Under these conditions, the most energetically favorable mechanism for the photolysis of gas-phase pyruvic acid involves a hydrogen atom transfer and C–C bond cleavage, processing through a five-membered cyclic transition state to yield acetaldehyde and CO<sub>2</sub>.<sup>44,45</sup> This concerted reaction is preceded by hydrogen atom chattering. Acetic acid and CO were also detected as photochemical products via a lactone intermediate,<sup>5</sup> a mechanism supported by theoretical calculations.<sup>45</sup>

Aqueous-phase pyruvic acid has a very different photochemistry from that in the gas phase due to differences in reaction energetics and molecular speciation. In aqueous environments, water catalysis<sup>49</sup> leads to the hydration of pyruvic acid to, 2, 2-dihydroxypropanoic acid (DHPA), a geminal-diol form of pyruvic acid which is not photoactive at wavelengths present near the Earth's surface.<sup>50–54</sup> However the keto form of pyruvic acid absorbs a near UV photon for a transition to the S<sub>1</sub> <sup>1</sup>(n, π\*) state and then undergoes intersystem crossing to a T<sub>1</sub> <sup>3</sup>(n, π\*) state.<sup>55</sup> Griffith et al. proposed a mechanism, in which the T<sub>1</sub>(n, π\*) state of pyruvic acid acts as a radical initiator by abstracting the acidic hydrogen atom from DHPA. The presence of oxygen has also been studied by Harris et al.<sup>5</sup>, who demonstrated that O<sub>2</sub> quenches radicals, thus, favoring the formation of acetic acid and inhibiting the radical recombination reactions which generate dimethyl tartaric acid (DMTA). More complex oligomeric species, including covalently-bonded dimers and trimers of pyruvic acid, are found to be the main products in the aqueous phase.<sup>6,20,25,27,29,54</sup> These higher carbon number species can lead to secondary organic aerosol (SOA) formation due to the decrease in volatility of these species.<sup>55</sup>

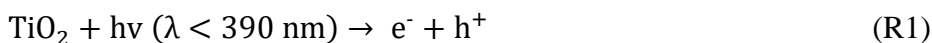
Since pyruvic acid undergoes photochemistry in the troposphere in both the aqueous and gas phase, the multiphase photochemistry of pyruvic acid was recently studied using an



environmental simulation chamber.<sup>6</sup> Upon irradiation of nebulized pyruvic acid, acetic acid and CO<sub>2</sub> were generated as the two major products, consistent with studies for bulk photolysis reactions.<sup>5,25,29</sup> However, more interestingly, a new higher carbon number product, a C<sub>6</sub> product, zymonic acid was also observed to form at the surface of nebulized drops in the simulation chamber.<sup>6</sup>

In this chapter, the heterogenous interactions of pyruvic acid with oxide surfaces, such as Al<sub>2</sub>O<sub>3</sub> and TiO<sub>2</sub>, and their photochemical reactions are explored. Al<sub>2</sub>O<sub>3</sub> is a major component of mineral dust, occupying 10 to 15 % of the oxide fraction.<sup>56</sup> Heterogeneous reactions between atmospheric trace gases and Al<sub>2</sub>O<sub>3</sub>, as well as the photochemistry of Al<sub>2</sub>O<sub>3</sub> have been widely studied.<sup>56-62</sup> Furthermore, mineral dust has been reported to contain TiO<sub>2</sub>, a photoactive semiconductor oxide, in the range of 1 to 10% by mass.<sup>63,64</sup> Previous studies have shown that organic acids can adsorbed onto different types of oxide particles.<sup>63,65</sup> For example, the adsorption of formic acid (HCOOH, a carbonyl acid) on SiO<sub>2</sub> has been observed to be a reversible, molecular process, while adsorbed bridged bidentate formate (HCOO<sup>-</sup>) is irreversibly formed on a TiO<sub>2</sub> surface.<sup>65,66</sup> In addition to outdoor mineral dust, surfaces composed of oxides in indoor environments can also play a major role in air quality indoors.<sup>67-70</sup> TiO<sub>2</sub>, in micro and nanoscale form, is also a major component of self-cleaning surfaces and paints.<sup>71-74</sup>

For semiconductor oxides such as TiO<sub>2</sub>, An electron-hole pair is generated when excited with light of wavelength no less than the band gap energy of TiO<sub>2</sub> (~ 3.2 eV; λ ~390 nm) as seen in R1.<sup>63,64</sup>



The three major pathways following the photogeneration of electron-hole pairs include: recombination of electrons and holes on the surface; reduction of electron acceptors; and

oxidation of electron donors by photogenerated holes.<sup>63,75,76</sup> The reduction of pyruvic acid to lactic acid has been observed at metal and semiconductor surfaces<sup>77–80</sup> including the direct photoconversion of pyruvate to lactate in aqueous TiO<sub>2</sub> dispersions.<sup>81</sup> In contrast, the different polymorphs of Al<sub>2</sub>O<sub>3</sub>,  $\gamma$ ,  $\delta$ , and  $\alpha$  have a much higher band gap around 7.6 eV and only direct photochemistry of the adsorbed pyruvic acid is operative for UV irradiation above 280 nm.<sup>82</sup>

Given the importance of heterogeneous interactions and photochemical reactions of atmospheric gases with mineral dust surfaces in the atmosphere, the role of surface chemistry in indoor environments, and the importance of pyruvic acid in prebiotic Earth,<sup>3,4,20,22,24</sup> the surface chemistry of pyruvic acid on Al<sub>2</sub>O<sub>3</sub> and TiO<sub>2</sub> surfaces under dark and light conditions is investigated via both FTIR and high resolution mass spectrometry (HRMS) to better understand the chemistry of pyruvic acid in outdoor and indoor environments.

### 6.3 Experimental Methods

Transmission FTIR spectroscopy, coupled with a modified Teflon-coated infrared cell, was used to study the adsorption of pyruvic acid on mineral dust oxides surfaces at  $296 \pm 1$  K. Additional details of this system have been described in previous studies.<sup>66,83,84</sup> Approximately 5 mg of metal oxide particles, Al<sub>2</sub>O<sub>3</sub>, (Degussa, AlumOxid C, 101 m<sup>2</sup> g<sup>-1</sup>) and TiO<sub>2</sub> (Sigma Aldrich, 50 m<sup>2</sup> g<sup>-1</sup>), was pressed separately onto one half of a tungsten grid in the sample cell compartment, held by two Teflon coated jaws. Following the preparation of the oxide sample and placement in the IR cell, the system is evacuated for 6 hours using a turbo-molecular pump. After evacuation, the sample was exposed to the desired pressure of gaseous pyruvic acid (97%, Alfa Aesar) for 20 minutes under dry conditions (RH < 1%). The pyruvic acid sample was first distilled and then degassed at least three times with consecutive freeze-pump-thaw cycles prior to use.

Photochemistry experiments were carried out using a broadband 500 W Hg arc lamp (Oriel, Model 66033, > 280 nm). Infrared radiation was removed via a water filter placed directly after the lamp output. After 6 hours of evacuation, Al<sub>2</sub>O<sub>3</sub> and TiO<sub>2</sub> surfaces were exposed to 100 mTorr pyruvic acid vapor for 20 minutes, followed by overnight evacuation to remove all weakly-bonded species, leaving pyruvate adsorbed on the oxide surface. Isolation of the reaction mixing chamber from the evacuation system is achieved by closing the valve between the customized infrared cell and the glass mixing chamber.

Prior to and following the exposure of pyruvic acid, the single beam spectra (250 scans) of surface- and gas- phase were acquired using a resolution of 4 cm<sup>-1</sup> and covering the spectral range of 800 to 4000 cm<sup>-1</sup>. During the exposure, single beam spectra of the silica surface (10 scans) were acquired using a Macro (OMNIC Macro Basics) at 60s-time intervals. Absorbance spectra of pyruvic acid on oxide particles are reported as the difference in the oxide spectra before and after exposure to pyruvic acid. Absorption bands due to gas-phase pyruvic acid, measured through the blank half of the tungsten grid, were subtracted to obtain FTIR spectra of the particles loaded on the tungsten grid.

Products formed on these surfaces following adsorption of pyruvic acid were obtained using a direct-injection linear ion trap (ThermoFisher Orbitrap) high resolution mass spectrometry (HRMS). Adsorbed products were removed from the oxide solid substrate using acetonitrile (LC-MS Optima-grade) and methanol (Fisher Scientific). Sample vial, syringe, and all other glassware used in the transfer process were cleaned prior to use with acetonitrile and Milli-Q water [18.2 MΩ.cm] and baked in an oven at 500 °C to further remove trace organics. All samples were stored at -20 °C and analyzed within 24 hours of collection.

HRMS analysis in both positive and negative mode was used, although the majority of detected ions were observed in negative mode ( $[M-H]^-$ ). The heated electrospray ionization (HESI) source was operated at 50°C. The ESI capillary was set to a voltage of 2.8 kV at 325°C. Internal standards in negative mode included high-purity deuterated hexanoic-d<sub>11</sub> acid and octanoic-d<sub>15</sub> acid (CDN Isotopes). Positive mode internal standards included hexylamine (99%) and hexadecylamine (98%) (both purchased from Sigma-Aldrich). The HESI-Orbitrap MS was calibrated prior to use. Spectra were acquired with a mass range of 80-2000 Da. Peaks with a mass error > 2 ppm were rejected and were calculated for composition with the following element ranges: <sup>12</sup>C, 0–30; <sup>1</sup>H, 0–50; <sup>16</sup>O, 0–10. The list of mass signatures having no labelled composition are found in Supporting Information (SI). Contamination was minimized by employing consistent method and instrumental blanks.

## 6.4 Results and Discussion

### *Pyruvic acid adsorption on Al<sub>2</sub>O<sub>3</sub> and TiO<sub>2</sub>: In-situ FTIR spectroscopy.*

Following exposure of aluminum oxide particle surfaces to pyruvic acid as a function of pressure under dry conditions (RH < 1%), new spectral features become apparent as shown in Figure 6.1a. Most notable is the infrared absorption bands in the region from 2500 to 4000 cm<sup>-1</sup> and from 900 to 1800 cm<sup>-1</sup>. Furthermore, the spectrum upon evacuation of gas-phase pyruvic acid, i.e., the dashed line spectrum shown in Figure 6.1a, shows that most of the adsorbed species remains on the Al<sub>2</sub>O<sub>3</sub> surface. Similarly, following exposure of the aluminum oxide surface to pyruvic acid at a fixed pressure of 20 mTorr, the time dependent spectrum shows infrared absorption bands in the region from 900 to 1900 cm<sup>-1</sup> which also remain in the spectrum following evacuation of gas-phase pyruvic acid. Although intensities of some of the infrared

absorption bands slightly decrease after evacuation, suggesting that there may be a very small amount of pyruvic acid that reversibly adsorbs on the Al<sub>2</sub>O<sub>3</sub> surface at 296 K.

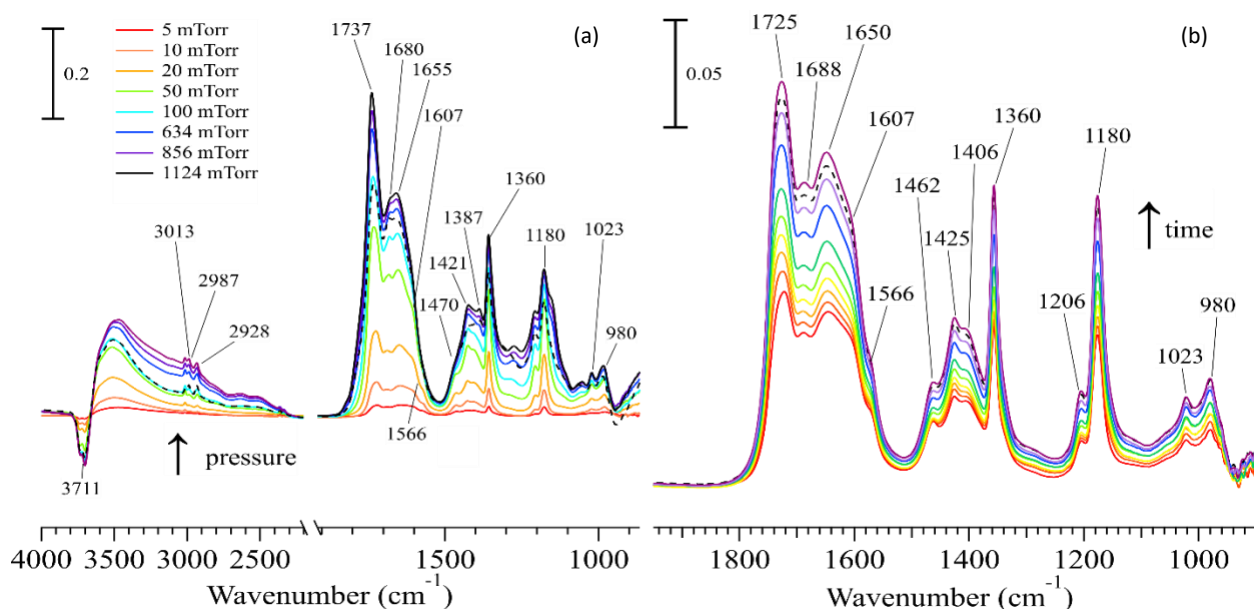


Figure 6.1. FTIR spectra of (a) Al<sub>2</sub>O<sub>3</sub> following exposure to gas-phase pyruvic acid for 20 minutes under dry conditions as a function of pyruvic acid pressure (5, 10, 20, 50, 100, 634, 856 and 1124 mTorr) in the spectral range from ca. 2500 to 4000 cm<sup>-1</sup> and 900 to 1900 cm<sup>-1</sup>; (b) Exposure of to 20 mTorr of gas-phase pyruvic acid as a function of time in the spectral range extending from 900 to 1950 cm<sup>-1</sup>, spectra are collected every 60 seconds. Spectra collected following evacuation of gas-phase pyruvic acid from the sample cell (shown by dashed line (---)). Differences and changes in frequencies for some of the absorption bands in the collected spectra shown in (a) and (b) are due to possible coverage effects as well as product formation (vide infra). Absorbance scale bars are shown in both (a) and (b). *Data and figure collected and analyzed by Dr. Yuan Fang.*

Similar to Al<sub>2</sub>O<sub>3</sub>, following exposure of gas-phase pyruvic acid to TiO<sub>2</sub> particle surfaces at 298 K under dry conditions (RH < 1%), as a function of pressure (Figure 6.2a) and time at a fixed pressure (Figure 6.2b) new peaks are observed in the infrared spectrum. In addition, the adsorption of pyruvic acid is irreversible as seen in the dotted spectrum shown in Figure 6.2b following evacuation of pyruvic acid vapor.

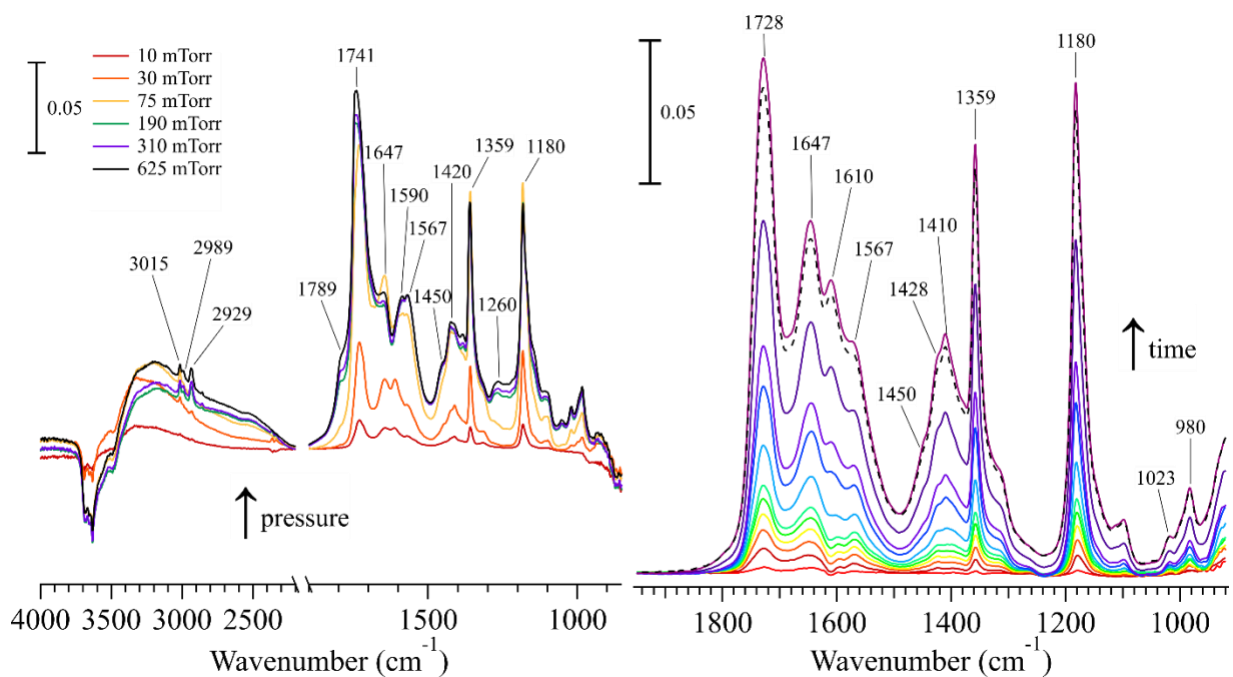


Figure 6.2. (a) FTIR spectra (800 to 4000  $\text{cm}^{-1}$ ) of  $\text{TiO}_2$  following exposure to gas-phase pyruvic acid for 20 minutes under dry conditions as a function of pressure (10, 30, 75, 190, 310 and 625 mTorr) in the spectral range from ca. 2500 to 4000  $\text{cm}^{-1}$  and 900 to 1900  $\text{cm}^{-1}$ ; (b) FTIR spectra (900 to 1900  $\text{cm}^{-1}$ ) of  $\text{TiO}_2$  following exposure to 50 mTorr pyruvic acid under dry conditions as a function of time, each spectrum collected every 60 seconds. The spectrum collected after evacuation (---) of gas-phase pyruvic acid in the time course measurements is shown in (b). Differences and changes in frequencies for some of the absorption bands in the collected spectra shown in (a) and (b) are due to possible coverage effects as well as product formation (vide infra). Absorbance scale bars are shown in both (a) and (b). *Data and figure collected and analyzed by Dr. Yuan Fang.*

These spectra for pyruvic acid adsorbed on the aluminum oxide and titanium dioxide surface differ from what is seen for pyruvic acid adsorption on hydroxylated silicon dioxide particles. In particular, following exposure of pyruvic acid to hydroxylated SiO<sub>2</sub> at similar pressures a very different spectrum is observed as shown in Figure 6.3. The spectrum has been previously assigned to vibrational modes of molecularly adsorbed pyruvic acid.<sup>82</sup> Additionally, upon evacuation of gas-phase pyruvic acid, the absorption bands disappear indicating reversible adsorption of pyruvic acid to the hydroxylated SiO<sub>2</sub> surface (see Ref 82 for more details). As seen in Figure 6.3, there are no absorptions in the region extending from 1450 to 1700 cm<sup>-1</sup> for pyruvic acid adsorbed on SiO<sub>2</sub>. In contrast, both Al<sub>2</sub>O<sub>3</sub> and TiO<sub>2</sub> exposed to similar pressures of pyruvic acid show broad absorptions in this region with multiple peaks and shoulders as seen in Figure 6.3 and these bands remain on the surface after evacuation of gas-phase pyruvic acid.

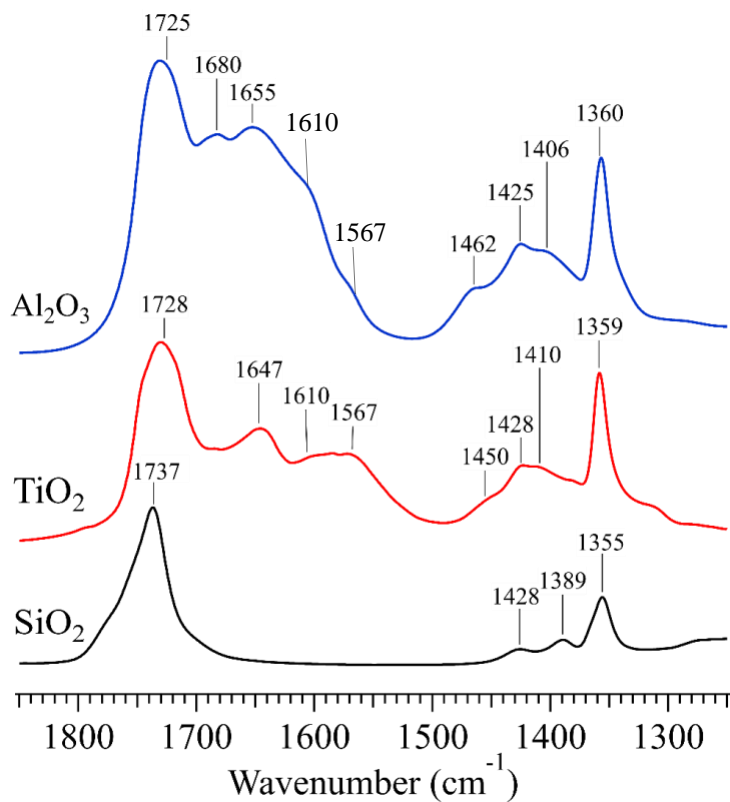
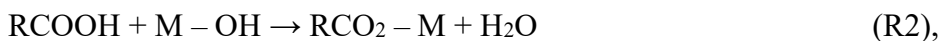


Figure 6.3. FTIR spectra in the region extending from 1250 to 1850 cm<sup>-1</sup> of Al<sub>2</sub>O<sub>3</sub>, TiO<sub>2</sub>, and SiO<sub>2</sub> following exposure to ca. 50 mTorr of pyruvic acid. Each spectrum was taken 20 minutes after introduction of gas-phase pyruvic acid under dry conditions (RH < 1%). *Data and figure collected and analyzed by Dr. Yuan Fang.*

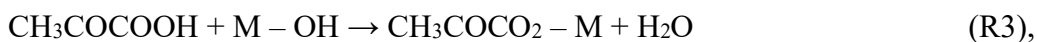


Previous studies have shown that on TiO<sub>2</sub> and Al<sub>2</sub>O<sub>3</sub> surfaces, organic acids including formic acid and acetic acid, can deprotonate on the surface according to the general reaction



where M = Al or Ti.<sup>85</sup>

This leaves a strongly adsorbed deprotonated carboxylate form on the surface. The carboxylate group has symmetric and asymmetric stretching modes in the spectral region between ca. 1400 and 1650 cm<sup>-1</sup>. Therefore, the adsorption of pyruvic acid on both TiO<sub>2</sub> and Al<sub>2</sub>O<sub>3</sub> surfaces can be represent by R3:



where M = Al or Ti.

The loss of -OH groups can be seen in the spectra shown in Figures 6.1a and 6.2a for Al<sub>2</sub>O<sub>3</sub> and TiO<sub>2</sub>, respectively, consistent with this reaction. In addition, the adsorbed water bending mode on Al<sub>2</sub>O<sub>3</sub> and TiO<sub>2</sub> surface is around 1640 cm<sup>-1</sup>, which overlaps with other absorption bands in this region most likely due to adsorbed pyruvate as well as other products that form on the surface (*vide infra*).

Assignment of the vibrational bands of adsorbed pyruvate is complex due to the presence of possible different binding modes to the surface and surface coverage effects that may play a role in the exact frequencies of the absorption bands. Focusing on the spectra shown in Figure 6.3 at a pressure around 50 mTorr, and comparison to the frequencies observed for sodium pyruvate, the following tentative assignment for the different absorption bands observed in the Al<sub>2</sub>O<sub>3</sub> and TiO<sub>2</sub> spectra shown are given in Table 6.1.

Table 6.1. Vibrational mode assignment ( $\text{cm}^{-1}$ ) for adsorbed pyruvate formed on the surface of  $\text{Al}_2\text{O}_3$  and  $\text{TiO}_2$  following adsorption of gas-phase pyruvic acid.\*

Mode	$\text{Al}_2\text{O}_3$	$\text{TiO}_2$	range of literature values for m pyruvate)
$\nu(\text{C}=\text{O})$	1725	1728	1709 <sup>86-88</sup>
$\nu_{\text{as}}(\text{CO}_2^-)$	1655, 1610,	1647, 1610	1657 to 1634 <sup>86,87</sup>
$\nu_{\text{s}}(\text{CO}_2^-)$	1462, 1406	1450, 1410	1421 to 1406 <sup>86-89</sup>
$\delta_{\text{as}}(\text{CH}_3)$	1425	1428	1460 to 1381 <sup>86-88</sup>
$\delta_{\text{s}}(\text{CH}_3)$	1360	1359	1430 to 1354 <sup>86-89</sup>

<sup>1</sup>. \*Frequencies reported in the table correspond to the spectra shown in Figure 6.3

When comparing the proposed assignments of adsorbed pyruvate to that of sodium pyruvate there are shifts in some of the absorption bands. For adsorbed pyruvate, there can be different coordination modes to the metal oxide surface that include: (1) monodentate mode in which only one carboxylate O atom is coordinated to a surface M atom; (2) bridged bidentate mode in which two carboxylate O atoms are coordinated to two different surface M atoms; and (3) chelating bidentate mode in which two carboxylate O atoms are coordinated to the same surface M atom.<sup>90-92</sup> The coordination modes is often determined through the difference in frequency between  $\nu_{\text{s}}(\text{CO}_2^-)$  and  $\nu_{\text{as}}(\text{CO}_2^-)$ , i.e.,  $\Delta\nu(\text{CO}_2^-)$ . However, given the broad features and the complexity of the spectra, a definitive assignment cannot be made. It has been reported that acetic acid coordinates via the chelating bidentate mode on these oxide surfaces, which could suggest that pyruvic acid (an  $\alpha$ -carbonyl acid), has similar adsorption behavior.<sup>85</sup>

Other absorbance bands centered at  $1680\text{ cm}^{-1}$  and  $1567\text{ cm}^{-1}$  are assigned to surface reaction products. For example, zymonic acid<sup>93</sup>, a closed enol ring dimer of pyruvic acid reported by Reed Harris et al.,<sup>6</sup> as well as other tautomers of zymonic acid<sup>6,93</sup>, can form on these oxide surfaces as well as potentially other forms of pyruvic acid dimers. Mass spectrometry

has been applied to further identify and analyze the products as presented below (vide infra) following discussion of pyruvic acid photochemistry.

Photochemistry of adsorbed pyruvic acid on Al<sub>2</sub>O<sub>3</sub> and TiO<sub>2</sub>: In situ FTIR spectroscopy. The photochemistry of adsorbed pyruvic acid on Al<sub>2</sub>O<sub>3</sub> and TiO<sub>2</sub>, respectively, was investigated using FTIR following 150 minutes of irradiation. Sample collection was performed following experiments, as well as after evacuation for further MS analysis. As seen in the difference spectra shown in Figure 6.4a and 6.4b, the intensity of infrared peaks attributed to the C=O ketone stretching mode and the C-C stretching mode of adsorbed pyruvate, as well as some other modes, decrease with irradiation time suggesting that adsorbed pyruvate photolyzes during the irradiation. Concomitant with the decrease in intensity of the pyruvate absorption bands, several positive infrared bands at between 1350 and 1800 cm<sup>-1</sup>, indicating the formation of new photochemical products. Peaks near 1568 and 1415cm<sup>-1</sup> on Al<sub>2</sub>O<sub>3</sub>, and peaks at 1577 and 1418 cm<sup>-1</sup> on TiO<sub>2</sub>, can be assigned to the  $\nu_{as}(\text{CO}_2^-)$  and  $\nu_s(\text{CO}_2^-)$  stretching modes of possibly other adsorbed carboxylate species, potentially adsorbed lactate<sup>94</sup>. However, detail product identification is needed because these infrared bands are broad, and in many cases, overlapping.

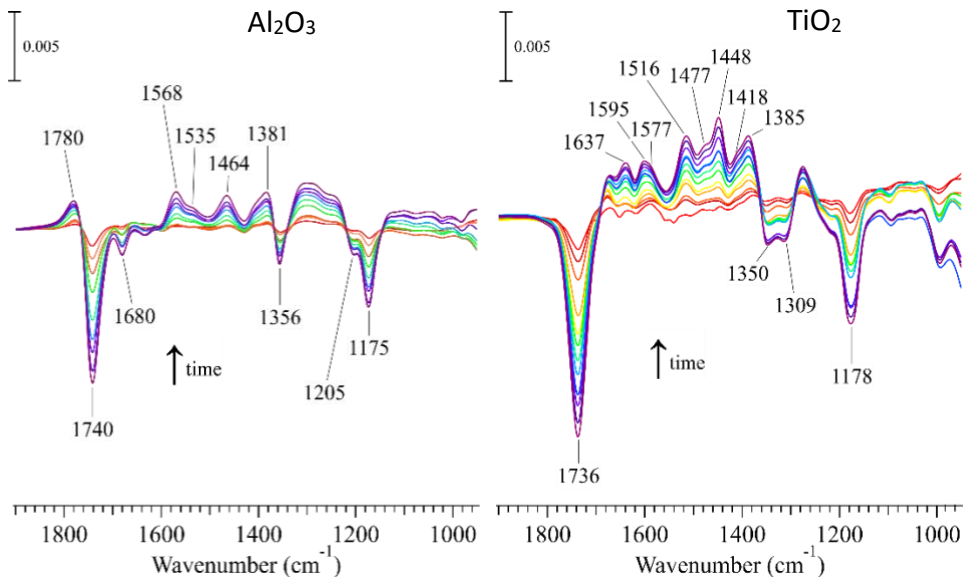


Figure 6.4. FTIR difference spectra in the spectral region extending from 950 to 1900  $\text{cm}^{-1}$  is shown. Following introduction of 100 mTorr of pyruvic acid followed by evacuation, adsorbed pyruvate remains on the surface of  $\text{Al}_2\text{O}_3$  and  $\text{TiO}_2$ . Each spectrum was collected every 15 minutes for a total 150 minutes. Difference spectra were obtained by subtracting the spectrum shown to the spectrum taken prior to irradiation. Difference spectra absorbance scale bars are shown for both  $\text{Al}_2\text{O}_3$  and  $\text{TiO}_2$ . *Data and figure collected and analyzed by Dr. Yuan Fang.*

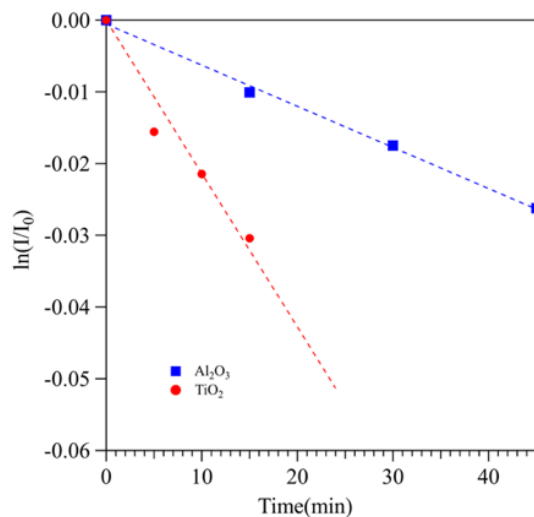


Figure 6.5. Comparison of the pyruvate loss from  $\text{Al}_2\text{O}_3$  and  $\text{TiO}_2$  surfaces during irradiation. The peak intensity of the C=O stretch for adsorbed pyruvate (near  $1730 \text{ cm}^{-1}$ ) before irradiation is used as  $I_0$ . The first order rate constant determined from the slope  $0.6 \times 10^{-4} \text{ min}^{-1}$  for  $\text{Al}_2\text{O}_3$  and  $2.1 \times 10^{-3} \text{ min}^{-1}$  for  $\text{TiO}_2$  respectively. *Data and figure collected and analyzed by Dr. Yuan Fang.*

Additionally, it was found that the initial loss rate of adsorbed pyruvate from TiO<sub>2</sub> surface is higher than that on Al<sub>2</sub>O<sub>3</sub> as shown in Figure 6.5. In agreement with a previous study by Gankanda et al<sup>56</sup> which shows that the initial rate of NO<sub>2</sub> formation from adsorbed nitrate dissociation is always higher on TiO<sub>2</sub> than Al<sub>2</sub>O<sub>3</sub>, our current study show that the photochemical loss of adsorbed pyruvate on semiconductor oxide (TiO<sub>2</sub>) is enhanced by ca. 3.5 times compared to an insulator oxide (Al<sub>2</sub>O<sub>3</sub>) indicating that electron hole pair formation at the semiconductor surface can play a role in the photochemistry of adsorbed pyruvate.

High resolution mass spectrometry of extracted products under dark and light conditions. To further determine the photochemical reaction products and possible pathways of adsorbed pyruvic acid on Al<sub>2</sub>O<sub>3</sub> and TiO<sub>2</sub>, extracts of adsorbed products on oxide surfaces were analyzed via mass spectrometry. The study of adsorbed pyruvic acid on oxide surfaces in dark conditions is also crucial to understand as it is necessary to consider contributions from any surface-mediated oligomerization processes. In fact, HRMS used in this study shows that adsorbed pyruvic acid on oxide surfaces, in dark conditions, produced many such oligomers as shown in Table 6.2.

The categories in Table 6.2 were assigned in a manner similar to previous studies<sup>55</sup>, and are as follows. First, “below threshold” was determined as ten times greater than the average noise for that system. The following three categories (termed “weak,” “medium” and “strong”) were then each identified as being an order of magnitude higher than the previous threshold. For example, for TiO<sub>2</sub> with irradiation, the noise average was between 102 counts, giving a “below threshold” value of 103 counts. “weak” signals then had intensities greater than 103 counts, “medium” signals had intensities greater than 104 counts, and “strong” signals had intensities greater than 105 counts.

Among many other produced oligomers, zymonic acid was specifically observed in our mass spectra as one of the major products in all experiments, including its fragment at  $m/z$  113. After evacuation to remove weakly bonded surface species, zymonic species (zymonic acid and its tautomers) exhibit a much higher intensity relative to pyruvate on  $\text{TiO}_2$  compared to  $\text{Al}_2\text{O}_3$ , suggesting that the zymonic species more readily forms on  $\text{TiO}_2$ . Both zymonic acid, other C5 species, and a few larger oligomers were observed in aqueous pyruvic acid dark conditions (see Table 6.2). Zymonic acid has also been detected in multiphase pyruvic acid photochemistry and can be formed via the dehydration of parapyrucic acid at the air-water interface as shown in Figure 6.6.<sup>6</sup>

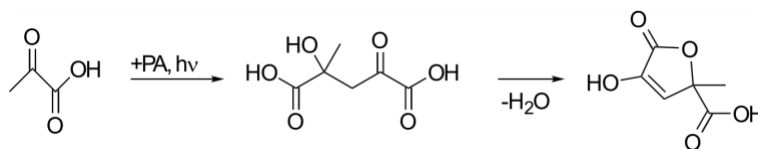


Figure 6.6. Possible photochemical formation pathway for zymonic acid from pyruvic acid (PA). This reaction has also been shown to proceed spontaneously through the dimerization of pyruvic acid.

We speculate that the pyruvic acid oligomers, those with two carboxyl groups or more, will be the more energetically stable (irreversible adsorbed) as it has been observed for other carboxylic acids that the most stable adsorption geometry, calculated by theoretical work on adsorption of oxalic acid on  $\text{TiO}_2$ , is expected to be deprotonation of both carboxyl groups.<sup>95,96</sup> In another study, attenuated total reflection Fourier-transform infrared spectroscopy (ATR-FTIR) was used to investigate malonic acid adsorbed on particulate  $\text{TiO}_2$  (P25 Degussa), suggesting adsorption of malonic acid on the  $\text{TiO}_2$  surface occurred via one bridging bidentate and one monodentate carboxylate group.<sup>96,97</sup> These other studies provide some insights into the potential bonding of zymonic acid on  $\text{TiO}_2$  and  $\text{Al}_2\text{O}_3$ .

Table 6.2. Selected Compiled Photochemistry HRMS Data of Adsorbed Pyruvic Acid on Al<sub>2</sub>O<sub>3</sub>

Assigned formula [M-H] <sup>-</sup>	Molecular compound	Average experimental m/z	Mass error (ppm)	Relative intensity dark conditions	Relative intensity light conditions	Comments
<b>C<sub>3</sub>H<sub>5</sub>O<sub>3</sub></b>	lactic acid	89.02467	2.85	Below threshold	Weak	increases with irradiation
<b>C<sub>5</sub>H<sub>5</sub>O<sub>3</sub></b>	zymonic acid fragment	113.02469	2.42	Medium	Medium	significant decrease after irradiation relative to pyruvate signal (see Figure 6.6)
<b>C<sub>5</sub>H<sub>7</sub>O<sub>4</sub></b>	acetolactic acid	131.03529	2.35	Below threshold	Medium	increases with irradiation
<b>C<sub>5</sub>H<sub>9</sub>O<sub>4</sub></b>	Unassigned	133.05090	2.02	Strong	Weak	strongest peak and decreases with irradiation
<b>C<sub>6</sub>H<sub>5</sub>O<sub>5</sub></b>	zymonic acid	157.01440	1.00	Medium	Medium	decreases with irradiation (see Figure 6.6)
<b>C<sub>6</sub>H<sub>9</sub>O<sub>5</sub></b>	lactic acid dimer	161.04575	1.28	Weak	Medium	increases with irradiation
<b>C<sub>6</sub>H<sub>7</sub>O<sub>6</sub></b>	parapyruvic acid	175.02495	0.8	Below threshold	Medium	increases with irradiation
<b>C<sub>6</sub>H<sub>9</sub>O<sub>4</sub></b>	Unassigned	145.05082	1.3	Weak	Strong	increases with irradiation
<b>C<sub>7</sub>H<sub>9</sub>O<sub>5</sub></b>	Unassigned	173.04572	1.03	Below threshold	Strong	strongest peak after irradiation
<b>C<sub>7</sub>H<sub>11</sub>O<sub>5</sub></b>	DMOHA	175.06134	0.81	Below threshold	Strong	increases with irradiation
<b>C<sub>8</sub>H<sub>11</sub>O<sub>6</sub></b>	Unassigned	203.05603	-0.38	Weak	Below threshold	decreases below threshold after irradiation
<b>C<sub>9</sub>H<sub>11</sub>O<sub>6</sub></b>	Unassigned	215.05611	-0.02	Below threshold	Below threshold	only present on TiO <sub>2</sub>
<b>C<sub>9</sub>H<sub>13</sub>O<sub>7</sub></b>	lactic acid trimer	233.06667	-0.02	Below threshold	Weak	increases with irradiation
<b>C<sub>12</sub>H<sub>13</sub>O<sub>4</sub></b>	Unassigned	221.08200	0.32	Below threshold	Strong	drastic increase with irradiation not seen on TiO <sub>2</sub>

Table 6.3. Selected Compiled Photochemistry HRMS Data of Adsorbed Pyruvic Acid on TiO<sub>2</sub>

Assigned formula [M-H] <sup>-</sup>	Molecular compound	Average experimental m/z	Mass error (ppm)	Relative intensity dark conditions	Relative intensity light conditions	Comments
<b>C<sub>3</sub>H<sub>5</sub>O<sub>3</sub></b>	lactic acid	89.02467	2.85	Below threshold	Weak	increases with irradiation
<b>C<sub>5</sub>H<sub>5</sub>O<sub>3</sub></b>	zymonic acid fragment	113.02468	2.36	Strong	Medium	significant decrease after irradiation relative to pyruvate signal (see Figure 6.7)
<b>C<sub>5</sub>H<sub>7</sub>O<sub>4</sub></b>	acetolactic acid	131.03526	2.11	Below threshold	Weak	increases with irradiation
<b>C<sub>5</sub>H<sub>9</sub>O<sub>4</sub></b>	Unassigned	133.05089	1.96	Medium	Weak	decreases with irradiation
<b>C<sub>6</sub>H<sub>5</sub>O<sub>5</sub></b>	zymonic acid	157.01443	1.17	Strong	Strong	strongest peak in both experiments
<b>C<sub>6</sub>H<sub>9</sub>O<sub>5</sub></b>	lactic acid dimer	161.04575	1.28	Weak	Medium	increases with irradiation
<b>C<sub>6</sub>H<sub>7</sub>O<sub>6</sub></b>	parapyruvic acid	175.02495	0.8	Below threshold	Medium	increases with irradiation
<b>C<sub>6</sub>H<sub>9</sub>O<sub>4</sub></b>	Unassigned	145.05082	1.27	Below threshold	Medium	increases with irradiation
<b>C<sub>7</sub>H<sub>9</sub>O<sub>5</sub></b>	Unassigned	173.04569	0.82	Below threshold	Medium	increases with irradiation
<b>C<sub>7</sub>H<sub>11</sub>O<sub>5</sub></b>	DMOHA	175.06134	0.84	Below threshold	Medium	increases with irradiation
<b>C<sub>8</sub>H<sub>11</sub>O<sub>6</sub></b>	Unassigned	203.05611	-0.01	Medium	Below threshold	decreases with irradiation
<b>C<sub>9</sub>H<sub>11</sub>O<sub>6</sub></b>	Unassigned	215.05611	-0.02	Medium	Medium	decreases with irradiation (see Figure 6.7); not detectable on Al <sub>2</sub> O <sub>3</sub> samples
<b>C<sub>9</sub>H<sub>13</sub>O<sub>7</sub></b>	lactic acid trimer	233.06667	-0.02	Below threshold	Weak	increases with irradiation
<b>C<sub>12</sub>H<sub>13</sub>O<sub>4</sub></b>	Unassigned	221.08189	-0.18	Weak	Weak	decreases with irradiation



Following irradiation for 150 minutes, products were extracted from the two oxide surfaces for HRMS analysis. Parapyruvic acid (and its other forms) is formed on both surfaces but only present following irradiation. Parapyruvic acid, a dimer of pyruvic acid is detected at  $m/z$  175.02495 (0.80 ppm mass error) by MS, in good agreement with previous photochemical studies by Rapf et al.<sup>55</sup> who calculated that it is energetically possible to photochemically generate parapyruvic acid. Zymonic acid, a closed enol ring dimer of pyruvic acid, is also detected here using MS at  $m/z$  157.01440 (1.17 ppm mass error) and its fragment 113.0268(2.3 ppm mass error). However, in our studies, zymonic acid is detected in both light and dark conditions, while parapyruvic acid is only seen as a photoproduct. This finding suggests that zymonic acid is a result of a thermally driven mechanism on the surface whereas parapyruvic acid can only be produced via photochemical processes. Furthermore, although zymonic acid is thought to be produced via a parapyruvic acid intermediate, in aqueous phase systems, these findings might also suggest that adsorbed zymonic acid is more energetically favored on the surface compared to parapyruvic acid. Selected oligomers of pyruvic acid, previously observed by Rapf and coworkers<sup>55</sup> were detected in this study, such as: DMOHA ( $m/z$  175.0607),  $C_{10}H_{14}O_6$  ( $m/z$  229.07176), and  $C_{10}H_{16}O_6$  ( $m/z$  231.0874). Interestingly, mass spectra of irradiated samples, for both  $Al_2O_3$  and  $TiO_2$ , showed dozens of unassigned oligomers ( $C > 10$ ) not observed in previous aqueous photochemical studies, possibly suggesting that pyruvic acid undergoes oligomerization pathways not available to purely aqueous systems.

Studies of aqueous pyruvic acid by Griffith et. al., Rapf et al and Guzman et al have shown the formation of  $C_6$  oligomers under irradiation.<sup>28,29, 55</sup> Either pure or aqueous pyruvic acid has been proved to spontaneously dimerize, likely through an aldol addition reaction,

forming parapyrvic acid and zymonic acid, as well as their tautomers and hydrates, in a known equilibrium dependent on pH and concentration as shown in Scheme 6.2.55,93

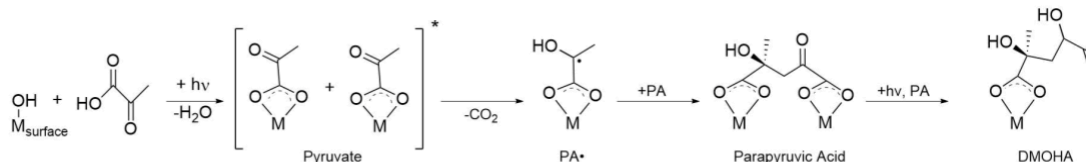


Figure 6.7. A proposed mechanism, adapted from Rapf and coworkers<sup>48</sup>, involves two excited state adsorbed pyruvate molecules, where one pyruvate undergoes hydrogen-abstraction via another pyruvate, leading to the formation of  $\text{CO}_2$ ,  $\text{CH}_3\text{-CO}\cdot$ , and  $\text{PA}\cdot$ . It is important to note that this mechanism does not proceed to form DMTA, a major product in the aqueous phase photochemistry of pyruvic acid.<sup>98</sup>

In addition, Rapf and coworkers<sup>55</sup> showed that dimer and trimer photoproducts could to undergo further photochemical reactions to form larger oligomeric products such as DMOHA through a CDMOHA intermediate, the adapted reaction scheme from this pathway can be seen in Figure 6.7. In this study, there is very little CDMOHA is detected, in amounts close to threshold counts. Thus, (but only in the  $\text{Al}_2\text{O}_3$  experiment)– differences in photoproducts on these metal oxide surfaces, compared to aqueous photochemical studies, might indicate the presence of additional mechanisms in the production of these oligomers., their presence and amounts, compared to past aqueous pyruvic acid studies further indicates that the surface plays a strong role in the stabilization of certain products compared to others. When comparing MS signal intensity ratios between DMOHA and lactate or pyruvate, an enhancement factor of over twenty of the C7 oligomer signal in both  $\text{TiO}_2$  and  $\text{Al}_2\text{O}_3$  is observed after irradiation.

For pyruvate, found on both  $\text{Al}_2\text{O}_3$  and  $\text{TiO}_2$  surfaces, only the methyl group is available for H-abstraction.<sup>98</sup> Furthering photochemical processing, after generating and combining the following radicals: geminal diol product  $\text{CH}_3\text{C}(\text{OH})_2$  (GD) and the hydroxyl acid product  $\text{CH}_2\text{C}(\text{O})\text{CO}_2\text{H}$  (OA); recombination products, dimethyltartaric acid, and 2, 5- dioxohexanedioic

acid, are not detected within the threshold of our HRMS results suggesting that intersystem crossing back to the singlet state is the dominant pathway for photochemistry of adsorbed pyruvate as these other products are due to triplet state chemistry. It is important to note, though, that oligomeric species can decompose into smaller product species. In the aqueous-phase, products resulting from the GD radical were also not detected (above threshold) in the HRMS analysis, suggesting that a GD radical pathway is not favorable for adsorbed pyruvic acid.

Furthermore, although photoproducts detected on both  $\text{TiO}_2$  and  $\text{Al}_2\text{O}_3$  are for the most part similar as determined by mass spectrometry, the rate of loss of pyruvate  $\text{TiO}_2$ , as seen in the FTIR experiments, is enhanced by a factor of 3.5. This suggests that both the adsorbed pyruvate and the semiconductor oxide facilitate photochemical product formation.

## 6.5 Conclusions

The surface chemistry of gas-phase pyruvic acid on hydroxylated oxide surfaces,  $\text{Al}_2\text{O}_3$  and  $\text{TiO}_2$ , at 298 K shows reaction with surface hydroxyl groups on these surfaces which yields predominantly adsorbed pyruvate and water. Upon irradiation on both oxide surfaces, adsorbed pyruvate forms various higher molar mass species such as parapyruvic acid. Zymonic species can also form under dark conditions, suggesting that the production of zymonic acid and its tautomers is a thermally driven oligomerization process whereas parapyruvic acid is produced through light-driven processes. Parapyruvic acid is reported to undergo further photolysis, forming pyruvic acid trimers and other larger molecules. However, parapyruvic acid is still observed after irradiation (under all conditions), suggesting that  $\text{Al}_2\text{O}_3$  and  $\text{TiO}_2$  surfaces and adsorbed irradiated pyruvic acid proceeds in an alternate pathway not previously suggested under different conditions. The observation that the formation of more complex, oligomeric species, including: zymonic acid, DMOHA, parapyruvic acid, C5 unassigned species,  $\text{C}_9\text{H}_{11}\text{O}_6$ , and

$C_{12}H_{13}O_4$  are favored on surfaces and under anoxic conditions raises intriguing possibilities for the relevance of this chemistry in the ancient, prebiotic environment, which contained very little  $O_2$  and ozone, allowing more UV light to reach the troposphere and Earth's surface. Parapyruvic acid has been observed in meteorites suggesting that an abiotic source exists for this compound.<sup>18</sup> Thus this chapter highlights the complex nature of heterogeneous photochemistry of pyruvic acid by identifying compounds which are not produced in the gas or aqueous-phase suggesting that heterogeneous and multiphase mineral-mediated chemistry and photochemistry of pyruvic acid warrants further study under various environmental conditions.

## 6.6 Acknowledgements

The authors gratefully acknowledge the support of the Alfred P. Sloan Foundation under grant number G-2017-9692 and the National Science Foundation Graduate Research Fellowship Program (DGE1650112). The contents of this study do not necessarily reflect the official views of the Alfred P. Sloan Foundation. The Alfred P. Sloan Foundation does not endorse the purchase of the commercial products used in this report. VV acknowledges partial support by the national Science Foundation (CHE 1611107) and by the US Army Research Laboratory and the US Army Research Office (Grant W911NF1710115).

Chapter 6 was reproduced with permission from: Alves, M. R.; Fang, Y.; Wall, K. J.; Vaida, V.; Grassian, V. H. Chemistry and Photochemistry of Pyruvic Acid Adsorbed on Oxide Surfaces. *J. Phys. Chem. A* 2019, 123 (35), 7661–7671. The dissertation author is the primary investigator and author of this paper.

## 6.7 Supporting Information

Two additional figures are shown in Supporting Information. Figures 6.6 and 6.7 show relative abundance of chosen assigned molecular formulas normalized to the intensity peak of pyruvate following extraction from  $\text{Al}_2\text{O}_3$  and  $\text{TiO}_2$ , respectively. This material is available free of charge on the ACS Publications website at <http://pubs.acs.org/>.

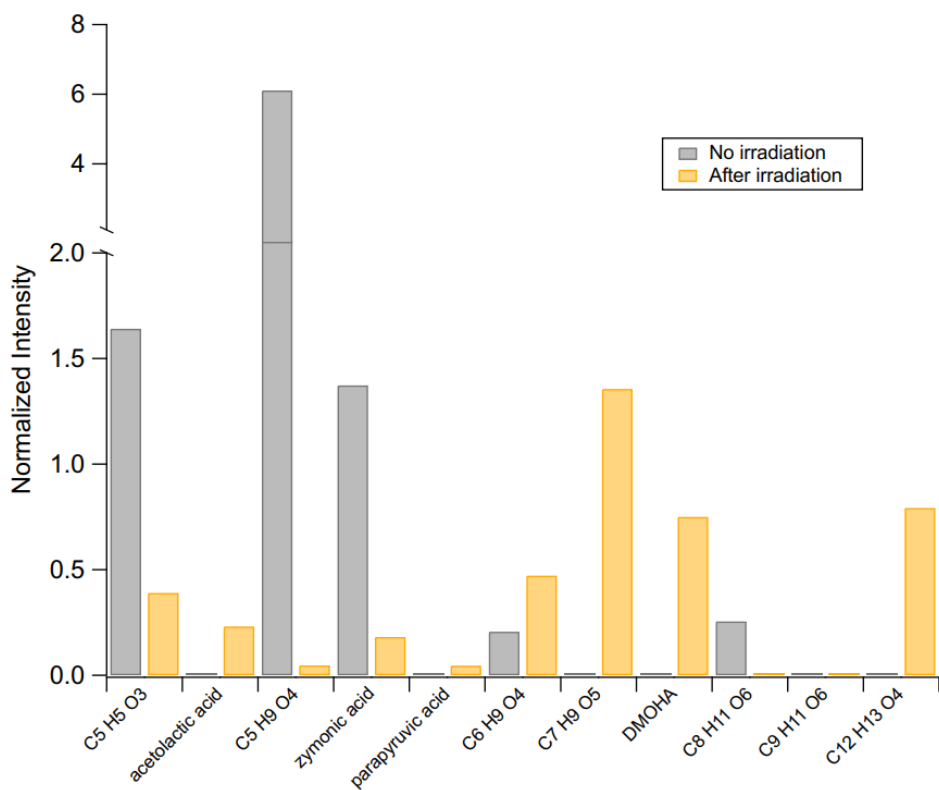


Figure 6.8. Relative abundance of chosen assigned molecular formulas normalized to the intensity peak of pyruvate following extraction from  $\text{Al}_2\text{O}_3$ .

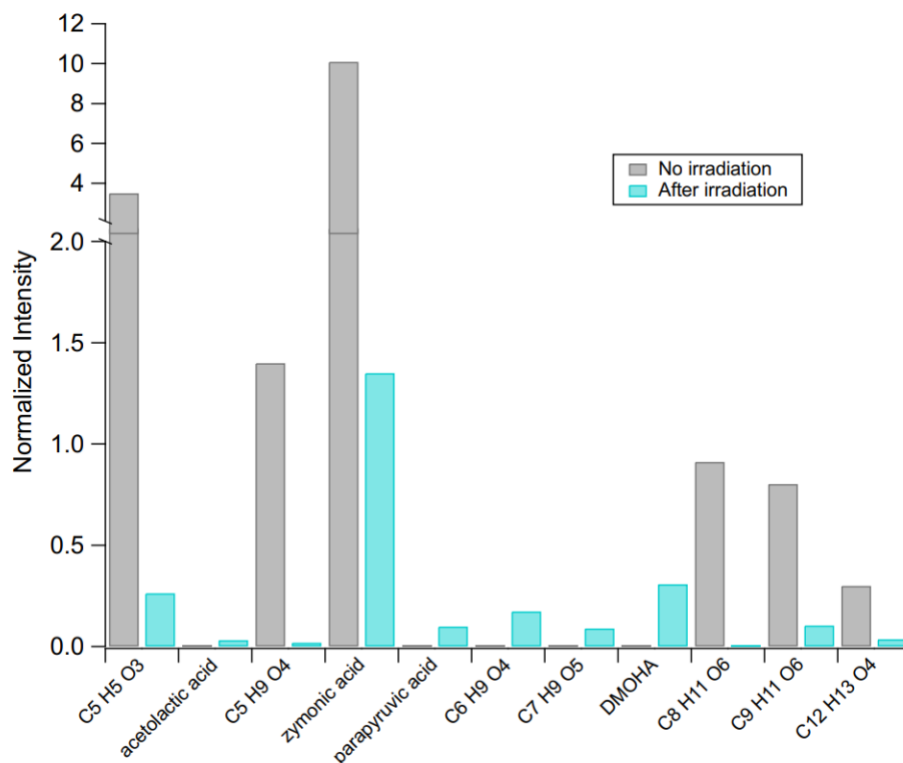


Figure 6.9. Relative abundance of chosen assigned molecular formulas normalized to the intensity peak of pyruvate following extraction from  $\text{TiO}_2$ .

## 6.8 References

- (1) George, C.; D'Anna, B.; Herrmann, H.; Weller, C.; Vaida, V.; Donaldson, D. J.; Bartels-Rausch, T.; Ammann, M. Emerging Areas in Atmospheric Photochemistry. In *Atmospheric and Aerosol Chemistry*; McNeill, V. F., Ariya, P. A., Eds.; Springer Berlin Heidelberg: Berlin, Heidelberg, **2014**; pp 1–53.
- (2) George, C.; Ammann, M.; D'Anna, B.; Donaldson, D. J.; Nizkorodov, S. A. Heterogeneous Photochemistry in the Atmosphere. *Chem. Rev.* **2015**, *115* (10), 4218–4258.
- (3) Rapf, R. J.; Vaida, V. Sunlight as an Energetic Driver in the Synthesis of Molecules Necessary for Life. *Phys. Chem. Chem. Phys.* **2016**, *18* (30), 20067–20084.
- (4) Vaida, V. Spectroscopy of Photoreactive Systems: Implications for Atmospheric Chemistry. *J. Phys. Chem. A* **2009**, *113* (1), 5–18.
- (5) Reed Harris, A. E.; Doussin, J. F.; Carpenter, B. K.; Vaida, V. Gas-Phase Photolysis of Pyruvic Acid: The Effect of Pressure on Reaction Rates and Products. *J. Phys. Chem. A* **2016**, *120* (51), 10123–10133.

- (6) Reed Harris, A. E.; Pajunoja, A.; Cazaunau, M.; Gratien, A.; Pangui, E.; Monod, A.; Griffith, E. C.; Virtanen, A.; Doussin, J. F.; Vaida, V. Multiphase Photochemistry of Pyruvic Acid under Atmospheric Conditions. *J. Phys. Chem. A* **2017**, *121* (18), 3327–3339.
- (7) Gligorovski, S.; Strekowski, R.; Barbati, S.; Vione, D. Environmental Implications of Hydroxyl Radicals ( $\bullet\text{OH}$ ). *Chem. Rev.* **2015**, *115* (24), 13051–13092.
- (8) S. A. Epstein, E. Tapavicza, F. Furche, and S. A. N. Direct Photolysis of Carbonyl Compounds Dissolved in Cloud and Fog Droplets. *Atmos. Chem. Phys. Discuss.* **2013**, *13*, 10905–10937.
- (9) Andreae, M. O.; Talbot, R. W.; Li, S.M. . Atmospheric Measurements of Pyruvic and Formic Acid. *J. Geophys.* **1987**, *92*, 6635–6641.
- (10) Bao, L.; Matsumoto, M.; Kubota, T.; Sekiguchi, K.; Wang, Q.; Sakamoto, K. Gas/Particle Partitioning of Low-Molecular-Weight Dicarboxylic Acids at a Suburban Site in Saitama, Japan. *Atmos. Environ.* **2012**, *47*, 546–553.
- (11) Chebbi, A.; Carlier, P. Carboxylic Acids in the Troposphere, Occurrence, Sources and Sinks: A Review. *Atmos. Environ.* **1996**, *30* (24), 4223–4249.
- (12) Ho, K. F.; Lee, S. C.; Cao, J. J.; Kawamura, K.; Watanabe, T.; Cheng, Y.; Chow, J. C. Dicarboxylic Acids, Ketocarboxylic Acids and Dicarboxyls in the Urban Roadside Area of Hong Kong. *Atmos. Environ.* **2006**, *40* (17), 3030–3040.
- (13) Khwaja, H. A. Atmospheric Concentrations of Carboxylic Acids and Related Compounds at a Semiurban Site. *Atmos. Environ.* **1995**, *29* (1), 127–139.
- (14) Limbeck, A.; Puxbaum, H.; Otter, L.; Scholes, M. C. Semivolatile Behavior of Dicarboxylic Acids and Other Polar Organic Species at a Rural Background Site (Nylsvley, RSA). *Atmos. Environ.* **2001**, *35* (10), 1853–1862.
- (15) Kawamura, K.; Kasukabe, H.; Barrie, L. A. Source and Reaction Pathways of Dicarboxylic Acids, Ketoacids and Dicarboxyls in Arctic Aerosols: One Year of Observations. *Atmos. Environ.* **1996**, *30* (10–11), 1709–1722.
- (16) Talbot, R. W.; Andreae, M. O.; Berresheim, H.; Jacob, D. J.; Beecher, K. M. Sources and Sinks of Formic, Acetic, and Pyruvic Acids over Central Amazonia: 2. Wet Season. *J. Geophys. Res. Atmos.* **1990**, *95*, 16799–16811.
- (17) Kawamura, K.; Bikkina, S. A Review of Dicarboxylic Acids and Related Compounds in Atmospheric Aerosols: Molecular Distributions, Sources and Transformation. *Atmos. Res.* **2016**, *170*, 140–160.
- (18) Cooper, G.; Reed, C.; Nguyen, D.; Carter, M.; Wang, Y. Detection and Formation

- Scenario of Citric Acid, Pyruvic Acid, and Other Possible Metabolism Precursors in Carbonaceous Meteorites. *Proc. Natl. Acad. Sci.* **2011**, *108* (34), 14015–14020.
- (19) Bikkina, S.; Kawamura, K.; Miyazaki, Y. Latitudinal Distributions of Atmospheric Dicarboxylic Acids, Oxocarboxylic Acids, and  $\alpha$ -Dicarbonyls over the Western North Pacific: Sources and Formation Pathways. *J. Geophys. Res.* **2015**, *120* (10), 5010–5035.
- (20) Griffith, E. C.; Shoemaker, R. K.; Vaida, V. Sunlight-Initiated Chemistry of Aqueous Pyruvic Acid: Building Complexity in the Origin of Life. *Orig. Life Evol. Biosph.* **2013**, *43* (4–5), 341–352.
- (21) Shapiro, R. Small Molecule Interactions Were Central to the Origin of Life. *Q. Rev. Biol.* **2006**, *81* (2), 105–126.
- (22) Guzman, M. I.; Martin, S. T. Prebiotic Metabolism: Production by Mineral Photoelectrochemistry of  $\alpha$ -Ketocarboxylic Acids in the Reductive Tricarboxylic Acid Cycle. *Astrobiology* **2009**, *9* (9), 833–842.
- (23) Orgel, L. E. The Implausibility of Metabolic Cycles on the Prebiotic Earth. *PLoS Biol.* **2008**, *6* (1), 0005–0013.
- (24) Griffith, E. C.; Tuck, A. F.; Vaida, V. Ocean-Atmosphere Interactions in the Emergence of Complexity in Simple Chemical Systems. *Acc. Chem. Res.* **2012**, *45* (12), 2106–2113.
- (25) Reed Harris, A. E.; Ervens, B.; Shoemaker, R. K.; Kroll, J. A.; Rapf, R. J.; Griffith, E. C.; Monod, A.; Vaida, V. Photochemical Kinetics of Pyruvic Acid in Aqueous Solution. *J. Phys. Chem. A* **2014**, *118* (37), 8505–8516.
- (26) Hall, G. E.; Muckerman, J. T.; Preses, J. M.; Weston, R. E.; Flynn, G. W. Time-Resolved FTIR Studies of the Photodissociation of Pyruvic Acid at 193 Nm. *Chem. Phys. Lett.* **1992**, *193* (1–3), 77–83.
- (27) Rincón, A. G.; Guzman, M. I.; Hoffmann, M. R.; Colussi, A. J. Optical Absorptivity versus Molecular Composition of Model Organic Aerosol Matter. *J. Phys. Chem. A* **2009**, *113* (39), 10512–10520.
- (28) Guzmán, M. I.; Colussi, A. J.; Hoffmann, M. R. Photoinduced Oligomerization of Aqueous Pyruvic Acid. *J. Phys. Chem. A* **2006**, *110* (10), 3619–3626.
- (29) Griffith, E. C.; Carpenter, B. K.; Shoemaker, R. K.; Vaida, V. Photochemistry of Aqueous Pyruvic Acid. *Proc. Natl. Acad. Sci.* **2013**, *110* (29), 11714–11719.
- (30) Grosjean, D. Atmospheric Reactions of Pyruvic Acid. *Atmos. Environ.* **1983**, *17* (11), 2379–2382.
- (31) Yamamoto, S.; Back, R. A. The Photolysis and Thermal Decomposition of Pyruvic Acid



- in the Gas Phase. *Can. J. Chem.* **1985**, *63* (2), 549–554.
- (32) Davidson, R. S.; Goodwin, D.; Violet, D. E. And Ph. FORNIER DE VIOLET. **1981**, *78* (3), 1–4.
- (33) Schreiner, P. R.; Reisenauer, H. P.; Ley, D.; Gerbig, D.; Wu, C.-H.; Allen, W. D. Methylhydroxycarbene: Tunneling Control of a Chemical Reaction. *Science* (80-. ). **2011**, *332* (6035), 1300–1303.
- (34) Closs, G. L.; Miller, R. J. Photoreduction and Photodecarboxylation of Pyruvic Acid. Applications of CIDNP to Mechanistic Photochemistry. *J. Am. Chem. Soc.* **1978**, *100* (11), 3483–3494.
- (35) Mellouki, A.; Mu, Y. On the Atmospheric Degradation of Pyruvic Acid in the Gas Phase. *J. Photochem. Photobiol. A Chem.* **2003**, *157* (2–3), 295–300.
- (36) Berges, M. G. M.; Warneck, P. Product Quantum Yields for the 350 Nm Photodecomposition of Pyruvic Acid in Air. *Berichte der Bunsengesellschaft für Phys. Chemie* **1992**, *96* (3), 413–416.
- (37) Carlton, A. G.; Turpin, B. J.; Lim, H. J.; Altieri, K. E.; Seitzinger, S. Link between Isoprene and Secondary Organic Aerosol (SOA): Pyruvic Acid Oxidation Yields Low Volatility Organic Acids in Clouds. *Geophys. Res. Lett.* **2006**, *33* (6), 2–5.
- (38) Stefan, M. I.; Bolton, J. R. Reinvestigation of the Acetone Degradation Mechanism in Dilute Aqueous Solution by the UV/H<sub>2</sub>O<sub>2</sub> Process. *Environ. Sci. Technol.* **1999**, *33* (6), 870–873.
- (39) Saito, K.; Sasaki, G.; Okada, K.; Tanaka, S. Unimolecular Decomposition of Pyruvic Acid: An Experimental and Theoretical Study. *J. Phys. Chem.* **1994**, *98*, 3756–3761.
- (40) Taylor, R. The Mechanism of Thermal Eliminations Part XXIII: The Thermal Decomposition of Pyruvic Acid. *Int. J. Chem. Kinet.* **1987**, *19* (8), 709–713.
- (41) Plath, K. L.; Takahashi, K.; Skodje, R. T.; Vaida, V. Fundamental and Overtone Vibrational Spectra of Gas-Phase Pyruvic Acid. *J. Phys. Chem. A* **2009**, *113* (26), 7294–7303.
- (42) Larsen, M. C.; Vaida, V. Near Infrared Photochemistry of Pyruvic Acid in Aqueous Solution. *J. Phys. Chem. A* **2012**, *116* (24), 5840–5846.
- (43) Takahashi, K.; Plath, K. L.; Skodje, R. T.; Vaida, V. Dynamics of Vibrational Overtone Excited Pyruvic Acid in the Gas Phase: Line Broadening through Hydrogen-Atom Chattering. *J. Phys. Chem. A* **2008**, *112* (32), 7321–7331.
- (44) Chang, X. P.; Fang, Q.; Cui, G. Mechanistic Photodecarboxylation of Pyruvic Acid:

- Excited-State Proton Transfer and Three-State Intersection. *J. Chem. Phys.* **2014**, *141* (15), 2–10.
- (45) Da Silva, G. Decomposition of Pyruvic Acid on the Ground-State Potential Energy Surface. *J. Phys. Chem. A* **2016**, *120* (2), 276–283.
- (46) Murto, J.; Raaska, T.; Kunttu, H.; Räsänen, M. Conformers and Vibrational Spectra of Pyruvic Acid: An Ab Initio Study. *J. Mol. Struct. THEOCHEM* **1989**, *200* (C), 93–101.
- (47) Rosenfeld, R. N.; Weiner, B. Energy Disposal in the Photofragmentation of Pyruvic Acid in the Gas Phase. *J. Am. Chem. Soc.* **1983**, *105* (11), 3485–3488.
- (48) Leermakers, P. A.; Vesley, G. F. The Photochemistry of  $\alpha$ -Keto Acids and  $\alpha$ -Keto Esters. I. Photolysis of Pyruvic Acid and Benzoylformic Acid. *J. Am. Chem. Soc.* **1963**, *85* (23), 3776–3779.
- (49) Kramer, Z. C.; Takahashi, K.; Vaida, V.; Skodje, R. T. Will Water Act as a Photocatalyst for Cluster Phase Chemical Reactions Vibrational Overtone-Induced Dehydration Reaction of Methanediol. *J. Chem. Phys.* **2012**, *136* (16).
- (50) Hans-Jürgen, B.; Edward, D.; Wilhelm, K. The Reversible Hydration of Carbonyl Compounds in Aqueous Solution Part II: The Kinetics of the Keto/Gem-diol Transition. *Berichte der Bunsengesellschaft für Phys. Chemie* **2018**, *86* (2), 129–134.
- (51) Pocker, Y.; Meany, J. E.; Nist, B. J.; Zadorojny, C. The Reversible Hydration of Pyruvic Acid. I. Equilibrium Studies. *J. Phys. Chem.* **1969**, *73* (9), 2879–2882.
- (52) Schnitzler, E. G.; Seifert, N. A.; Ghosh, S.; Thomas, J.; Xu, Y.; Jäger, W. Hydration of the Simplest  $\alpha$ -Keto Acid: A Rotational Spectroscopic and Ab Initio Study of the Pyruvic Acid-Water Complex. *Phys. Chem. Chem. Phys.* **2017**, *19* (6), 4440–4446.
- (53) Maroń, M. K.; Takahashi, K.; Shoemaker, R. K.; Vaida, V. Hydration of Pyruvic Acid to Its Geminal-Diol, 2,2-Dihydroxypropanoic Acid, in a Water-Restricted Environment. *Chem. Phys. Lett.* **2011**, *513* (4–6), 184–190.
- (54) Kroll, J. A.; Hansen, A. S.; Møller, K. H.; Axson, J. L.; Kjaergaard, H. G.; Vaida, V. Ultraviolet Spectroscopy of the Gas Phase Hydration of Methylglyoxal. *ACS Earth Sp. Chem.* **2017**, *1* (6), 345–352.
- (55) Rapf, R. J.; Perkins, R. J.; Carpenter, B. K.; Vaida, V. Mechanistic Description of Photochemical Oligomer Formation from Aqueous Pyruvic Acid. *J. Phys. Chem. A* **2017**, *121* (22), 4272–4282.
- (56) Gankanda, A.; Grassian, V. H. Nitrate Photochemistry on Laboratory Proxies of Mineral Dust Aerosol: Wavelength Dependence and Action Spectra. *J. Phys. Chem. C* **2014**, *118* (50), 29117–29125.

- (57) Rubasinghege, G.; Grassian, V. H. Surface-Catalyzed Chlorine and Nitrogen Activation: Mechanisms for the Heterogeneous Formation of ClNO, NO, NO<sub>2</sub>, HONO, and N<sub>2</sub>O from HNO<sub>3</sub> and HCl on Aluminum Oxide Particle Surfaces. *J. Phys. Chem. A* **2012**, *116* (21), 5180–5192.
- (58) Rubasinghege, G.; Grassian, V. H. Photochemistry of Adsorbed Nitrate on Aluminum Oxide Particle Surfaces. *J. Phys. Chem. A* **2009**, *113* (27), 7818–7825.
- (59) Baltrusaitis, J.; Schuttlefield, J.; Jensen, J. H.; Grassian, V. H. FTIR Spectroscopy Combined with Quantum Chemical Calculations to Investigate Adsorbed Nitrate on Aluminium Oxide Surfaces in the Presence and Absence of Co-Adsorbed Water. *Phys. Chem. Chem. Phys.* **2007**, *9* (36), 4970–4980.
- (60) Li, P.; Perreau, K. A.; Covington, E.; Song, C. H.; Carmichael, G. R.; Grassian, V. H. Heterogeneous Reactions of Volatile Organic Compounds on Oxide Particles of the Most Abundant Crustal Elements: Surface Reactions of Acetaldehyde, Acetone, and Propionaldehyde on SiO<sub>2</sub>, Al<sub>2</sub>O<sub>3</sub>, Fe<sub>2</sub>O<sub>3</sub>, TiO<sub>2</sub>, and CaO. *J. Geophys. Res. Atmos.* **2001**, *106*, 5517–5529.
- (61) Hanisch, F.; Crowley, J. N. Heterogeneous Reactivity of Gaseous Nitric Acid on Al<sub>2</sub>O<sub>3</sub>, CaCO<sub>3</sub>, and Atmospheric Dust Samples: A Knudsen Cell Study. *J. Phys. Chem. A* **2001**, *105*, 3096–3106.
- (62) Liu, Y.; He, H.; Mu, Y. Heterogeneous Reactivity of Carbonyl Sulfide on  $\alpha$ -Al<sub>2</sub>O<sub>3</sub> and  $\gamma$ -Al<sub>2</sub>O<sub>3</sub>. *Atmos. Environ.* **2008**, *42* (6), 960–969.
- (63) Chen, H.; Nanayakkara, C. E.; Grassian, V. H. Titanium Dioxide Photocatalysis in Atmospheric Chemistry. *Chem. Rev.* **2012**, *112* (11), 5919–5948.
- (64) Nanayakkara, C. E.; Larish, W. A.; Grassian, V. H. Titanium Dioxide Nanoparticle Surface Reactivity with Atmospheric Gases, CO<sub>2</sub>, SO<sub>2</sub>, and NO<sub>2</sub>: Roles of Surface Hydroxyl Groups and Adsorbed Water in the Formation and Stability of Adsorbed Products. *J. Phys. Chem. C* **2014**, *118* (40), 23011–23021.
- (65) Tang, M.; Larish, W. A.; Fang, Y.; Gankanda, A.; Grassian, V. H. Heterogeneous Reactions of Acetic Acid with Oxide Surfaces: Effects of Mineralogy and Relative Humidity. *J. Phys. Chem. A* **2016**, *120* (28), 5609–5616.
- (66) Fang, Y.; Tang, M.; Grassian, V. H. Competition between Displacement and Dissociation of a Strong Acid Compared to a Weak Acid Adsorbed on Silica Particle Surfaces: The Role of Adsorbed Water. *J. Phys. Chem. A* **2016**, *120* (23), 4016–4024.
- (67) Weschler, C. J.; Shields, H. C. Potential Reactions among Indoor Pollutants. *Atmos. Environ.* **1997**, *31* (21), 3487–3495.

- (68) Yu, B. F.; Hu, Z. B.; Liu, M.; Yang, H. L.; Kong, Q. X.; Liu, Y. H. Review of Research on Air-Conditioning Systems and Indoor Air Quality Control for Human Health. *Int. J. Refrig.* **2009**, *32* (1), 3–20.
- (69) Tham, K. W.; Zuraimi, M. S. Size Relationship between Airborne Viable Bacteria and Particles in a Controlled Indoor Environment Study. *Indoor Air* **2005**, *15 Suppl 9* (Suppl 9), 48–57.
- (70) Cox, S. S.; Little, J. C.; Hodgson, A. T. Predicting the Emission Rate of Volatile Organic Compounds from Vinyl Flooring. *Environ. Sci. Technol.* **2002**, *36* (4), 709–714.
- (71) Fujishima, A.; Rao, T. N.; Tryk, D. A. Titanium Dioxide Photocatalysis. *J. Photochem. Photobiol. C Photochem. Rev.* **2000**, *1* (1), 1–21.
- (72) Romeas, V.; Pichat, P.; Guillard, C.; Chopin, T.; Lehaut, C. Testing the Efficacy and the Potential Effect on Indoor Air Quality of a Transparent Self-Cleaning TiO<sub>2</sub>-Coated Glass through the Degradation of a Fluoranthene Layer. *Ind. Eng. Chem. Res.* **1999**, *38* (10), 3878–3885.
- (73) Paz, Y.; Luo, Z.; Rabenberg, L.; Heller, A. Photooxidative Self-Cleaning Transparent Titanium Dioxide Films on Glass. *J. Mater. Res.* **1995**, *10* (11), 2842–2848.
- (74) Anandan, S.; Narasinga Rao, T.; Sathish, M.; Rangappa, D.; Honma, I.; Miyauchi, M. Superhydrophilic Graphene-Loaded TiO<sub>2</sub> thin Film for Self-Cleaning Applications. *ACS Appl. Mater. Interfaces* **2013**, *5* (1), 207–212.
- (75) Linsebigler, A. L.; Lu, G.; Yates, J. T. Photocatalysis on TiO<sub>2</sub> Surfaces: Principles, Mechanisms, and Selected Results. *Chem. Rev.* **1995**, *95* (3), 735–758.
- (76) Hurum, D. C.; Agrios, A. G.; Gray, K. A.; Rajh, T.; Thurnauer, M. C. Explaining the Enhanced Photocatalytic Activity of Degussa P25 Mixed-Phase TiO<sub>2</sub> Using EPR. *J. Phys. Chem. B* **2003**, *107* (19), 4545–4549.
- (77) Jones, G.; Jenkins, S. J. Insight into the Reduction of Pyruvic Acid to Lactic Acid over Cu{110}: The Crucial Role of Intramolecular Tunneling in Direct Hydrogenation. *J. Am. Chem. Soc.* **2008**, *130* (44), 14483–14492.
- (78) Martin, C.; Huser, H.; Servat, K.; Kokoh, K. B. Electrosynthesis of Lactic Acid on Copper and Lead Cathodes in Aqueous Media. *Electrochim. Acta* **2005**, *51* (1), 111–117.
- (79) Martin, C.; Huser, H.; Servat, K.; Kokoh, K. B. Electrosynthesis of Lactic Acid and 2,3-Dimethyltartaric Acid from Pyruvic Acid on Lead Cathode in Aqueous Medium. *Tetrahedron Lett.* **2006**, *47* (20), 3459–3462.
- (80) Fang, Y.; Lesnicki, D.; Wall, K. J.; Gaigeot, M. P.; Sulpizi, M.; Vaida, V.; Grassian, V. H. Heterogeneous Interactions between Gas-Phase Pyruvic Acid and Hydroxylated Silica

- Surfaces: A Combined Experimental and Theoretical Study. *J. Phys. Chem. A* **2019**, *123* (5), 983–991.
- (81) Cuendet, P.; Graetzel, M. Direct Photoconversion of Pyruvate to Lactate in Aqueous Titanium Dioxide Dispersions. *J. Phys. Chem.* **2005**, *91* (3), 654–657.
- (82) Filatova, E. O.; Konashuk, A. S. Interpretation of the Changing the Band Gap of Al<sub>2</sub>O<sub>3</sub> Depending on Its Crystalline Form: Connection with Different Local Symmetries. *J. Phys. Chem. C* **2015**, *119* (35), 20755–20761.
- (83) Goodman, A. L.; Bernard, E. T.; Grassian, V. H. Spectroscopic Study of Nitric Acid and Water Adsorption on Oxide Particles: Enhanced Nitric Acid Uptake Kinetics in the Presence of Adsorbed Water. *J. Phys. Chem. A* **2001**, *105* (26), 6443–6457.
- (84) Goodman, A. L.; Underwood, G. M.; Grassian, V. H. A Laboratory Study of the Heterogeneous Reaction of Nitric Acid on Calcium Carbonate Particles. *J. Geophys. Res.* **2000**, *105* (D23), 29053–29064.
- (85) Tong, S. R.; Wu, L. Y.; Ge, M. F.; Wang, W. G.; Pu, Z. F. Heterogeneous Chemistry of Monocarboxylic Acids on  $\alpha$ -Al<sub>2</sub>O<sub>3</sub> at Different Relative Humidities. *Atmos. Chem. Phys.* **2010**, *10* (16), 7561–7574.
- (86) Katon, J. E.; Covington, D. T. The Vibrational Spectra of Crystalline Sodium Pyruvate. *Spectrosc. Lett.* **1979**, *12* (10), 761–766.
- (87) Kakihana, M.; Okamoto, M. Vibrational Analysis of Pyruvate Ion Molecules and Estimation of Equilibrium Constants for Their Hydrogen Isotopic Exchange Reactions. *J. Phys. Chem.* **1984**, *88* (9), 1797–1804.
- (88) Long, B. D. A.; George, W. Spectroscopic Study of the Pyruvate Ion. **1960**.
- (89) Ray, W.; Katon, J.; Phillips, D. Structure, Hydrogen Bonding and Vibrational Spectra of Pyruvic Acid. *J. Mol. Struct.* **1981**, *74* (1), 75–84.
- (90) Sokolow, J. D.; Trzop, E.; Chen, Y.; Tang, J.; Allen, L. J.; Crabtree, R. H.; Benedict, J. B.; Coppens, P. Binding Modes of Carboxylate- and Acetylacetonate-Linked Chromophores to Homodisperse Polyoxotitanate Nanoclusters. *J. Am. Chem. Soc.* **2012**, *134* (28), 11695–11700.
- (91) Dobson, K. D.; McQuillan, A. J. In Situ Infrared Spectroscopic Analysis of the Adsorption of Aromatic Carboxylic Acids to TiO<sub>2</sub>, ZrO<sub>2</sub>, Al<sub>2</sub>O<sub>3</sub>, and Ta<sub>2</sub>O<sub>5</sub> from Aqueous Solutions. *Spectrochim. Acta - Part A Mol. Biomol. Spectrosc.* **2000**, *56* (3), 557–565.
- (92) Dobson, K. D.; McQuillan, A. J. In Situ Infrared Spectroscopic Analysis of the Adsorption of Aliphatic Carboxylic Acids to TiO<sub>2</sub>, ZrO<sub>2</sub>, Al<sub>2</sub>O<sub>3</sub>, and Ta<sub>2</sub>O<sub>5</sub> from Aqueous Solutions. *Spectrochim. Acta Part A Mol. Biomol. Spectrosc.* **1999**, *55* (7–8), 1395–1405.

- (93) Perkins, R. J.; Shoemaker, R. K.; Carpenter, B. K.; Vaida, V. Chemical Equilibria and Kinetics in Aqueous Solutions of Zymonic Acid. *J. Phys. Chem. A* **2016**, *120* (51), 10096–10107.
- (94) Chen, Y. K.; Lin, Y. F.; Peng, Z. W.; Lin, J. L. Transmission FT-IR Study on the Adsorption and Reactions of Lactic Acid and Poly(Lactic Acid) on TiO<sub>2</sub>. *J. Phys. Chem. C* **2010**, *114* (41), 17720–17727.
- (95) Fahmi, A.; Minot, C.; Fourre, P.; Nortier, P. A Theoretical Study of the Adsorption of Oxalic Acid on TiO<sub>2</sub>. *Surf. Sci.* **1995**, *343*, 261–272.
- (96) Thomas, A. G.; Syres, K. L. Adsorption of Organic Molecules on Rutile TiO<sub>2</sub> and Anatase TiO<sub>2</sub> Single Crystal Surfaces. *Chem. Soc. Rev.* **2012**, *41* (11), 4207.
- (97) Dolamic, I.; Bürgi, T. Photoassisted Decomposition of Malonic Acid on TiO<sub>2</sub> Studied by in Situ Attenuated Total Reflection Infrared Spectroscopy. *J. Phys. Chem. B* **2006**, *110* (30), 14898–14904.
- (98) Rapf, R. J.; Dooley, M. R.; Kappes, K.; Perkins, R. J.; Vaida, V. PH Dependence of the Aqueous Photochemistry of  $\alpha$ -Keto Acids. *J. Phys. Chem. A* **2017**, *121* (44), 8368–8379.

## **Chapter 7: SiO<sub>2</sub> Interactions with Hypochlorous Acid: Insights into the Interaction of Cleaning Products with Glass Surfaces**

### **7.1 Abstract**

Indoor chemistry, i.e. the chemistry that occurs in indoor environments, has recently received increased attention in the scientific community due the fact that there is so little known given its unique environment relative to outdoors including point combustion sources (candles, gas stoves, etc.), high aerosol concentrations, high surface:volume ratios, and the important role of human occupants. During the 2018 HOMEChem campaign, a large collaborative study aimed at identifying important aspects of indoor chemistry, observed evidence of certain surface-initiated reactions during cleaning events – chlorine cleaning in particular.<sup>1</sup> Although these observations represent new findings, it was clear that little was known about the indoor chemistry of chlorine-containing cleaning products in the air and with indoor surfaces. Therefore, in this study, we probe the interaction of bleach headspace gas with high surface area silica as a proxy for window glass – an “inert” and impervious surface. Using attenuated total reflectance Fourier Transform infrared (ATR-FTIR) spectroscopy, results suggest irreversible chemical transformation occurs at the silica surface. Conductivity and ion chromatography methods support the presence of surface chloride (Cl<sup>-</sup>) and possibly chlorine oxyanions (ClO<sub>x</sub>) after surfaces have been exposed to bleach and HOCl. Such interactions between HOCl and indoor relevant surfaces at room temperature have not been studied previously and introduce the question of possible surface-mediated reactions with gas- or condensed- phase species.

### **7.2 Introduction**

While people spend the large majority of their lives in indoor spaces containing a chemical “cocktail” containing a myriad of different surfaces, gases, and combustion and light sources, our

understanding of how these unique components interact with each other is greatly lacking.<sup>2-4</sup> The possible implications for human health concern necessitates the study of the indoors to constrain the major variables that control this convoluted chemical paradigm. The use of strong household cleaners indoors is a significant topic of interest due to their powerful oxidizing or reducing capabilities – likely producing a variety of byproducts with unknown properties.<sup>5</sup> Overall, strong oxidizers such as quaternary ammonia compounds,  $\text{OCl}^-$  and other oxychlorides, peroxygens ( $\text{H}_2\text{O}_2$  or peracetic acid), phenolics, and alcohols make up the vast majority of household disinfection products in the United States.<sup>6</sup> These disinfection products can be incredibly effective in their purpose, are widely used, and yet they are one of the least understood aspects of indoor air chemistry and health.<sup>7</sup> A few studies have significantly correlated usage of caustic cleaners in the home to adverse health effects such as asthma and wheezing in children.<sup>8,9</sup> Conversely, some studies showed no significant connection between cleaners and respiratory issues where the possible differences in conclusions being age of subjects, location, or many other unknown factors.<sup>10</sup> Whether these negative health effects are due to: the primary ejection of the cleaner sprays as aerosols, the active disinfection chemical products themselves, the gas-phase form of the cleaners and the secondary organic aerosol they can form, or the oxidized/reacted products of the initial active component – is completely unknown. Studying the mechanism of which these strong and caustic chemical components interact with the indoor environment could facilitate more accurate and holistic understanding of how these chemicals impact human health.

Hypochlorous acid ( $\text{HOCl}$ ) is produced in the gas phase during and after cleaning events with bleach products. This oxidative compound is formed from the natural acidification of the main active ingredient, hypochlorite ( $\text{OCl}^-$ ), present in the bleach solution as the aqueous solution uptakes  $\text{CO}_2$  and the pH of the solution increases leading to  $\text{HOCl}$  emission as shown in Eq. (1).





How HOCl interacts with its environment in the indoor space, via gas-phase reactions, condensed- and surface-phase interactions, are poorly understood. Other important gas phase compounds can also be produced from bleach products, from the reaction between HOCl/OCl<sup>-</sup> and ammonia (NH<sub>3</sub>) or nitrogen pentoxide (N<sub>2</sub>O<sub>5</sub>), such as chloramines (NH<sub>x</sub>Cl<sub>y</sub>) and nitryl chloride (ClNO<sub>2</sub>).<sup>5,11</sup> Recently, a study published by Mattila and coworkers, observed the presence of a large unidentified reservoir for hypochlorous acid indoors during the 2018 HOMEChem campaign – larger than what could be attributed to gases and aerosols.<sup>12</sup> Tentatively, this reservoir was hypothesized to be due to surfaces. Whether or not these supposed surface interactions are reversible, reactive, or produce other unique products is currently not known.

Silica, or SiO<sub>2</sub>, has been studied extensively over the past century and continues to be an area of interest for material and surface scientists. Though window glass (amorphous SiO<sub>2</sub>) can be commonly considered as a relatively inert substrate which is an insulator and not a semiconductor such as titanium dioxide (TiO<sub>2</sub>), surface hydroxyl groups formed in the presence of water (relative humidity > 5%) gives the surface adsorptive properties.<sup>13,14</sup> Despite SiO<sub>2</sub> being a ubiquitous surface, its interaction with HOCl, a common oxidative gas molecule, under room temperature conditions is not well studied. In this study, we look at the interaction between silica and HOCl.

### 7.3 Experimental Methods

To probe the chemistry of HOCl on an indoor surface, silica (SiO<sub>2</sub>, OX50 Aerosil) was used as a window glass proxy and baked at 500 °C for 12 hours to remove trace organics prior to exposure. Thin films of the silica were created by suspending the silica in water and were

allowed to dry on an AMTIR crystal (Amorphous Material Transmitting IR radiation, Pike Technologies) overnight. Hypochlorous acid was generated by either buffering a 10-15% sodium hypochlorite solution (Sigma Aldrich) or bleach (Clorox), with monosodium phosphate to achieve a slightly acidic pH of 6.4, the method being adapted from Schwartz-Narbonne and coworkers.<sup>5</sup>

A flow of 10 sccm of HOCl gas was transferred into a dilution line containing 0.1 slpm of zero air, achieving a concentration of 61 +/- 1 ppm. The concentration of HOCl and Cl<sub>2</sub> was measured using a 53.5 cm gas-phase UV-VIS cell, using wavelengths of 242 nm and 330 nm respectively to calculate concentration. The absorption cross sections used to calculate the concentration of HOCl and Cl<sub>2</sub>, were  $2.03 \times 10^{-19} \text{ cm}^2 \text{ molecule}^{-1}$  and  $2.55 \times 10^{-19} \text{ cm}^2 \text{ molecule}^{-1}$  respectively.<sup>15</sup> A pulsed Xe lamp (company) was used as a source and a diode array detector (Ocean Optics USB 3000) to measure the change in absorbance respective to the background. ATR-FTIR spectra were obtained using a Nicolet iS10 FTIR spectrometer (Thermo Fisher) equipped with an MCT/A detector and the AMTIR crystal base at 4 cm<sup>-1</sup> resolution using an average of 256 scans over a spectral range of 600–4000 cm<sup>-1</sup>. Measurements of chlorine oxyanions were carried out using ion chromatography (ICS-2000 ThermoFisher) and TraceCERT™ IC standards including chlorite, chlorate, and perchlorate (Sigma Aldrich).

## 7.4 Results and Discussion

Due to the complex nature of the indoor environment, studying surface-level and mechanistic chemistry can be challenging. To find which surface (or surfaces) are acting as a sink for gas-phase HOCl, silica or window glass was used as a simple starting point. Initial hypotheses suggested the HOCl will most likely interact with surface hydroxyl groups via hydrogen-bonding and subsequently desorb upon evacuation of the AMTIR chamber. A

surprising result shows that products are actually formed at the surface, as shown in Figure 1 where the positive growing peaks in the difference spectra seem to be irreversibly bound. Desorption over long periods of time (hours) with clean dry air do not remove these species. The infrared data show HOCl covalently interacting with the silica with multiple peaks upon adsorption observed at 963, 859, and 730  $\text{cm}^{-1}$ . These peaks suggest there might be multiple species being produced. Possibly as chlorine oxyanions (e.g., chlorate) or functionalized silica (e.g. Si-Cl, Si-ClO<sub>x</sub>, etc.). For reference, the spectrum of gas-phase HOCl shows the  $\nu$ O-Cl stretch is measured to be around 725  $\text{cm}^{-1}$ , suggesting that ClO<sub>x</sub> species are being formed. The appearance of these unknown products is well-correlated with the decrease of Si-O-Si bands around 1200  $\text{cm}^{-1}$ . It should be noted that this experiment occurred under a faster rate than normal as the concentration of HOCl is around 64 ppm during exposure. Many studies observing gas phase HOCl in indoor spaces report levels between 0.1 and 5 ppm during cleaning events.<sup>5,12</sup>

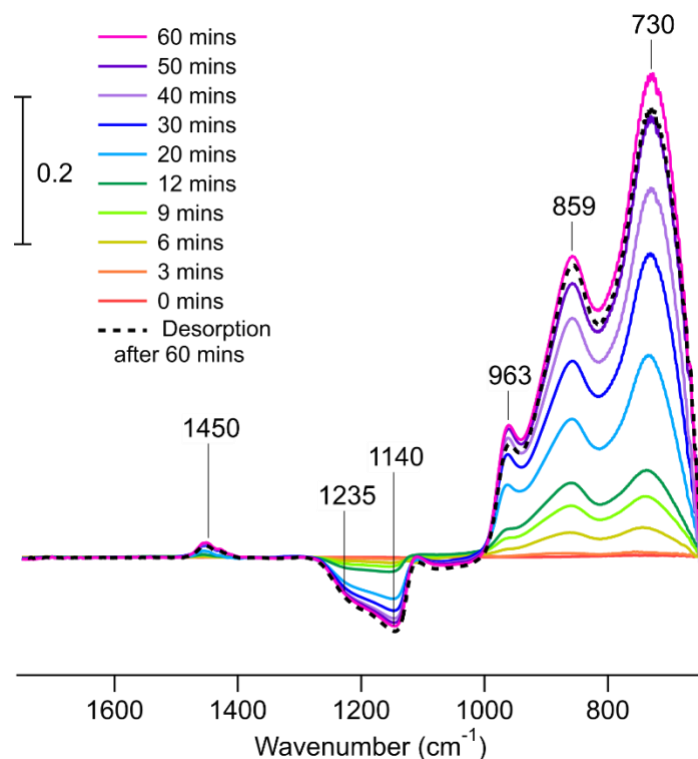


Figure 7.1. FTIR difference spectra of SiO<sub>2</sub> following exposure to gas-phase HOCl and Cl<sub>2</sub> for 60 mins under relatively dry conditions (RH < 15%) as a function of time. A spectrum was collected following 60 minutes of dry clean air flowing over the chlorine-exposed silica thin film (shown by the black dashed line). Spectrum used for background subtraction was a clean silica thin film in dry air.

The presence of products at the surface was further proven through the use of conductivity measurements and ion chromatography. Batches of silica were exposed to similar conditions from the ATR-FTIR studies for up to two hours. After a one-hour period of desorption using dry zero air, the exposed silica nanoparticles were immersed in Milli-Q water and sonicated for 2 hours. Blanks containing just Milli-Q water as well as clean silica nanoparticles were also sonicated as a solvent blank and method blank. Conductivity of the HOCl exposed samples increased above twice the background and the ion concentration of Cl<sup>-</sup> and ClO<sub>3</sub><sup>-</sup> was enhanced above a magnitude in comparison to the blank.

Though AMTIR crystals are normally used for somewhat caustic and/or acidic systems, it was evident throughout this experiment that the crystal itself was reacting with the HOCl/Cl<sub>2</sub> gas. Not only does a singular peak increase over time around 850 cm<sup>-1</sup>, eventually after many

uses and long term exposures, an oxide layer will form on the crystal. Diamond powder (Pike Technologies) at various grit sizes were used to clean this oxide layer and regenerate the flat AMTIR crystal surface. The crystal is made up of a brittle alloy of selenium, arsenic, and germanium. It can be hypothesized that the chemical similarity between germanium and silicon possibly led to a similar interaction with the oxidant. A ZnSe crystal (Pike Technologies) exposed to the same conditions did not show any unwanted byproducts, however due to its limitations in pH range and weak signal below  $1000\text{ cm}^{-1}$ , it was not further used for this study.

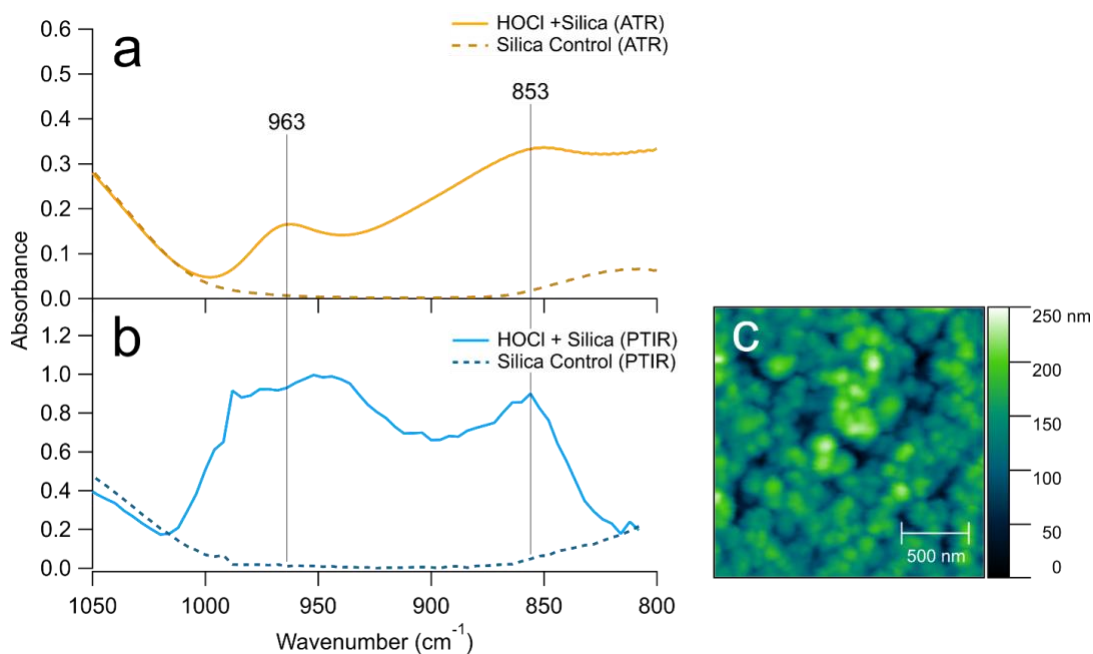


Figure 7.2. Comparison of infrared spectra of HOCl absorbing and reacting with (a)  $\text{SiO}_2$  collected using ATR-FTIR spectroscopy, via online analysis, using an AMTIR crystal (solid orange) and, (b) via offline analysis, AFM-PTIR spectroscopy (solid light blue). Controls of unreacted bare silica are shown in the dashed lines for both methods. Height image of the exposed silica thin film in (c) measured using AFM. *Data and images by Victor Or.*

To show that the product peaks could be formed independent of the AMTIR crystal surface, a silica substrate with a thin film of the silica nanoparticles was exposed to similar conditions of HOCl and  $\text{Cl}_2$  gas for about two hours. After the period of desorption, the infrared spectra of the surface were measured using atomic force microscopy photothermal infrared

(AFM-PTIR) spectroscopy. In the absence of the AMTIR crystal, the interaction between the gas and silica surface shows similar results in Figure 2 – namely the 963 and 853  $\text{cm}^{-1}$  peaks. The third peak at 730  $\text{cm}^{-1}$  could not be seen due to the spectral limitations of the AFM-PTIR below 800  $\text{cm}^{-1}$ . The height comparisons between the two peaks shown in Figure 2 are clearly different. It could be simply hypothesized that this could be a difference between methods.

An amorphous  $\text{SiO}_2$  pseudo structure was formed using a total of 62 atoms using Spartan Software (Wavefunction Inc.). The geometries of the energy minimized cluster were calculated at the B3LYP/6-311+G\*\* level of theory. Molecular vibrational frequency calculations performed at the EDF2 DFT level of theory.<sup>16</sup> Scaling factors to account for anharmonicity in the calculated frequencies were not used in this study. Similar to the B3LYP model, the EDF2 functional provides slightly more accurate results for vibrational spectra while also decreasing computation time.

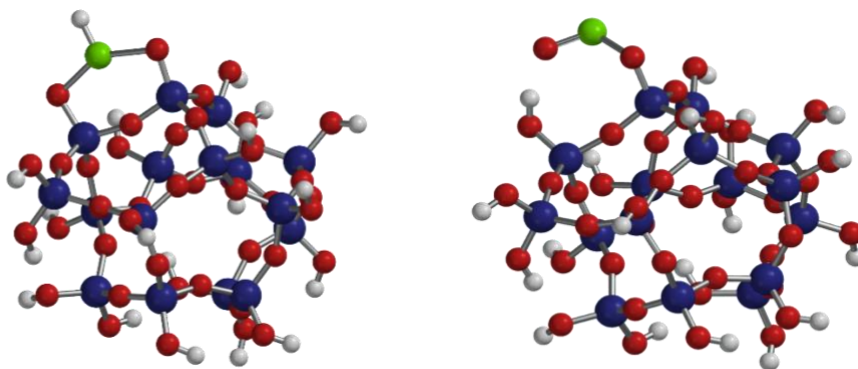


Figure 7.3. Images of the  $-\text{ClO}_2$  molecule bonded to an  $\text{SiO}_2$  surface in two different hypothetical conformations: a) bridging bidentate and b) monodentate, surrounded by surface hydroxyl groups. The chlorine atoms are colored green, the silicon atoms blue, the oxygen atoms red, and the hydrogen atoms are white.

Of the different possible binding modes, the monodentate form and the bridging bidentate forms (in this case of  $\text{Si-ClO}_2$ ), were found to have the most similar vibrational modes to the

experimental data. The theoretical monodentate major vibrational modes included 988 and 827  $\text{cm}^{-1}$ ,  $\delta(\text{Si-OCIO})$  with contributions from nearby Si-OH and  $\nu(\text{Si-OCIO})$  respectively. Thus, the experimental peak at 963  $\text{cm}^{-1}$  can be tentatively assigned as the monodentate form of Si-ClO<sub>2</sub>. Shown in Table 1,  $\nu(\text{Si-OCIO})$  in the theoretical calculations was shown to be smaller in intensity and is possibly present as a shoulder in the spectral peaks. The theoretical bridging bidentate major vibrational modes included 726, 743, and 844  $\text{cm}^{-1}$ , where 726 and 743  $\text{cm}^{-1}$  were defined as  $\omega(\text{Cl-H})$  with contributions from the ring breathing and 844  $\text{cm}^{-1}$  was defined as  $\nu(\text{SiO-ClO}_2\text{-H})$ . These calculated vibrational modes can be tentatively assigned as the 953 and 730  $\text{cm}^{-1}$  peaks found in Figure 1 as the bridging bidentate form of Si-ClO<sub>2</sub>. As scaling factors accounting for anharmonicity were not used for this study, it should be noted that the agreement between the theoretical and experimental frequencies for the  $\nu(\text{SiO-H})$  mode can be considered abnormal. While it would be expected that the difference in these frequencies at the higher energies should be larger, on the order of 100-300  $\text{cm}^{-1}$ , the variance in frequencies below 1000  $\text{cm}^{-1}$  should be quite close to accurate (around 20-80  $\text{cm}^{-1}$ ).<sup>17</sup> Thus, for this preliminary investigation into this interaction between silica and HOCl where product vibrational frequencies are between 700 and 1000  $\text{cm}^{-1}$ , these calculations are deemed to be sufficient but should be considered with caution.

Table 7.1 Theoretical and Experimental Vibrational Mode Assignments (in  $\text{cm}^{-1}$ ) for Adsorbed HOCl (as surface  $-\text{ClO}_2$ ) on the Surface of Silica

Experimental IR Frequency	Theoretical IR Frequency	Calculated Normalized Intensity	Assigned mode	Literature Values
3751	3740, 3713	0.23, 1.00	$\nu(\text{SiO-H})$	3742
1200	1252	0.6	$\nu(\text{SiOSi, cyc})$	1200-1250
1112	1095, 1099	0.53, 0.59	$\nu(\text{SiOSi,as})$	1100
	785	0.18	$\nu(\text{SiOSi,sym})$	800
963	988	0.31	OCIO-Si-OH H bonding bending (monodentate)	
	827	0.22	$\nu(\text{Si-OCIO})$ (monodentate)	
859	844	0.2	$\nu(\text{SiO-ClO}_2\text{-H ring})$ (bridging bidentate)	
730	726, 743	0.14, 0.26	Cl-H wagging/rocking with contributions from ring breathing (bridging bidentate)	

An AFM image of the exposed silica thin film is seen in Figure 2c. A closer look at the surface can be achieved with TEM, as shown in Figure 4. Clean silica nanoparticles in Figure 3a are expectedly very smooth, while images of the particles taken after exposure to the HOCl gas show an increase in surface roughness. This data further hints at the possibility of surface roughening and maybe even etching due to the presence of the strong oxidant. Further studies should be prepared to distinguish between etching and surface functionalization – as each of



these mechanisms will have various impacts on the chemical and physical properties of the surface itself.

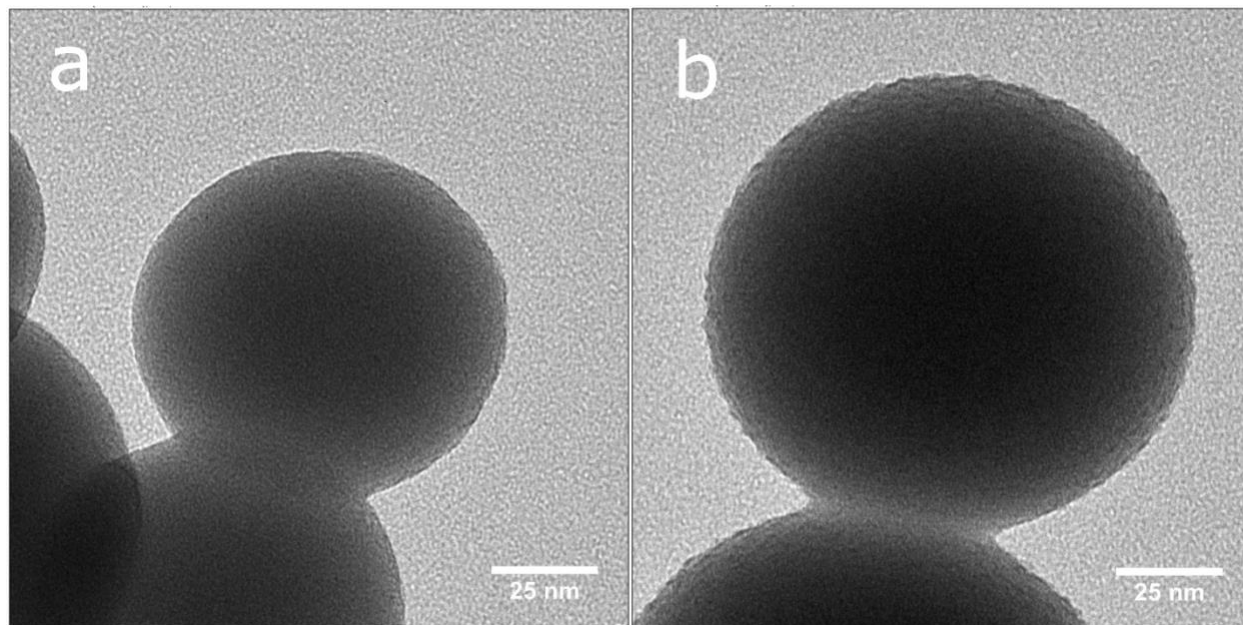


Figure 7.4. TEM images of a silica nanoparticle that is a) clean and b) exposed to HOCl/Cl<sub>2</sub>. Images taken by Izaak Sit.

Commercial bleach products contain a multitude of other ingredients besides sodium hypochlorite, including (but not limited to): anionic and non-ionic organic surfactants, carbonates, dye transfer inhibitors using polyamine N-oxide polymers or various other imidazole/pyrrolidone based polymers, organic acids, and more. To measure the impact this realistic model of chlorine cleaning would have on the silica, a bleach solution (Clorox) was acidified and its headspace (measured RH < 20%) was allowed to interact with a silica thin film. As shown in Figure 5, similar partially and irreversibly bound chlorine-oxide peaks appear, albeit in different relative intensities compared to the model HOCl + silica experiment. However, unlike the model experiment, many other additional peaks are observed to reversibly adsorb onto the silica thin film and possibly compete for active sites with the produced HOCl gas. The largest peak at 3202 cm<sup>-1</sup> clearly indicates the presence of a secondary, and likely aliphatic, amine

probably derived from one of the nitrogen-containing polymers commonly found in bleach patents. Additional new peaks between 1700-1200  $\text{cm}^{-1}$  shows some absorbed water at 1640  $\text{cm}^{-1}$ , methylene groups (surfactants/polymers) at 1445  $\text{cm}^{-1}$ , and other modes at 1200 and 1096  $\text{cm}^{-1}$  or other various organic species such as the N-H bending mode, that all eventually desorb upon the use of dry zero air an hour after the experiment. The change in relative intensities of the chlorine oxyanion peaks between 1000 and 700  $\text{cm}^{-1}$  in the bleach experiment compared to the HOCl + silica model experiment could be due to many reasons, the most likely being 1) the presence of surface water, and/or 2) the presence of a large amount of heteroatom-containing organic molecules. Nevertheless, it seems that even with water and a significant number of organic species nearby on the surface, HOCl irreversibly interacts with the silica surface.

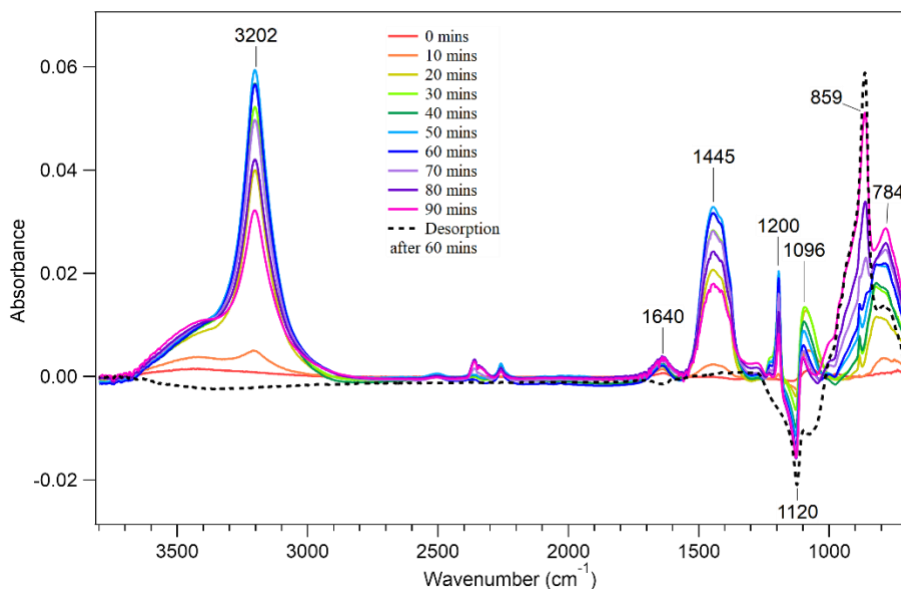


Figure 7.5. FTIR difference spectra of  $\text{SiO}_2$  following exposure to the headspace gases collected from an acidified bleach (Clorox) solution under relatively dry conditions ( $\text{RH} < 15\%$ ) as a function of time. A spectrum was collected following 60 minutes of dry clean air flowing over the bleach-exposed silica thin film (shown by the black dashed line). Spectrum used for background subtraction was a clean silica thin film in dry air.

Thus, these bleach cleaning experiments show that several different chemical species partition onto the surface. Several of these species are similar to when HOCl absorbs onto  $\text{SiO}_2$

to form the suspected  $\text{ClO}_x$  surface bound products that remain on the surface after the bleach headspace gas is no longer in the flow system. In contrast, all other chemical species, including secondary amines, desorb from the surface after flowing bleach-free air over the sample.

## 7.5 Conclusions

Multiple species, tentatively identified as  $\text{ClO}_x$ , at the surface are formed from the exposure of  $\text{HOCl}$  gas to hydroxylated  $\text{SiO}_2$  as identified by vibrational spectroscopy. Some of these species were successfully desorbed and analyzed using ion chromatography. The enrichment of  $\text{Cl}^-$  and presence of  $\text{ClO}_x^-$ , along with the decrease in the Si-O-Si bonds as indicated from infrared spectroscopy, highlight that there are possibly multiple mechanisms involved in these interactions. Calculation of a model  $\text{ClO}_x$  species associated with the silica surface further show the low frequency region between  $1000$  and  $725\text{ cm}^{-1}$  is due to Cl-O stretching motion consistent with the ATR-FTIR and AFM-PTIR spectra. Attempts to analyze these surface products using x-ray photoelectron spectroscopy (XPS) proved null (i.e. no enhancement in the Cl or O regions), showing these products desorb from the surface under vacuum conditions. This was perhaps suggested by the ATR-FTIR experiments, where the products showed slight but incomplete reversibility during desorption. Images of the silica particles using TEM may show evidence that the surface is being roughened by the highly oxidative gas, which could also account for some peak shifting in the IR spectra. Nevertheless, these results show that the use of chlorine cleaning products leads to complex and currently unknown surface chemistry. While the work here was done purely between gas and solid phases, bleach is commonly applied directly onto surfaces. Other common surfaces, such as those containing  $\text{TiO}_2$  or  $\text{Al}_2\text{O}_3$ , are expected to also have unique interactions with  $\text{HOCl}$  and organics present. Future work should aim to qualitatively determine the compositions of such systems so

that a quantitative understanding of the sources and sinks of indoor relevant oxidants may be further developed. The studies of bleach with SiO<sub>2</sub> show similar interactions with HOCl and other components including buffers, secondary amines, polymers, aromatics, and more.

## 7.6 Acknowledgements

The authors gratefully acknowledge the support of the Alfred P. Sloan Foundation under grant number G-2017-9692 and the National Science Foundation Graduate Research Fellowship Program (DGE1650112).

Chapter 7 is in preparation: Alves, M.R.; Deelepojananan, C.; Or, V.W.; Sit, I.; Grassian, V.H. SiO<sub>2</sub> Interactions with Hypochlorous Acid: Insights into the Interaction of Cleaning Products with Glass Surfaces. 2021. The dissertation author is the primary investigator and author of this paper.

## 7.7 References

- (1) Farmer, D. K.; Vance, M. E.; Abbatt, J. P. D.; Abeleira, A.; Alves, M. R.; Arata, C.; Boedicker, E.; Bourne, S.; Cardoso-Saldaña, F.; Corsi, R.; Decarlo, P. F.; Goldstein, A. H.; Grassian, V. H.; Hildebrandt Ruiz, L.; Jimenez, J. L.; Kahan, T. F.; Katz, E. F.; Mattila, J. M.; Nazaroff, W. W.; Novoselac, A.; O'Brien, R. E.; Or, V. W.; Patel, S.; Sankhyan, S.; Stevens, P. S.; Tian, Y.; Wade, M.; Wang, C.; Zhou, S.; Zhou, Y. Overview of HOMEChem: House Observations of Microbial and Environmental Chemistry. *Environ. Sci. Process. Impacts* **2019**, 21 (8), 1280–1300.
- (2) Weschler, C. J. The Influence of Ventilation on Reactions among Indoor Pollutants: Modeling and Experimental Observations. *Indoor Air* **2000**, 10 (2), 92–100.
- (3) Nazaroff, W. W.; Weschler, C. J. Cleaning Products and Air Fresheners: Exposure to Primary and Secondary Air Pollutants. *Atmos. Environ.* **2004**, 38 (18), 2841–2865.
- (4) Gligorovski, S.; Abbatt, J. P. D. An Indoor Chemical Cocktail. *Science* (80-. ). **2018**, 359 (6376), 632–633.

- (5) Wong, J. P. S.; Carslaw, N.; Zhao, R.; Zhou, S.; Abbatt, J. P. D. Observations and Impacts of Bleach Washing on Indoor Chlorine Chemistry. *Indoor Air* **2017**, *27* (6), 1082–1090.
- (6) Fu, E.; McCue, K.; Boesenberg, D. Chemical Disinfection of Hard Surfaces – Household, Industrial and Institutional Settings. In *Handbook for Cleaning/Decontamination of Surfaces*; Elsevier, **2007**; pp 573–592.
- (7) Weschler, C. J.; Wells, J. R.; Poppendieck, D.; Hubbard, H.; Pearce, T. A. Workgroup Report: Indoor Chemistry and Health. *Environ. Health Perspect.* **2006**, *114* (3), 442–446.
- (8) Parks, J.; McCandless, L.; Dharma, C.; Brook, J.; Turvey, S. E.; Mandhane, P.; Becker, A. B.; Kozyrskyj, A. L.; Azad, M. B.; Moraes, T. J. Association of Use of Cleaning Products with Respiratory Health in a Canadian Birth Cohort. *Cmaj* **2020**, *192* (7), E154–E161.
- (9) Quirce, S.; Barranco, P. Cleaning Agents and Asthma. *J. Investig. Allergol. Clin. Immunol.* **2010**, *20* (7), 542–550.
- (10) Bukalasa, J. S.; Brunekreef, B.; Koppelman, G. H.; Vonk, J. M.; Gehring, U. Use of Cleaning Agents at Home and Respiratory and Allergic Symptoms in Adolescents: The PIAMA Birth Cohort Study. *Environ. Int.* **2019**, *128*, 63–69.
- (11) Valentine, R. L.; Jafvert, C. T. Reaction Scheme for the Chlorination of Ammoniacal Water. *Environ. Sci. Technol.* **1992**, *26* (3), 577–586.
- (12) Mattila, J. M.; Lakey, P. S. J.; Shiraiwa, M.; Wang, C.; Abbatt, J. P. D.; Arata, C.; Goldstein, A. H.; Ampollini, L.; Katz, E. F.; DeCarlo, P. F.; Zhou, S.; Kahan, T.F.; Cardoso-Saldaña, F.J.; Ruiz, L.H., Abeleira, A.; Boedicker, E.K.; Vance, M.E.; Farmer, D.K. Multiphase Chemistry Controls Inorganic Chlorinated and Nitrogenated Compounds in Indoor Air during Bleach Cleaning. *Environ. Sci. Technol.* **2020**, acs.est.9b05767.
- (13) Suh, M.; Bagus, P. S.; Pak, S.; Rosynek, M. P.; Lunsford, J. H. Reactions of Hydroxyl Radicals on Titania, Silica, Alumina, and Gold Surfaces. *J. Phys. Chem. B* **2000**, *104* (12), 2736–2742.
- (14) Fang, Y.; Lakey, P. S. J.; Riahi, S.; McDonald, A. T.; Shrestha, M.; Tobias, D. J.; Shiraiwa, M.; Grassian, V. H. A Molecular Picture of Surface Interactions of Organic Compounds on Prevalent Indoor Surfaces: Limonene Adsorption on SiO<sub>2</sub>. *Chem. Sci.* **2019**, *10* (10), 2906–2914.
- (15) Burkholder, J. B.; Sander, S. P.; Friedl, R. R.; Golden, D. M.; Kurylo, M. J.; Moortgat, G. K.; Wine, P. H.; Ravishankara, a R.; Kolb, C. E.; Molina, M. J.; et al. Chemical Kinetics and Photochemical Data for Use in Atmospheric Studies Evaluation Number 15. *Cross Sect.* **2015**, *California* (15), 1–153.

## Chapter 8: Future Directions

The work described in Chapter 5 effectively highlights the future work planned for the studies involving marine dissolved organic matter and marine chromophoric dissolved organic matter. This large-scale collaboration will continue to model experiments around a central stock of the organic matter samples, while also establishing collaborative publications in high impact journals. While Chapter 4 used the progression of biology and some advanced analyses of the mass spectra data, more effort is needed to isolate and characterize the chromophoric fraction of marine dissolved organic matter. Tandem mass spectrometry and the molecular networking databases like GNPS seems to be promising for this type of work. Thus far, a thorough fractionation of the organic matter (such as size exclusion chromatography) coupled with ultraviolet visible spectroscopy has not been carried out using the networking method. Additionally, preliminary experiments of introducing certain oxidants such as ozone or  $\text{NO}_x$  to irradiated marine dissolved organic matter, led to some very interesting but uncharacterized products. The mechanisms involved with these products and their possible impact on climate relevant processes are interesting concepts that should be investigated. Finally, the work concerning the search for a new marine-relevant molecular model for marine chromophoric dissolved organic matter is a currently ongoing research project amongst multiple collaborators. The ability to provide relevant mechanistic and kinetic data on marine organic photochemistry, using a widely available model system, would be incredibly useful. Whether this model is one or more molecular species or combined with other components such as ions and metals still needs to be determined. Certainly, this model must contain some sort of unsaturation and aromatic center as well as a relatively long-lived triplet state. Recent studies, as well as the ones presented in this dissertation, also point toward the inclusion of nitrogen moieties in this possible model.

Chapter three of this thesis presented a study conducted to frame the usage and comparison of marine organic matter to other model systems. Since photochemical processes drive a significant fraction of the daytime gas-phase production chemistry in the atmosphere, an investigation aimed at understanding the role of photosensitizers in the marine environment was carried out. Marine photosensitizers are not well characterized, as dissolved organic matter is notoriously complex. Traditionally, terrestrial based matter and models are used for marine relevant systems. However, in this study, we show that this may not be the best course of action. Molecular analysis of three different photosensitizers, and their photochemical properties, are presented. This study sheds light on the relevance of photochemical reactions in the marine environment and the need for more relevant experimental models.

Chapter four highlighted the results from the dissolved organic matter collected from the 2019 SeaSCAPE campaign. Similar to Chapter 3, the marine dissolved organic matter is extracted using the solid phase extraction method. However, the extractions take place over the course of a microbial bloom set inside a mesocosm, and thus isolated, environment. Using this time resolved data, newly produced species correlated with the increases in the ultraviolet absorption spectra, provides unique insight into possible markers of chromophores. The high-resolution mass spectra allow for molecular characterization while additional MS/MS data can be used to discover structural matches from a centralized database (GNPS). This study provides a much-needed foundation for experimentalists looking to model marine organic matter and relevant photochemical mechanisms.

Chapter five initially provides an overview of a large-scale collaborative effort put together over the last two years. Understanding the scale of complexity of marine dissolved organic matter from chapter three and four, and the lack of a central sample for it, a large amount

of the sample was collected from the SeaSCAPE 2019 campaign. To date, twelve research groups have joined the collaborative to focus on four major areas related to understanding marine dissolved organic matter: 1) Characterization, 2) Reactivity, 3) Properties, and a 4) Molecular Model Search. Though the COVID-19 pandemic has delayed a lot of the progress, as many others likely can agree with, the collaboration had begun to publish high impact studies involving the use of the sample. The latter part of chapter five partially reproduces a manuscript currently accepted for publication, co-first authored by Emily Barnes-Franklin. This study used the sample, which extracted from coastal seawater, to characterize the presence and reactivity of a class of anthropogenic compounds called benzothiazoles. How man-made compounds that ultimately enter the environment can impact vital natural processes is a field of current interest.

Chapter six investigates the interaction of a simple two-component model system containing a keto-acid, pyruvic acid, and a metal oxide such as titanium dioxide (paint) and aluminum oxide (plastics, additives, etc.). All such components are relevant to the indoor environment. The field of indoor chemistry, gaining considerable interest in scientific community in the past decade, has resulted in a surge of questions related to indoor pollution, chemistry, and public health. This study hypothesizes the unique adsorption and photochemistry that would occur on a metal oxide surface, especially those with semi-conductive properties. Interestingly, not only did pyruvic acid oligomerize significantly when exposed to light, but it also went through unique dark reactions on the surface upon adsorption. This research presented some unique mechanistic information to the chemistry of keto acids, but also outlined the importance of surfaces on the fates of volatile organic compounds relevant to the indoor environment.



Chapter seven expands upon the surface chemistry questions from chapter six by investigating the role of cleaning products on indoor surfaces – specifically the hypochlorous acid generated by bleach. Strong oxidizers that are commonly used in the indoor environment can dominate the indoor chemical “cocktail” on short time scales, yet it is one of the least understood aspects of the field. Window glass, or silica, is used as an initial and “inert” surface for the study. However, it was found that the hypochlorous acid and chlorine gas were able to uniquely react with the silica surface – as supported by infrared spectroscopy. The unknown and partially irreversibly bound products on the surface raises an interesting question of how such cleaners are capable of altering surface physiochemical properties and what exactly that means for the indoor environment.

Results from Chapter 7 showed the interactions between strong oxidants and indoor relevant surfaces. Future projects aim to recreate the adsorption of hypochlorous acid on other type of surfaces as well as introduce organics like limonene to investigate changes in surface properties or surface catalyzed chlorination products. The importance of surface adsorbed water in surface chemical mechanisms has been highlighted in many past studies and should likely be further explored for the surface chemistry of indoor oxidants.

In conclusion, the studies and future work discussed throughout this thesis offers better understanding of the controlling factors in the marine environment and relevance of environmental heterogeneous chemistry and photochemistry in addition to the role of surface chemistry in indoor environments. These studies, as well as similar ones, ultimately aim to improve our ability to model and characterize the world around us – whether that be outdoors, the Earth’s climate, or in our homes and workplaces.